LBNL-45193

ERNEST ORLANDO LAWRENCE
BERKELEY NATIONAL LABORATORY

Nuclear Magnetic Resonance of Laser-Polarized Noble Gases in Molecules, Materials, and Organisms

Boyd M. Goodson

Materials Sciences Division

December 1999

Ph.D. Thesis

DISCLAIMER

Portions of this document may be illegible in electronic image products. Images are produced from the best available original document.

LBNL-45193

Nuclear Magnetic Resonance of Laser-Polarized Noble Gases in Molecules, Materials, and Organisms

Boyd McLean Goodson
(Ph.D. Thesis)

Materials Sciences Division
Ernest Orlando Lawrence Berkeley National Laboratory
University of California
Berkeley, California 94720

December 1999

This work was supported by the Director, Office of Science, Office of Basic Energy Sciences, Materials Sciences Division, of the U.S. Department of Energy under Contract No. DE-AC03-76SF00098.

Abstract

Nuclear Magnetic Resonance of Laser-Polarized Noble Gases in Molecules, Materials, and Organisms

by

Boyd McLean Goodson

Doctor of Philosophy in Chemistry

University of California at Berkeley

Professor Alexander Pines, Chair

Conventional nuclear magnetic resonance (NMR) spectroscopy and magnetic resonance imaging (MRI) are fundamentally challenged by the insensitivity that stems from the ordinarily low spin polarization achievable in even the strongest NMR magnets. However, by transferring angular momentum from laser light to electronic and nuclear spins, optical pumping methods can increase the nuclear spin polarization of noble gases by several orders of magnitude, thereby greatly enhancing their NMR sensitivity.

This dissertation is primarily concerned with the principles and practice of optically pumped nuclear magnetic resonance (OPNMR). The enormous sensitivity en-

hancement afforded by optical pumping noble gases can be exploited to permit a variety of novel NMR experiments across many disciplines. Many such experiments are reviewed, including the void-space imaging of organisms and materials, NMR and MRI of living tissues, probing structure and dynamics of molecules in solution and on surfaces, and zero-field NMR and MRI.

Nuclear Magnetic Resonance of Laser-Polarized Noble Gases in Molecules, Materials, and Organisms

by

Boyd McLean Goodson

For Amy

Contents

List of Figures

List of Tables

Introduction

Nuclear Magnetic Resonance of Laser-Polarized Noble Gases

in Molecules, Materials, and Organisms

The phenomenon of nuclear magnetic resonance (NMR) is the basis for what are arguably the most powerful analytical tools in the spectroscopist's arsenal. Over the fifty-five-year history of its study, countless NMR techniques have been developed to permit, for example, the detailed study of structure and dynamics of molecules in solution, the characterization of the bulk and surface properties of materials, and the imaging of tissues in living organisms. Unfortunately, conventional NMR methods suffer from a common drawback that in many circumstances, can limit their power and applicability—a notorious lack of sensitivity. This fundamental insensitivity originates from the miniscule size of nuclear magnetic moments, which results in an exceedingly small equilibrium nuclear spin polarization in even the largest magnets.

In certain systems, however, the sensitivity of NMR spectroscopy and magnetic resonance imaging (MRI) can be greatly enhanced via optical pumping. In optical pumping, angular momentum can be transferred from laser photons to electronic and nuclear spins, thereby transiently enhancing the nuclear spin polarization in these systems by four to five orders of magnitude.

This dissertation reviews selected topics in optically pumped nuclear magnetic resonance (OPNMR). Examples provided from our laboratory and elsewhere are described that demonstrate the power and promise of various novel approaches.

In the first two chapters, relevant portions of theoretical and experimental aspects of NMR and optical pumping are briefly reviewed. The remainder of this thesis deals exclusively with the development and application of novel NMR techniques using laser-polarized noble gases. Following an introduction of the properties of laser-polarized gases in the third chapter, the fourth and fifth chapters are concerned with using laser-polarized xenon to probe structure and dynamics of molecules in solution. Of particular interest is the spin polarization-induced nuclear Overhauser effect (SPINOE), which can result in selective polarization transfer from laser-polarized xenon to solution species, in a manner dictated by the relative distance and dynamics between xenon and molecules in solution.

The sixth and seventh chapters describe how laser-polarized gases can be used to study materials with a variety of imaging and spectroscopic techniques, including enhanced ^{129}Xe NMR spectroscopy, polarization transfer to surface spins via SPINOE and cross-polarization, studies of boundary restricted diffusion, void-space imaging, and the imaging of flow through porous materials.

The eighth chapter presents work from the fastest growing segment of the OP-NMR field: the application of laser-polarized gases for biomedical and clinical studies. Following a description of *in vivo* void-space imaging of the lungs, recent studies using laser-polarized gases to probe living tissues will be discussed, with special attention given to issues of noble gas relaxation and delivery *in vivo*. The ninth and final chapter of this work describes new low/zero-field experiments permitted by the inherent

non-equilibrium nature of the laser-induced polarization of these gases, and concludes by considering some possible future directions of this exciting field.

Acknowledgements

During my four years as a graduate student at U.C. Berkeley, literally hundreds of individuals have contributed in some part to my growth as a scientist, as a teacher, and as a person. Naturally, space does not permit me to address each person by name; however, I will do my best to acknowledge those to whom I am most indebted.

First, I would like to thank my advisor, Alexander Pines for his support, encouragement, and inspiration, as well as for providing me with a stimulating, exciting, and fun research environment. Second, I would like to thank our group's secretary and honorary "Queen Mum", Dione Carmichael, for her indispensable aid in the day-to-day operations of the Pines Group and her helpful advice during my tenure over the last four years.

Without a doubt, the people that I have had the pleasure to work with on the optical pumping project made my Ph.D. research such a wonderful experience. The very nature of the optical pumping experiments described in this thesis *demands* teamwork; as such, I am indebted to a great many people who have been my friends and colleagues for the last four years on the optical pumping project. I owe my greatest thanks to postdocs Yi-Qiao Song and Rebecca Taylor, who took me under their collective wing when I first joined the OP project. Since that time I have thoroughly enjoyed working with postdocs Stephan Appelt, Eike Brunner, Thomas de Swiet, Mathias Haake, Michel Luhmer, Thomas Meersmann, Thomas Rõõm, Sunil Saxena, Roberto Seydoux, and Roberto Simonutti; Graduate students David Laws,

Hans Bitter, Lana Kaiser, Annjoe Wong-Foy, Robert Havlin, John Logan, Adam Moule, and Megan Spence; and undergraduates Michelle Cyrier and Bhima Sheridan.

I have also had the distinct pleasure of collaborating with a variety of excellent scientists in many of the projects in which I have participated in the Pines Group. Professor Gil Navon (Tel Aviv) was a constant source of ideas and advice during our collaborations studying SPINOE polarization transfer in solution and the biomedical applications of laser-polarized xenon. Dr. Thomas Budinger of LBNL was especially helpful in our work investigating potential *in vivo* applications of laser-polarized xenon; I greatly appreciate the fact that Dr. Budinger would often take hours out of his busy schedule to speak with me regarding numerous matters from the behavior of MRI tracers *in vivo* to the physics of ice bergs. Victor Schepkin and Katie Brennan were instrumental in many of the experimental aspects of the *in vivo* imaging experiments; I also enjoyed working with Angelo Bifone (ICR London) and Tanja Pietraß (NM Tech) in the earlier *in vitro* xenon/blood experiments. A.C. Gossard and K. Maranowski (UCSB) worked with Yi-Qiao and myself on the quantum well experiments and were responsible for the fabrication and initial characterization of the quantum well samples we studied. Professor Jeffrey Reimer was very helpful with considerations of high-pressure NMR, along with materials applications of laser-polarized gases. It was a pleasure working with Professor Robert Bergman and Jake Yeston in experiments attempting to directly observe xenon-metal bonds in photo-excited inorganic complexes. Most recently, I have enjoyed working along side

Robert McDermott as a part of the long-running SQUID collaboration between the Pines Group and the group of Professor John Clarke in the Physics Department. Finally, Professor David Wemmer, along with Wemmerites Jonathan Heller, Corey Liu, and Seth Rubin have been wonderful colleagues throughout our numerous studies of xenon/protein interactions.

More recently, I have had the distinct pleasure of becoming an "honorary" member of the NMR quantum computing project, which has given me the opportunity to participate in many stimulating discussions regarding NMRQC, liquid crystals, and laser-polarized xenon with Issac Chaung (IBM Almaden), as well as with fellow PineNuts Maggie Marjanska, Mark Kubinec, Jamie Walls, Bo Blanton and Franca Castiglione.

I would also like to collectively thank the rest of the PineNuts, past and present, along with a variety of associated collaborators for providing me with a challenging, stimulating environment in which to work; I am especially grateful to Matt Augustine, Seth Bush, Stefano Calderelli, Gerry Chingas, Yung-Ya Lin, David Pripstein (Caltech), Fred Salsbury, Marco Tomaselli, and Jeff Yarger for countless helpful discussions and advice.

On a more editorial note, I am indebted to numerous individuals who granted me access to their figures and data (both published and unpublished) so that I could include them in my reviews (and ultimately compile them in this dissertation). Other than members of the Pines Group (past and present), I would specifically like to

thank the OP NMR/MRI groups at Duke (G. Allan Johnson, Harald Möller, and Mark Chawla), ENS Paris (Genevieve Tastevin), Harvard (HSCfA: Glenn Wong and Ronald Walsworth; Brigham and Women's Hospital: Mitchell Albert and Arvind Venkatesh), ICR London (Angelo Bifone), Michigan (Scott Swanson), MIT (David Cory), Princeton (Karen Sauer and William Happer), and Virginia (John Mugler and James Brookeman).

Financially, I am grateful to the Eastman Chemical Company for awarding me with a fellowship in the area of Physical Chemistry. I am also grateful to the Department of Energy, which has funded our research through Lawrence Berkeley National Laboratory.

Next, I would like to thank my friends that made these four years fly by so fast, from David Laws and the rest of the Magnetic Fielders, to my classmates from Old Nassau that (sooner or later) came out with me to Berkeley, especially Hans Bitter, Paul Cernota, Peter Dosa and David "Netscape Dave" Wagner; all provided friendly, familiar faces that helped to make Berkeley seem much closer to home. I would also like to thank my undergraduate advisor, Professor Warren Warren, who helped suggest that Berkeley, and the Pines Group in particular, would be an ideal place to obtain my Ph.D. Incidentally, I am also very grateful to Professor Ahmed Zewail, who by offering me a post-doctoral position in Femtoland, has given me considerable encouragement to finish this thesis as expeditiously as possible!

I am most indebted to my family for their love and support through my education,

and I am particularly thankful for the examples set by my parents and siblings. Finally and most importantly, I thank my wife Amy for her unwaivering love, devotion, support, encouragement, and drive, and for faithfully tolerating my research habit.

Chapter 1

Relevant Components of the NMR Hamiltonian

1.1 Introduction

In order to preface the detailed discussions of OPNMR that comprise this thesis, the fundamentals of NMR phenomena must first be briefly introduced. However, space does not permit an all-inclusive description of NMR principles and techniques. Instead, important features of the NMR Hamiltonian will be described here in a general way, while the portions of NMR theory and experiment that are particularly relevant to the material presented in this thesis will be described later within the context of such work. When greater depth into NMR theory and practice is required, the reader is directed to Refs. [1, 2, 3, 4, 5, 6] for a selection of excellent NMR books

and monographs. In addition to these works, Refs. [7, 8, 9] should prove especially helpful for grounding NMR in the general perspective of quantum mechanics and spectroscopy. Throughout this thesis, the simplest possible notation and means of description permitted by the material will often be employed, and formalism will be borrowed from many of the sources listed above and elsewhere.

1.2 Spins in Applied Fields

1.2.1 The Effects of a Static Magnetic Field

The Zeeman Interaction

In most circumstances relevant to this thesis, the Zeeman interaction is the most important contribution to the nuclear spin Hamiltonian. Consider a nucleus with spin quantum number $I \neq 0$, with magnetic dipole moment $\vec{\mu} = \gamma\hbar\vec{I}$, where γ is the nuclear gyromagnetic ratio, $\hbar$ is Planck's constant divided by 2π, and $\vec{I}$ is the nuclear spin operator. The magnitude of $\vec{\mu}$ is given by $\mu = \hbar\gamma\sqrt{I(I+1)}$. In the absence of an external magnetic field, a nucleus with spin quantum number I possesses $(2I+1)$ degenerate eigenstates $|I, m_I\rangle$, where the magnetic quantum number $m_I = -I, -I+1, ..., I-1, I$. However, the application of a strong external magnetic field $\vec{B_0}$ removes this degeneracy, owing to the interaction between the field and the

magnetic dipole moment:

$$H_Z = -\vec{\mu} \cdot \vec{B_0}, \tag{1.1}$$

$$= -\gamma \hbar B_0 I_z, \tag{1.2}$$

where H_Z is the Zeeman Hamiltonian; here, the direction of $\vec{B_0}$ is defined to be along the $\vec{z}$-axis.

In a classical picture, $\vec{B_0}$ causes each nuclear moment to precess about the $\vec{z}$-axis. The angular rate of precession is given by

$$\omega_0 = -\gamma B_0, \tag{1.3}$$

where ω_0 is known as the Larmor frequency of the system. The projection of $\vec{\mu}$ along $\vec{z}$, $\mu_z = \hbar \gamma I_z$, is naturally given by the angle α between $\vec{\mu}$ and $\vec{B_0}$ ($\cos\alpha = \mu_z/\mu$). However, quantum mechanics dictates that α is quantized; the operator I_z has the familiar eigenvalue relation:

$$I_z|I, m_I\rangle = m_I|I, m_I\rangle. \tag{1.4}$$

Therefore, α will be constrained according to the values of m_I (e.g., giving $\alpha \approx 54.74°$ for $I = 1/2$).

Additionally, we can manipulate the time-independent Schödinger equation

$$H|\psi_i\rangle = E_i|\psi_i\rangle, \tag{1.5}$$

to obtain the eigenengergies of $|I, m_I\rangle$:

$$E(m_I) = \langle I, m_I|H_Z|I, m_I\rangle, \tag{1.6}$$

$$= -\gamma\hbar B_0 m_I. \tag{1.7}$$

The Zeeman energy is the difference in energy between two adjacent levels (i.e., $\Delta m_I = \pm 1$:

$$\Delta E = \gamma\hbar B_0. \tag{1.8}$$

Thus, a photon with frequency equal to the Larmor frequency $\omega_0 = \gamma B_0$ will be resonant with these levels.

Given a typical magnetic field strength of 10 T, the Larmor frequency will be in the radio frequency (rf) regime of the electromagnetic spectrum (10s to 100s of MHz). Other contributions to the NMR Hamiltonian (described in the following sections) are normally orders of magnitude smaller that the Zeeman contribution, and therefore they generally can be considered as perturbations to the Zeeman Hamiltonian.

Consider an ensemble of spin $I = 1/2$ nuclei (with positive γ) in a magnetic field.

Each nuclear spin will precess about the $\vec{z}$-axis at the Larmor frequency, drawing out a cone. Specifically, the spins with $m_I = +1/2$ will draw out a cone with its mouth pointing "up" with respect to the $\vec{z}$-axis, while the cone of the spins with $m_I = -1/2$ will open downward. We will assume that there is no correlation between the relative positions of the different spins in the cones (i.e. the random phase approximation) giving an effectively equal distribution about $\vec{z}$ in each cone. Therefore, the vector sum of all the magnetic moments of the ensemble will be entirely along $\vec{z}$; the magnitude of the bulk magnetization, $\vec{M}_0$, will be dictated by the relative populations of the m_I levels. We may define the nuclear spin polarization, P, according to the following relation:

$$P = \frac{N_\uparrow - N_\downarrow}{N_\uparrow + N_\downarrow}, \tag{1.9}$$

where $N_\uparrow$ and $N_\downarrow$ are respectively the numbers of spins in the $m_I = 1/2$ and $m_I = -1/2$ states. The number of spins in each level at equilibrium is dictated by the Boltzmann distribution, giving

$$P = \tanh\left(\frac{\gamma\hbar B_0}{2kT}\right), \tag{1.10}$$

where k is Boltzmann's constant and T is the temperature. The magnitude of $\vec{M}_0$ is

proportional to P:

$$M_0 = \frac{1}{2} N_s \gamma \hbar P, \tag{1.11}$$

where N_s is the number nuclear spins.

The Chemical Shift

When an atom is placed in an external magnetic field, the nucleus of that atom will experience a local field that is generally different from the external field. This difference is due to weak local fields originating from electronic orbital angular momentum induced by the external magnetic field. In other words, the external field generates ring currents in the electron cloud surrounding a given nucleus. These weak local fields are proportional to the external field strength, normally opposite in direction, thereby partially "shielding" the nuclear spin from the external field. This shielding effect results in a slightly different Larmor frequency than that expected from the Zeeman Hamiltonian alone, known as the chemical shielding. When this shift in frequency is compared to an arbitrary frequency reference, the effect is commonly known as the chemical shift.

When a molecule or bulk material is placed in a magnetic field, the same effect is observed. However, the electron density around a nucleus is not generally spherical in nature, giving an orientationally dependent tensor quantity known as the chemical-shift anisotropy or chemical-shielding anisotropy (CSA), σ. It can be shown that

the orientational dependence is proportional to $[1 - 3(\cos^2\theta)]$, where θ is the angle between the external field $\vec{B_0}$ and the principle axis of the CSA. The chemical shielding Hamiltonian has the form

$$H_{CS} = \hbar \sum_{k=1}^{N} \vec{I_k} \cdot \sigma_{\mathbf{k}} \cdot \vec{B_0}. \tag{1.12}$$

In gases and liquids, the rapid isotropic tumbling of molecules averages away the orientational dependence of the CSA, yielding a single isotropic chemical shift, σ^{iso}, normally included into the NMR Hamiltonian as:

$$H_Z + H_{CS} = -\hbar \sum_{k} \gamma_k \left(1 - \sigma_k^{iso}\right) B_0 I_{kz}, \tag{1.13}$$

where k indexes each nucleus. The relative strength of the chemical shift depends largely on the element in question and its local surroundings. To give two examples, The chemical shift range of protons is typically around 15 ppm (~6 kHz at 10 T), while the range for xenon is roughly 7500 ppm (~900 kHz at 10 T), owing to xenon's highly polarizable electron cloud.

In bulk materials, the CSA can also be reduced to the isotropic shift by magic-angle sample spinning (MAS). If the sample is spun rapidly (i.e., with a rotor frequency greater than the spectral width of the CSA), then the term $[1 - 3(\cos^2\theta)]$ will tend to zero if $\theta \approx 54.74°$; 54.74° is thus referred to as the magic angle. MAS can yield much higher spectral resolution for amorphous solids compared to that obtained

from static samples, at the cost of lost structural information contained in the original CSA lineshape.

1.2.2 Resonant Radio-Frequency Fields

Most of the NMR pulse sequences used in the work reviewed in this dissertation are well-known, simple, and easily understood; as such, only the briefest mention of radiation-spin interactions is given here. As mentioned earlier, the NMR resonance condition for an ensemble of nuclear spins with gyromagnetic ratio γ and chemical shift σ is given by

$$\omega_0 = -\gamma (1 - \sigma) B_0; \tag{1.14}$$

thus, an applied rf field $\vec{B_1}$ with angular frequency $\omega = \omega_0$ will be absorbed by the ensemble, exciting spins to flip between Zeeman levels.

Alternatively, the total magnetization $\vec{M_0}$ of the spin ensemble may be considered to evolve classically under the influence of $\vec{B_1}$ in a reference frame rotating at ω_0. Prior to the application of $\vec{B_1}$, $\vec{M_0}$ is aligned with $\vec{B_0}$ along the $\vec{z}$-axis. However, the application of $\vec{B_1}$ in a plane perpandicular to B_0 (say, along the $\vec{x}$-axis) will cause $\vec{M_0}$ to tip out of alignment of $\vec{B_0}$ and rotate in a plane perpandicular to $\vec{B_1}$. The angular frequency of the rotation of $\vec{M_0}$ caused by $\vec{B_1}$, known as the Rabi frequency, is given by: $\omega_1(t) = \gamma B_1(t)$, where $B_1(t)$ is the time-dependent amplitude of $\vec{B_1}$. The

degree to which $\vec{M}_0$ has deviated from alignment with $\vec{B}_0$ immediately following the application of the $\vec{B}_1$ rf pulse, known as the pulse tipping angle, Θ, is given by:

$$\Theta = \int_0^{\tau_p} \omega_1(t)dt, \tag{1.15}$$

where τ_p is the time duration of the rf pulse.

Consider an rf field $\vec{B}_1$ of constant amplitude and duration chosen such that once applied along the x-axis, $\vec{M}_0$ has been tipped 90°, leaving $\vec{M}_0$ parallel to the $\vec{y}$-axis; naturally, such an rf pulse is referred to as a 90° pulse. Following the application of $\vec{B}_1$, in the laboratory reference frame $\vec{M}_0$ will precess in the xy plane at the Larmor frequency, permitting the magnetization to be detected via the alternating current induced by the precessing magnetization in a coil aligned perpandicular to $\vec{B}_0$. A rectangular rf pulse of identical amplitude but with twice the duration of the previous $\vec{B}_1$ (known as a 180° pulse) would instead leave $\vec{M}_0$ aligned anti-parallel to $\vec{B}_0$.

$\vec{B}_1$ must leave some portion of $\vec{M}_0$ in the xy plane if any signal is to be detected by the induction coil. In other words, all observable signals in NMR are proportional to the operators I_x and I_y. Conceptually, this idea may be united with the previous statement that the absorption of resonant rf photons causes individual spins to flip, as the $|I, m_I\rangle$ kets do not comprise an eigenbasis of I_x or I_y; I_x and I_y are responsible for spin flips, as can be seen more simply by applying linear combinations of these

terms:

$$I_+ = I_x + iI_y, \tag{1.16}$$

$$I_- = I_x - iI_y, \tag{1.17}$$

where

$$I_+|I, m_I\rangle = \sqrt{I(I+1) - m_I(m_I+1)}|I, m_I+1\rangle, \tag{1.18}$$

$$I_-|I, m_I\rangle = \sqrt{I(I+1) - m_I(m_I-1)}|I, m_I-1\rangle, \tag{1.19}$$

giving, for the example of $I = 1/2$, $m_I = -1/2$:

$$I_+\left|\frac{1}{2}, -\frac{1}{2}\right\rangle = \left|\frac{1}{2}, \frac{1}{2}\right\rangle. \tag{1.20}$$

Thus, I_+ and I_- are often referred to respectively as the raising and lowering operators.

1.2.3 Spins in Magnetic Field Gradients

In the description of the Zeeman interaction, it was assumed that the external magnetic field $\vec{B}_0$ was completely homogeneous, causing all the identical spins of a sample to have the same Larmor frequency. However, if a linear magnetic field gradient $\vec{G}$ is placed across the sample along $\vec{r}$, then the Larmor frequency is given

by:

$$\omega(\vec{r}) = -\gamma B_0 + \gamma \vec{G} \cdot \vec{r}, \tag{1.21}$$

neglecting the chemical shift. Thus, displacements in space along $\vec{r}$ correspond with linear displacements in Larmor frequency.

Magnetic field gradients have numerous applications in NMR. Two applications relevant to the work presented in this thesis are imaging and studying diffusion. The reader is directed to Refs. [10, 11, 12, 13] for discussions of both subjects in the context of magnetic resonance. More detailed discussions of MRI, the effects of diffusion on MRI, and the measurement of diffusion with pulsed gradient methods can be found in Chapter 7 and references therein.

Gradients are used in MRI to encode spatial information from the sample into the detected NMR spectrum, thereby permitting the generation of an image of the spin density of a given sample (modulated by a variety of contrasting effects). In this discussion it is convenient to employ the reciprocal space vector $\vec{k}$, where

$$\vec{k} = \frac{\gamma \vec{G} \tau}{2\pi}, \tag{1.22}$$

where τ is the duration of the applied gradient. Thus, from Eq. 1.22 it can be seen that systematic variation of $\vec{G}$ and τ can be used to traverse $\vec{k}$-space. The observed

signal in MRI, S, is given as a function of $\vec{k}$:

$$S(\vec{k}) = \int \rho(\vec{r}) e^{i2\pi\vec{k}\cdot\vec{r}} d\vec{r}, \tag{1.23}$$

where $\rho(\vec{r})$ is the spatially-dependent nuclear spin density of a given sample. Thus, one can employ Fourier transformation to recover an image of $\rho(\vec{r})$ from $S(\vec{k})$:

$$\rho(\vec{r}) = \int S(\vec{k}) e^{-i2\pi\vec{k}\cdot\vec{r}} d\vec{k}. \tag{1.24}$$

Encoding spatial information according to Eq. 1.21 is known as frequency encoding. Alternatively, one may obtain spatial information by via phase encoding, which entails generating a spatially-dependent phase change in the NMR signal. If a gradient of duration τ is applied prior to signal acquisition, then the spatially-dependent phase is given by:

$$\phi(\vec{r}) = \int_0^\tau \left(-\gamma B_0 + \gamma \vec{G} \cdot \vec{r}\right) dt. \tag{1.25}$$

Unlike frequency encoding, phase encoding requires the acquisition of multiple signals with an appropriate variation of the amplitude of $\vec{G}$ for each scan.

In reality, three mutually perpendicular gradients must be used to obtain a 3-D image. The application of one gradient will naturally give only an integrated projection of the spin density along the direction of that gradient; this type of image

is called a projection image. Multi-dimensional imaging experiments often (but not always) employ both frequency and phase encoding. For example, a 2-D image may be obtained by frequency encoding along one dimension (with say, G_x), with phase encoding obtained by stepping through G_y in subsequent acquisitions, producing a 2-D data set. The image is obtained by Fourier transforming the 2-D data set in both dimensions in much the same way that 2-D NMR spectra are obtained in correlated spectroscopy experiments.

Measurement of the true spin density via MRI is difficult (and often not desired), as the signal is generally modulated by a variety of physical phenomena (e.g., longitudinal and transverse spin relaxation, chemical shift, and diffusion). Indeed, such phenomena are often exploited to create different types of contrast in MRI. For a detailed description of contrast mechanisms in MRI, the reader is directed to Ref. [11].

Independent of MRI, pulsed gradients can be used to study diffusion. Consider the application of a gradient-echo pulse sequence in which, following an rf pulse to generate xy magnetization, two gradient pulses of equal strength (G) but opposite in direction are applied, spaced by a time delay (Δt), immediately followed by detection. In the absence of diffusion, the second gradient will completely refocus the spin dephasing caused by the first gradient, and the maximum signal is recovered. However, if diffusion is present, the amplitude of the detected signal will have decayed

somewhat according to the equation:

$$S(t, G) = S_0 \exp\left[-\gamma^2 G^2 D(\Delta t)^3/12\right], \tag{1.26}$$

Where D is the diffusion coefficient (see for example, Ref. [14] and references therein). Thus, by measuring the strength of multiple signals with variation in G, D may be simply obtained from the slope of a plot of $\ln[S(t,G)/S(t,0)]$ versus G^2.

1.3 Spin-Spin Couplings

1.3.1 Scalar (J) Couplings

Scalar or J couplings are indirect spin-spin couplings mediated by electron-nuclear interactions. Specifically, such electron-nuclear interactions can originate from Fermi-contact hyperfine interactions and couplings between nuclear spins and electronic orbital angular momentum. J-couplings provide the principle means of transferring coherence between spins within the same molecule in liquids. On a more practical level, observed J-couplings are nearly always mediated by chemical bonds, and thus are particularly important in liquid-state NMR to organic chemists and structural biologists as they provide information regarding the structural connectivity of atoms in molecules.

The Hamiltonian for indirect spin-spin couplings has the form:

$$H_J = h \sum_{k<l} \vec{I}_k \cdot \mathbf{J}_{kl} \cdot \vec{I}_l, \tag{1.27}$$

where $\mathbf{J}_{kl}$ is the indirect spin-spin coupling tensor (following the formalism of Ernst et al. [3]). However, the isotropic term of $\mathbf{J}_{kl}$ may be separated from the anisotropic term, yielding

$$H_J^{iso} = h \sum_{k<l} J_{kl} \vec{I}_k \cdot \vec{I}_l, \tag{1.28}$$

where

$$J_{kl} = \frac{1}{3} \mathrm{Tr} \left[\mathbf{J}_{kl} \right]. \tag{1.29}$$

The anisotropic portion, $\mathbf{J}_{kl}^{aniso}$, is averaged away in isotropic liquids, and in general, is difficult to separate from the direct dipolar couplings (discussed later); for these reasons, only the isotropic term $\mathbf{J}_{kl}^{iso}$ will be considered throughout the remainder of this thesis. By definition, $\mathbf{J}_{kl}^{iso}$ is independent of orientation, and therefore is not averaged away in isotropic liquids. Thus, the NMR spin Hamiltonian in isotropic liquids is comprised of Zeeman, chemical shift, and J-coupling terms:

$$H_0 = -\hbar \sum_k \gamma_k \left(1 - \sigma_k^{iso} \right) B_0 I_{kz} + h \sum_{k<l} J_{kl} \vec{I}_k \cdot \vec{I}_l. \tag{1.30}$$

Two-bond proton-proton J-couplings are typically Hz or 10s of Hz in size; directly bonded ^{1}H-^{13}C J-couplings are normally on the order of 100s of Hz.

1.3.2 Dipolar Couplings

A pair of nuclear moments can possess a direct spin-spin interaction whose strength is determined by the relative internuclear distance between the spins and the orientation of the internuclear vector $\vec{r}_{kl}$ with respect to the external magnetic field. As such, measurements of dipolar couplings between two or more spins in a lattice can in principle yield substantial structural information. The dipolar Hamiltonian has the following explicit form:

$$H_D = \sum_{k<l} \vec{I}_k \cdot \mathbf{D}_{kl} \cdot \vec{I}_l, \tag{1.31}$$

$$= \sum_{k<l} \frac{\mu_0 \gamma_k \gamma_l \hbar^2}{4\pi r_{kl}^3} \left[\vec{I}_k \cdot \vec{I}_l - 3\frac{1}{r_{kl}^2} \left(\vec{I}_k \cdot \vec{r_{kl}} \right) \left(\vec{I}_l \cdot \vec{r_{kl}} \right) \right]. \tag{1.32}$$

By implementing the high-field approximation [3], the non-secular terms are neglected, and a simplified ("truncated") dipolar Hamiltonian may be obtained:

$$H_D^{trunc} = \sum_{k<l} \frac{\mu_0 \gamma_k \gamma_l \hbar^2}{8\pi r_{kl}^3} \left(1 - 3\cos^2 \theta_{kl}\right) \left[3I_{kz} I_{lz} - \vec{I}_k \cdot \vec{I}_l \right], \tag{1.33}$$

which for a heteronuclear two-spin system, further simplifies to

$$H_D^{IS} = \frac{\mu_0 \gamma_I \gamma_S \hbar^2}{4\pi r_{IS}^3} \left(1 - 3\cos^2\theta_{IS}\right) I_{Iz} I_{Sz}, \tag{1.34}$$

where I and S denote two different spins and θ_{IS} is the angle between $\vec{r}_{IS}$ and $\vec{B}_0$.

In solids, nuclear dipole-dipole interactions can be extremely important; for example, the strength of a typical directly-bonded ^{1}H-^{13}C dipole coupling is ~20 kHz, much greater than the J-coupling. Moreover, the sensitivity with which the dipolar coupling depends on r and θ should make it a powerful probe of structure in materials. However, the exponential increase in spectral complexity suffered when the number of strongly coupled spins is increased, as well as decreased transverse relaxation times yields broad, intractable lines. As with the case of the CSA, the θ-dependence of the dipolar coupling enables its removal via MAS techniques (if the sample can be spun with a significantly higher frequency than the dipolar coupling itself); unfortunately, this spectral simplification often "throws the baby out with the bath water," as the structural information provided by the dipolar couplings is also lost in fast MAS. Therefore, numerous rf and spatial manipulation techniques have been developed to selectively re-introduce chosen dipolar couplings (thereby providing structural information about the chosen dipole pair), while still averaging away the other remaining couplings. This work is an enormous field of NMR in its own right, but is outside the scope of this thesis.

1.3.3 Quadrupolar Couplings

Nuclei with $I \geq 1$ possess an asymmetric charge distribution, permitting coupling with local electric field gradients. The quadrupolar Hamiltonian is given by

$$H_Q = \sum_{k=1}^{N} \vec{I}_k \cdot \mathbf{Q}_k \cdot \vec{I}_k, \tag{1.35}$$

where $\mathbf{Q}_k$ is the quadrupole coupling tensor for the kth spin, which in turn can be written in terms of the electric field gradient tensor $\mathbf{V}$ at each nucleus:

$$\mathbf{Q}_k = \frac{eQ_k}{2I_k(2I_k-1)\hbar}\mathbf{V}_k. \tag{1.36}$$

The characteristically short relaxation times of quadrupolar nuclei make them unfavorable for the vast majority of OPNMR experiments described in this thesis; thus quadrupolar nuclei will be mentioned only sparingly. For recent examples of NMR experiments involving quadrupolar nuclei, the reader is referred to the Ph.D. dissertations of S.M. De Paul [15] and S. Wang [16].

Chapter 2

Optical Pumping of Noble Gases

2.1 Introduction

The fundamental insensitivity of NMR and MRI stems from the exceedingly low nuclear polarization generated in even the strongest available magnetic fields. Consider an ensemble of spin-$I = 1/2$ nuclei at thermal equilibrium with a strong external magnetic field, B_0, and at temperature T, shown in the top portion of the cartoon in Fig. 2.1). The functional form of the nuclear polarization P was given in the previous chapter:

$$P = \tanh\left(\frac{\gamma\hbar B_0}{2kT}\right). \tag{2.1}$$

Because of the minuscule size of nuclear magnetic moments, it is generally true that $\gamma\hbar B_0 \,/\, kT << 1$, yielding:

$$P \approx \frac{\gamma\hbar B_0}{2kT}. \tag{2.2}$$

For a collection of nuclei at room temperature and at typical NMR magnetic field strengths, Eq. 2.2 gives $P \sim 10^{-5} - 10^{-6}$. For example, given a field strength of 9.4 T (roughly the strength of a 400 MHz magnet) at room temperature, the polarization for a collection of protons would be only $\approx 3.2 \times 10^{-5}$. Naturally, the polarization would be even lower for samples in the weaker fields used in most medically oriented experiments, or when observing nearly all other NMR-active nuclei. It was shown in the previous chapter that the magnitude of the equilibrium nuclear spin magnetization M_0 was proportional to P. Thus, improving the equilibrium magnetization for a given sample can be performed only by increasing B_0 (which grows progressively expensive and difficult), or by drastically lowering T (inappropriate for various types of samples, especially living organisms).

Instead, a different approach would be to achieve high nuclear polarization [Fig. 2.1(b)] by some *non-equilibrium* means, even if the polarization would eventually succumb to spin-lattice relaxation. If useful experiments can be performed faster than such relaxation occurs, it may well be worth the trouble to "beat" Boltzmann, even if only for a short time.

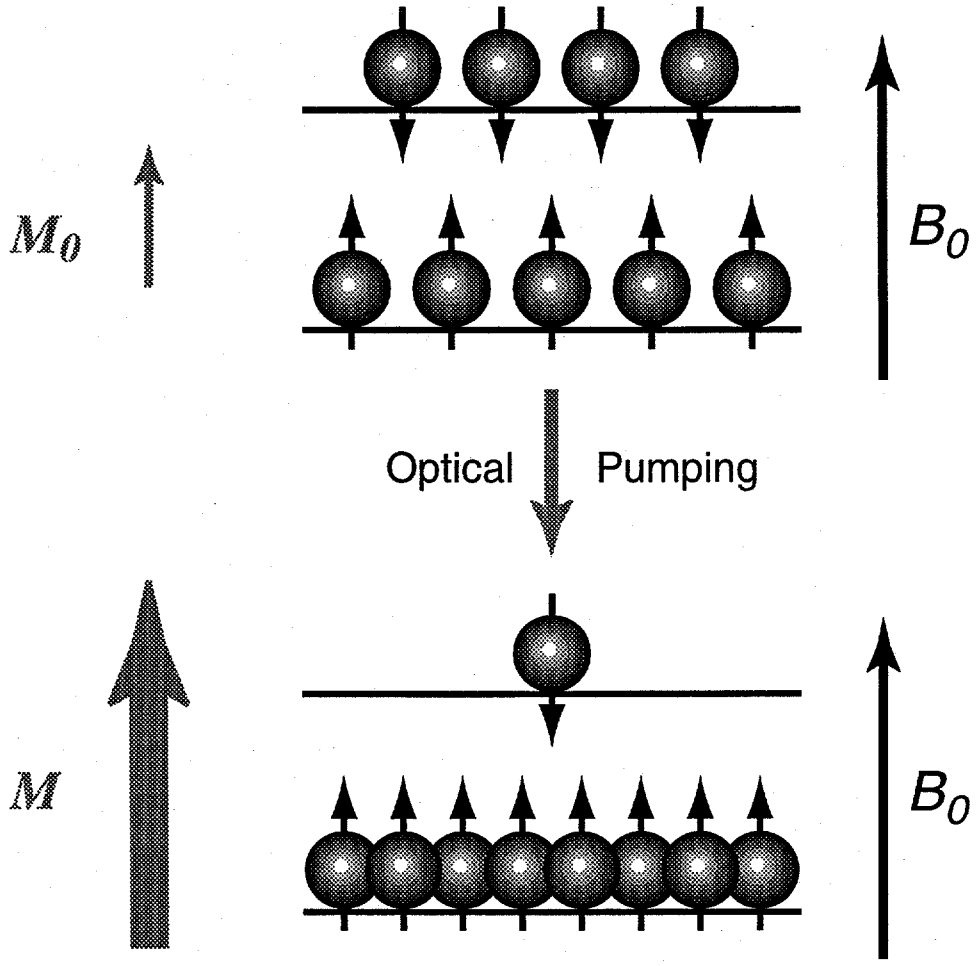

Figure 2.1: Cartoon depicting the effect of laser-polarization for a collection of spin-1/2 nuclei (assuming positive gyromagnetic ratio). Normally, the number of spins aligned antiparallel to the magnetic field (B_0) is nearly equal to the number of spins aligned with B_0, leading to a tiny detectable magnetization, M_0. However, with optical pumping, the population distribution of the spins can be driven far away from equilibrium, thereby increasing the magnetization to order unity. Figure adapted from Ref. [17].

Optical pumping methods can be exploited to obtain highly non-equilibrium nuclear spin polarizations, thereby increasing M by four to five orders of magnitude (shown in the bottom portion of Fig. 2.1). Optical pumping methods achieve highly non-Boltzmann population distributions by exploiting the quantum mechanical selection rules of angular momentum. It was first shown by Kastler [18, 19, 20] in 1950 that circularly polarized light could be used to pump electronic spins of gaseous metal vapors into non-equilibrium population distributions, an accomplishment which earned him the Nobel Prize. Later work [21] showed that the nuclear polarization of noble gases present in the pumping cell could be greatly enhanced through collision and spin exchange with electronically spin-polarized alkali atoms. This process has since been studied in considerable detail by Happer and co-workers (see for example, Refs. [22, 23]), with the original motivation being the creation of nuclearly polarized spin targets for particle physics experiments.

It should be mentioned that the NMR signals of other systems besides gas-phase monatomic species have been successfully enhanced through optically pumping. For example, the optical pumping of nuclear spins in certain semiconductors (e.g. GaAs and InP) has permitted a variety of novel studies of these materials, most notably the use of optical pumping in semiconductor quantum wells to study the effects of reduced dimensionality on the fundamental behavior of electrons within these structures, and the quantum Hall effects specifically (for a sampling of the field of semiconductor OPNMR, see Refs. [24, 25, 26, 27, 28, 29, 30, 31, 32, 33, 34, 35, 36]). Semiconductor

OPNMR has yet to see wider application to other fields (although the potential for using optically pumped semiconductor wafers as substrates for polarization transfer to species (e.g. proteins and other biological molecules of interest) adsorbed to their surfaces has recently been discussed [34]). In any case, this work is beyond the scope of this thesis.

This chapter prefaces the work presented in the remainder of this thesis by introducing many of the principles and practices involved in the optical pumping of noble gases. The primary method of noble gas optical pumping, namely alkali metal spin exchange, is introduced, and different experimental methods employing this technique are described. An alternative method for producing laser-polarized helium directly (without the need for an alkali vapor intermediary) called metastability exchange has also been developed, but is beyond the scope of this thesis; for a discussion of this approach, see Refs. [37, 38]. For a recent review of spin exchange optical pumping, see Ref. [23]. For an in depth introduction into the physics of optical pumping in general, the reader is directed to the monograph of Bernheim [39]; this work also contains reprints of a number of the important articles from the early days of optical pumping.

2.2 Alkali Metal Spin Exchange

Alkali metal spin exchange is the primary method for generating optically pumped noble gases, and is capable of achieving high nuclear spin polarization in both xenon

and helium at low and high magnetic fields. The two-step process that comprises alkali metal spin exchange is shown schematically in Fig. 2.2. In the first step, the spins of unpaired electrons of alkali metal atoms are polarized with laser light (Fig. 2.2(a)). By applying circularly polarized light tuned to the D_1 transition of the alkali metal (e.g., 794.7 nm for Rb), population can be selectively depleted from one of the m_J sublevels in the ground state; as shown in Fig. 2.2(a), σ^+ light drives population from $m_J = -1/2$ in the ground state into $m_J = 1/2$ in the excited state. Collisions with other gas-phase species equalize the populations of the excited-state sublevels, equilibrating the relaxation rates to the ground m_J sublevels. The depletion of the ground $m_J = -1/2$ sublevel (and subsequent accumulation of population in the ground $m_J = 1/2$ sublevel) rapidly reaches steady state, leaving the metal vapor electronically spin-polarized.

Often, nitrogen is added to the gas mixture to quench the fluorescence (radiative decay) of the electronically excited alkali metal atoms, which would otherwise depolarize the electron spins. The probability for radiative decay for the electronically excited Rb is given by the branching ratio, w_γ [42]:

$$w_\gamma \approx \frac{3}{3 + 7.5\frac{p_{N_2}}{\text{kPa}}}, \tag{2.3}$$

where p_{N_2} is the partial pressure of nitrogen at 300 K. Thus, a nitrogen partial pressure of about 40 kPa would give $w_\gamma \approx 0.01$.

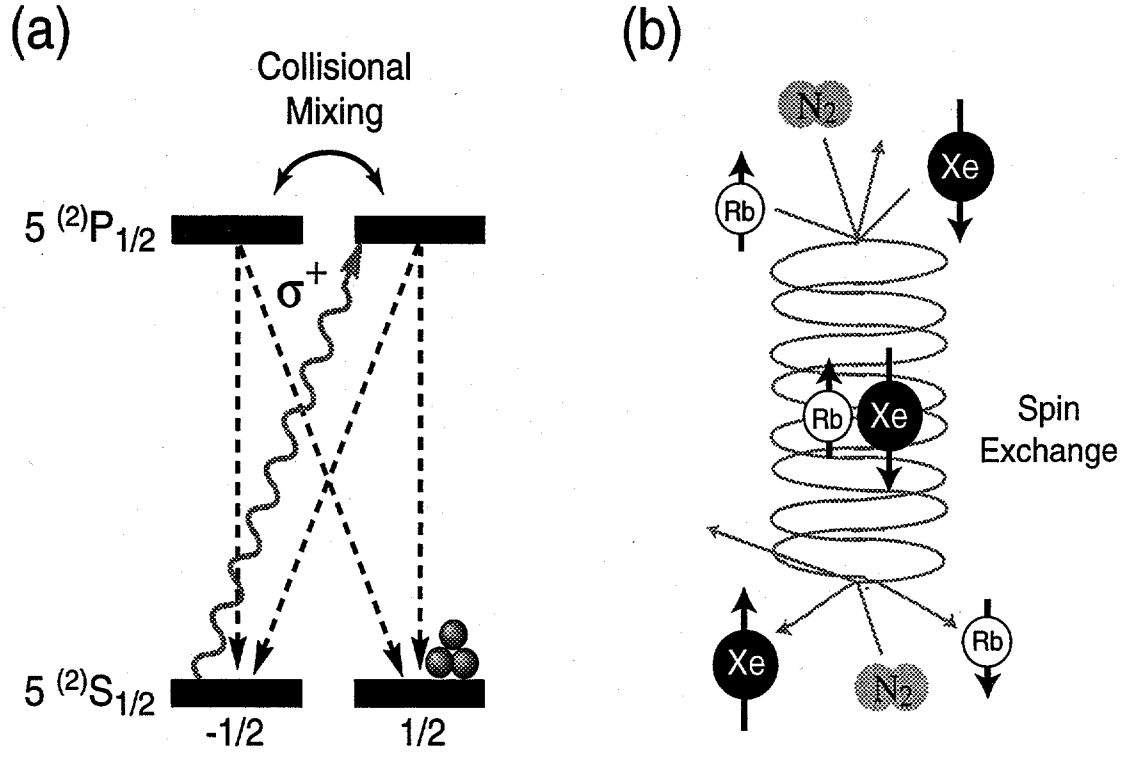

Figure 2.2: Cartoons of the optical-pumping/spin-exchange processes [22]. (a) Optical pumping of the electronic spins of the alkali atoms (neglecting the hyperfine ($F = I + J$) couplings between the electronic and nuclear spins of the alkali metal atom). (b) Polarization of the xenon nuclei via collision and spin-exchange.

In the second step of the optical pumping process (Fig. 2.2(b)), collisions between unpolarized noble gas atoms and electronically spin-polarized alkali metal atoms permit spin exchange via Fermi-contact hyperfine interactions between the electron spins (S) and the noble gas nuclear spins (I) [40]:

$$\alpha\vec{S}\cdot\vec{I} = \frac{\alpha}{2}\left[S_+I_- + S_-I_+\right] + \alpha S_zI_z, \tag{2.4}$$

where the "flip-flop" term in brackets gives the spin exchange between the alkali metal and the noble gas, and the coupling constant α is proportional to the probability of finding the unpaired electron of the alkali atom at the nucleus of the noble gas atom, and is given by:

$$\alpha = \frac{8\pi}{3}\gamma_S\gamma_I\hbar^2\delta(r); \tag{2.5}$$

here $\delta(r)$ is the Dirac delta function depending upon the relative distance between the electron and the nucleus.

The collisions may be three-body (as shown in the figure, with nitrogen molecules participating in the formation and destruction of the complex) or two-body in nature, depending on the species and experimental conditions involved. However, the overall spin exchange may be effectively treated as a two-body process under conditions typically encountered for NMR applications [23]. The nuclear polarization P of the

noble gas after a given duration of optical pumping (t) is governed by the relation:

$$P = \frac{\rho_{SE}}{\rho_{SE} + \rho_o} P_{Rb} \left(1 - \mathrm{e}^{-(\rho_{SE}+\rho_o)t}\right), \tag{2.6}$$

where P_{Rb} is the electron spin polarization of the Rb, ρ_{SE} is the rate of spin exchange between the noble gas nuclei and the rubidium electrons, and ρ_o contains all other contributions to the longitudinal relaxation of the noble gas nuclei (e.g. wall collisions). Over time (seconds to hours, depending upon the experimental conditions), the nuclear polarization of the noble gas will accumulate, yielding values as high as several tens of percent.

The enhanced polarization can be calibrated with a variety of methods [23, 41]. The signal enhancement generated with optical pumping is trivially calculated from the polarization (or vice versa); For ^{129}Xe polarized to 10%, the enhancement is $\approx$11,000 compared to ^{129}Xe at equilibrium in a 9.4 T magnet at room temperature.

2.3 Experimental Methods

2.3.1 The Batch Optical Pumping Apparatus

There are several variants of the experimental setups used for optically pumping noble gases via alkali metal spin-exchange; however, these methods usually fall within one of two categories. The first, which will be referred to as the "batch" method,

is shown in Fig. 2.3; the particular optical pumping setup shown in the figure is similar to that originally used for ^{129}Xe NMR studies of materials surfaces with laser-polarized xenon [46]. The batch method is the simplest, and is normally used for polarizing small amounts of the noble gas at low field and at relatively low pressure.

A narrow-bandwidth continuous-wave laser (usually a Ti:Sapphire or diode laser) produces a beam tuned to the D_1 resonance of Rb. The laser beam becomes circularly polarized by passing through a quarter-wave plate. Once expanded with a lens, the beam is directed into a glass pumping cell residing in a weak (~20-30 G) but homogeneous magnetic field produced by a Helmholtz coil pair; the pumping cell usually contains a few hundred torr of xenon, a drop of Rb, and a small amount of nitrogen buffer gas. By uniformly heating the cell (to usually 60-100 °C), a small amount of Rb will be vaporized so that it may be optically pumped by the laser. The Rb partial pressure, p_{Rb} can be estimated using the relation:

$$\log\left(\frac{p_{Rb}}{\mathrm{Pa}}\right) \approx 9.318 - \frac{4040}{\frac{T}{\mathrm{K}}} \tag{2.7}$$

when performing optical pumping between the melting point of Rb (312.46 K) and about 550 K. Ideally, the "dark space" in the pumping cell (i.e., regions not illuminated by the pumping laser) should be minimized.

Throughout the optical pumping process, the gas line is evacuated (ideally to ~10^{-5} torr or less) in order to minimize oxygen contamination of the laser-polarized

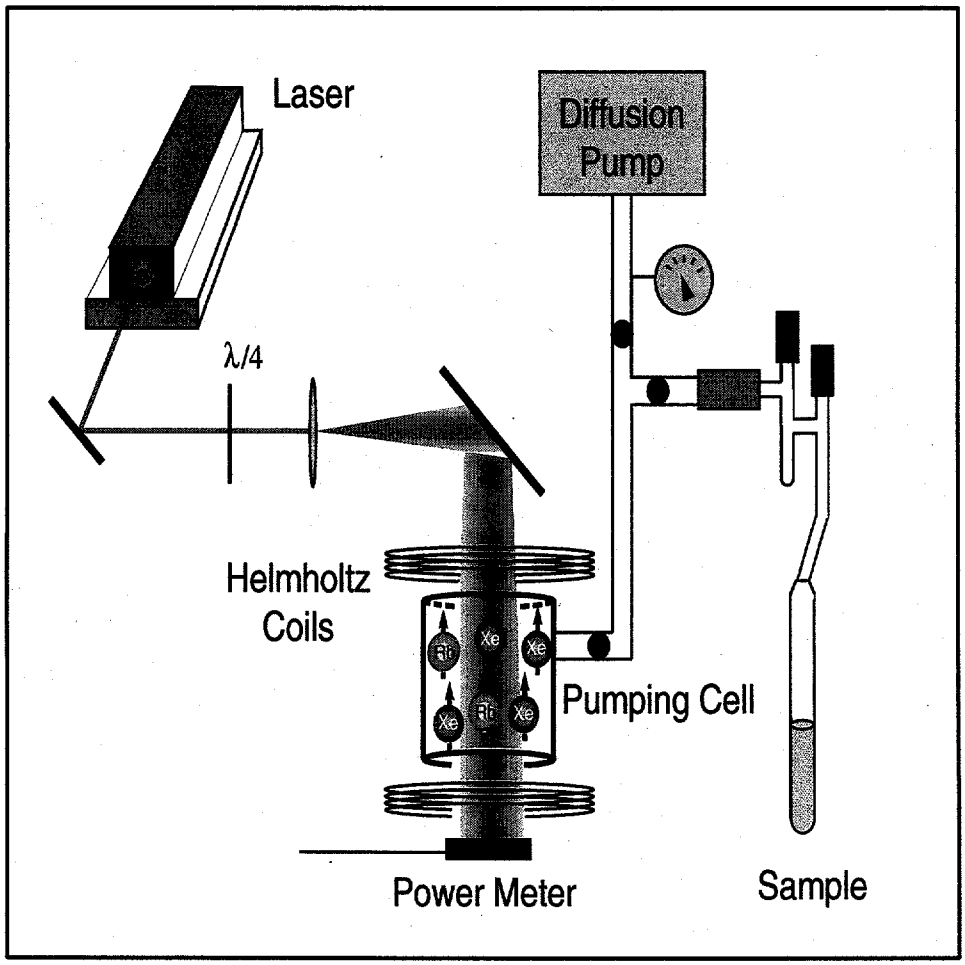

Figure 2.3: Schematic of the classic "batch" optical pumping apparatus (see, for example, Refs. [46, 47]).

xenon during transfer to the sample. Once the xenon has been polarized, the pumping cell is rapidly cooled to condense the Rb. The laser-polarized xenon may be removed from the cell and transported to the NMR magnet via a direct transfer line and a pump, or as in the case shown in the figure, the xenon may be cryopumped into an NMR sample tube by immersing the sample's cold-finger in liquid nitrogen. Once the xenon has been frozen into the cold-finger, the sample tube may be transported at leisure to the NMR magnet, where for experiments involving liquid samples (see Chapters 4, 5 and 8) the xenon is rapidly sublimated and delivered to the solution prior to signal acquisition. The high xenon polarization can be maintained in the cold finger for long periods of time by exposing the frozen xenon to a strong magnetic field ($\geq$500 G [48]), as discussed in the next chapter. Alternatively, the noble gas may be optically pumped at high field within the NMR magnet if the laser beam can be directed into the magnet's bore. For a description of high-field alkali metal spin-exchange experiments, the reader is directed to the work of Augustine and Zilm [49, 50, 51].

Such "batch" optical pumping apparati as that shown in Fig. 2.3 are capable of producing xenon with nuclear polarization on the order of tens of percent, as shown by the ^{129}Xe NMR spectra in Fig. 2.4. In fact, following careful optimization of the experimental conditions and the design of the apparatus, a batch optical pumping setup has recently been used to produce small amounts of xenon with a nuclear polarization approaching 70% [52, 53].

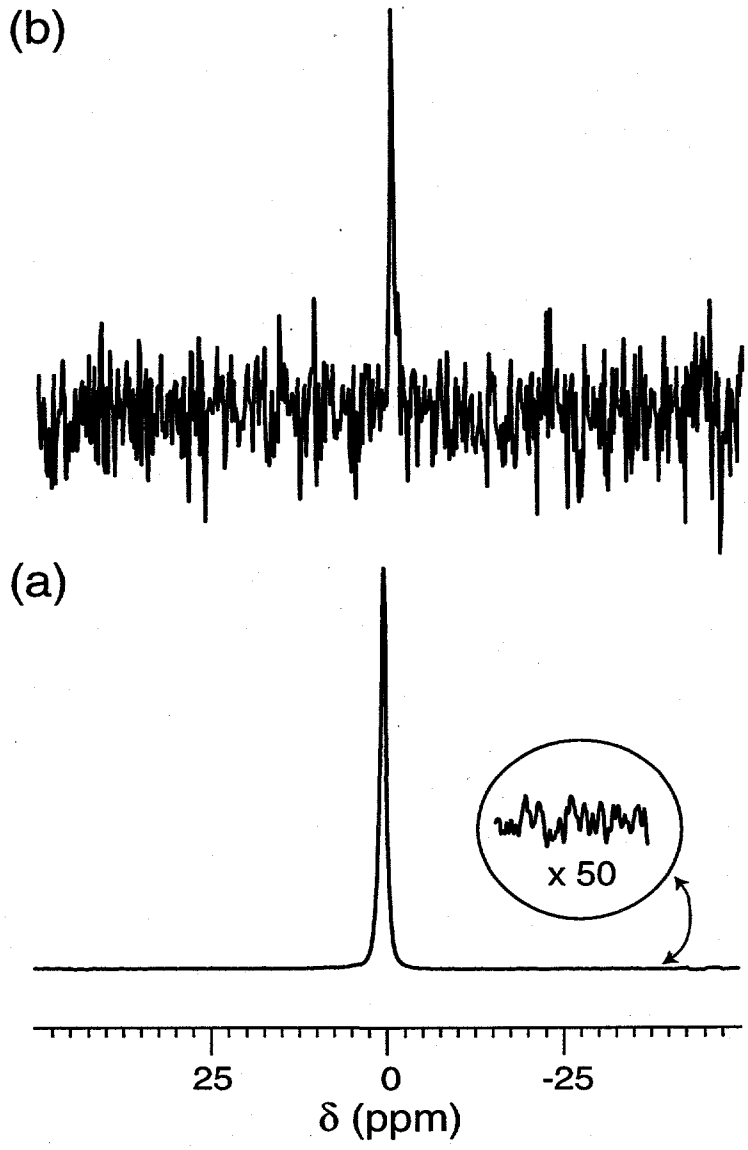

Figure 2.4: ^{129}Xe NMR signal from xenon gas, obtained with (a) and without (b) laser-polarization. (a) One scan from a sample containing 2×10^{17} Xe atoms; (b) one scan from a sample containing 5×10^{19} Xe atoms. The spectrum in (a) reflects a ^{129}Xe NMR signal enhancement of $\sim$55,000 given a magnetic field of about 7 T, corresponding to a ^{129}Xe nuclear spin polarization of $\sim$35% [45]. Figure courtesy of Holly Gaede.

2.3.2 The Continuous-Flow Apparatus

A second type of apparatus used for producing large quantities of polarized gases is shown schematically in Fig. 2.5, and will be referred to as the "continuous-flow" setup [54]. We have used our continuous-flow setup exclusively for pumping xenon [43, 44]. In our apparatus, 5-10 atm of a gas mixture (comprised of a few percent Xe and N_2, with the remainder being helium-4) first flows through a heated chamber containing Rb ($\sim$1 g) on glass wool, where it becomes saturated with Rb, and then flows into the pumping cell. The Rb is optically pumped with a wide-bandwidth, high-power ($\geq$ 130 W) laser diode array (OptoPower, Inc.). For a review of optical pumping with high-power diode arrays, see Ref. [42]. However, this high of power is apparently unnecessary, as a reduction in laser power by half results in only a very small reduction in spin polarization. Too much laser power can also cause over-heating problems with the pumping cell, and one must guard carefully against explosions. The purpose of the helium buffer gas is to pressure-broaden the Rb absorption line, increasing the pumping efficiency of the wide-bandwidth output of the laser. In the near future, more efficient high-power diode lasers will likely be developed with far narrower bandwidths, potentially obviating the need for the high-pressure buffer gas.

Once polarized in the cell, the xenon may be collected in a U-tube immersed in liquid N_2, while the buffer gas is released into the atmosphere. Alternatively, the U-tube may be removed and the gas flow may be directed into the NMR magnet for studying surfaces under continuous-flow conditions; in fact, the polarized gas flow

may be recirculated for optical pumping *ad infinitum* by adding a recirculating pump after the NMR magnet and closing the loop by redirecting the exit flow into the pumping cell [43, 44] (see Chapters 6 and 7). By using a continuous-flow apparatus, on the order of 1 L/hr of laser-polarized xenon can be obtained. A complete continuous flow optical pumping apparatus is now commercially available from Magnetic Imaging Technologies, Inc. (Durham, NC). Different continuous-flow setups generate ^{129}Xe spin polarizations on the order of 1-20%. Finally, an alternative design that is also capable of generating large quantities of laser-polarized noble gases has recently appeared in the literature [55].

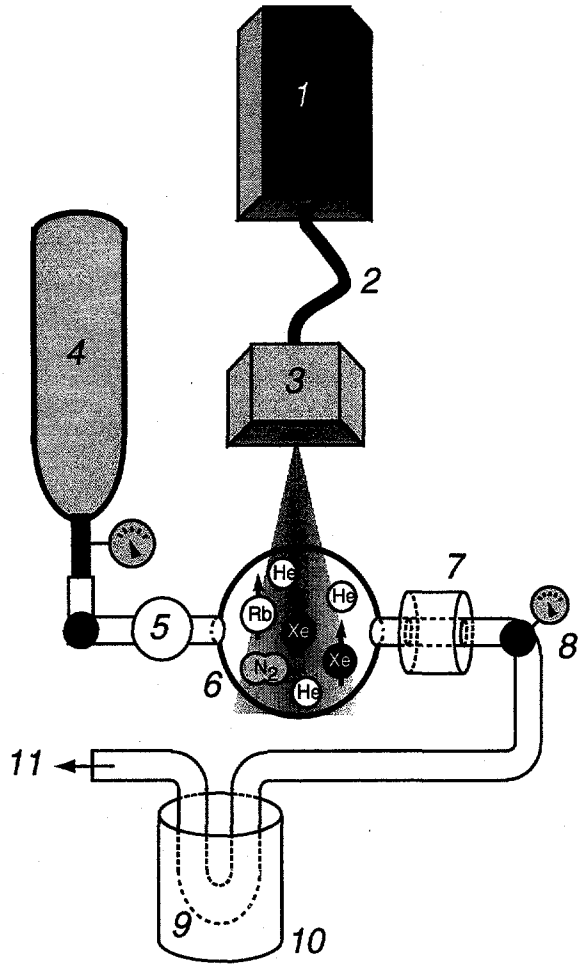

Figure 2.5: Continuous-flow apparatus, adapted from the original design in Ref. [54]. The broad-band output from a high-power laser diode array (*1*, 130 W) is coupled through optical fibers (*2*) into a quarter-wave box (*3*) that expands the beam and renders it circularly polarized. A high-pressure gas cylinder (*4*) contains a pumping mixture composed of a few hundred torr of xenon, a few hundred torr of nitrogen, and 8-10 atm of helium buffer gas. The gas mixture flows from the cylinder through the rubidium storage region (*5*). Both this region and the pumping cell (*6*) are heated to ~160-180 °C during pumping. The mixture then flows from the cell through the rubidium condenser (*7*); the flow rate is determined by a valve/flowmeter (*8*). Xenon is condensed over time in a U-tube (*9*) immersed in a dewar of liquid nitrogen (*10*), while the rest of the gas mixture is blown off into the atmosphere (*11*). The entire pumping process occurs within the fringe field of a superconducting NMR magnet or Helmholtz coil pair (not shown). Figure from Ref. [17].

Chapter 3

Properties of Laser-Polarized Noble Gases

3.1 Physical Properties of Xenon and Helium

The various phases of xenon conveniently exist in relatively accessible ranges, as shown in the phase diagram in Fig. 3.1. While gaseous at room temperature, xenon is rapidly frozen at liquid-nitrogen temperatures, facilitating accumulation and storage of laser-polarized xenon [56]. Liquid xenon may be obtained at moderate pressures (1-10 atm) via condensation at ~170-200 K, and the supercritical phase can be attained under conditions that appear mild when compared to most other substances [114]. Xenon is a surprisingly effective solvent (see discussion in Chapter 4, and references therein). Helium, on the other hand, liquefies at about 4.2 K at 1 atm, and thus

virtually all OPNMR applications of helium are performed in the gas phase.

Helium possesses a self-diffusion constant roughly thirty times that of xenon. The self-diffusion constant for helium was recently measured to be 1.8 cm^2/s at 1 atm and 20 °C (a measurement made via NMR experiments with laser-polarized helium [199]), compared with a value for xenon of 0.0565 cm^2/s [198].

Chemically speaking, helium is unreactive; with a few notable exceptions, xenon is also chemically inert. However, the highly polarizable electron cloud of xenon causes it to be relatively lipophilic, permitting xenon to participate in specific interactions with various substances (see Chapter 5). Xenon readily adsorbs to numerous surfaces under experimentally convenient conditions (see Chapter 6). Xenon is also more soluble than helium by 10-100 times in different solvents and tissue environments [59]).

Xenon is well known in the medical community for its anesthetic properties [60, 61] (which likely originate from its lipophilicity), suggesting that xenon NMR may be instrumental in elucidating the mechanism of general anesthesia [63]. Both ^{129}Xe and ^{3}He are non-toxic, and can therefore be used in high concentration in breathing mixtures for *in vivo* studies. However, xenon's anesthetic properties require that fractional xenon concentrations below 35% be used in breathing mixtures during occasions when it is necessary to avoid residual anesthetic effects [62].

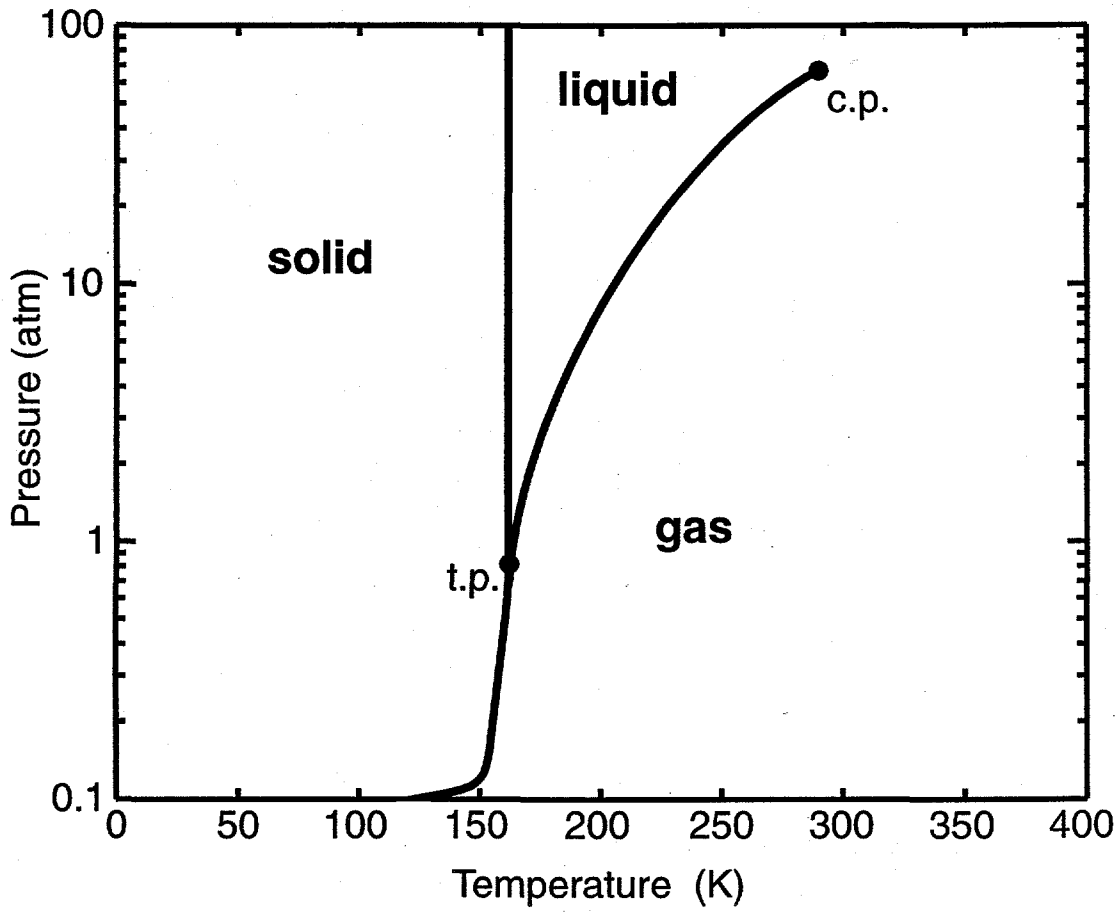

Figure 3.1: Phase diagram of xenon. Triple point: 166.1 K, 0.8 atm; critical point: 289.7 K, 58 atm. Adapted from Ref. [58].

3.2 NMR Properties of Xenon and Helium

As summarized in Table 3.1, xenon possesses two NMR-active isotopes (^{129}Xe, $I = 1/2$ and ^{131}Xe, $I = 3/2$), both with sufficient natural abundance. ^{3}He ($I = 1/2$) is also commonly used in OPNMR experiments. While noble gas isotopes with $I > 1/2$ can be optically pumped, their quadrupolar moments give spin-lattice relaxation times in condensed phases that are too short to be practical for most NMR applications. With careful preparation of storage vessels, the high polarization of ^{129}Xe and ^{3}He can be maintained for long periods of time (hours to days). For example, The T_1 of ^{129}Xe was measured to be $\sim$3 hrs at 77 K, and $\geq$100 hrs at 4.2 K [48, 56] when kept at high field ($>$ 500 G); without the external field, the polarized ^{129}Xe will relax by coupling to the quadrupolar ^{131}Xe present in the lattice. When delivered to samples for NMR study, the T_1 of ^{129}Xe is typically over two orders of magnitude longer than that of ^{131}Xe. For these reasons, ^{129}Xe is the xenon isotope predominately used in OPNMR applications.

Isotope	Natural abundance (%)	Spin (I)	γ/γ_H
^{129}Xe	26.44	1/2	-0.2781
^{131}Xe	21.24	3/2	0.0824
^{3}He	1.3×10^{-4}	1/2	-0.7618

Table 3.1: Some physical parameters of three noble-gas isotopes

Neither helium nor xenon is naturally present in most samples of interest (e.g. living organisms), and thus there is no background signal to complicate experimental

interpretation. In principle, ^{3}He would be the preferred isotope for MRI experiments because of its higher gyromagnetic ratio; however, its higher diffusion constant could limit the gas-phase image resolution in some circumstances. These properties also require that the experimentalist take special care to minimize moving the helium through strong field gradients when transporting laser-polarized helium from the pumping chamber to the sample; the longitudinal relaxation rate resulting from diffusion in an inhomogeneous field is given by:

$$\rho_I^{\nabla B} \approx \frac{2}{3}\tau_c\langle v^2\rangle \left(\frac{\gamma_I G}{\omega_I}\right)^2, \tag{3.1}$$

where $\langle v^2\rangle$ is the averaged square of the velocity of the gas atoms, τ_c is the mean time between atomic collisions, and G is the field gradient transverse to the external magnetic field. ^{3}He also has the disadvantage of uncertain long-term availability. While ^{129}Xe is present as a trace gas in the atmosphere with relatively high natural isotopic abundance, ^{3}He is effectively a non-renewable resource. Once ^{3}He is obtained (from tritium decay) and used, it eventually escapes the atmosphere and is lost.

Because of xenon's highly polarizable electron cloud, the chemical shift of xenon is exquisitely sensitive to its surroundings. Streever and Carr were the first to observe an apparently linear dependence of the xenon chemical shift on the density at moderate pressures [64]. Subsequent work by Jameson and co-workers yielded an empirical

equation for determining the xenon chemical shift [65]:

$$\delta = [\mathrm{Xe}]\delta_1(\mathrm{Xe}-\mathrm{Xe}) + [\mathrm{Xe}]^2\delta_2(\mathrm{Xe}-\mathrm{Xe}) + ... \tag{3.2}$$

where the parameter $\delta_1(\mathrm{Xe}-\mathrm{Xe})$ is a temperature-dependent quantity. For example, the ^{129}Xe resonance was determined to shift 0.539 ppm/amagat at 298 K (an amagat is the density of an ideal gas at STP, and corresponds to 2.69×10^{19} atoms / cm^3) [65]. The parameter $\delta_2(\mathrm{Xe}-\mathrm{Xe})$ was also determined to be temperature-dependent; however at temperatures greater than about 298 K, $\delta_2(\mathrm{Xe}-\mathrm{Xe})$ is effectively constant, with a value of $\approx 0.169 \times 10^{-3}$ ppm/amagat [65]. The dependence of the xenon chemical shift on density and pressure at different temperatures is plotted in Fig. 3.2. The linear dependence of the chemical shift upon the density (shown in Fig. 3.2(a)) is clear, and holds for densities below 100 amagat. However, the dependence of the shift upon the pressure (shown in Fig. 3.2(b)) becomes nonlinear at ~30 atm, resulting from the non-ideal behavior of xenon at increasingly high pressures.

The chemical shift range of xenon in different chemical environments is over 7000 ppm wide (Fig. 3.3), again resulting from the highly polarizable electron cloud of xenon. While the large shift range results largely from strong electron de-shielding in the xenon compounds, it is impressive to note that a range of over 200 ppm may be obtained merely by dissolving xenon in different liquids [66]. Considerable work has therefore exploited such properties by using xenon as a non-destructive

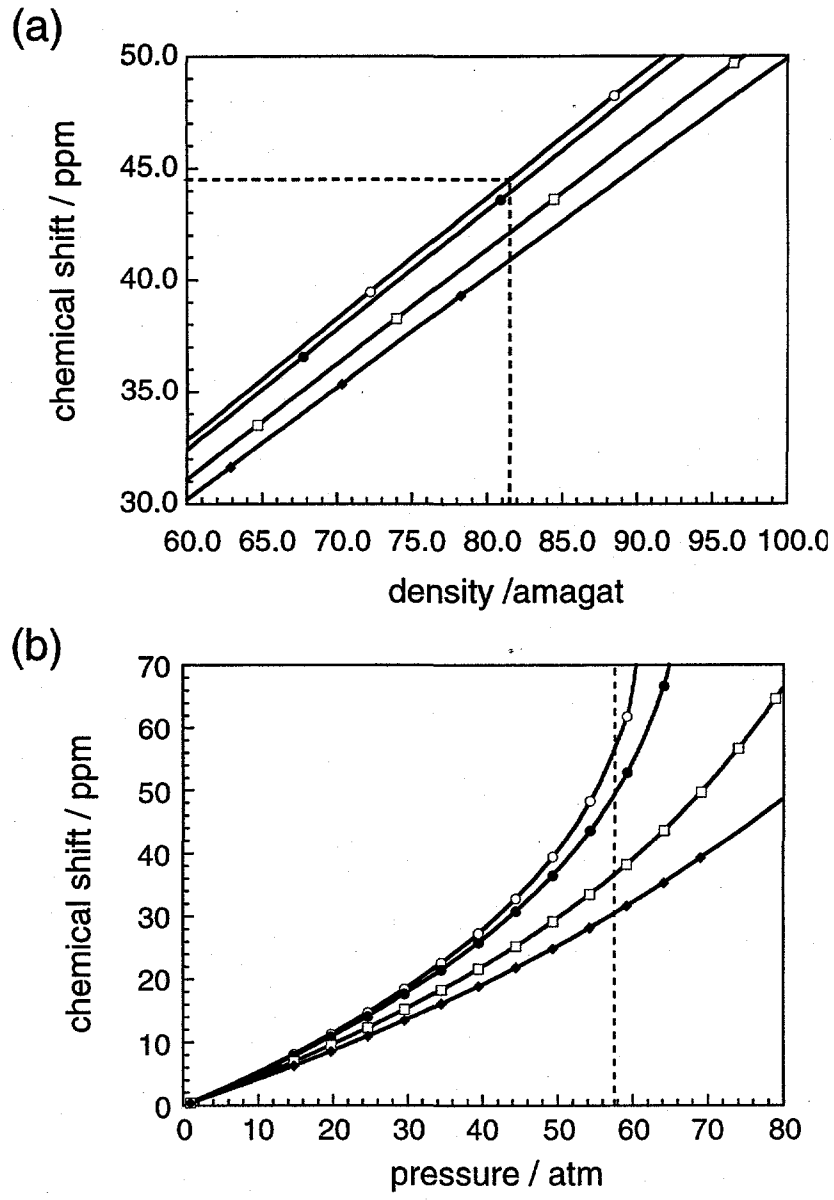

Figure 3.2: Chemical shift of gaseous xenon as a function of density (a) and pressure (b) at 22 °C (open circles), 27 °C (filled circles), 47 °C (open squares), and 67 °C (filled diamonds). The curves were calculated from the temperature and density dependence of the xenon chemical shift described in Ref. [65]; the xenon pressure was determined from the specific volume, i.e., the inverse density of the xenon which is tabulated as a function of pressure and temperature [79]. The dashed lines in (a) indicate the conditions under which the spectrum in Fig. 4.9 was obtained, while the dashed line in (b) marks the critical pressure of xenon.

magnetic resonance probe of various chemical environments (for review, see Refs. [67, 66, 68, 69, 70, 71]). Numerous examples where optically pumped ^{129}Xe NMR is used to probe such environments can be found throughout this thesis.

Except in cases involving xenon compounds (e.g., XeF_6 and XeO_4), NMR studies of xenon will usually occur in the presence of exchange phenomena. Thus, multi-site exchange models are often used to interpret ^{129}Xe spectra. Naturally, the simplest non-trivial version, the two-site exchange model, can be adopted for discussions regarding xenon exchange between two different environments (e.g., red blood cells and plasma, discussed in detail in Chapter 8).

We say that the exchange between two sites is "slow" on the NMR time scale when two lines can be resolved in the NMR spectra originating from the exchanging species. In general, for chemical exchange between two equally populated sites, the limiting condition of slow exchange can be written as:

$$[2\pi(\Delta\nu)\tau_{res}]^2 >> 1, \tag{3.3}$$

where $\Delta\nu$ is the difference in frequency between the resonances of the species at each site, and τ_{res} is the average residence time; $\tau_{res} = (k)^{-1}$, where k is the exchange rate. A derivation of the equivalent form of Eq. 3.3 for the case of asymmetric exchange is beyond the scope of this thesis; a discussion of this topic, and dynamic NMR spectroscopy in general, can be found in Ref. [80]. The trends predicted by

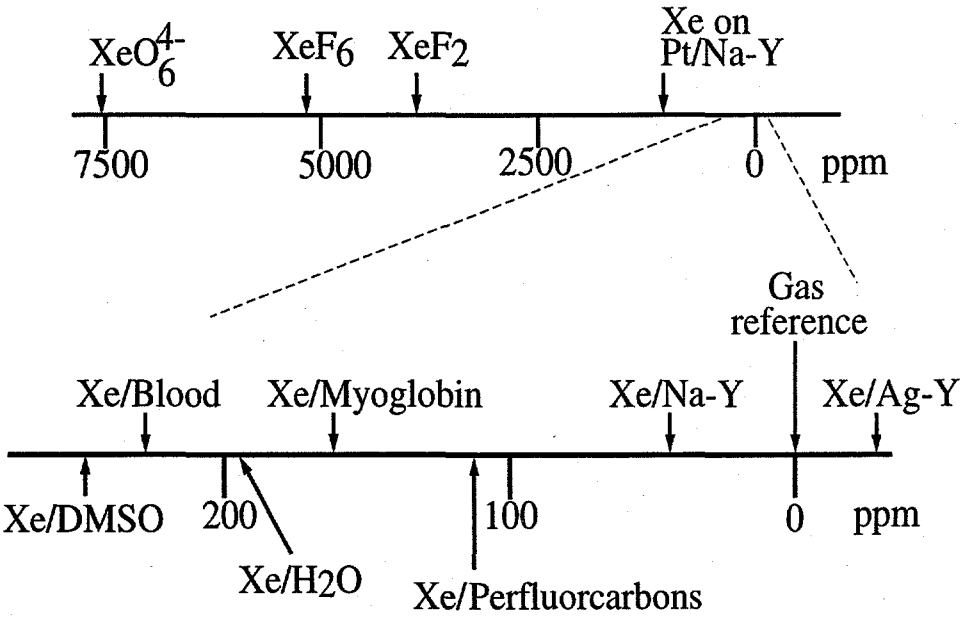

Figure 3.3: Chemical shift values for xenon in various environments. Adapted from Ref. [45].

Eq. 3.3 can still be helpful, however, even under conditions of asymmetric exchange. In conditions of fast xenon exchange (such as that observed in solutions of xenon and hemoglobin, where $\tau_{res} \sim 3$ μs [81]), only one peak is observed, whose chemical shift is a population-weighted average of the two (or more) different environments. Thus, under conditions of slow exchange, it is easier to extract information regarding the different xenon environments. Luckily, the wide chemical shift range of xenon lowers the limit of slow exchange (as suggested by Eq. 3.3); naturally, this condition can also be somewhat extended by using stronger external magnetic fields.

3.3 Some Experimental Considerations for Laser-Polarized Noble Gases

With the additional property of increased nuclear polarization from optical pumping, laser-polarized noble gases have attracted considerable interest for greatly enhancing sensitivity when probing substances and living tissues via NMR and MRI (for review, see Refs. [57, 45, 63, 67, 17, 40, 74, 73]. The non-renewable nature of the polarization does, however, complicate their use for many NMR/MRI applications. For most experiments, acquisition pulses applied directly to resonances of laser-polarized gases must be of small tipping angle in order to avoid using up all of the polarization at once; the application of each rf observation pulse of tipping angle α reduces the remaining z-component of the magnetization by a factor of $\cos(\alpha)$.

The only way to replenish the signal for averaging (or repetition) is to deliver fresh polarized gas to the sample (e.g., by continuous flow [43, 44]). This decrease in z magnetization with pulsing can also cause artifacts in images and spectra. Ameliorating these and other problems with the application of cleverly-designed NMR pulse sequences has already been the subject of considerable work (see for example, Refs. [75, 76, 77, 78]).

The non-renewable nature of the polarization can also be *advantageous* in biomedical applications for two reasons: 1) the polarization can be permanently destroyed at will with high efficiency and locality using standard MRI techniques, and 2) dilution and short *in vivo* relaxation times should cause contribution to the signal from recirculation to be negligible. These characteristics should greatly simplify interpretation when using polarized gases as tracers to measure local blood flow. Additionally, because the non-equilibrium nuclear polarization of laser-polarized gases is independent of the applied magnetic field, OPNMR/MRI can be performed at low fields. This potential advantage will be discussed in greater detail in Chapter 9.

Chapter 4

"Lighting Up" the NMR of Molecules I: Non-Specific Interactions

4.1 Introduction

The increased nuclear polarization from optical pumping has attracted considerable interest for using laser-polarized ^{129}Xe to enhance sensitivity when probing substances via ^{129}Xe NMR (for review, see Refs. [57, 45, 63, 67, 17, 40, 74]). However, the information obtained in this manner is still indirect, requiring that underlying structure and dynamics be inferred from the observed chemical shift, chemical-shift anisotropy, or relaxation parameters of xenon in intimate contact with the substance

being studied. Thus, in many circumstances a more direct method of probing such substances would be desired. Moreover, any means by which the overall NMR signal from molecules and materials themselves can be increased would be generally welcomed. For these reasons, considerable work has investigated the possibility of transferring polarization from laser-polarized xenon (and helium) to other nuclei, thereby "lighting up" the NMR of species interacting with laser-polarized noble gases.

The following two chapters contain numerous examples of polarization transfer experiments used to enhance the NMR signals of molecules, particularly in solution. This chapter is concerned with non-specific effects, i.e., situations in which there are no specific interactions between the laser-polarized gases and the molecules being studied (xenon binding in the hydrophobic pockets of molecules, for example). Of particular interest is the so-called spin polarization-induced nuclear Overhauser effect (or SPINOE). Special attention is given towards a theoretical description of the SPINOE, which will be useful for much of the remainder of this thesis, as well as a description of recent experimental work involving SPINOE enhancement of NMR signals of various solute species. Finally, this chapter assesses the feasibility of using laser-polarized xenon as a polarizing solvent to enhance the NMR signals of dissolved species, and concludes with a discussion of the ultimate limitations on SPINOE enhancement.

4.2 Polarization Transfer via Low-Field Thermal Mixing

Soon following predictions that polarization could be transferred from laser-polarized xenon to enhance the NMR signals of other substances [46], polarization transfer was first experimentally demonstrated when ^{131}Xe NMR signals from xenon ice were enhanced by low-field thermal mixing with laser-polarized ^{129}Xe [48]. Low-field mixing involves adiabatically sweeping the external magnetic field through a regime where the difference between the Zeeman energies of the two spin baths (in this case, ^{129}Xe ^{131}Xe spins in xenon ice) is matched by their dipolar coupling.

Following thermal mixing, the two spin baths (generally speaking, I and S=^{129}Xe) share a common inverse temperature, β, given by:

$$\beta \approx \frac{\alpha}{1 + \frac{\gamma_S^2 N_S}{\gamma_I^2 N_I}}, \tag{4.1}$$

where α is the inverse spin temperature of ^{129}Xe given by optical pumping; it has been assumed that $I = 1/2$.

Low-field thermal mixing has since been used to enhance the spin polarization of other nuclei in intimate contact with laser-polarized xenon [82, 83]. In one study, the ^{13}C NMR signals from CO_2 molecules embedded in a laser-polarized xenon ice matrix were enhanced by a factor of $\sim$200 (at 4.2 T), as shown in Fig. 4.1 [82]. Figure 4.1(a)

shows the enhanced ^{13}C CSA of CO_2 following zero-field mixing with laser-polarized xenon; Fig. 4.1(b) shows a spectrum taken from a sample prepared identically as that observed in (a), except that the xenon was prepared with the opposite polarization. The change in phase of the ^{13}C NMR signal demonstrates that the observed effect originates from polarization transfer from the laser-polarized xenon in the matrix.

Polarization has also been transferred successfully from laser-polarized xenon to materials surfaces by rf-driven Hartmann-Hahn cross-polarization [84, 85, 86] through dipolar couplings at high field [87, 88] (discussed in more detail in Chapter 6). Both low-field mixing and high-field cross-polarization require either a) that the nuclei to be polarized have been embedded in a laser-polarized xenon ice matrix [48, 82] or b) that laser-polarized xenon has been immobilized onto the material's surface [83, 87, 88]. Both of these preparations can be difficult to achieve in practice. Moreover, these methods cannot be employed for intermolecular polarization transfer in isotropic liquids, because dipolar couplings are averaged away by the rapid tumbling and translational diffusion of molecules in solution. Therefore, a different physical process must be exploited in order to obtain polarization transfer and subsequent signal enhancement in solution.

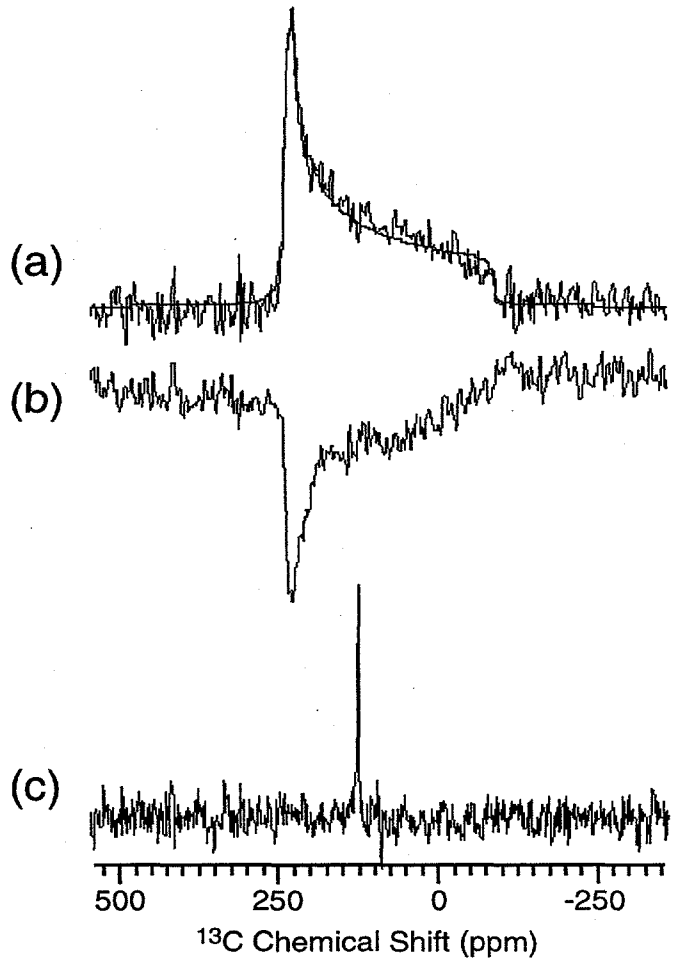

Figure 4.1: Enhancement of NMR signals of $^{13}CO_2$ obtained from low-field thermal mixing. (a) ^{13}C NMR signal obtained with one scan following low-field thermal mixing of a matrix comprised of spin-labeled CO_2 embedded in laser-polarized xenon ice. The curve superimposed upon the experimental data represents a theoretical fit to the ^{13}C CSA. (b) As in (a), but with oppositely polarized xenon. (c) Control spectrum obtained by taking 64 scans of $^{13}CO_2$ gas. Figure adapted from Ref. [82].

4.3 The Spin Polarization-Induced Nuclear Overhauser Effect

4.3.1 First SPINOE Experiments

It was recently shown that when laser-polarized xenon was dissolved in benzene, an enhancement of the benzene ^{1}H NMR signal could be observed [89], shown in Fig. 4.2. This transient enhancement of the ^{1}H signal is a consequence of cross-relaxation and polarization transfer between the dissolved laser-polarized xenon and the surrounding solution spins, a novel manifestation of the nuclear Overhauser effect (NOE). The ^{1}H NMR signal of pure benzene was observed to be enhanced by about 10% (at 4.3 T) following dissolution of laser-polarized xenon, while the ^{1}H NMR signal of partially deuterated benzene (25% C_6D_5H, 75% C_6D_6) was enhanced by a factor of $\sim$2. As shown in Fig. 4.2, reversing the polarization of the laser-polarized xenon brought about a concomitant change in the sign of the observed signal enhancement, again demonstrating that the effect resulted from the enhanced polarization of the laser-polarized xenon. Finally, it was demonstrated that the enhanced proton polarization could be imaged (shown in Fig. 7.3 of Chapter 7), suggesting the possibility of using cross-relaxation with dissolved laser-polarized xenon to perform novel *in vivo* ^{1}H MRI experiments.

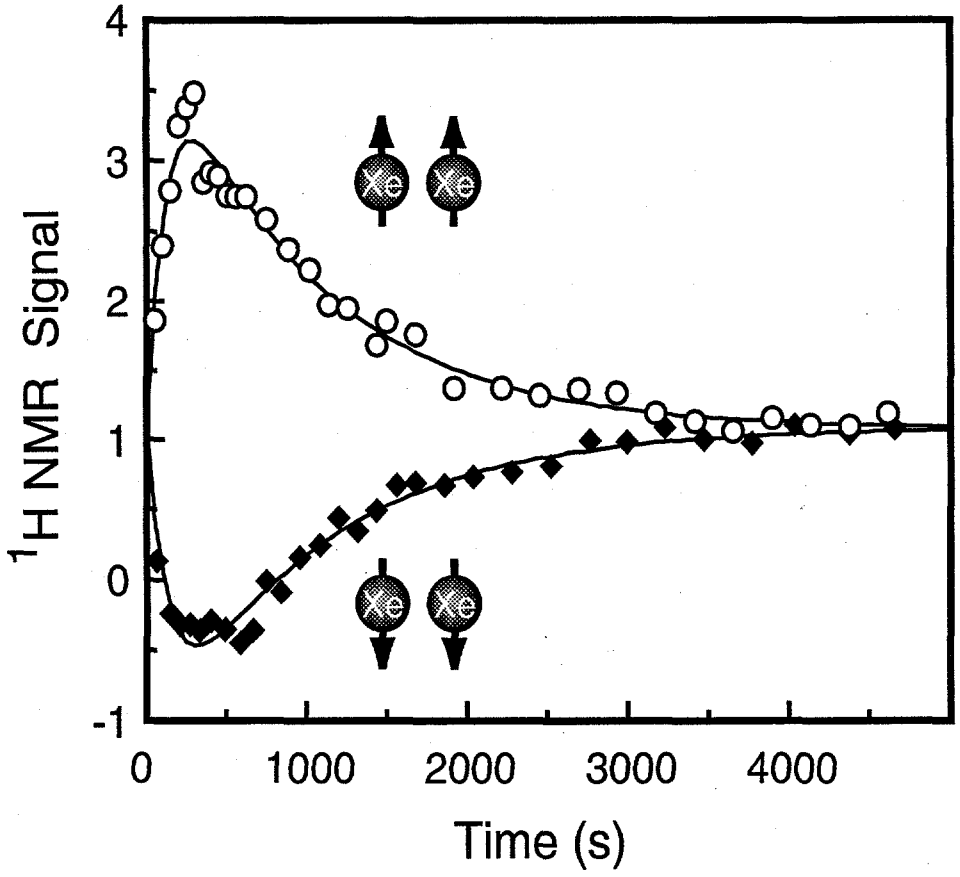

Figure 4.2: Time dependence of the integrated ^{1}H NMR signal from a partially deuterated benzene solution containing dissolved laser-polarized xenon [89]. The SPINOE produced positive benzene ^{1}H NMR signal enhancements when "positively" polarized xenon was dissolved (open circles), and negative signal enhancements when "negatively" polarized xenon was dissolved (filled diamonds). Adapted from figure courtesy of Yi-Qiao Song.

4.3.2 Theoretical Background

The above phenomenon has been called the spin polarization-induced nuclear Overhauser effect (SPINOE) [89]. In order to better understand the SPINOE, the underlying principles of nuclear dipolar cross-relaxation are reviewed, and slightly recast in light of the unique properties of laser-polarized noble gases.

Consider two ensembles comprised of spins I and S (where, for the time being, we will assume that I=^{1}H and S=^{129}Xe) participating in mutual dipolar cross-relaxation (Fig. 4.3). The time-dependent behavior of the coupled spin baths can be described by the Solomon equations [92, 93, 94]:

$$\frac{d\langle I_z\rangle}{dt} = -\rho_I\left(\langle I_z\rangle - I_0\right) - \sigma_{IS}\left(\langle S_z\rangle - S_0\right), \tag{4.2}$$

$$\frac{d\langle S_z\rangle}{dt} = -\rho_S\left(\langle S_z\rangle - S_0\right) - \sigma_{SI}\left(\langle I_z\rangle - I_0\right). \tag{4.3}$$

ρ_I (ρ_S) is the auto-relaxation rate for spin I (S), σ_{IS} (σ_{SI}) is the I←S (S←I) cross-relaxation rate, $\langle I_z\rangle$ and $\langle S_z\rangle$ are respectively the ensemble-average values of the z component of the $\vec{I}$ and $\vec{S}$ nuclear spin operators, and I_0 and S_0 are their equilibrium values; for example,

$$I_0 = \frac{I\left(I+1\right)\hbar\gamma_I B_0}{3kT}. \tag{4.4}$$

For spin-$I = 1/2$ nuclei, $I_0 = P/2$.

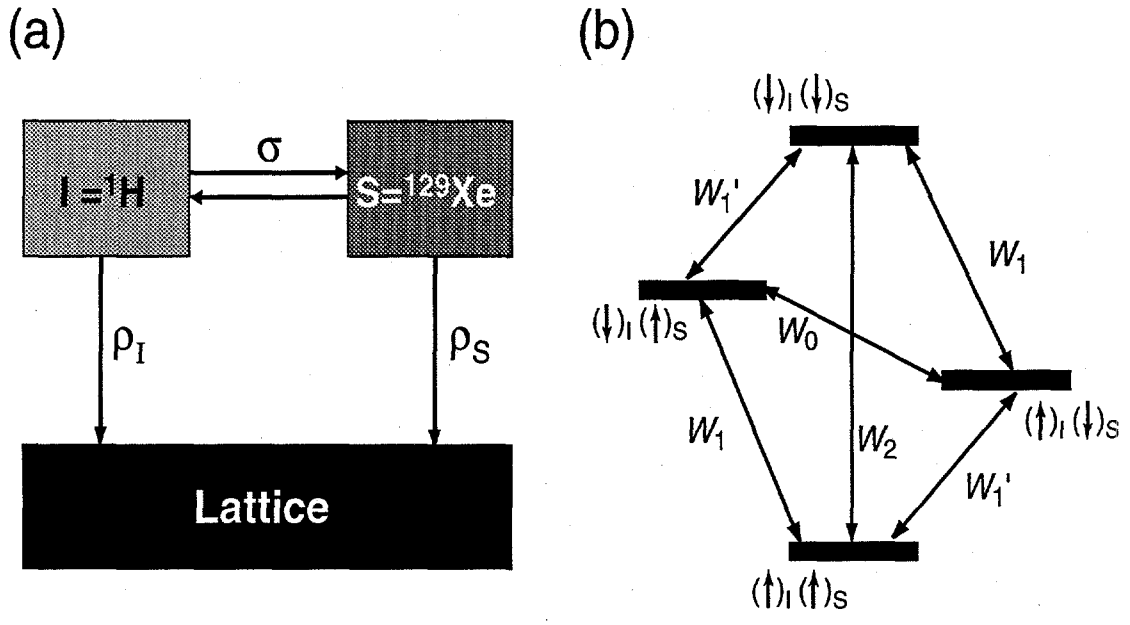

Figure 4.3: Macroscopic (a) and microscopic (b) pictures of the SPINOE. (a) Polarization enhancement of the proton spin bath (I) is achieved via cross-relaxation with laser-polarized xenon (S), governed by the cross-relaxation rate, σ ($\sigma_{IS} = \sigma_{SI} \cdot (N_S/N_I)$). The polarization enhancement for the protons is limited by the respective autorelaxation rates of both spin baths, ρ_I and ρ_S. (b) General two-spin model for the NOE, assuming positive gyromagnetic ratio for both spins. The transfer of population among the four levels is governed by W_1 and W_1' (the single-quantum transition probabilities), which contribute to the autorelaxation of the spins, and W_0 and W_2 (respectively the zero-quantum and double-quantum transition probabilities), which contribute to both the cross-relaxation and autorelaxtion rates.

A full solution of Eqs. 4.2, 4.3 can be found in the literature [95], as can a detailed review of the SPINOE [96]. The SPINOE enhancement for an ensemble of proton spins participating in dipolar cross-relaxation with laser-polarized ^{129}Xe is well-approximated by:

$$f_H(t) = -\frac{\gamma_{Xe}}{\gamma_H} f_{Xe}(0) \frac{\sigma_{HXe}}{\rho_H} \left(1 - \mathrm{e}^{-\rho_H \cdot t}\right), \tag{4.5}$$

where $f_H(t) = [\langle I_z(t) \rangle - I_0]/I_0$ is the fractional polarization enhancement of the protons, and $f_{Xe}(0)$ is the fractional polarization enhancement for the xenon endowed by optical pumping. Figure 4.4 shows the time dependence of the SPINOE enhancement as calculated by Eq. 4.5. Equation 4.5 assumes that the spin-lattice relaxation time of ^{129}Xe, ${T_1}^{Xe}$, is much greater than that measured for the protons, ${T_1}^{H}$ (generally true for ^{129}Xe in solution), or that the xenon spin polarization is maintained by continuous flow (Fig. 4.4) [43, 44].

Equation 4.5 governs the initial rise in signal shown in the curves in Fig. 4.4 (as well as that manifested in the experimental data shown in Fig. 4.2); the latter exponential decay towards equilibrium is governed by ${T_1}^{Xe}$. Given the value of ${T_1}^{H}$, the initial ^{1}H NMR enhancement observed over a given time can be used to compute σ_{HXe}. As will be discussed in the next chapter, σ_{HXe} not only governs the polarization transfer, but can yield important structural and dynamical characteristics of the molecule-xenon interaction.

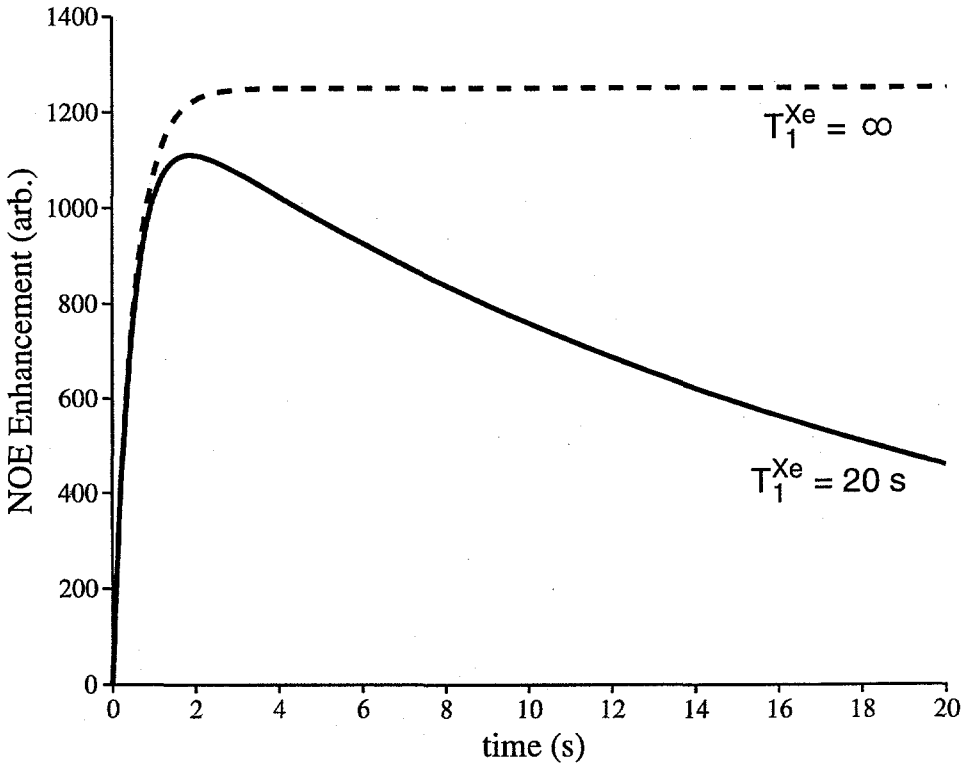

Figure 4.4: Calculated time dependence of the SPINOE signal, including (solid line) and not including (dotted line) the exponential decay caused by the eventual ^{129}Xe spin-lattice relaxation. Curves were calculated with $\rho_H = 2$ s^{-1}, $\sigma_{HXe} = 0.001$ s^{-1} and $\rho_{Xe} = 0.05$ s^{-1} (for the solid curve). Behavior such as that shown with the dotted line may also be seen under conditions of continuous flow of laser-polarized xenon (see Refs. [43, 44] and the discussion in Chapter 6).

Recall that in the two-spin model, the nuclear spin cross-relaxation and auto-relaxation rates are generally given by (for example) [93]:

$$\sigma_{IS} = W_2 - W_0, \tag{4.6}$$

$$\rho_I = W_2 + 2W_1 + W_0, \tag{4.7}$$

where each transition probability between two given states $(|\psi_i\rangle, |\psi_j\rangle)$, W_{ij} can be derived from the familiar Fermi Golden Rule:

$$W_{ij} = \frac{1}{t\hbar^2}\left|\int_0^t dt' \langle\psi_i|H_D(t)|\psi_j\rangle e^{-it'\frac{(E_j-E_i)}{\hbar}}\right|^2, \tag{4.8}$$

where each state is a member of the four-level diagram shown in Fig. 4.3, and $H_D(t)$ is the (time-dependent) dipolar Hamiltonian from Chapter 1; the time-dependence originates from the random reorientations and relative diffusive motion of the species involved.

It can be shown that the SPINOE cross-relaxation rate between laser-polarized xenon and protons can be explicitly written as:

$$\sigma_{HXe} = \left(\frac{\mu_0}{4\pi}\right)^2 \frac{\hbar^2 {\gamma_H}^2 {\gamma_{Xe}}^2}{10} \left\langle \frac{1}{{r^6}_{HXe}} \right\rangle \left[6J\left(\omega_H + \omega_{Xe}\right) - J\left(\omega_H - \omega_{Xe}\right)\right], \tag{4.9}$$

where r_{HXe} is the proton-xenon internuclear distance, $\langle\rangle$ denotes the ensemble aver-

age, and the spectral density $J(\omega)$ is given by

$$J(\omega) = \frac{\tau_c}{1 + \omega^2 {\tau_c}^2}, \tag{4.10}$$

where τ_c is the correlation time associated with the fluctuations of the H-Xe dipolar interactions. Thus, both $\langle {r^{-6}}_{HXe} \rangle$ and τ_c control the size and selectivity of the observed H-Xe cross-relaxation rates.

A plot of the dependence of σ_{HXe} on the correlation time is shown in Fig. 4.5. From Eq. 4.9 it can be shown that σ_{HXe} is always positive (regardless of the correlation time or the external field strength), resulting from the large difference between the gyromagnetic ratios of ^{1}H and ^{129}Xe. Therefore, it is expected that when "positively" polarized xenon is dissolved into solution, positive SPINOEs will be observed (to avoid confusion with the previous literature originating from the negative sign of γ_{Xe}, here we define "positively" polarized xenon to be xenon laser-polarized in the same direction as its equilibrium polarization (with the population of $m_I = -1/2$ greater than the population of $m_I = +1/2$), therefore giving a positive value for $f_{Xe}(0)$). This behavior is, in fact, observed in Fig. 4.2; conversely, the admission of "negatively" polarized xenon (produced by inverting the magnetic field in which the xenon was laser-polarized) brought about a corresponding negative SPINOE in the benzene ^{1}H NMR signal. Fig. 4.5 also predicts that the cross-relaxation rate will have its greatest value at $\omega_H \tau_c \approx 0.68$. An increase in the correlation time from a

few ps ($\omega_H \tau_c = 0.01 - 0.02$ at 9.4 T) to a value corresponding to the maximum (with τ_c in the range 0.2-0.5 ns) gives rise to a ~20-fold increase in the cross-relaxation rate. However, this increase in σ_{HXe} does not necessarily translate into an increase in the observed SPINOE enhancement. For example, in real systems large enough to bind xenon, the increased correlation time characterizing the H-Xe dipolar interactions would generally be accompanied by a corresponding increase in the correlation time characterizing the H-H dipole-dipole interactions, and a concomitant reduction of proton auto-relaxation time.

Diffusion-Modulated Dipolar Cross-Relaxation

The dipolar relaxation between xenon and benzene is modulated by the relative diffusive motion between these two species. The time scale for such an interaction is typically short (a few ps), thereby fulfilling extreme narrowing conditions. From the data shown in Fig. 4.2, it was determined that cross-relaxation rate was $\sim 1.9 \times 10^{-6}$ s^{-1}, in general agreement with theoretical estimates of diffusion-modulated cross-relaxation between protons and ^{129}Xe in solution [89], as discussed below.

Molecular dynamics simulations can be extremely helpful for understanding intermolecular relaxation (for examples regarding xenon spin relaxation in solution, see Refs. [97, 98]), however, such simulations tend to be computationally expensive. Instead, simpler models of intermolecular relaxation exist that despite their reliance upon crude assumptions [93], can give reasonable qualitative descriptions of

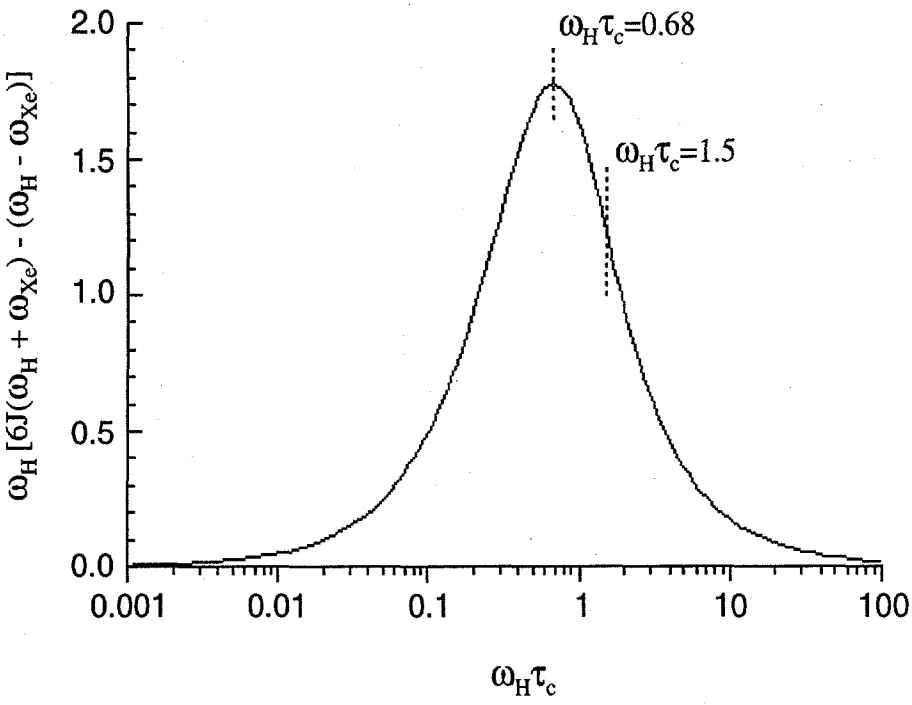

Figure 4.5: Illustration of the dependence of the ^{1}H-^{129}Xe cross-relaxation rate, σ_{HXe}, on the correlation time [47], where $\omega_H[6J(\omega_H + \omega_{Xe}) - J(\omega_H - \omega_{Xe})] = 6\omega_H\tau_c/[1 + (|\gamma_{Xe}/\gamma_H|)^2\omega_H^2\tau_c^2] - \omega_H\tau_c/[1 + (1 - |\gamma_{Xe}/\gamma_H|)^2\omega_H^2\tau_c^2]$. Two points on the curve are marked; $\omega_H\tau_c \approx 0.68$ corresponds to the curve's maximum, while $\omega_H\tau_c \approx 1.5$ corresponds to the experimentally measured value for xenon in cryptophane-A at 9.4 T, a system described in detail in the following chapter.

intermolecular dipole-dipole relaxation processes. For example, it can be shown that when the cross-relaxation is modulated by relative diffusive motion, σ_{IS} should be linearly dependent upon the concentration of molecules bearing spin S; thus in our case, σ_{HXe} is dependent on [Xe]. In fact, such a dependence arises from the ensemble average of r_{HXe}^{-6}. In a pairwise additivity scheme for xenon-solute interactions, $\langle r_{HXe}^{-6} \rangle$ is given by the relation:

$$\langle r_{HXe}^{-6} \rangle = \left[4\pi N_A 10^{-27} \int_0^\infty dR \cdot R^2 \frac{\int d\Omega \cdot g(R,\Omega) \cdot r_{HXe}^{-6}}{\int d\Omega} \right] \cdot [\mathrm{Xe}], \tag{4.11}$$

where R is the distance between the center-of-mass of the solute molecule and the xenon atom (with both R and r_{HXe} in Å), N_A is Avogadro's number, Ω represents the angular variables specifying the relative orientation of the solute-xenon pair, and $g(R,\Omega)$ is the solute-xenon pair distribution function. Incidentally, because (to a good approximation) $\langle r_{HXe}^{-6} \rangle$ is proportional to [Xe], a concentration-normalized H-Xe cross-relaxation rate, σ_{HXe}^n ($\mathrm{s^{-1}M^{-1}}$), may be defined such that

$$\sigma_{HXe}^d = \sigma_{HXe}^n [\mathrm{Xe}], \tag{4.12}$$

where σ_{HXe}^d explicitly refers to cross-relaxation originating from purely diffusive coupling.

Concerning the dynamics of the diffusive coupling, it is clear that an upper bound for the correlation time is provided by the residence time of xenon in the solvation shell

of the solute (usually a few picoseconds). Thus, the condition of extreme narrowing ($(\omega\tau_c)^2 << 1 spintheory$)) is thereby fulfilled in normal circumstances. The proton-xenon cross-relaxation rate resulting from diffusive coupling is then given by:

$$\sigma^d_{HXe} = \left(\frac{\mu_0}{4\pi}\right)^2 \frac{\hbar^2\gamma_H^2\gamma_{Xe}^2}{10}\langle r^{-6}_{HXe}\rangle 5\tau_c^d, \tag{4.13}$$

where τ_c^d explicitly refers to the correlation time governing the diffusive coupling between xenon and the other spin.

One should remember that τ_c^d may be completely unrelated to the correlation time controlling the proton dipole-dipole intramolecular relaxation of the solute molecule participating in cross-relaxation with xenon. For instance, in circumstances where the molecular mass of the solute significantly exceeds the xenon atomic mass, the tumbling motion of the solute molecule is expected to be slow on the timescale of the residence of xenon atoms in the solvation shell of the solute. Consequently, the magnitude of the SPINOE signal resulting from diffusive coupling should generally decrease for increasing solute size (not because σ^d_{HXe} is affected, however, but because the proton auto-relaxation time is reduced).

The order of magnitude of σ^n_{HXe} and σ^d_{HXe} can now be estimated by assuming the system is a monatomic fluid and by using a Heaviside step function as an approximation for the radial pair distribution function ($g(r) = 0$ for $r < r_0$ and 1 otherwise) in

Eq. 4.13, giving:

$$\langle r_{HXe}^{-6} \rangle \approx \frac{4}{3}\pi N_A 10^{-27} r_0^{-3}[\mathrm{Xe}], \tag{4.14}$$

where r_0 is the proton-xenon minimum approach distance. Thus, given $\tau_c^d = 5$ ps and $r_0 \sim 3.0-3.2$ Å, σ_{HXe}^n is estimated to be on the order of 10^{-5} $s^{-1}M^{-1}$ from Eq. 4.13). Finally, because the solubility of xenon in organic solvents under standard conditions is on the order of 0.1 M, σ_{HXe}^d is expected to be on the order of 10^{-6} s^{-1}. Indeed, this prediction is in excellent agreement with the value of $\sim 1.9 \times 10^{-6}$ s^{-1} observed between benzene protons and dissolved laser-polarized xenon [89].

In the framework of the dipolar-coupled two-spin model, the auto-relaxation of the protons would be solely a consequence of dipole-dipole interactions with laser-polarized ^{129}Xe. However, molecules in solution contain many-spin systems, so intermolecular ^{1}H-^{129}Xe dipole-dipole interactions are not likely to contribute significantly to the ^{1}H auto-relaxation rate. For solutes at low concentration in deuterated solvents, when no paramagnetic species are present, intramolecular ^{1}H-^{1}H dipole-dipole interactions normally dominate the auto-relaxation of protons (especially in molecules large enough to bind xenon), although other mechanisms, such as spin-rotation coupling, may contribute to the relaxation of small molecules such as benzene or parts of molecules, like methyl groups. Therefore, the simplest realistic model for ^{129}Xe$\rightarrow$^{1}H polarization transfer requires at least a three-spin system comprised of two interact-

ing protons and one xenon atom participating in dipolar interactions with only one of the proton sites. Such a three-spin model can be found in Ref. [47]. However, for the purpose of interpreting experimental SPINOE spectra, the two-spin model is usually sufficient, provided that the *experimental* spin-lattice proton relaxation times are considered.

4.3.3 Pulse Sequence Considerations

In the Xe/benzene experiments discussed above, the SPINOE enhancements were between 10% and 200%, large enough to observe by acquiring the ^{1}H signal as a function of time, and carefully subtracting the equilibrium ^{1}H signal from each spectrum. In many cases, the NMR signal enhancement obtained via the SPINOE will be small compared to the equilibrium NMR signal for a given species, necessitating an NMR pulse sequence designed to directly obtain the SPINOE contribution to a given signal. A heteronuclear NOE sequence adapted from the sequences of Shaka and co-workers [99, 100] is shown in Fig. 4.6; an NMR signal obtained with this sequence will be referred to as a SPINOE spectrum. The sequence in Fig. 4.6 effectively suppresses the equilibrium NMR signal, conveniently allowing direct detection of NOE signals as weak as $\sim 10^{-4}$ of the equilibrium signal.

The first element of the sequence, a small tipping-angle observation pulse on the ^{129}Xe, is applied prior to the acquisition of ^{1}H SPINOE spectra, and is necessary only for calibrating the xenon polarization to calculate absolute values for the Xe-H

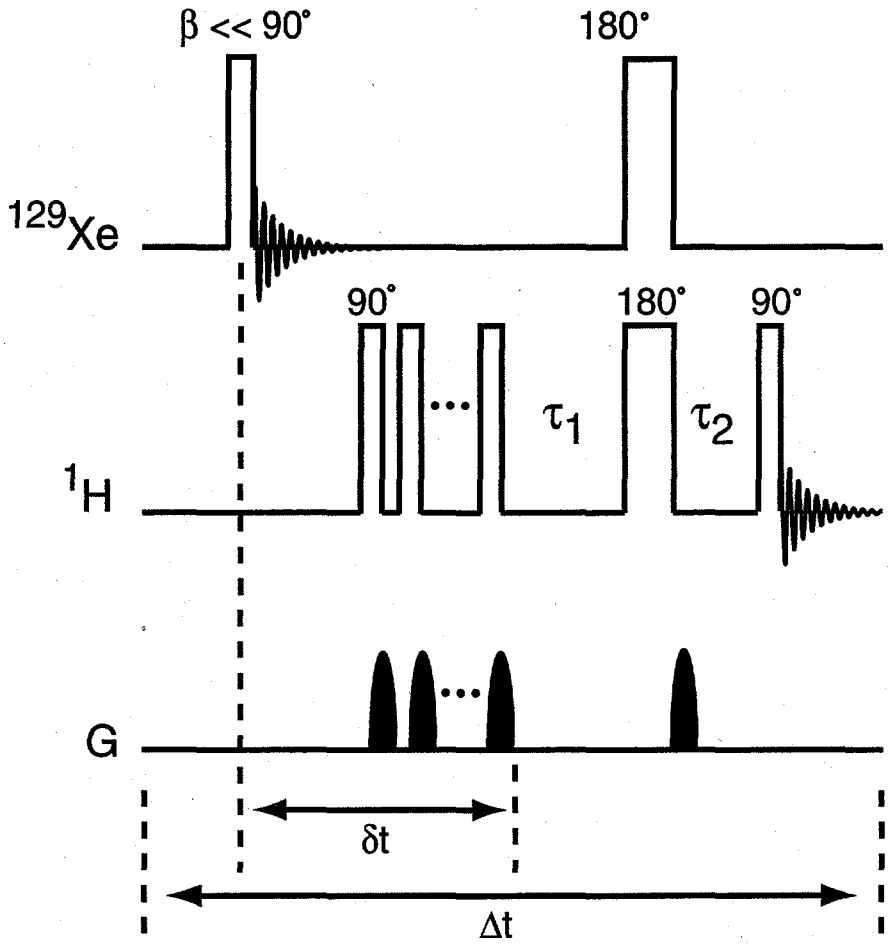

Figure 4.6: Heteronuclear difference NOE pulse sequence for obtaining SPINOE spectra [47], adapted from sequences developed by Shaka and co-workers [99, 100].

cross-relaxation rates. Saturation of the equilibrium ^{1}H signal is first achieved by the application of the 90° and gradient pulses; the saturation is then maintained by a 180° pulse followed by a gradient pulse. The ^{129}Xe pulse permits the SPINOE signal to accumulate during τ_1 and τ_2. The values of τ_1 and τ_2 are normally chosen such that their sum is much less than T_1^{Xe}, and their ratio minimizes the equilibrium proton signal detected in the absence of SPINOE polarization transfer. The ^{1}H and ^{129}Xe 180° pulses are often adiabatic, modulated pulses (see for example, Refs. [101, 102]) to insure efficient, wide-band inversion. Generally, each SPINOE spectrum is the difference of two acquisitions.

The difference SPINOE pulse sequence in Fig. 4.6 was first applied to directly observe the cross-relaxation between dissolved laser-polarized xenon and *p*-nitrotoluene in a perdeuterated benzene solution [103]; the corresponding SPINOE spectra are shown in Fig. 4.7. Specifically, Figs. 4.7(a,c) show the NMR signal originating exclusively from cross-relaxation with laser-polarized xenon, while Fig. 4.7(b) contains the NMR signal observed with the same pulse sequence, except without the application of the ^{129}Xe 180° pulse (thereby preventing SPINOE accumulation). The lack of signal in Fig. 4.7(b) demonstrates the effectiveness of the pulse sequence in Fig. 4.6 for suppressing the equilibrium signal.

In rare circumstances (e.g., with systems that participate in strong xenon binding such that the xenon exchange is slow with respect to the NMR time scale) it may be experimentally difficult to achieve perfect inversion of the xenon magnetization. In

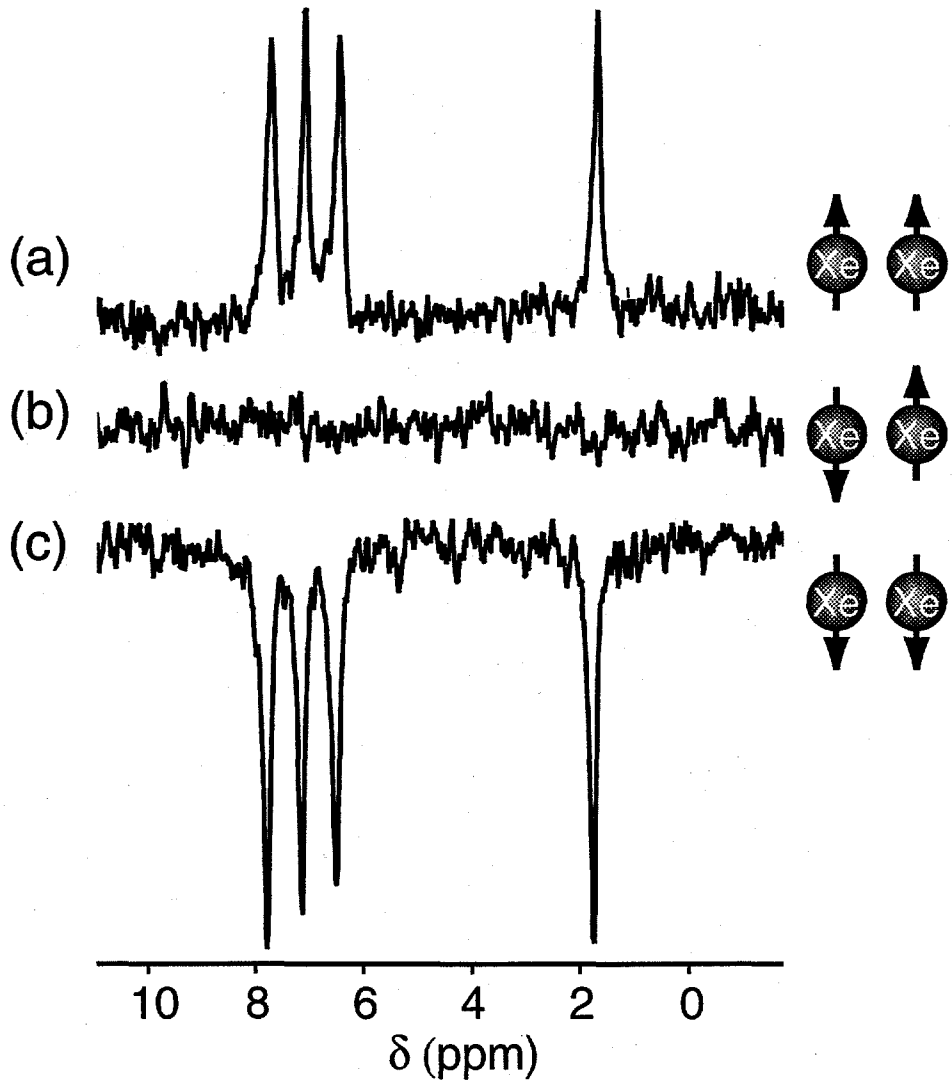

Figure 4.7: ^{1}H SPINOE spectra from a solution of 0.1 M *p*-nitrotoluene and d_5/d_6-benzene containing dissolved laser-polarized xenon [103]. (a) Spectrum acquired following the introduction of "positively" polarized xenon. (b) As in (a), but without the application of the ^{129}Xe 180° pulse, demonstrating complete suppression of the equilibrium proton signal. (c) As in (a), but with "negatively" polarized xenon, yielding a corresponding sign change in the ^{1}H SPINOE spectrum.

such cases, it may be necessary to explicitly account for the inefficiency of the ^{129}Xe 180° inversion pulses when calculating the experimental cross-relaxation rates [47].

4.4 Using Xenon as a Polarizing Solvent

In the absence of strong xenon binding, the observed Xe-H cross-relaxation rate is proportional to the concentration of xenon in the solution; therefore, higher concentrations of laser-polarized xenon should yield larger SPINOE enhancements for other solute species. To maximize this effect, recent work has investigated the use of laser-polarized xenon as the *solvent* in SPINOE experiments. Increasing the nuclear spin polarization of molecules in solution could be useful for a variety of liquid-state NMR and MRI experiments, especially in circumstances where the observed nucleus is in low natural abundance or the species in question are short-lived. Moreover, because xenon is transparent to UV, visible, and mid-IR radiation, it is an attractive solvent for *in situ* spectroscopy (e.g. for studying the photochemistry of organometallic substances).

4.4.1 Liquid Laser-Polarized Xenon

Liquid xenon is a surprisingly effective solvent for small organic molecules; it can even be used to dissolve certain inorganic complexes and biomolecules [104, 105, 106, 111]. Liquid laser-polarized xenon has been successfully produced and studied

via NMR [107, 108, 109]. For example, by carefully preventing contamination from paramagnetic oxygen, it was determined that the T_1 of liquid laser-polarized xenon was about 25 min. [107], long enough to permit significant polarization transfer to solute species. And unlike the solid phase, it was shown that the high, non-equilibrium polarization of liquid laser-polarized xenon could be maintained for long times at low field; the dipolar coupling between laser-polarized ^{129}Xe and quadrupolar ^{131}Xe that dominate ^{129}Xe T_1 in the solid phase is quenched by the random diffusive motion in solution.

Liquid laser-polarized xenon has since been used to significantly enhance the NMR signals of dissolved molecules [110]. By performing the experiments below 200 K, such experiments could be performed at relatively low pressures without prohibitively sacrificing the solubility of the small organic molecules being studied. For example, when toluene was dissolved in liquid laser-polarized xenon, ^{1}H NMR signals from the aromatic and methyl protons were respectively enhanced by factors of 16 and 6 at 1.4 T, as shown in Fig. 4.8. It is also interesting to note that the observed differential enhancement cannot be entirely attributed to the large difference between the ${T_1}^H$ values measured for these protons (aromatic protons: ${T_1}^H = 21$ s; methyl protons: ${T_1}^H = 6.1$ s), suggesting either a physical difference between the respective xenon-proton interactions (e.g., a difference in average xenon proximity for the two types of protons), or more simply, significant ^{1}H-^{1}H polarization transfer via "relayed" SPINOE (see Ref. [47]). A factor of 45 enhancement was achieved for the ^{1}H NMR

signal of dissolved cyclopropane by using 71% ^{129}Xe-enriched laser-polarized liquid xenon (again at 1.4 T and 200 K). Such polarization-transfer experiments are not limited to enhancing the NMR signals of protons, however. By dissolving $^{13}CS_2$ in liquid laser-polarized xenon, it was shown that the ^{13}C NMR signal could be enhanced by a factor of 74 at 1.4 T.

4.4.2 High-Pressure Experiments

The feasibility of using supercritical laser-polarized xenon as a polarizing solvent was also recently investigated [58]. While requiring the use of high-pressure sample tubes, the supercritical phase offers many tantalizing advantages. The solubility characteristics of xenon improve significantly in the supercritical phase [112, 113, 114], and the higher and broader temperature range is generally more convenient for a variety of chemical and biophysical experiments. The low viscosity of supercritical solvents leads to narrow solute linewidths, especially for those containing quadrupolar nuclei [115, 116, 117]. Furthermore, the density of supercritical xenon, and hence its physical properties (e.g., the solubility parameters and dielectric constant), are strongly pressure dependent [118]; the physical properties of the solvent can therefore be manipulated to provide specific solvent environments [113]. The enhanced thermal stability of biomolecules in supercritical solvents may also prove advantageous for certain experiments [119, 120].

In the first experiments, the supercritical laser-polarized xenon samples were pre-

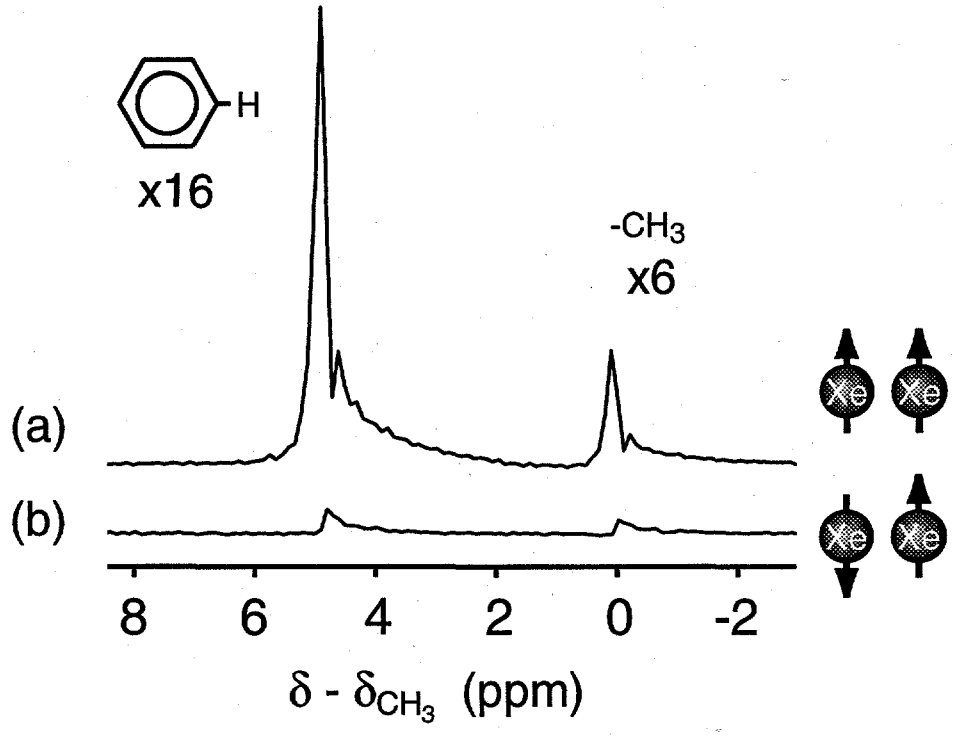

Figure 4.8: ^{1}H NMR signal from toluene dissolved in liquid xenon at 200 K and 1.4 T, with (a) and without (b) laser-polarization [110]. By dissolving toluene in liquid laser-polarized xenon, the NMR signal from the methyl protons was enhanced by a factor of 6, while the signal from the aromatic protons was enhanced by a factor of 16. These enhancements were obtained with natural isotopic abundance of ^{129}Xe, and with ^{129}Xe nuclear polarization of about 7%. Figure adapted from data courtesy of Karen Sauer.

pared in a high-pressure Pyrex capillary tube. This tube had to be pressure-checked frequently in order to guard against explosions. Such Pyrex tubes have now been discarded in favor of sapphire tubes which are considerably more pressure-tolerant. Following optical pumping in a batch apparatus, the laser-polarized xenon gas was first cryopumped into a region of smaller volume, and re-sublimated to generate a moderately high xenon pressure ($\sim$10 atm). This initial step permitted the xenon to be condensed as a liquid into the the high-pressure capillary tube, conveniently preventing solid xenon blockages from forming in the capillary tube during freezing. The sample tube was then immersed in a beaker of hot water and placed in the NMR magnet.

Figure 4.9(a) shows a ^{129}Xe NMR spectrum of supercritical laser-polarized xenon, while the corresponding equilibrium spectrum taken several hours later is shown in Fig. 4.9(b). The inverted phase of the signal in Fig. 4.9(a) results from the direction of the magnetic field in which the xenon was laser-polarized. The chemical shift of the equilibrium spectrum (44.5 ppm) taken at room temperature ($\approx$22 °C) corresponds to a xenon density of approximately 81.5 amagat [65]. The difference in chemical shift between the laser-polarized and equilibrium spectra (combined with knowledge of the internal xenon density) can be used to calculate an internal temperature and pressure of $\sim$52°C and $\sim$65 atm for the conditions in which spectrum (a) was taken, well beyond the critical point of xenon (16.6 °C, 57.6 atm) [124]. The broader linewidth of the spectrum in Fig. 4.9(a) may be a result of local density fluctuations in the

thermally non-equilibrated sample.

The laser-polarized ^{129}Xe signal indicated a nuclear spin polarization about 140 times that of the equilibrium polarization. Of course, this enhancement factor represents a loss of almost two orders of magnitude compared to the ^{129}Xe polarization typically prepared by the batch optical pumping apparatus; it is likely that paramagnetic impurities in the metal valves and tubing were responsible for this loss in polarization. Since this preliminary work, the use of sapphire tubes and improved efficiency of sample preparation have permitted supercritical laser-polarized xenon samples to be created in our laboratory with nuclear spin polarization greater than 1%, with densities greater than 140 amagat. In principle, there is no reason why the polarization could not eventually approach that of the gas when in the pumping cell.

The T_1 of the supercritical laser-polarized xenon was shown to be several hundred seconds, in general agreement with previous work involving unpolarized xenon [123]. Indeed, T_1 values of about 1000 s have recently been observed in supercritical laser-polarized xenon samples in our laboratory.

Finally, the solubility characteristics of both liquid and supercritical xenon can be improved by the addition of small amounts of other compounds [121, 122]. An example of this phenomenon is given in Fig. 4.10. Specifically, Fig. 4.10 shows ^{1}H NMR spectra taken from a sapphire tube containing thermally-polarized xenon at high pressure (about 900 p.s.i.) and cyclosporin, a small cyclic peptide used clinically to suppress unwanted immune responses in organ-transplant patients. Fig. 4.10(a)

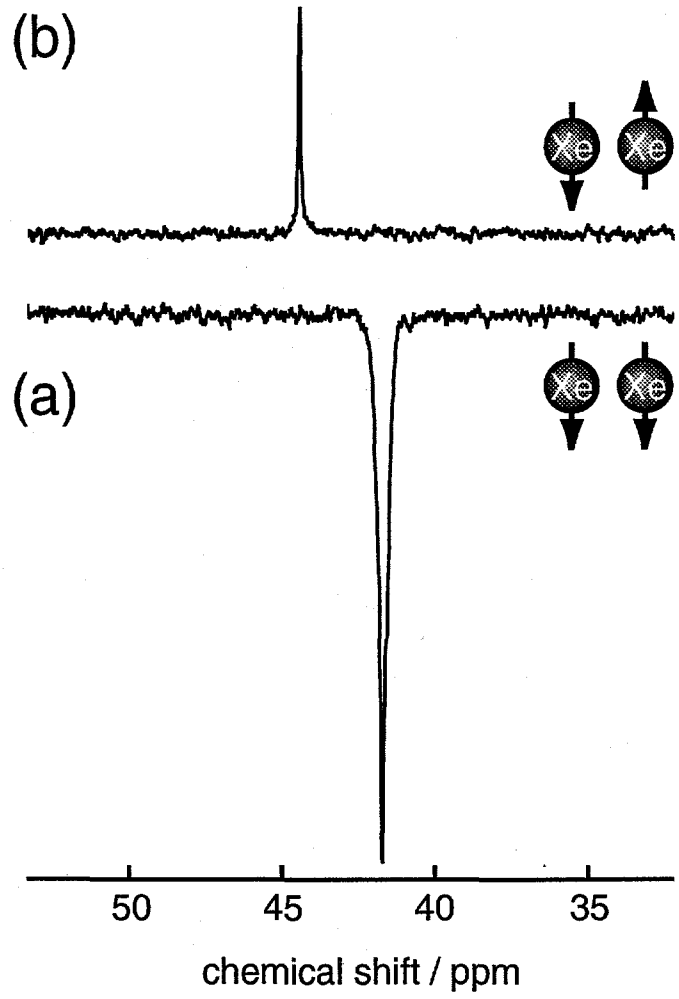

Figure 4.9: First NMR spectrum of laser-polarized supercritical xenon [58]. (a) Spectrum of supercritical laser-polarized xenon at about 52 °C and 65 atm. The spectrum was acquired with one pulse of small tipping angle (3°). (b) Spectrum of ^{129}Xe at 22 °C obtained with a ≈90° pulse after reaching an equilibrium polarization over several hours. The 44.5 ppm ^{129}Xe chemical shift in (b) indicates a pressure of ∼54 atm, slightly below the critical pressure (57.6 atm).

exhibits broad lines indicative of the cyclosporin remaining in an undissolved polycrystalline state. The addition of a small amount of benzene to the sample tube, however, permitted complete dissolution of the cyclosporin in the xenon/benzene mixture, as shown by the high-resolution spectrum in Fig. 4.10(b). Using laser-polarized xenon as the solvent may have many potential applications for enhancing the NMR signals of solute species for various kinetic and analytical studies.

4.4.3 Theoretical Limit of the SPINOE Enhancement

In light of the relatively large SPINOE enhancements achieved by using laser-polarized xenon as the solvent, it is instructive to investigate the physical limit for polarizing nuclei (say protons) via the SPINOE. At steady-state,

$$\frac{d\langle I_z\rangle}{dt} = 0, \tag{4.15}$$

giving, from Eq. 4.2:

$$\langle I_z\rangle - I_0 = -\frac{\sigma_{IS}}{\rho_I}\left(\langle S_z\rangle - S_0\right) \tag{4.16}$$

Dividing both sides of Eq. 4.16 by I_0 and remembering that $\langle S_z\rangle >> S_0$ for laser-polarized xenon, one obtains the steady-state maximum enhancement of the proton magnetization, assuming a continuous, virtually infinite supply of laser-polarized

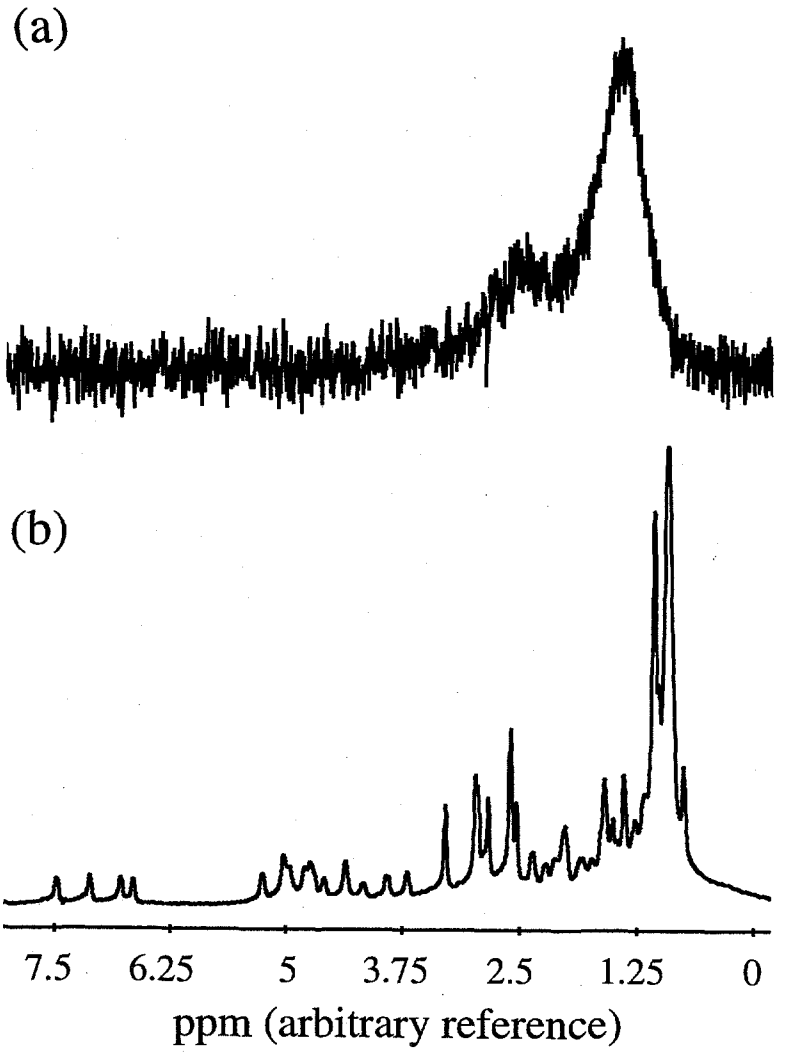

Figure 4.10: ^{1}H NMR spectra of cyclosporin in liquid xenon at room temperature in a high-pressure sapphire tube. (a) Broad spectrum acquired with 1024 scans without the addition of benzene to the liquid xenon. (b) High-resolution spectrum obtained with 16 scans with the addition of benzene to facilitate dissolution of the cyclosporin.

xenon:

$$f_H^{max} = -\frac{\sigma_{HXe}}{\rho_H} \cdot \frac{\langle S_z \rangle}{I_0}, \tag{4.17}$$

$$= -\frac{\sigma_{HXe}}{\rho_H} \cdot \frac{P_{Xe}}{P_H{}^{eq}}, \tag{4.18}$$

where $P_H{}^{eq}$ is the equilibrium polarization of the protons and P_{Xe} is the xenon polarization, which we will assume is 100% (i.e., $P_{Xe} = 1$ (or -1)).

In a best-case scenario, the relaxation of the protons would result entirely from dipolar interactions with ^{129}Xe. In this case, the autorelaxation rate of the protons can be written as [93]:

$$\rho_H = W_2 + 2W_1 + W_0, \tag{4.19}$$

$$= \left(\frac{\mu_0}{4\pi}\right)^2 \frac{\hbar^2 {\gamma_H}^2 {\gamma_{Xe}}^2}{10} \left\langle \frac{1}{{r^6}_{HXe}} \right\rangle \tag{4.20}$$

$$\times \left[6J\left(\omega_H + \omega_{Xe}\right) + 3J\left(\omega_H\right) + J\left(\omega_H - \omega_{Xe}\right)\right]. \tag{4.21}$$

Therefore, in the extreme narrowing limit,

$$\frac{\sigma_{HXe}}{\rho_H} = \frac{6\alpha\tau_c - \alpha\tau_c}{6\alpha\tau_c + 3\alpha\tau_c + \alpha\tau_c}, \tag{4.22}$$

$$= \frac{1}{2}, \tag{4.23}$$

where

$$\alpha = \left(\frac{\mu_0}{4\pi}\right)^2 \hbar^2 {\gamma_H}^2 {\gamma_{Xe}}^2 \left\langle \frac{1}{{r^6}_{HXe}} \right\rangle. \tag{4.24}$$

Thus, from Eqs. 4.18, 4.23 we can write:

$$|{P_H}^{max}| = |{f_H}^{max} \cdot {P_H}^{eq}| = \frac{1}{2}. \tag{4.25}$$

Therefore, the maximum polarization that can be achieved via SPINOE polarization transfer cannot exceed 50%. This limit is independent of the type of nucleus being polarized and the experimental conditions involved. However, even if it were possible to obtain 100% polarized ^{129}Xe, this limit would be extremely difficult to approach in practice. The intermolecular cross-relaxation between xenon and protons is simply too inefficient (even with high xenon concentrations and/or xenon binding) for xenon-proton dipolar interactions to be the dominant mechanism for proton relaxation.

A more realistic maximum enhancement can be estimated simply by taking the previously described signal enhancements obtained in laser-polarized liquid xenon [110], and scale them accordingly with 100% polarized, 100% ^{129}Xe-enriched xenon. Doing so would yield maximum enhancement factors of about 500 and 1000, respectively, for protons in cyclopentane and carbons in CS_2 at 200 K and 1.4 T. Such polarization enhancements under those experimental conditions would translate to polarization values of $P_H \sim 0.36\%$ and $P_C \sim 0.23\%$, values over two orders of mag-

nitude less than the physical limit of 50%.

Chapter 5

"Lighting Up" the NMR of Molecules II: Specific Xenon-Binding Interactions

5.1 Introduction

Xenon, while chemically inert, is known to participate in host-guest interactions with a variety of molecules. Xenon has been shown to bind to various proteins in crystals and in solution [66, 125, 126, 81, 127, 128, 129, 130, 131, 132]. The formation of xenon clathrates has also been investigated extensively with both thermally polarized and laser-polarized xenon (see for example, Refs. [133, 134]). Studies using xenon dissolved in lipid vesicles as a model for anesthetic action showed that xenon is pref-

erentially attracted to amphiphilic regions in lipid membranes [135]. Finally, xenon forms inclusion compounds with various organic molecules possessing accessible cavities, including α-cyclodextrin, hemicarcerands, self-assembling dimers, calixarenes, and cryptophane-A [133, 136, 137, 138, 139, 140, 141, 142].

Many of the above experiments that probed xenon binding in molecules utilized the highly sensitive chemical shift of xenon in order to reveal properties of the xenon environment via ^{129}Xe NMR spectroscopy. Alternatively, NOE polarization transfer from molecular protons to neighboring ^{129}Xe spins can be achieved via selective irradiation of the ^{1}H resonances and subsequent detection of the ^{129}Xe resonance; this approach was employed to investigate xenon binding in α-cyclodextrin [139] and xenon preferential solvation in lipid vesicles [135]. Such experiments have the advantage of providing direct microscopic information regarding the xenon surroundings (and incidentally, may aid in the interpretation of empirical xenon chemical shifts), but they rely on the weak intermolecular cross-relaxation between ^{129}Xe and the molecules being studied. Furthermore, selective irradiation in complex ^{1}H NMR spectra can be difficult to achieve, and 2-D heteronuclear ^{1}H-^{129}Xe NOESY experiments would be enormously time-consuming. In the absence of laser polarization, the ^{1}H$\leftarrow$^{129}Xe NOE enhancement is minuscule ($\sim 10^{-5}$), resulting from low xenon concentration, as well as weak ^{129}Xe-^{1}H coupling. With the use of laser-polarized xenon, however, the ^{129}Xe-^{1}H SPINOE enhancement ($\sim 10^{-2}$–10^{-1}) can be directly observed in the resolved ^{1}H NMR spectrum.

In two recent studies, the transient binding of laser-polarized xenon to organic molecules in solution produced differential enhancements in the ^{1}H NMR spectra resulting from distance-selective xenon-proton cross-relaxation; the degree of cross-relaxation was dictated by the proximity of a given proton to each molecule's xenon binding site [103, 47]. These results suggest that SPINOE polarization transfer could be utilized to study structure and dynamics in molecules that interact with xenon, and to map their hydrophobic potentials. SPINOE experiments could also be used to identify those regions of macromolecules and biological systems that are accessible to and interact with xenon atoms; thus, in light of xenon's anesthetic properties [60, 61], SPINOE spectroscopy may give new insight into the molecular mechanisms of general anesthesia (for review of this controversial field, see for example, Refs. [143, 144, 145, 146]).

This chapter continues the discussion of polarization transfer from dissolved laser-polarized xenon to other species in solution, concentrating on the site-specific xenon-molecule interactions described above. Considerable attention is given to the sensitive dependence of the SPINOE on local structure and dynamics of xenon-binding complexes, as well as its dependence upon the xenon concentration and a given molecule's xenon-binding constant. While much of the chapter is dedicated toward a description of the successful SPINOE experiments involving xenon inclusion compounds, future possibilities involving the study of xenon-protein interactions are discussed. Finally, a new means of efficiently transferring polarization from laser-polarized xenon to

molecules in solution is proposed that would exploit re-introduced dipolar couplings in anisotropic liquid-crystalline environments.

5.2 SPINOE Cross-Relaxation Rates and Xenon-Molecule Interactions

The values of xenon-proton cross-relaxation rates depend on the structural and dynamical characteristics of the intermolecular couplings between xenon and a given molecular environment. A molecule (M) may participate in various types of interactions with a xenon atom, including non-specific interactions (i.e., diffusive coupling, described in detail in the previous chapter), preferential solvation, and xenon binding (which results in the formation of a Xe:M complex). Exchange phenomena are normally involved among these various situations, but such exchange is generally rapid with respect to both the proton and xenon relaxation rates. Furthermore, proton chemical shifts are usually insensitive to intermolecular interactions with xenon, and therefore in most cases, exchange is likely to be rapid with respect to the proton chemical-shift time scale. This conclusion implies that ^{1}H NMR spectra will not be resolved according to the solute-xenon interactions, and that observed ^{1}H SPINOE enhancements may result from a combination of interaction modes. Therefore, the

experimental H-Xe cross-relaxation rate can be written most generally as:

$$\sigma_{HXe} = \sum_i \frac{[\mathrm{M}]_i}{[\mathrm{M}]_\mathrm{T}} \sigma^i_{HXe}, \tag{5.1}$$

where i denotes the interaction mode, $[\mathrm{M}]_\mathrm{T}$ is the total concentration of the solute, $[\mathrm{M}]_i$ is the molar concentration of the solute involved in the ith interaction mode, and σ^i_{HXe} is the H-Xe cross-relaxation rate associated with that mode.

For a dilute solution of xenon-binding molecules, one may consider two modes of interaction: diffusive coupling, (governed by σ^d_{HXe}), which exists for any kind of solute molecule, and xenon binding (governed by σ^b_{HXe}):

$$\sigma_{HXe} = \sigma^d_{HXe} + \frac{[\mathrm{Xe:M}]}{[\mathrm{M}]_\mathrm{T}} \sigma^b_{HXe}, \tag{5.2}$$

The form of Eq. 5.2 assumes that both molecules *without* included xenon and molecules *with* included xenon experience identical diffusive coupling with unbound xenon. [Xe:M] is the equilibrium molar concentration of the xenon:molecule complex. Hereafter, bound xenon is referred to as $\mathrm{Xe_{in}}$, whereas unbound xenon will be referred to as $\mathrm{Xe_{out}}$. Naturally, $[\mathrm{Xe:M}] = [\mathrm{Xe}]_\mathrm{in}$.

5.2.1 The Cross-Relaxation Rate Resulting from Xenon Binding

Xenon binding requires that a particular configuration of a xenon-solute pair exists long enough to be considered as a supramolecule. Specifically, the time scale relevant to $^{129}Xe \rightarrow ^{1}H$ cross relaxation and polarization transfer is the correlation time, τ_r, for tumbling motion of the transient Xe-molecule pair; xenon binding implies that the lifetime of the complex is much greater than the correlation time for its overall tumbling motion. Xenon-molecule configurations possessing lifetimes significantly longer than the average residence time of xenon in the molecule's solvation shell, but are short-lived in the sense that they do not reorient as a whole, could be regarded as specific preferential solvation.

Thus in cases of xenon binding, τ_r controls the dynamics of σ^b_{HXe}. Under these circumstances, the description of the Xe-H cross-relaxation rate reduces to the intramolecular case, and Eq. 4.9 of the previous chapter may be used with $\tau^b_c = \tau_r$ to obtain average distances between bound xenon and nuclear spins of the molecule that characterize the structure of the xenon-host complex. Of course, the validity of this treatment of experimental σ^b_{HXe} data depends on the importance of internal dynamics of the molecule being studied. The consequences of internal motions of the host molecule, in addition to the motion of xenon within a binding site, are $\tau^b_c < \tau_r$ and $\langle r^{-6}_{HXe} \rangle^b$ values which may be difficult to interpret because they correspond to weighted averages over multiple configurations. Molecular dynamics simulations may

prove helpful in such cases.

One can now estimate an upper bound for σ^b_{HXe} using Eq. 4.9 in the previous chapter with $\omega\tau^b_c = 0.68$ (recall Fig. 4.5), and $\langle r^{-6}_{HXe}\rangle^b = (3.2\ \text{Å})^{-6}$ (an estimate for the xenon-proton minimum approach distance). Given a magnetic field of 9.39 T (in which the proton resonance frequency is about 400 MHz), Eq. 4.5 yields a σ^b_{HXe}value of $3 \times 10^{-3}\ \text{s}^{-1}$, a figure three orders of magnitude greater than the value expected for the cross-relaxation rate resulting only from diffusive coupling. Indeed, σ^b_{HXe} values of this order have been observed for xenon bound to α-cyclodextrin in solution, as described below.

5.2.2 Dependence of the Cross-Relaxation Rate on the Xenon Concentration

In the previous chapter it was shown that to a good approximation, σ^d_{HXe} is proportional to the concentration of unbound xenon. An additional concentration dependence of the experimental cross-relaxation rate may arise from the effect of the xenon concentration on the binding equilibrium. Based on the definition of the binding constant, K, for the equilibrium

$$\text{Xe}_{\text{out}} + \text{M} \rightleftharpoons \text{Xe} : \text{M}, \tag{5.3}$$

we obtain

$$\frac{[\mathrm{Xe:M}]}{[\mathrm{M}]_\mathrm{T}} = \frac{K[\mathrm{Xe}]_\mathrm{out}}{1 + K[\mathrm{Xe}]_\mathrm{out}}, \tag{5.4}$$

which for weak xenon binding reduces to:

$$\frac{[\mathrm{Xe:M}]}{[\mathrm{M}]_\mathrm{T}} \approx K[\mathrm{Xe}]_\mathrm{out}, \tag{5.5}$$

and for strong xenon binding and excess xenon reduces to:

$$\frac{[\mathrm{Xe:M}]}{[\mathrm{M}]_\mathrm{T}} \approx 1. \tag{5.6}$$

Equations 5.4, 5.5, and 5.6 are written in terms of $[\mathrm{Xe}]_\mathrm{out}$ (and not as a function of the total xenon concentration) because for dilute solutions of host molecules, $[\mathrm{Xe}]_\mathrm{out}$ is well approximated by the equilibrium solubility of xenon in the pure solvent.

Consider the example of xenon binding to α-cyclodextrin. An equilibrium binding constant of $\sim$2 M^{-1} has been reported for this system in dimethyl sulfoxide (DMSO) at 298 K [139]. For an equilibrium xenon gas overpressure of 1 atm, the solubility of xenon in DMSO gives an equilibrium xenon concentration of 0.024 M at 298 K. Therefore, Eq. 5.5 applies to this system, and a linear increase in the SPINOE originating from binding is expected upon increasing xenon pressures (at least for xenon pressure in the range of a few atm), as shown in Fig. 5.1. However, in

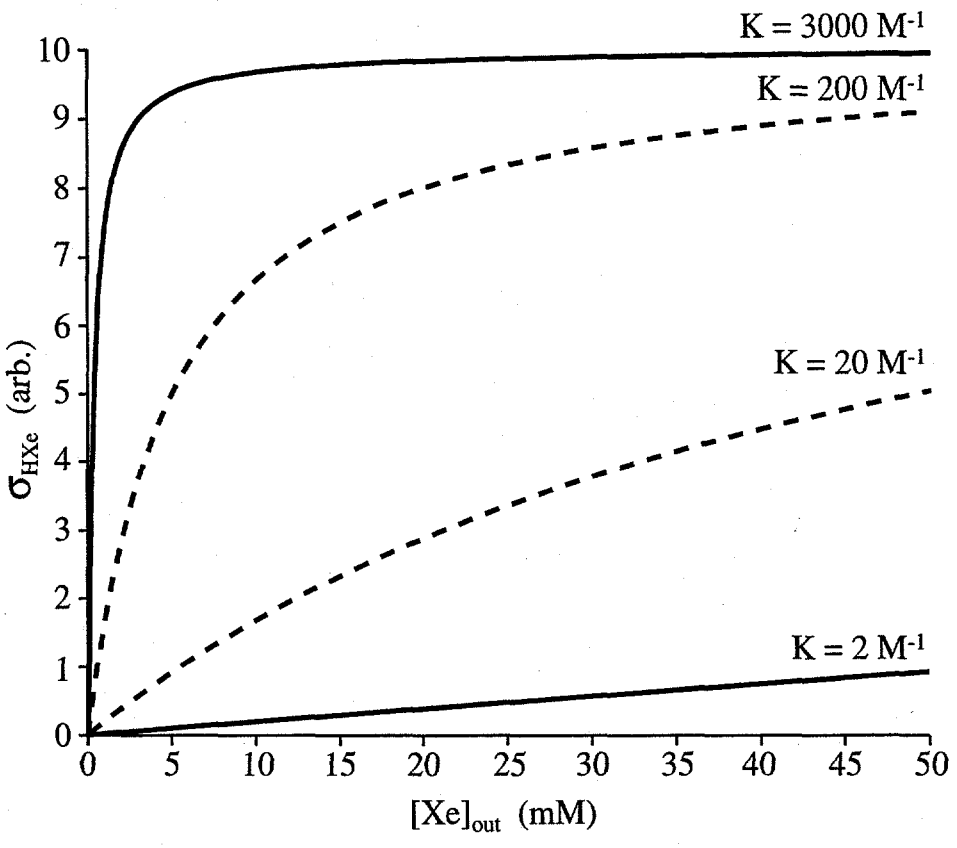

Figure 5.1: Dependence of the experimental Xe-H cross-relaxation rate (σ_{HXe}) originating from xenon binding on the equilibrium xenon concentration in the solvent for various association constants, K. Curves with solid lines are for systems that have been studied via SPINOE experiments (Xe/cyclodextrin in DMSO, $K = 2$ M^{-1}; Xe/cryptophane-A in $(CDCl_2)_2$, $K = 3000$ M^{-1}). The dotted curves, added for illustrative purposes, correspond to what would be expected for Xe/cyclodextrin in H_2O, $K \sim 20$ M^{-1} [139, 141], and xenon/myoglobin or xenon/hemicarcerand, $K \sim 200$ M^{-1} [81, 136].

tetrachloroethane (for which the xenon solubility has been estimated to be ~0.1 M/atm), the equilibrium constant for the binding of xenon to cryptophane-A was estimated to be larger than 3000 M^{-1} at 278 K [142], and therefore Eq 5.6 is more appropriate (as shown in Fig. 5.1). Using Eq. 4.12 from the previous chapter and Eq. 5.4, Eq. 5.2 can now be rewritten, taking into account the isotopic abundance of ^{129}Xe, A_{129}:

$$\sigma_{HXe} = A_{129}\left[\sigma^{n}_{HXe}[\mathrm{Xe}]_{\mathrm{out}} + \frac{K[\mathrm{Xe}]_{\mathrm{out}}}{1+K[\mathrm{Xe}]_{\mathrm{out}}}\sigma^{b}_{HXe}\right]. \tag{5.7}$$

5.3 The SPINOE in the Weak Xenon-Binding Limit: α-Cyclodextrin

One molecule shown to weakly bind xenon is α-cyclodextrin [133, 139], a cup-shaped six-membered cyclic oligosaccharide (Fig. 5.2). Specifically, α-cyclodextrin transiently binds xenon within its hydrophobic pocket; cyclodextrins are well-known in the chemical industry for their ability to bind a variety of chemical species for numerous applications (e.g., masking tastes and odors, delivering drugs, and catalyzing reactions) [147, 148, 149]. As mentioned above, the association constant for xenon binding of α-cyclodextrin in DMSO was estimated to be ~2 M^{-1} at 298 K [139], well within the regime of weak binding as governed by Eq. 5.3.

For the experiments described below, samples of α-cyclodextrin were dehydrated

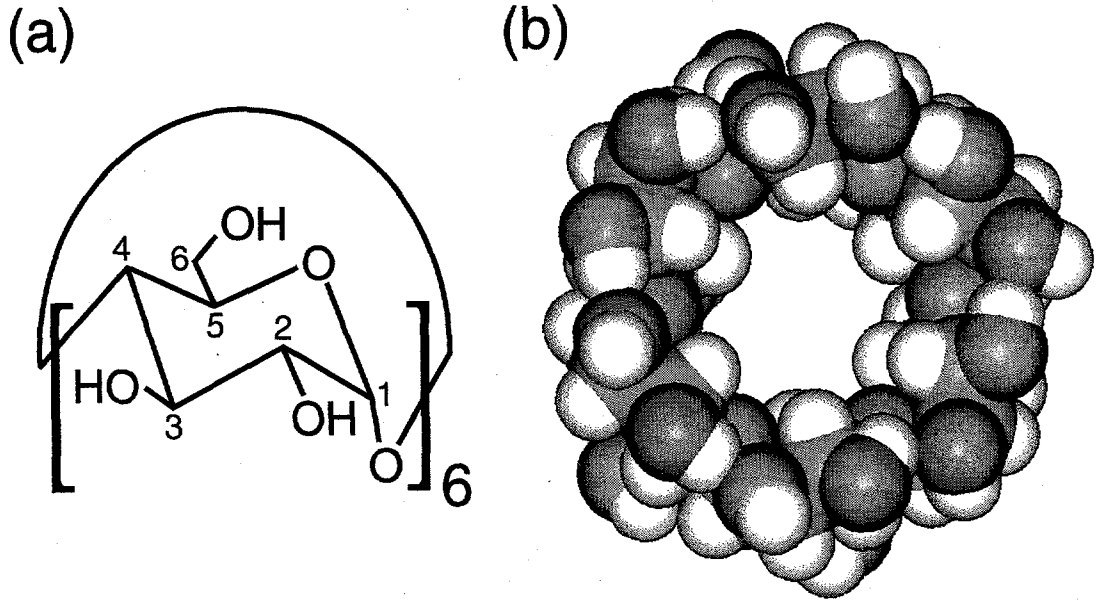

Figure 5.2: (Color) α-cyclodextrin. (a) Structural formula. (b) CPK model based upon X-ray crystallographic data [150]. Color scheme: oxygen atoms (red); carbon atoms (green); hydrogen atoms (white). Adapted from Ref. [103].

and dissolved in perdeuterated DMSO at concentrations of 0.1 M and 0.05 M. The samples were then degassed by several freeze-pump-thaw cycles on a vacuum line in order to remove paramagnetic molecular oxygen from the solutions.

When laser-polarized xenon was dissolved in a 0.1 M α-cyclodextrin/DMSO solution, one solution ^{129}Xe resonance was observed, consistent with xenon being in fast exchange between the solvent and the α-cyclodextrin (in agreement with previous results [139]). The ^{129}Xe was observed to rapidly decay with a spin-lattice relaxation time of $\sim$20 s, which indicated stronger dipolar interactions compared to benzene and p-nitrotoluene, in which the ^{129}Xe T_1 was observed to be greater than 500 s for a solution of 0.1 M p-nitrotoluene/d_6-benzene.

The NMR pulse sequence shown in Fig. 4.6 of the previous chapter was used to directly observe SPINOE enhancements of ^{1}H NMR signals of α-cyclodextrin. It was observed that when laser-polarized xenon was dissolved in a 0.05 M solution of α-cyclodextrin in DMSO, selective enhancements in the ^{1}H SPINOE spectra were obtained [103]; these results are shown in Fig. 5.3. Figure 5.3(a) shows an equilibrium ^{1}H NMR spectrum of α-cyclodextrin with assignments obtained from a 2-D COSY spectrum (not shown), and should be compared with the ^{1}H SPINOE spectra in Figs. 5.3(b,d). The most striking features of the spectra in Figs. 5.3(b,d) are the relatively large SPINOE signals originating from the H3 and H5 protons of α-cyclodextrin. Interestingly, the H3 and H5 protons are the ones that reside on the inside of the hydrophobic pocket (shown in yellow in Fig. 5.4), and would therefore be the closest

to bound xenon.

The measured ^{129}Xe-^{1}H cross-relaxation rates for the individual α-cyclodextrin protons, along with their respective $T_1{}^H$ values, are summarized in Table 5.3; the results from the previous experiments involving the p-nitrotoluene/benzene solution are listed for comparison. Values for the cross-relaxation rates were calculated by fitting the data to the Eq. 4.5 in the previous chapter. Because we are in the weak-binding limit (Eqs. 5.4 and 5.5), the observed cross-relaxation rates are proportional to $[\mathrm{Xe}]_{\mathrm{out}}$; thus, we can obtain a concentration-independent cross-relaxation rate with the following relation:

$$\sigma^n_{HXe} = \frac{\sigma_{HXe}}{[\mathrm{Xe}]_{\mathrm{out}}}, \tag{5.8}$$

where

$$\sigma_{HXe} \approx A_{129} \cdot K[\mathrm{Xe}]_{\mathrm{out}} \cdot \sigma^b_{HXe}. \tag{5.9}$$

From the Table it can be seen that the transient binding of xenon to α-cyclodextrin produced cross-relaxation rates over two orders of magnitude higher than those observed between xenon and p-nitrotoluene or benzene, for which the cross-relaxation is modulated only by diffusive motion. This increase in couplings between xenon and α-cyclodextrin arising from xenon binding demonstrates the sensitivity of the cross-relaxation rate to the binding of xenon with molecules in solution. In comparison,

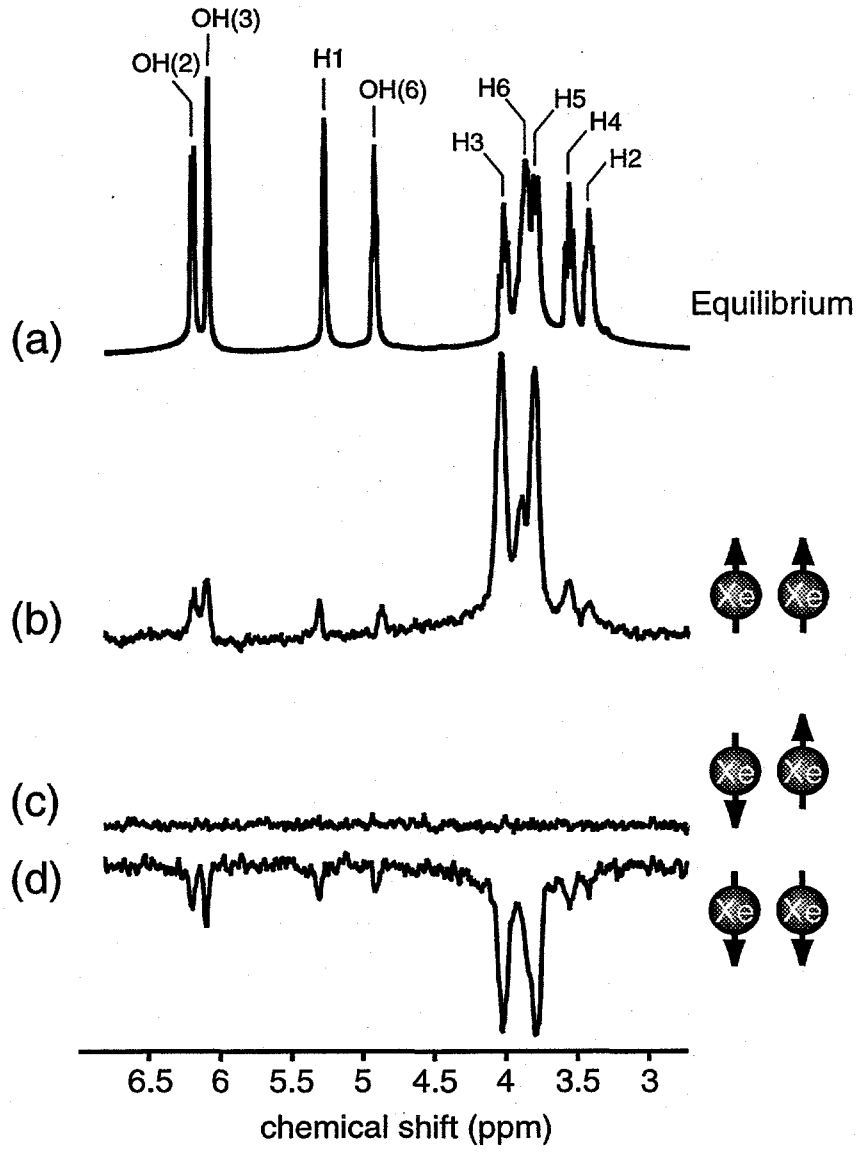

Figure 5.3: ^{1}H NMR spectra taken from a 0.05 M α-cyclodextrin/d_6-DMSO solution [103]. (a) Equilibrium ^{1}H NMR spectrum with assignments (see Fig. 5.2). (b) ^{1}H SPINOE spectrum taken using the pulse sequence shown in Fig. 4.6 after introduction of "positively" polarized xenon. (c) Baseline spectrum recorded under similar circumstances as (b), but without the ^{129}Xe 180° pulse, demonstrating the suppression capability of the pulse sequence. (d) As in (b), but with "negatively" polarized xenon. Values of $\tau_1 = 0.63$ s and $\tau_2 = 0.37$ s were used to obtain the SPINOE spectra shown here.

Molecule	Proton	σ^n_{HXe} (10^{-6} s^{-1} mM^{-1})	T_1 (s)
d_5-benzene	H	0.028 ± 0.007	110
p-nitrotoluene	CH_3	0.025 ± 0.007	6.8
	H3,H5	0.032 ± 0.006	35
	H2,H6	0.029 ± 0.005	23
α-cyclodextrin	H1	0.44 ± 0.14	1.1
	H2	1.3 ± 0.5	1.1
	H3	4.1 ± 0.8	1.2
	H4	1.6 ± 0.3	1.1
	H5	4.9 ± 1.2	0.87
	H6	1.2 ± 0.4	0.78
	OH(2)	0.70 ± 0.22	1.2
	OH(3)	0.86 ± 0.18	1.0
	OH(6)	0.36 ± 0.14	1.1

Table 5.1: Xenon-proton cross-relaxation rates and proton spin-lattice relaxation times [103]. The cross-relaxation rates are reported here as partial millimolar cross-relaxation rates (σ^n_{HXe}) in order to account for the different xenon concentrations present in the experiments. In the absence of strong binding, the observed cross-relaxation rates will be proportional to the xenon concentration. The data for the first four rows were obtained from the p-nitrotoluene/benzene experiments described in the previous chapter, and are listed here for comparison; the values for d_5-benzene were taken from the solvent in those experiments. The error range for the T_1 measurements was ±5%.

we measured cross-relaxation rates to be ~100 times smaller between xenon and β-cyclodextrin (the seven-membered cyclodextrin), in which the pocket diameter is 37% larger. Furthermore, as suggested by Eq. 4.9 the relative values for σ_{HXe} reflect the proximity of the respective protons of α-cyclodextrin to the xenon binding site. For example, assuming $\sigma_{HXe} \propto r^{-6}{}_{HXe}$, a ratio of 1:1.5 can be estimated for the range of distances between Xe-H5 and Xe-H1 (neglecting ^{1}H-^{1}H polarization transfer via "relayed" SPINOEs [47]). From an X-ray structure of α-cyclodextrin [150], this value is consistent with a distribution of xenon locations within the hydrophobic pocket, which predicts a value between 1:1.2 and 1:2. These ratios correspond to Xe-H5 distances of about 3 to 6 Å and Xe-H1 distances of about 6 to 8 Å.

5.4 The SPINOE in the Strong Xenon-Binding Limit: Cryptophane-A

More recently, SPINOE experiments were performed on cryptophane-A (Mol. wt.: 895.02 g/mol) in solutions of 1,1,2,2-tetrachloroethane [47]. The binding of laser-polarized xenon to cryptophane-A produced selective enhancements in the ^{1}H SPINOE spectra [47], permitting experimentally derived ^{1}H-^{129}Xe cross-relaxation rates to be correlated with internuclear distances. Furthermore, comparison of the values measured for the cross-relaxation rates with computational models permitted the determination of the preferred conformations of the cryptophane-A molecule when

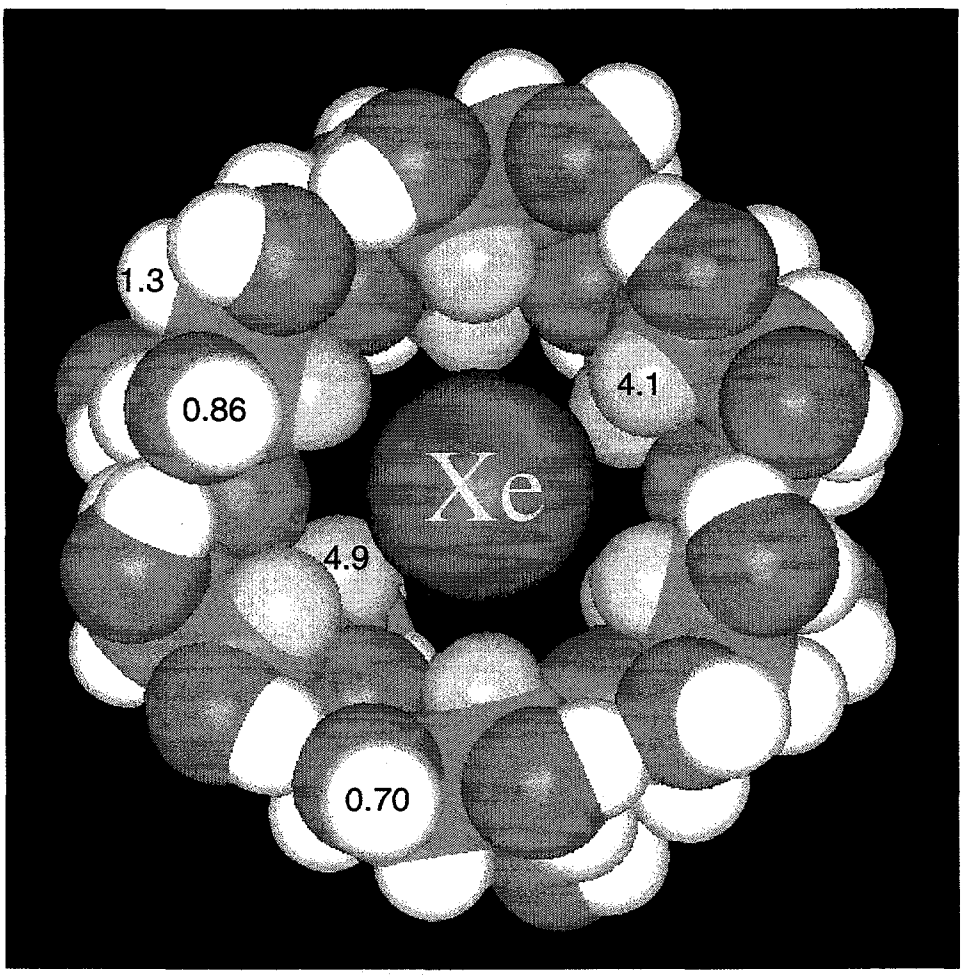

Figure 5.4: (Color) Laser-polarized xenon in the hydrophobic pocket of α-cyclodextrin. The H3 and H5 atoms are shown in yellow. In this "top" view of the complex, the six H3 atoms comprise the closer of the two rings of hydrogen atoms within the hydrophobic pocket. The numbers correspond to measured partial millimolar xenon-proton cross-relaxation rates as given in Table 5.3.

participating in xenon binding.

Cryptophane-A is an approximately spherical, cage-like organic molecule composed of two cyclotriveratrylene bowls connected by three OCH_2CH_2O spacer bridges; the structure of cryptophane-A is shown in Fig. 5.5. Cryptophane-A belongs to the D3 group of symmetry, and the spacer bridges give the molecule a high degree of intramolecular connectivity.

In previous work by Reisse, Collet, and co-workers, cryptophane-A was shown to to bind xenon very strongly, with an association constant greater than 3000 M^{-1} in 1,1,2,2-tetrachloroethane [142]. Unlike the complexes of xenon and hemicarcerands (which exhibit association constants on the order of $\sim$200 M^{-1}) [136], the Xe/cryptophane-A complex is formed without a high degree of constrictive binding (i.e., trapped xenon is not required to overcome large steric constraints of the portals of cryptophane-A in order to escape confinement), giving xenon residence times on the order of milliseconds instead of hours [142]. The relative mobility of the spacer bridges permit cryptophane-A to adopt various conformations that affect the size of the cavity and the stability of the host-guest complex; the dynamics of the host are expected to influence the manner in which the guest is bound and released [151].

Cryptophane-A was synthesized [152, 153] and generously provided by A. Collet and coworkers. The cryptophane-A sample used in the SPINOE experiments was a 0.05 M solution in perdeuterated 1,1,2,2-tetrachloroethane, $(CDCl_2)_2$. Helium gas was gently bubbled through the solution for 5-10 min. in order to displace any other gases

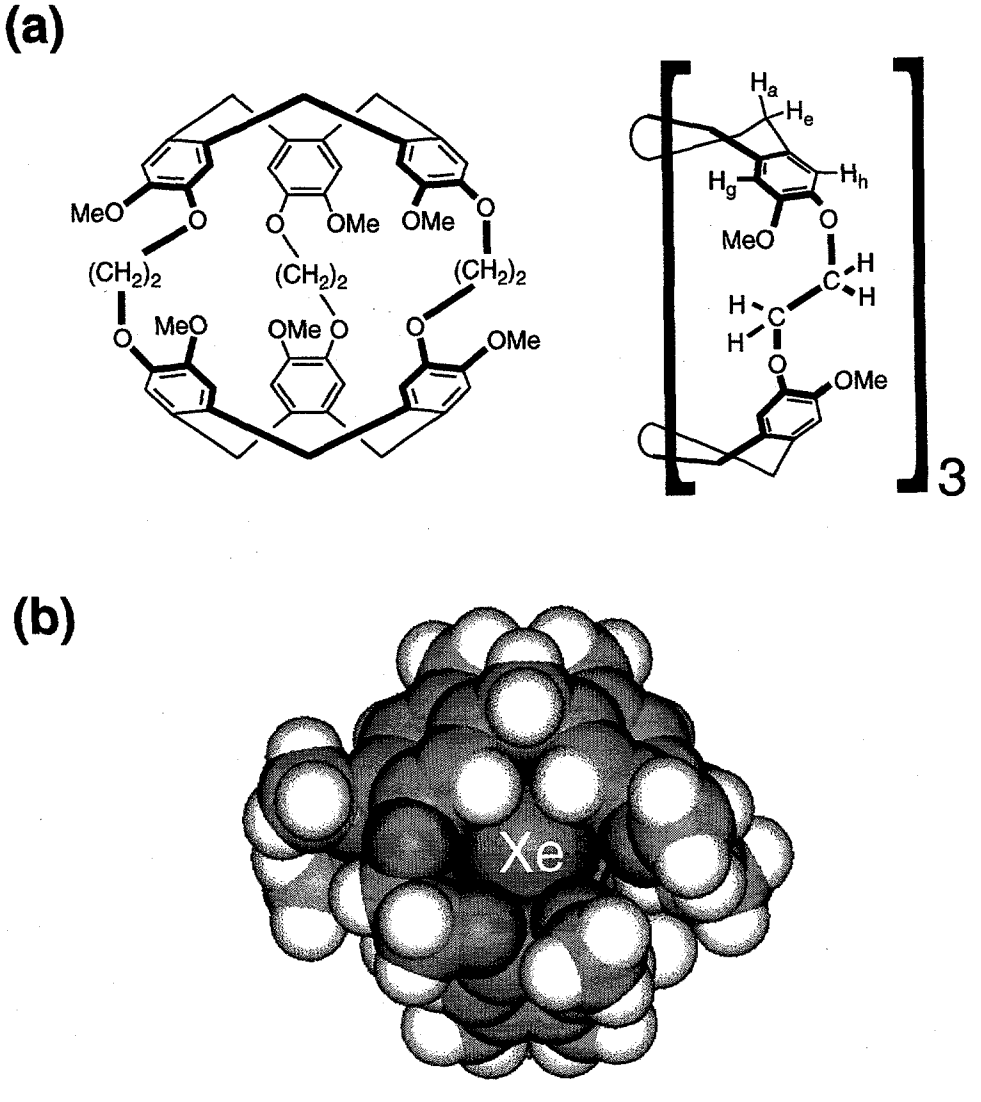

Figure 5.5: (a) (Color) Structure of cryptophane-A and atom labeling used in the ^{1}H NMR spectrum of Fig. 5.9(a). The assignment of the ^{1}H signals of the spacer bridges is discussed later in the chapter. (b) CPK model of one possible conformation of cryptophane-A with a xenon atom placed within the binding cavity.

complexed by cryptophane-A. The sample was then degassed by several freeze-pump-thaw cycles on a vacuum line. Computer modeling of the Xe/cryptophane-A complex was performed with Chem3D Plus™ (Cambridge Scientific Computing, Inc.); more details can be found in Ref. [47].

5.4.1 Spin-Lattice Relaxation Times of ^{129}Xe and ^{1}H

. As shown in the ^{129}Xe spectra in Fig. 5.6, the exchange of xenon between cryptophane-A and the solvent is slow with respect to the NMR time scale, in agreement with previous results [142]. Specifically, Fig. 5.6 shows ^{129}Xe NMR spectra of xenon dissolved in the cryptophane-A solution, with (Fig. 5.6(a)) and without (Fig. 5.6(b)) laser-polarization. Each ^{129}Xe spectrum exhibits two lines separated by $\sim$160 ppm and considerably broadened from chemical exchange. The higher field signal corresponds to the xenon trapped within the cavity of cryptophane-A, (Xe_{in}), with a chemical shift $\sim$60 ppm downfield with respect to the xenon gas resonance extrapolated to zero pressure. The second (down-field) peak corresponds to xenon in the solvent (Xe_{out}). The spectrum in Fig. 5.6(a) was obtained with a single scan using a rf pulse of small tipping angle ($\approx$2.5°). Obtaining comparable signal-to-noise with thermally polarized xenon would require several hours of signal averaging.

As shown in Fig. 5.7, the integrated intensities of both Xe_{in} and Xe_{out} decay with the same time evolution, indicating that the relaxation of ^{129}Xe is slow compared to the xenon exchange rate (an expected result). In one experiment where the molar

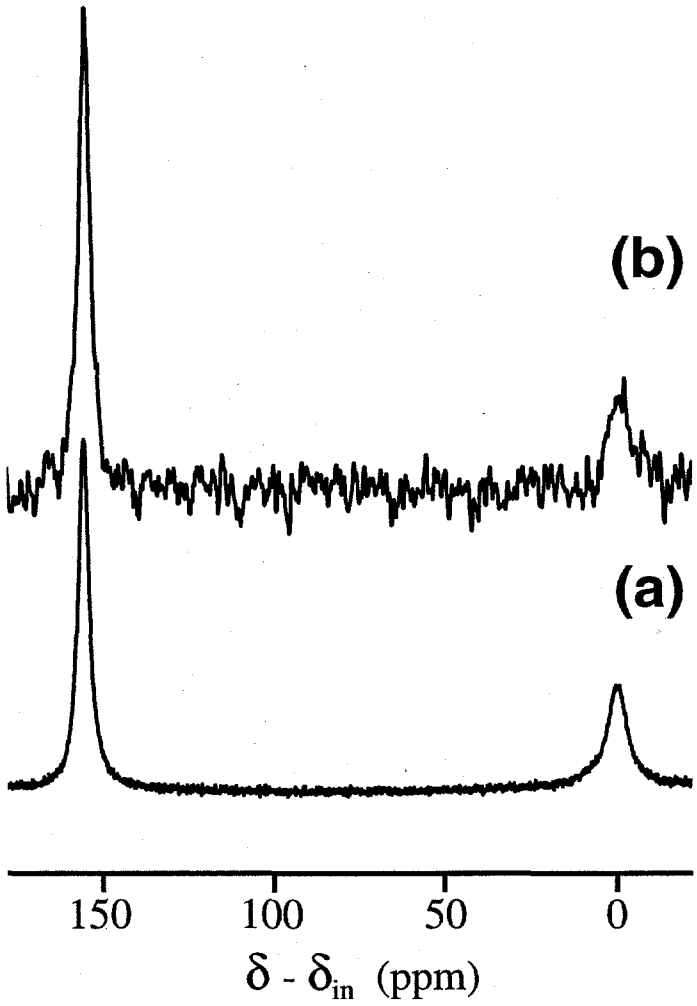

Figure 5.6: Typical ^{129}Xe NMR spectra for xenon dissolved in cryptophane-A/$(CDCl_2)_2$ solution, with (a) and without (b) laser-polarization [47]. Spectrum (a) was acquired with one scan using a pulse of small tipping angle ($\approx$2.5°); spectrum (b) was acquired with 8 scans using 90° pulses with a delay of 60 s between acquisitions. The ^{129}Xe spectra are referenced to the signal corresponding to xenon bound to cryptophane-A (Xe_{in}). A second signal can be seen roughly 160 ppm downfield from that of Xe_{in}, corresponding to unbound xenon residing in the $(CDCl_2)_2$ solvent Xe_{out}). ^{129}Xe was in considerable excess for these experiments, as reflected by $[Xe_{in}] < [Xe_{out}]$.

fraction of Xe_{in} was 0.74, the average ^{129}Xe T_1, T_1^{ave}, was measured to be 22.1 s. Given that the T_1 of ^{129}Xe is the pure solvent is quite long (hundreds of seconds in pure $(CDCl_2)_2$), it can be assumed that dipolar interactions with the solvent's spins do not contribute significantly to the average ^{129}Xe relaxation time. Thus, given the molar fraction of Xe_{in}, one can estimate the intrinsic T_1 of bound xenon to be $T_1^{ave} \cdot [Xe_{in}/(Xe_{in} + Xe_{out})] = 16.4$ s. A second experiment with a molar fraction of Xe_{in} of 0.92 gave an intrinsic T_1 of bound xenon of 16.2 s, in excellent agreement with the previous result.

The ^1H T_1 values for cryptophane-A are listed in Table 5.4.3. The longest relaxation times, ~0.8 s, are those of the methoxy and aromatic hydrogens. Therefore, relaxation of ^{129}Xe in this system is slow with respect to ^1H relaxation, and thus Eq. 4.5 of the previous chapter can be used to describe $^{129}Xe \rightarrow {}^1H$ SPINOE polarization transfer.

5.4.2 The Tumbling Motion of Cryptophane-A

In order to determine the rotational correlation time of crypto-phane-A in $(CDCl_2)_2$, it was necessary to perform CW-driven ^1H-^1H NOE experiments. For example, the accumulation of the NOE experienced by the equatorial protons, H_e, upon selective rf irradiation of the axial protons, H_a, was recorded at room temperature for saturation times ranging between 0.125 s and 2.0 s, as shown in Fig. 5.8. At room temperature, negative ^1H-^1H NOEs were observed. However, once the temperature was increased

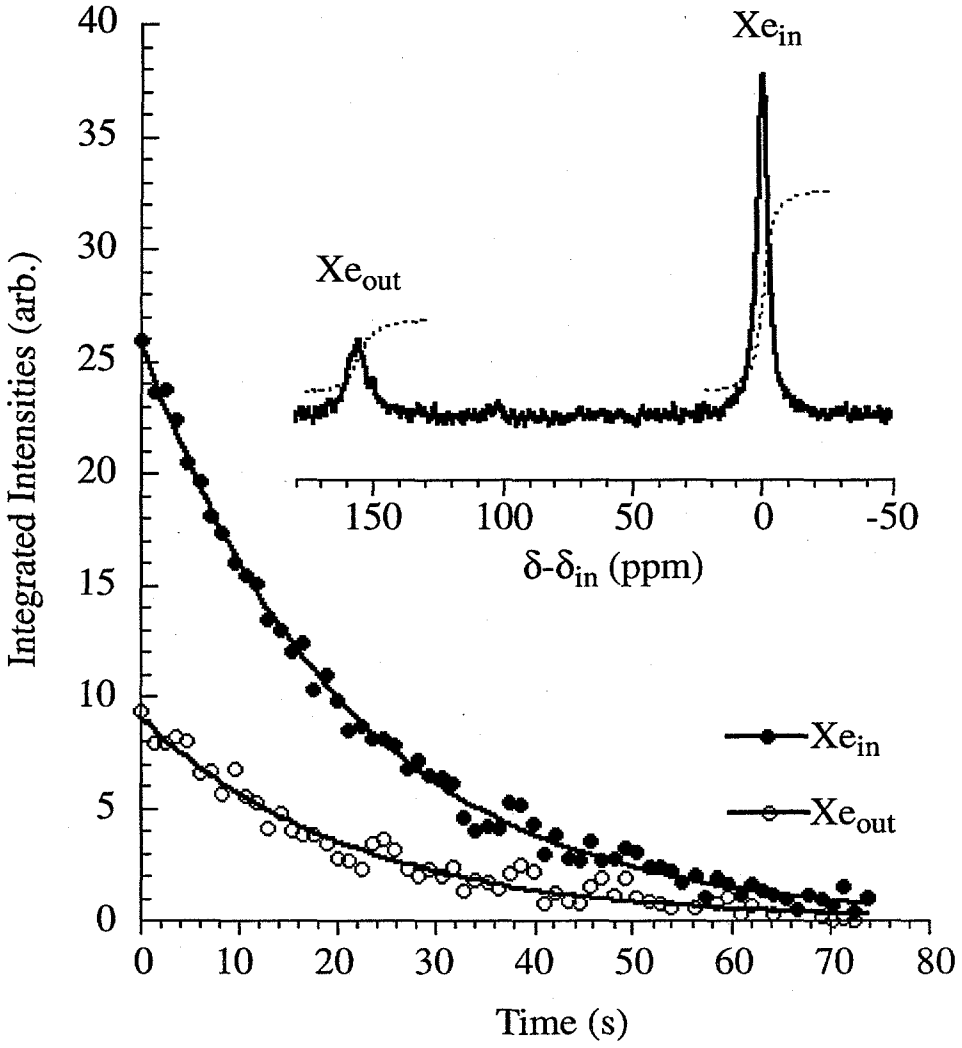

Figure 5.7: ^{129}Xe NMR spectrum of laser-polarized xenon dissolved in a ~0.05 M solution of cryptophane-A in $(CDCl_2)_2$ and time evolution of the integrated intensities [47]. The small amount of xenon used in this experiment is reflected in the fact that $[Xe]_{in} > [Xe]_{out}$.

approximately 20 °C, positive NOEs were observed. This result hints that at room temperature, $\omega_H \tau_r$ is at least sightly greater than 1.12, the value at which the ^{1}H-^{1}H cross-relaxation rate is equal to zero [94].

The steady-state ^{1}H-^{1}H NOE enhancement, η, and the auto-relaxation rate for H_e, ρ_{H_e}, were measured to be -0.148 and 3.64 s^{-1}, respectively; these values correspond to a cross-relaxation rate $\sigma_{H_eH_a} = 0.54\ s^{-1}$. Using the equation

$$\sigma_{HH} = \left(\frac{\mu_0}{4\pi}\right)^2 \frac{\hbar^2 {\gamma_H}^4}{10} \left\langle \frac{1}{{r^6}_{HH}} \right\rangle \left[6J\left(2\omega_H\right) - J\left(0\right)\right], \tag{5.10}$$

and $r_{H_eH_a} = 1.72$ Å (determined from computer modeling), the correlation time was estimated to be 0.60 ns, giving $\omega_H \tau_r = 1.5$ at 9.39 T. Assuming that this correlation time controls the ^{129}Xe→^{1}H polarization transfer (i.e., that $\tau_r = \tau_c^b$), Fig. 4.5 of the previous chapter indicates that σ_{HXe}^b values on the order of 70% of the maximum value can be expected for xenon bound to cryptophane-A.

5.4.3 The SPINOE in Cryptophane-A

Measurement of the Cross-Relaxation Rates

The equilibrium ^{1}H NMR spectrum of the cryptophane-A solution is shown with assignments in Fig. 5.9(a). The assignment of the cryptophane-A signals was performed elsewhere [142]; the proton NMR signals of the spacer bridges (which comprise an AA'BB' spin system) are discussed in greater detail below. Figs. 5.9(b-d) respec-

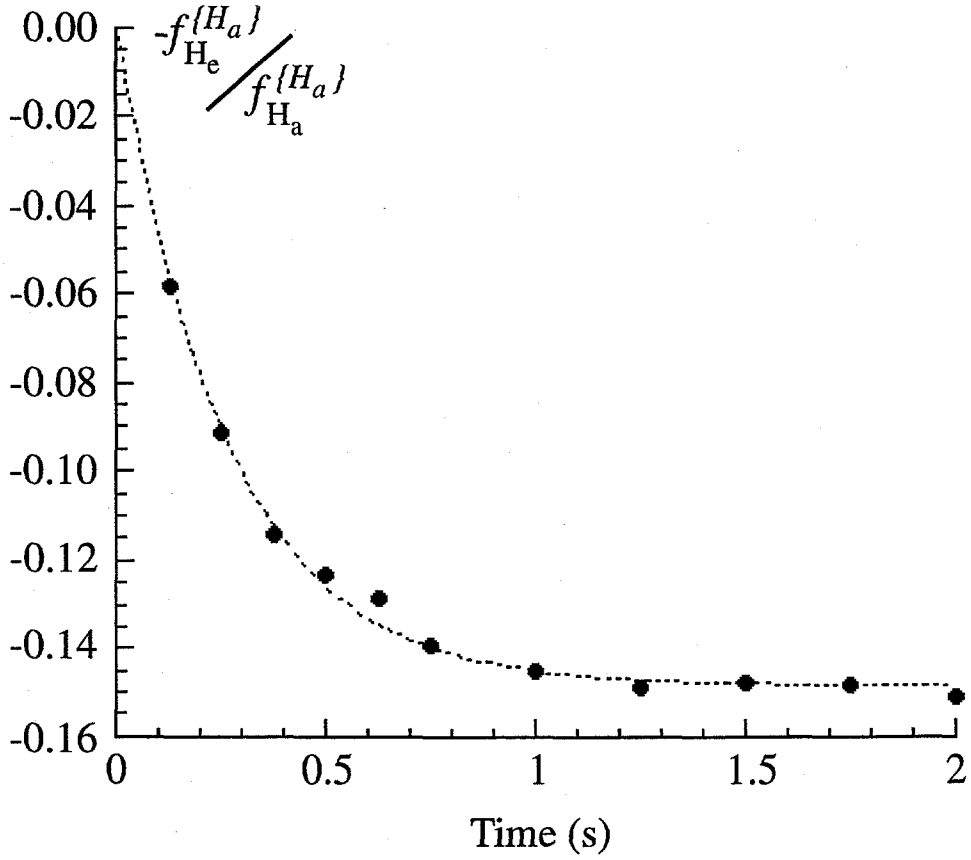

Figure 5.8: Time dependence of the NOE experienced by the equatorial protons (H_e) of cryptophane-A upon selective irradiation of the axial protons (H_a) at room temperature [47].

tively show SPINOE spectra obtained with positively laser-polarized xenon, with thermally polarized xenon, and with negatively laser-polarized xenon. As observed previously in α-cyclodextrin, The relative intensities in the SPINOE spectra obtained with laser-polarized xenon (Figs. 5.9(b,d)) are strikingly different from those in the equilibrium spectrum. While the equilibrium spectrum is dominated by the signal of the methoxy group, the signal from the aromatic protons is the most intense in the SPINOE spectra of Figs. 5.9(b,d). The ^{1}H signal enhancements observed in Fig. 5.9(b) varied between 3% and 13% (see Table 5.4.3). Additionally, the selectivity of the SPINOE was clearly not simply the result of vastly different ^{1}H auto-relaxation times, as the T_1^H values were nearly equal for the methoxy and aromatic protons.

In order to determine the absolute magnitude of H-Xe cross-relaxation rates, the value of the ^{129}Xe polarization enhancement must be obtained, according to Eq. 4.5 of the previous chapter. For the SPINOE experiment shown in Fig. 5.9(b), the ^{129}Xe polarization enhancement was estimated to be $\sim$13,000 at 9.39 T [47], based on quantitative comparison of the integrated intensities of the laser-polarized and equilibrium ^{129}Xe NMR spectra. However, the uncertainty on this value was high ($\sim$50%), resulting from experimental difficulties with inverting both ^{129}Xe resonances during SPINOE acquisition, exchange broadening of the ^{129}Xe lines (500 Hz), low signal-to-noise and long ^{129}Xe T_1's in the equilibrium spectra ($\sim$50 to 90 s), and the vastly different acquisition conditions (gain, pulse length, pulse power, etc.) under which the enhanced and thermal ^{129}Xe spectra were obtained. From the experimental

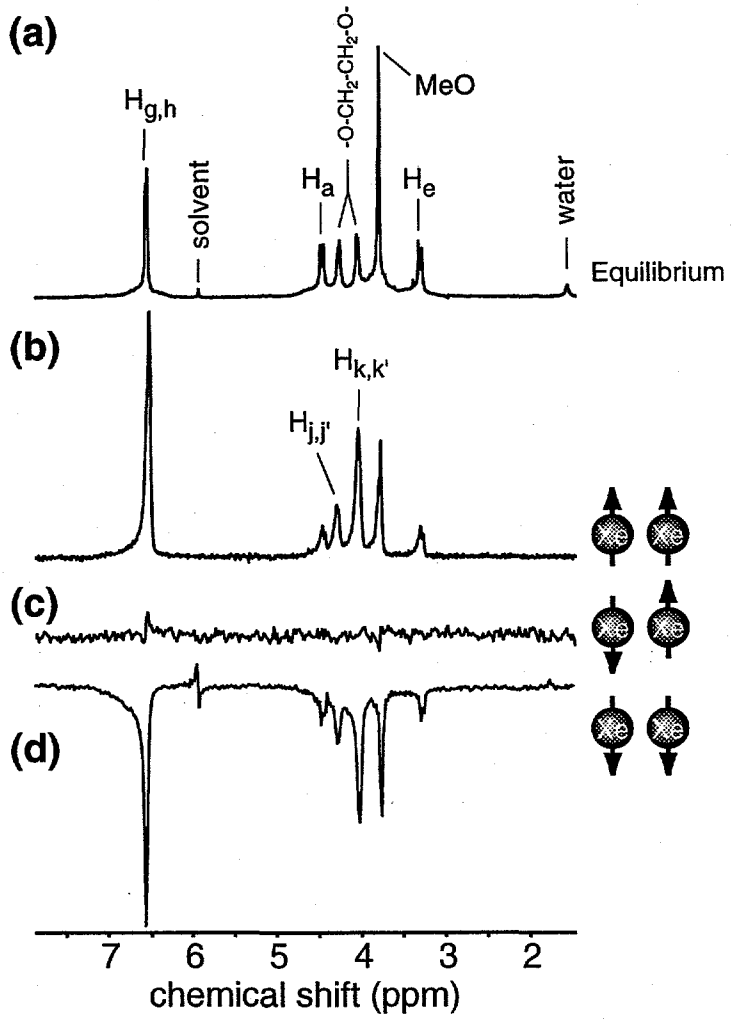

Figure 5.9: (a) ^{1}H NMR equilibrium spectrum of 0.05 M cryptophane-A in $(CDCl_2)_2$ with chemical shift assignments. (b) ^{1}H SPINOE spectrum acquired with the pulse sequence shown in Fig. 4.6 following introduction of positively polarized ^{129}Xe to the solution. (c) As in (b), but with ^{129}Xe at thermal equilibrium, demonstrating virtually complete suppression of all contributions to the ^{1}H NMR signal. (d) ^{1}H SPINOE spectrum acquired during a second experiment in which negatively polarized ^{129}Xe (prepared by inverting the direction of the magnetic field in which the ^{129}Xe is laser-polarized) was used, resulting in a corresponding sign change in the ^{1}H SPINOE spectrum. Values of τ_1=315 ms and τ_2=185 ms were used for the SPINOE experiments shown. Figure adapted from Ref. [47].

data given in Table 5.4.3, and the value for the xenon polarization enhancement, σ_{HXe}/A_{129} was estimated to be $\sim 1.2 \times 10^{-4}$ s^{-1} for the aromatic protons. From multiple experiments, σ_{HXe}/A_{129} values varying from $(1-4) \times 10^{-4}$ s^{-1} were found for the aromatic protons. This figure is two orders of magnitude greater than the value expected for H-Xe cross-relaxation rates originating from diffusive coupling alone; As with the case of α-cyclodextrin, the observed SPINOE enhancements can therefore be considered as originating entirely from the binding of laser-polarized xenon. Furthermore, the SPINOE spectra were obtained with dissolved xenon in excess with respect to the cryptophane-A concentration. Under these circumstances Eq. 5.6 is valid, thus giving $\sigma_{HXe}/A_{129} = \sigma^b_{HXe}$ from Eq. 5.7.

proton	label	T_1^H (s)	SPINOE[a] (%)	σ^b_{HXe} / $\sigma^b_{H_{g,h}Xe}$	$\langle r^{-6}_{HXe}\rangle$ / $\langle r^{-6}_{H_{g,h}Xe}\rangle$
aromatic	H_g, H_h	0.80	11.0	(1.00)	(1.00)
axial	H_a	0.27	3.0	0.47	0.3-0.4
linker	H_j, $H_{j'}$	0.36	5.2	0.67	0.3
linker	H_k, $H_{k'}$	0.41	13.0	1.55	1.5-1.8
methoxy	Me,	0.83	2.6	0.23	0.1-0.3
equatorial	H_e	0.35	2.7	0.35	0.3-0.4

Table 5.2: Spin-lattice relaxation times, SPINOE enhancements, relative H-Xe cross-relaxation rates, and calculated relative values in *gauche* conformations for the protons of cryptophane-A [47].

^{129}Xe-^{1}H Cross-Relaxation Rates in Cryptophane-A vs. α-Cyclodextrin

The largest σ^b_{HXe} values resulting from the binding of xenon to cryptophane-A were measured to be 5 to 10-fold smaller than the corresponding values resulting

from xenon binding to α-cyclodextrin [103]. However, it is unlikely that this discrepancy originates from differences in the dynamics of the ^{129}Xe$\rightarrow^{1}$H polarization transfer. As shown in Section 5.4.2, for the binding of xenon to cryptophane-A in $(CDCl_2)_2$ at room temperature, each σ^b_{HXe} should reach 70% of its maximum possible value in terms of τ_c. Instead, this difference in the magnitude of the σ^b_{HXe} values suggests differences in the structure of these xenon complexes. Given $\tau^b_c = 0.6$ ns and $\sigma^b_{HXe} = (1-4) \times 10^{-4}$ s^{-1}, Eq. 4.9 of the previous chapter gives a value for $\langle r^{-6}_{HXe} \rangle^b$ varying over $(0.5-2) \times 10^{-4}$ Å^{-6}; this range of values gives an average distance between the aromatic protons and the xenon atom of 4.1-5.2 Å. These results are in good agreement with computer modeling of minimum-energy structures of the xenon/cryptophane-A complex, which predicted average xenon-proton internuclear distances of 4.5-4.8 Å. In comparison, an X-ray structure of α-cyclodextrin [150] can be used to predict r_{HXe} values between a xenon atom positioned at the center of the cavity and the nearest protons to be in the range of 3.2-3.8 Å. These calculated ranges of proton-to-xenon distances would correspond to a 4 to 8-fold factor increase in the cross-relaxation rates for α-cyclodextrin compared to those of cryptophane-A (neglecting dynamical effects), in agreement with the experimental observations.

Relative σ_{HXe} Values and the Structure of the Complex

As discussed above, the observed SPINOE enhancement for the aromatic protons is clearly consistent with xenon binding within the cavity of cryptophane-A. Nev-

ertheless, detailed information regarding the structure of the xenon/cryptophane-A complex can be obtained in the absence of information about the *absolute* values of σ_{HXe}; furthermore, the use of relative H-Xe cross-relaxation rates avoids the uncertainty attached to the measurement of the absolute xenon polarization enhancement. Table 5.4.3 gives the σ^b_{HXe} values of the cryptophane-A protons relative to that measured for the aromatic protons. From this data it is clear that the binding of xenon to cryptophane-A gives rise to differential ^{1}H-^{129}Xe dipolar interactions. Provided that internal dynamics do not contribute significantly to the fluctuations of the intermolecular dipole-dipole interactions, the relative σ^b_{HXe} values listed in Table 5.4.3 reveal structural information regarding the xenon/cryptophane-A complex. Of particular interest are the results obtained for the protons belonging to the OCH_2CH_2O spacer bridges (also referred to as linkers). Indeed, one pair of these protons (labeled H_k and $H_{k'}$ in the spectrum of Fig. 5.9(b)) experiences, in the presence of xenon, a cross-relaxation rate more than twice as great as that between xenon and the other pair of protons (H_j and $H_{j'}$). Because the dynamics of both pairs of protons are most likely to be similar, these results indicate that H_k and $H_{k'}$ are, on average, closer to the xenon atom than H_j and $H_{j'}$.

While cryptophane-A is a somewhat rigid molecule, the internal degrees of freedom associated with the OCH_2CH_2O spacer bridges permit the molecule to adopt various conformations. Specifically, these conformations differ in the dihedral angle O-CH_2-CH_2-O and, in reference to the oxygen atoms, are either *gauche*-like or *anti*-like in

nature.

Minimum energy structures of the xenon/cryptophane-A complex were created via computer modeling. Four such structures are shown in Fig. 5.10 for different conformations of the displayed spacer bridge. In Figs. 5.10(a,b), the linkers are in an *anti* conformation. These conformations possess C_2 symmetry axes which bisect the C-C bond of the linkers and intercept at the center of the cavity where the xenon atom is found. Therefore, in Fig. 5.10(a) the protons labeled H and H' have the same chemical shift which, *a priori*, is different from the chemical shift of the other pair of protons. The structures shown in Figs. 5.10(b-d) were created based on the structure in Fig. 5.10(a), with the labels unchanged; i.e., the H and H' which were "remote" with respect to the xenon atom in Fig. 5.10(a) are the "proximal" protons in Fig. 5.10(b). In both of these *anti* conformations, the proton-xenon distances are nearly equal, and consequently yield similar relative values for $\langle r_{HXe}^{-6} \rangle^b$. From Table 5.4.3 it can be clearly observed that the calculated values for the "proximal" H's in the *anti* conformations are significantly different from the corresponding experimental result; even if it were considered that both *anti* structures were present simultaneously (therefore giving weighted-average values for σ_{HXe}^b), the experimental results could not be properly explained.

In Figs. 5.10(c,d), the linkers are in a *gauche* conformation. These structures do not possess C_2 symmetry axes, but for each of them an equivalent structure exists in which the position of the protons H and H' are interchanged. Therefore, for each

pair of protons, $\langle r_{HXe}^{-6} \rangle^b$ must be calculated as the average between the two protons. It is worth noting that in both of these *gauche* structures, the partner of the proton which is the nearest to xenon is actually the farthest proton; nevertheless, in Table 5.4.3 this pair is still referred to as the "proximal" protons, because it leads to the greatest value for $\langle r_{HXe}^{-6} \rangle^b$. Thus, the H and H' which are "remote" with respect to the xenon atom in Fig. 5.10(c) become the "proximal" protons in Fig. 5.10(d). From Table 5.4.3, it can be seen that both *gauche* structures lead to relative $\langle r_{HXe}^{-6} \rangle^b$ values in good agreement with the experimental results. Both of these *gauche* structures might be present simultaneously, but if this is the case, one conformation must be in considerable excess in order to explain the observed difference in cross-relaxation rates between the proton pairs.

The relative values for $\langle r_{HXe}^{-6} \rangle^b$ of the various protons of cryptophane-A calculated using the *gauche* structures are shown in the last column of Table 5.4.3. It was necessary to calculate the value for the methoxy group for numerous positions of these protons; the calculation leads to values in agreement with the experimental relative cross-relaxation rates, despite the fact that the dynamics of the polarization transfer might be somewhat different in this case.

The calculations shown here neglect the effects of relayed SPINOEs, which in the present system might be on the order of 10-15% between geminal protons (for a detailed explanation of relayed SPINOEs, see Ref. [47]). Nevertheless, on the basis of the experimental SPINOE cross-relaxation rates, one can conclude that the most

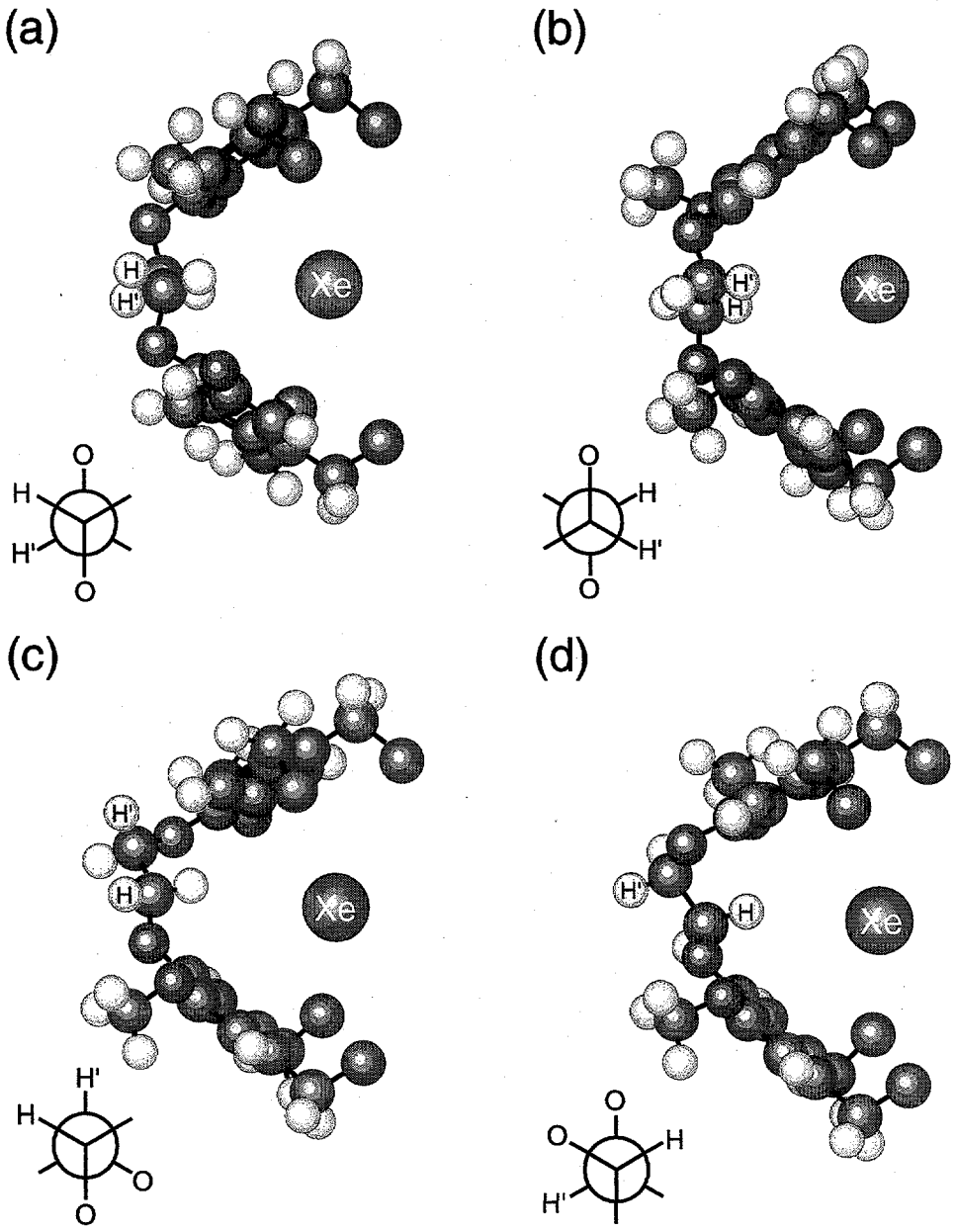

Figure 5.10: (Color) Minimum energy structures of cryptophane-A with bound xenon for the various conformations of the displayed spacer bridge (highlighted in yellow). The atoms of the cyclotriveratrylene subunits are at similar positions in each view; the molecule is slightly rotated such that the spacer bridge is clearly visible. In (a) and (b), the linkers are in an *anti* conformation. In (c) and (d), the linkers are in a *gauche* conformation. Figure adapted from Ref. [47].

probable conformation of the spacer bridges of cryptophane-A when the molecule complexes xenon (in $(CDCl_2)_2$ at room temperature) is a *gauche* conformation. This conclusion is in agreement with the simulation of resolution-enhanced ^{1}H NMR signals performed previously [142]. Additionally, one can conclude from these results that the chemical shifts of $H_{k,k'}$ and $H_{j,j'}$ characterize the protons of the spacer bridges of cryptophane-A which are, respectively, *gauche* and *anti* with respect to the vicinal oxygen atom; thus, the SPINOE results have permitted a more complete assignment of the ^{1}H NMR spectrum.

	proximal H's	remote H's
experimental	**1.55**	**0.67**
anti (a)	5.2	0.5
anti (b)	4.4	0.5
gauche(c)	1.8	0.3
gauche(d)	1.5	0.3

Table 5.3: Experimental H-Xe cross-relaxation rates (bold) for the protons of the spacer bridges of cryptophane-A relative to the value for the aromatic protons, and relative $\langle r^{-6} \rangle^b$ values calculated using the structures in Fig. 5.10.

5.5 Xenon and Proteins

Both the α-cyclodextrin and cryptophane-A experiments suggest that SPINOE polarization transfer can be useful for directly probing the structure and dynamics of molecules that interact with xenon. Most tantalizing is the prospect of using SPINOE experiments to study proteins. For example, because many of the xenon binding sites

in proteins (e.g. myoglobin [127]) are not solvent-accessible, it is believed that xenon binding may require cooperative motion on the part of the protein in such cases; thus, SPINOE experiments may shed light on dynamic binding processes in proteins.

The next step in this line of research is choosing an ideal model protein in which to perform SPINOE studies. As indicated in the Introduction, a surprising amount of work has been dedicated toward the study of xenon binding to various proteins [66, 125, 126, 81, 127, 128, 129, 130, 131, 132]. Much of the recent work studying xenon-binding in proteins has been motivated by the desire to map hydrophobic sites, and also to use xenon/protein complexes as highly isomorphous heavy-atom derivatives for solving the phase problem in X-ray structure determination [129, 130, 131].

Hemoglobin and myoglobin were the first two proteins shown to bind xenon [125, 126, 81, 127]. Hemoglobin is currently difficult to study via NMR because of its large size (~80 kD); the large number of protons and the broad spectral features resulting from slow molecular tumbling have (to date) precluded a complete structural assignment of hemoglobin's NMR spectra. Moreover, large proteins would be poor choices of model systems for SPINOE studies in general because proton-proton spin diffusion grows more efficient with increased molecular weight. Such spin diffusion will tend to "wash out" any selectivity of the SPINOE by bleeding polarization from the "lit up" protons neighboring bound laser-polarized xenon to the rest of the protons in the protein. Myoglobin, on the other hand, has a mass of only about 18 kD, and it has been well-characterized via NMR methods (see for example, Ref. [154]), facilitating

the interpretation of proposed SPINOE experiments. Moreover, myoglobin is known to bind xenon relatively strongly in solution (~2-6 specific sites as determined by both NMR and X-ray crystallography, depending on the experimental conditions), with $K \approx 200$ M^{-1} for its strongest binding site [81]; the corresponding value for hemoglobin is only about 10 M^{-1} [81]. A ribbon diagram of myoglobin is shown in Fig. 5.11 along with two blue spheres representing xenon atoms in two of the specific xenon binding sites [125]. The strongest of the xenon binding sites in myoglobin is the one adjacent to the heme, on the opposite side of the oxygen binding site.

Unfortunately for studies involving laser-polarized xenon, myoglobin possesses a paramagnetic center (specifically, the heme iron) that rapidly relaxes xenon in solution. For example, a value for the ^{129}Xe T_1 of ~0.1 s has been observed in aqueous solutions of metmyoglobin (Fe^{3+}, $S = 5/2$) [155]. This short relaxation time is likely a result of the close proximity of bound xenon to the paramagnetic iron in the heme.

In an attempt to increase the effective spin-lattice relaxation time of dissolved laser-polarized xenon, myoglobin samples were prepared according to a protocol designed to maximally remove the paramagnetism of the heme iron (see for example, Refs. [156, 157]). The myoglobin samples were poisoned with carbon monoxide gas, reduced with sodium dithionite, and subsequently purified with a salt column under an inert atmosphere, giving (carbon monoxy) myoglobin. Following rapid dissolution of laser-polarized xenon in a 6.6% (by weight) sample of (carbon monoxy)

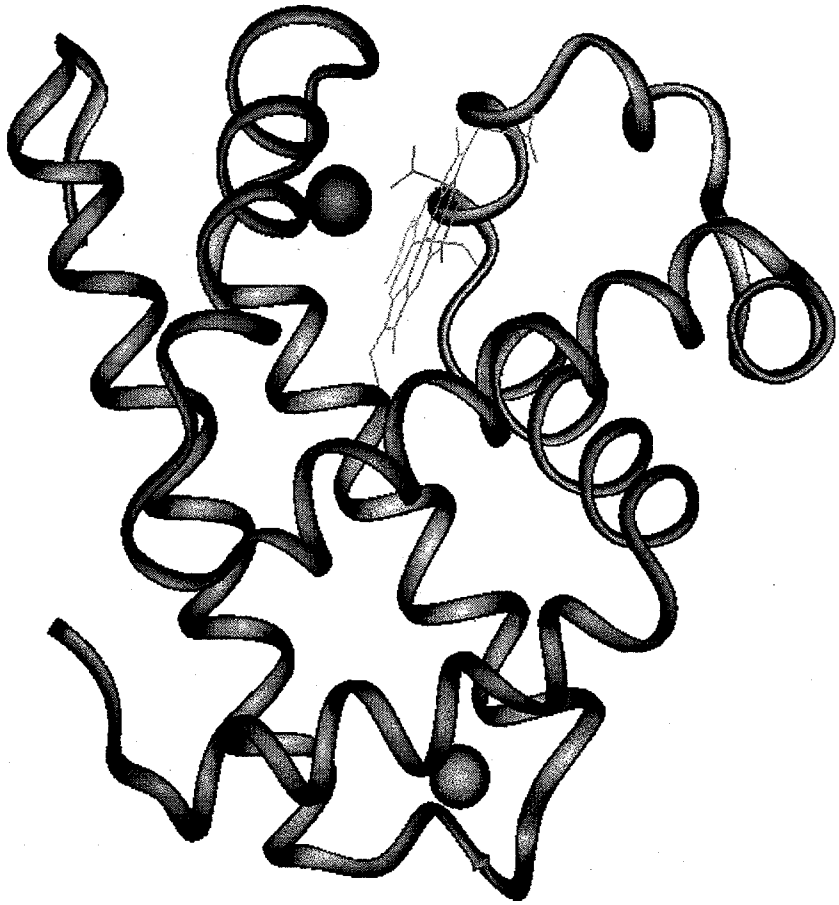

Figure 5.11: (Color) Ribbon diagram of myoglobin with two bound xenon atoms (blue spheres). The site associated with the strongest xenon binding ($K \approx 200$ M^{-1}) is adjacent to the heme (top). Figure created by J. Heller, according to crystallographic information in Ref. [125].

myoglobin, the ^{129}Xe magnetization was observed to decay with a time constant of 3.8 s, a significant improvement (a similar preparation applied to hemoglobin produced a somewhat longer ^{129}Xe T_1) [158]. However, this duration still proved too short for practical application in SPINOE experiments; it was experimentally difficult to mix and equilibrate laser-polarized xenon with the myoglobin solutions *in situ* on that time scale (however, in the future this problem might be combated with the use of a gated stopped-flow injection system). Moreover, given the relatively long intrinsic T_1 for xenon in cryptophane-A ($\approx$16 s [47]), it is possible that remaining unpaired electronic spins in the myoglobin heme iron may still have significantly contributed to the ^{129}Xe T_1, despite our best efforts to completely remove the paramagnetism of the myoglobin samples. As of the writing of this thesis, other options with myoglobin were being considered that would more effectively rid the protein of its inherent paramagnetism. However, instead of using apomyoglobin (myoglobin without the heme), which might adversely change the structure of the strong xenon binding site, the prospects for using myoglobin with non-iron heme (i.e., with non paramagnetic elements at the heme's center) were being investigated.

A second potential model protein that also was being investigated while this thesis was written was a particular mutant of phage lysozyme (99Leu$\rightarrow$Ala) [159]. This mutant of phage lysozyme possesses an internal cavity shown to bind benzene [160, 161] with a dissociation constant $K_d \sim 1$ mM at 25°C in solution. Given the volume of this internal cavity ($\sim$150 Å^3; the volume of a xenon atom is $\sim$40 Å^3) and its

hydrophobicity, it was proposed that this protein might transiently bind xenon. Our preliminary studies [162] using both thermally polarized and laser-polarized ^{129}Xe at 14.1 T are suggestive, but not yet conclusive, with respect to xenon binding in solution. Xenon binding is supported by a significant shift of the ^{129}Xe resonance with high protein concentration compared to the shift present in pure buffered water (or D_2O); for example, we observed a change in shift of $\Delta\nu \approx 15$ ppm for ^{129}Xe dissolved in 5.2 mM lysozyme solution with 4-5 atm overpressure of thermally polarized xenon. Xenon binding is also supported by a considerably broadened ^{129}Xe line ($\sim$ 720 Hz) compared to the line of the internal xenon gas reference, possibly broadened from fast chemical exchange between the protein and the solvent. However, this linewidth has yet to show a clear temperature dependence (although to date this has been tested only over a limited range); also, it is possible (though unlikely) that this linewidth results from broadening due to the paramagnetic salt added to the solution to reduce the ^{129}Xe T_1 for signal-averaging purposes. Moreover, preliminary measurements of the ^{129}Xe T_1 in the absence of paramagnetic salts suggest only slightly shortened relaxation times in lysozyme solutions compared to that measured in pure D_2O buffer.

Future studies will systematically characterize the concentration-dependent chemical shift of the ^{129}Xe resonance in solutions of the phage lysozyme mutant, measure the temperature dependence of the ^{129}Xe over a wider range with greater signal-to-noise, and more accurately measure the ^{129}Xe T_1. The results of these experiments should shed more light on the xenon-binding properties of the phage lysozyme mu-

tant, and indicate whether in fact the protein is a suitable model system for SPINOE experiments.

Regardless which proteins are eventually studied via SPINOE methods, it is likely that selective or stochastic deuterium labeling may be needed to suppress spin diffusion and aid in interpretation of any observed SPINOE enhancements in the protein's ^{1}H NMR spectra. Future work will also investigate the feasibility of actively transferring SPINOE magnetization from directly affected protons to other spins via more traditional NMR methods in order to improve the interpretability and information content of SPINOE experiments.

5.6 Cross-Polarization from Laser-Polarized Xenon via Re-Introduced Dipolar Couplings?

Cross-polarization [84, 85, 86] is a commonly used technique for enhancing the NMR sensitivity of rare spins in solids via polarization transfer through dipolar (spin-spin) couplings. In normal liquids, however, the dipolar couplings between nuclear spins are averaged away by the rapid isotropic tumbling and diffusion of molecules in solution. Dipolar interactions can still contribute to spin relaxation, permitting non-equilibrium polarization to be slowly transferred between neighboring spins through dipolar cross-relaxation (i.e., the nuclear Overhauser effect). As described earlier, these cross-relaxation pathways have been exploited to transfer nuclear spin polar-

ization from laser-polarized xenon to other substances in solution via the SPINOE. While the SPINOE can be quite useful for studying the structure and dynamics of molecules in solution, the cross-relaxation between xenon and a given target spin is usually slow compared to the auto-relaxation of the target spin, preventing large signal enhancements in all but the most favorable of circumstances. Only in the cases of high xenon concentration and extraordinarily long autorelaxation times have relatively large signal enhancements been achieved in solution from laser-polarized xenon. This fact begs the question: are there other means by which the polarization can be more efficiently transferred from laser-polarized xenon to other solution spins?

One mechanism that has been suggested is polarization transfer through the scalar (J) couplings between the spins of a molecule and bound laser-polarized xenon [103]. Normally, such J-couplings would be considered completely negligible; no covalent chemical bond connects the xenon atom and the molecule, and no line splittings attributable to "intermolecular" ^{129}Xe-^{1}H J-couplings have ever been directly observed. However, in light of the previously described SPINOE polarization transfer experiments involving xenon-binding molecules, density functional methods have been used to calculate estimated ^{129}Xe-^{1}H J-couplings in such systems [163]. For example, these calculations predict a ^{129}Xe-^{1}H J-coupling of $\sim$10-100 μHz for internuclear distances of 6-8 bohr ($\sim$3.2-4.2 Å).

Transferring polarization from one nucleus to another within the same molecule via adiabatic Hartmann-Hahn cross-polarization through J-couplings is a well-known

technique [164]. Indeed, the observation of any signal enhancement via adiabatic Hartmann-Hahn cross-polarization transfer from laser-polarized xenon to the binding molecule might be a good way to detect the existence of ^{129}Xe-^{1}H J-couplings and measure their strength. However, the minuscule size of such J-couplings is likely to be too small to practically improve upon the SPINOE merely for signal enhancement purposes.

At this point, the available components of the Hamiltonian that could be exploited for coupling laser-polarized xenon to other spins in solution have been exhausted. However, if the isotropic nature of the solution is removed, the Hamiltonian changes significantly; dipolar couplings between spins may no longer be averaged away, drastically increasing the observed couplings between spins.

This phenomenon is well-known in liquid crystalline systems (see for example, Refs. [165, 166, 167]). Consider the example of $^{13}CCl_3H$, whose isotropic ^{13}C NMR spectrum is comprised of two lines separated by ~200 Hz dictated by the strength of the scalar coupling between the proton and carbon spins. When $^{13}CCl_3H$ is dissolved in a nematic liquid crystalline solvent, the observed splitting in the ^{13}C NMR spectrum reaches nearly 5000 Hz (see for example, Ref. [168]). The magnitude of the splitting is a sum of the scalar coupling and the re-introduced dipolar coupling. The re-introduced dipolar coupling, D_{ij}, is given most simply by (in Hertz) [166]:

$$D_{ij} = S \cdot \frac{\mu_0 \gamma_i \gamma_j \hbar}{8\pi^2} \left\langle \frac{1}{r_{ij}^3} \right\rangle, \tag{5.11}$$

where S ($0 \leq S \leq 1$) is the order parameter that depends on the degree of solute ordering by the liquid crystalline solvent. This order parameter will depend upon a variety of experimental conditions, including the temperature and the nature of the liquid crystal and the dissolved molecule.

Here, we propose that if laser-polarized xenon were tempor-arily bound to a molecule in a liquid-crystalline environment, dipolar couplings between laser-polarized xenon and the xenon-binding molecule may be re-introduced, thereby creating a new, more efficient pathway for transferring polarization. Polarization could be transferred between the laser-polarized xenon and the molecule being studied via well-known double resonance radio-frequency techniques (e.g., adiabatic Hartmann-Hahn cross-polarization). If successful, such polarization transfer should compete more favorably with auto-relaxation, permitting larger, more selective enhancements of the NMR signals. However, any re-introduced dipolar couplings will be adversely affected (but not destroyed altogether) by chemical exchange of laser-polarized xenon between the molecule and the bulk liquid-crystalline environment. The effective coupling will also be scaled by the strength of the xenon binding, as the binding constant will dictate the occupancy of a given xenon-binding site in solution.

Because of the strong xenon binding and the relatively long xenon residence times of xenon in cryptophane-A (~01-10 ms at different temperatures and xenon concentrations, perhaps longer in a liquid-crystalline environment), it may serve as an ideal model system for evaluating this proposed method of polarization transfer. However,

despite the long xenon residence time, the exchange-broadened lines in the ^{129}Xe NMR spectra may cloak splittings due to dipolar couplings between bound xenon and the spins of cryptophane-A. Thus, the polarization transfer itself may be required to measure re-introduced dipolar couplings. The first obstacle that must be overcome is the unfavorable solution chemistry of liquid crystals; large molecules like cryptophane-A tend to be relatively insoluble in nematic liquid-crystalline solvents. If a stable system can be obtained, then polarization could be transferred via cross-polarization. However, transferring polarization to the protons would likely result in enhanced but unresolved broad lines in the ^{1}H spectrum without the application of significant decoupling or multiple-quantum pulse sequences (for review, see Refs. [4, 166, 167]).

Alternatively, a more effective experiment would involve the enhancement of rare spins (e.g. ^{13}C and ^{15}N) via cross polarization. Direct ^{129}Xe-^{13}C cross-polarization would be technologically demanding because of the similar values of the gyromagnetic ratios of these species. However, enhanced ^{13}C signals could still be obtained indirectly via a two-step polarization transfer from xenon to protons, and then from protons to carbon, with subsequent acquisition of an enhanced ^{13}C NMR signal under proton decoupling. Direct CP from laser-polarized xenon to rare nuclei may permit signal enhancements on the order of 10^4 in the limits of strong xenon binding, long xenon residence times, and long relaxation times.

Finally, this proposed technique may also permit novel NMR studies of proteins

in solution. Lipid bicelles could be used to re-introduce dipolar couplings between bound laser-polarized xenon and proteins (see for example, Ref. [169]). While the short xenon residence times and weak xenon binding in proteins should give smaller re-introduced dipolar couplings, they will likely be competitive with the spin-diffusion and autorelaxation rates of the protein spins, and be greater than the cross-relaxation rates exploited by SPINOE methods.

Chapter 6

Enhanced NMR Spectroscopy of Materials Surfaces

6.1 Introduction

In principle, NMR can be a powerful means of probing structure, dynamics, and chemical properties of surfaces of heterogenous materials under a wide range of experimental conditions. Thus, NMR can be better suited for the investigation of surfaces of a wide variety of organic solids and catalytic materials than the more conventional surface-science techniques normally used for single-crystal experiments (e.g. scanning tunneling microscopy), because of the inherent instability of such materials under ultra-high vacuum conditions. However, the NMR signals from the surfaces of low surface-area materials can often be difficult to observe, not only because the

number of spins contributing to the surface signal may be extremely small (especially in light of the inherently low sensitivity of NMR in general), but also because the surface signal may in many circumstances be virtually indistinguishable from that of the bulk. Therefore, methods capable of increasing the sensitivity and selectivity of the NMR of surfaces are highly desirable. Reviews of the application of laser-polarized xenon for enhancing the NMR of materials surfaces can be found in Refs. [24, 57, 45, 67, 40].

In this chapter, numerous examples of OPNMR of materials surfaces are described, with particular attention given to certain applications and technological advances of interest. The first section describes the first demonstrated application of OPNMR: probing low surface-area materials with enhanced ^{129}Xe signals from adsorbed laser-polarized xenon. The remaining sections of this chapter are mainly concerned with the direct observation of surface spins via polarization transfer from laser-polarized gases, especially within the context of more conventional NMR techniques commonly used in solid-state experiments (e.g., variable temperature studies, cross-polarization, and magic angle spinning).

6.2 Probing Surfaces with ^{129}Xe OPNMR

Adsorbed ^{129}Xe has long been used as a sensitive magnetic resonance probe of pore sizes and chemical properties of high-surface area materials like zeolites (for review, see Refs. [57, 67, 68, 69, 71]). For example, the measured value of xenon's

highly sensitive chemical shift can be empirically correlated with the number of xenon atoms located within a given cavity of a zeolite, providing information about available void space within the zeolite, as well as the localization and type of guest species within the zeolite's pores. Unfortunately, such studies would normally be limited to such materials with very high surface area (and short xenon spin-lattice relaxation times) to make up for the otherwise weak signal from the relatively low number of surface-adsorbed xenon spins. An additional complication arises from the fact that the adsorbed ^{129}Xe chemical shift can be very sensitive to xenon-xenon interactions, giving a xenon concentration dependence to the observed shift; often, one must perform multiple studies with varying xenon coverages to extrapolate the ^{129}Xe chemical shift to zero xenon concentration. Therefore, in some circumstances it would be advantageous to perform ^{129}Xe NMR studies with the minimal xenon coverage required to obtain sufficient signal-to-noise.

Following results of high-field NMR studies of solid laser-polarized xenon by Happer, Cates, and co-workers [56], experiments by Pines and co-workers [46] showed that laser-polarized xenon could be a sensitive NMR probe of low surface-area materials. In this work, a batch optical pumping apparatus similar to that shown in Fig. 2.3 was employed to produce small quantities of laser-polarized xenon and deliver it to samples of low surface-area materials within an NMR magnet. This early OP apparatus utilized a 30 mW diode laser, which could produce laser-polarized xenon with a polarization enhancement factor of about 750 (limited primarily by the laser

power).

At room temperature and low xenon overpressure (about 20 torr), it was shown that NMR signals from adsorbed xenon could be observed from particles of graphitized carbon and Na-Y zeolite. The graphitized carbon particles, which possessed a moderate surface area (10 m^2/g), shifted the resonance of the adsorbed xenon about 10 ppm downfield from the gas resonance. The signal for xenon adsorbed in the zeolite was shifted 59 ppm downfield from the gas resonance produced by 16 torr of xenon; at the time, this was the lowest xenon pressure reported for such NMR experiments.

Similar experiments were also performed on particles of powdered benzanthracene, which possessed a low surface area of only $\sim$0.5 m^2/g (the particle size was determined from electron micrographs). These results are shown in Fig. 6.1. At room temperature (Fig. 6.1(a)), only the signal from gaseous xenon could be observed in the ^{129}Xe NMR spectra. However, lowering the sample temperature to 158 K produced a second resonance 10 ppm downfield from the gas resonance (Fig. 6.1(b)), attributed to laser-polarized xenon adsorbed on the benzanthracene particles. Lowering the temperature five degrees further increased the shift to 32 ppm, and significantly changed the lineshape of the adsorbed xenon resonance (Fig. 6.1(c)), possibly resulting from the distortion of the electron clouds of the adsorbed xenon atoms. Overall, the chemical shift and linewidth were observed to increase with decreasing temperature, which is characteristic of increased residence time and decreased mobility for the adsorbed xenon. Finally, once the temperature was lowered to 123 K, only the signal from solid

laser-polarized xenon could be observed (Fig. 6.1(d)).

Many typical amorphous solid materials have relatively large particle sizes (~10 μm) giving them low surface areas (~1 m^2/g); thus, these results suggested that a wide variety of materials of interest in catalysis and surface science could be studied with laser-polarized xenon NMR. Moreover, the authors postulated that it might be possible to employ cross polarization methods to transfer polarization from laser-polarized xenon to spins on the surfaces of materials, thereby selectively enhancing the NMR of surfaces (discussed in the following section).

This pioneering work was soon followed by numerous studies using ^{129}Xe OPNMR to probe various materials surfaces. One such study investigated the interaction of laser-polarized xenon with a polymer surface [170]. In these experiments, laser-polarized xenon was adsorbed onto particles of powdered amorphous poly(acrylic acid) of moderate surface area (~15 m^2/g) at different temperatures. The xenon was observed to strongly interact with the polymer surfaces, which the authors suggest possibly resulted from the polar carboxylic acid functional groups present at the particle surfaces. The temperature dependence of the surface interaction, as measured by the ^{129}Xe chemical shift of the xenon resonance, fit well to a simple model of chemical exchange between gaseous and adsorbed xenon. Moreover, the pressure dependence of the xenon chemical shift permitted the diffusion constant of the surface-adsorbed xenon to be estimated (~3.3×10^{-5} cm^2/s).

In a second study, ^{129}Xe OPNMR was utilized to probe the surfaces of CdS

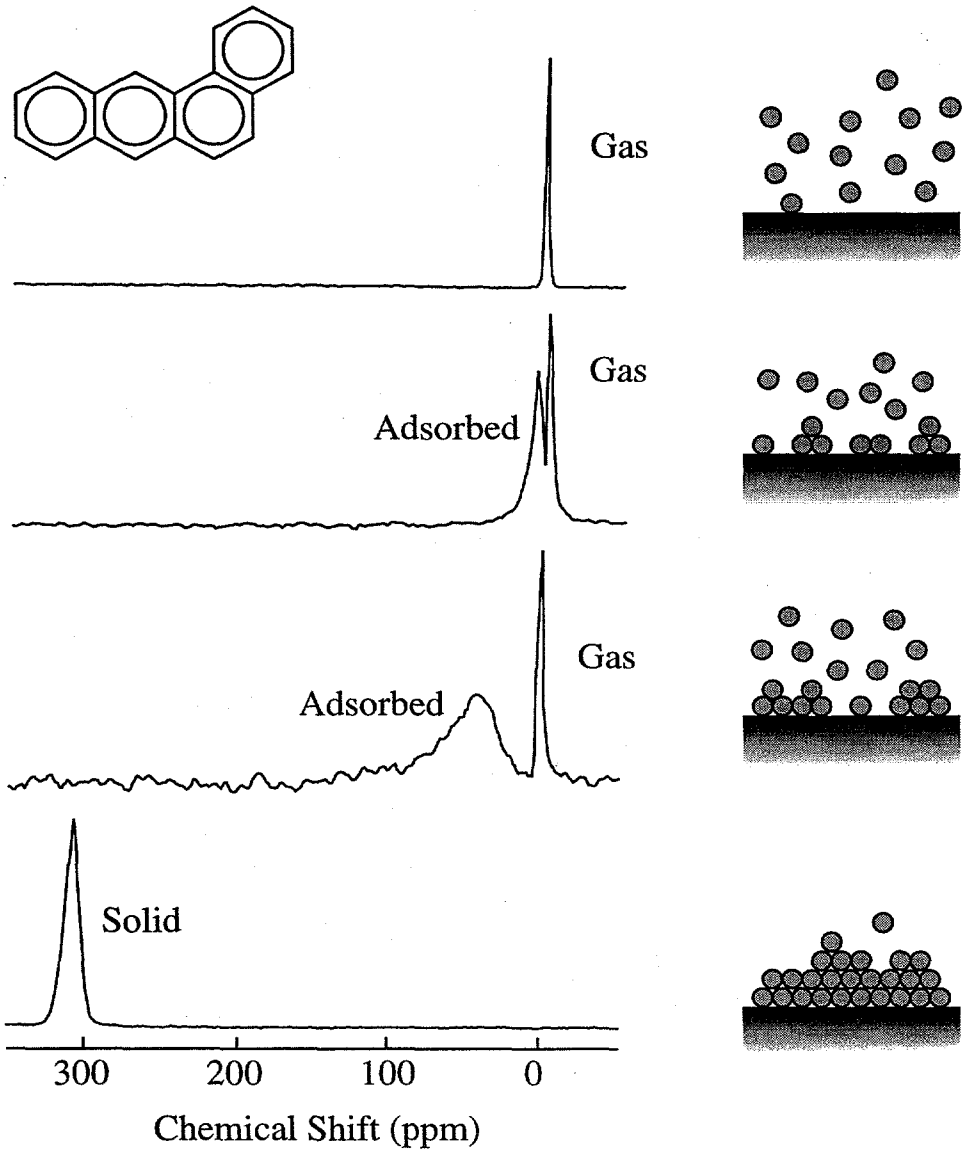

Figure 6.1: ^{129}Xe NMR spectra of laser-polarized xenon adsorbed onto powdered benzanthracene [46]. (a) Spectrum showing only gaseous xenon (298 K, 20 torr). (b,c) Spectra showing both gaseous and adsorbed xenon (158 K, 21 torr for (b), 153 K, 22 torr for (c)). (d) Spectrum showing only solid xenon (123 K). Figure courtesy of Thomas Meersmann.

nanocrystals [82]; specifically, laser-polarized xenon was used to probe the morphology of the thiophenol capping groups on the nanocrystals. One interesting result from this work was the observation of two partially superimposed lines for xenon adsorbed onto CdS nanocrystals with low thiophenol coverage, which was interpreted as evidence for two distinct surface domains of the thiophenyl groups on such nanocrystals. It was believed that such domains were formed by the aggregation of thiophenol molecules on the surfaces under conditions of incomplete coverage, a hypothesis consistent with previous results of studies using X-ray photoelectron spectroscopy and liquid-state ^{1}H NMR.

6.3 Polarization Transfer to Surfaces

6.3.1 Cross-Polarization and Zero-Field Mixing

As described in Chapter 4, polarization transfer from laser-polarized xenon to other nuclei was first achieved in the solid phase with low-field thermal mixing [48, 82, 83]. This technique involves adiabatically sweeping the external magnetic field through a regime where the difference between the Zeeman energies of the two spin baths is matched by their dipolar coupling. Following experiments where ^{129}Xe polarization was transferred to neighboring ^{131}Xe spins in xenon ice [48] and ^{13}C spins in a frozen CO_2/xenon matrix [82], zero-field mixing was used to transfer polarization to protons of a silicone surface coating (SurfaSil) on glass [83]. The enhancement of

the ^{1}H polarization of the surface protons was impressive in these experiments; a lower limit for the achieved value of P was estimated at 0.01, corresponding to an enhancement factor of ~300 for protons at 400 MHz.

Polarization has also been transferred to materials surfaces successfully by rf-driven Hartmann-Hahn cross-polarization [84, 85, 86] in the rotating frame through dipolar couplings at high field [87, 88]. In one experiment, the immobilization of laser-polarized xenon at 90 K onto a high surface-area (835 m^2/g) sample of poly(triaryl-carbinol) permitted the ^{1}H NMR signal of the polymer surface to be enhanced by a factor of about 800 at 4.2 T [88].

In order employ either zero-field mixing or Hartmann-Hahn CP to enhance the NMR signals of surface spins, it is required that either a) the nuclei to be polarized have been embedded in a laser-polarized xenon ice matrix [48, 82] or b) the laser-polarized xenon has been immobilized onto the material's surface [83, 87, 88]. However, both of these preparations can be difficult to achieve in practice, are also limited to temperatures below ~100 K.

6.3.2 SPINOE Enhancement of Surfaces

Following the successful solution-phase results obtained from laser-polarized xenon dissolved in liquid benzene [89], it was demonstrated that the nuclear spin polarization of both laser-polarized xenon and helium could be selectively transferred to nuclear spins on solid surfaces in high field (4.2 T) via the SPINOE [171]. In contrast to

the previous cross-polarization experiments, the magnetization transfer was established by dipole-dipole cross-relaxation between surface spins and mobile polarized gas atoms adsorbed on the surface, in a manner similar to that in the liquid-state NMR experiments described previously. It should be remembered that cross-relaxation is a less efficient means of transferring polarization than direct cross-polarization. However, while the overall signal enhancements observed with the SPINOE are smaller than those obtained via cross-polarization and zero-field mixing, surface selectivity can still be achieved with easier sample preparation over a much wider range of experimental conditions, without the need for strong rf fields or field cycling procedures.

Figure 6.2 shows the evolution of the ^{1}H magnetization of surface -OH groups on particles of Aerosil130 after exposure to laser-polarized ^{129}Xe. Each point in the plot corresponds to the integral of the Fourier-transformed free induction decay, proportional to the instantaneous total nuclear magnetization. The inset shows the corresponding ^{1}H spectrum at the Boltzmann equilibrium (top spectrum) and after negatively polarized xenon has caused an enhancement of the surface magnetization (bottom spectrum); the enhanced spectrum is shown for the time t_0 when the negative enhancement has reached a maximum. A maximum enhancement factor of -20 was observed for the ^{1}H magnetization. In this type of experiment, the magnitude of the SPINOE depends on the cross-relaxation rate (σ_{HXe}) and on the number of noble gas spins on the surface, which can depend on the sample temperature. SPINOE enhancements using adsorbed ^{129}Xe were measured between about 100 and 200 K,

with the greatest enhancement obtained at 130 K.

Experiments were also performed that demonstrated SPINOE polarization transfer from both laser-polarized xenon and helium to a polymer coating (polyethylene oxide (PEO), with an average molecular mass of ≈400,000) on Aerosil130 particles. The adsorption of laser-polarized xenon at 130 K permitted a fractional SPINOE enhancement of the PEO ^{1}H NMR signal of about 10, with an estimated value for σ_{HXe} of 7×10^{-4} s^{-1}. However, this value is about an order of magnitude lower than that expected based on the estimated number of adsorbed xenon spins (and other relevant experimental parameters). Possible origins of this disparity may have included the presence of other relaxation pathways (i.e., other than xenon-proton dipole-dipole interactions) such as paramagnetic centers and ^{129}Xe CSA, as well as the likelihood that not all of the protons were accessible to the adsorbed noble gas spins (this latter effect would make the cross-relaxation rate seem smaller than it actually is). By using laser-polarized ^{3}He, signal enhancements between 100% and 200% could be observed for protons of PEO coating the Aerosil surfaces at sample temperatures between 4 K and 10 K. The helium-proton cross-relaxation rate, σ_{HHe}, was estimated to be $\sim 1 \times 10^{-3}$ s^{-1}. Finally, the ability to enhance ^{13}C NMR signals via the SPINOE was demonstrated following the adsorption of laser-polarized xenon onto ^{13}C labelled CO_2 coating Aerosil300 particles. An enhancement factor of -4 was observed for the ^{13}C spins, with an estimated xenon-carbon cross-relaxation rate $\sigma_{CXe} \approx 4 \times 10^{-4}$.

More recently, it was shown that silicon nuclei could be polarized indirectly via

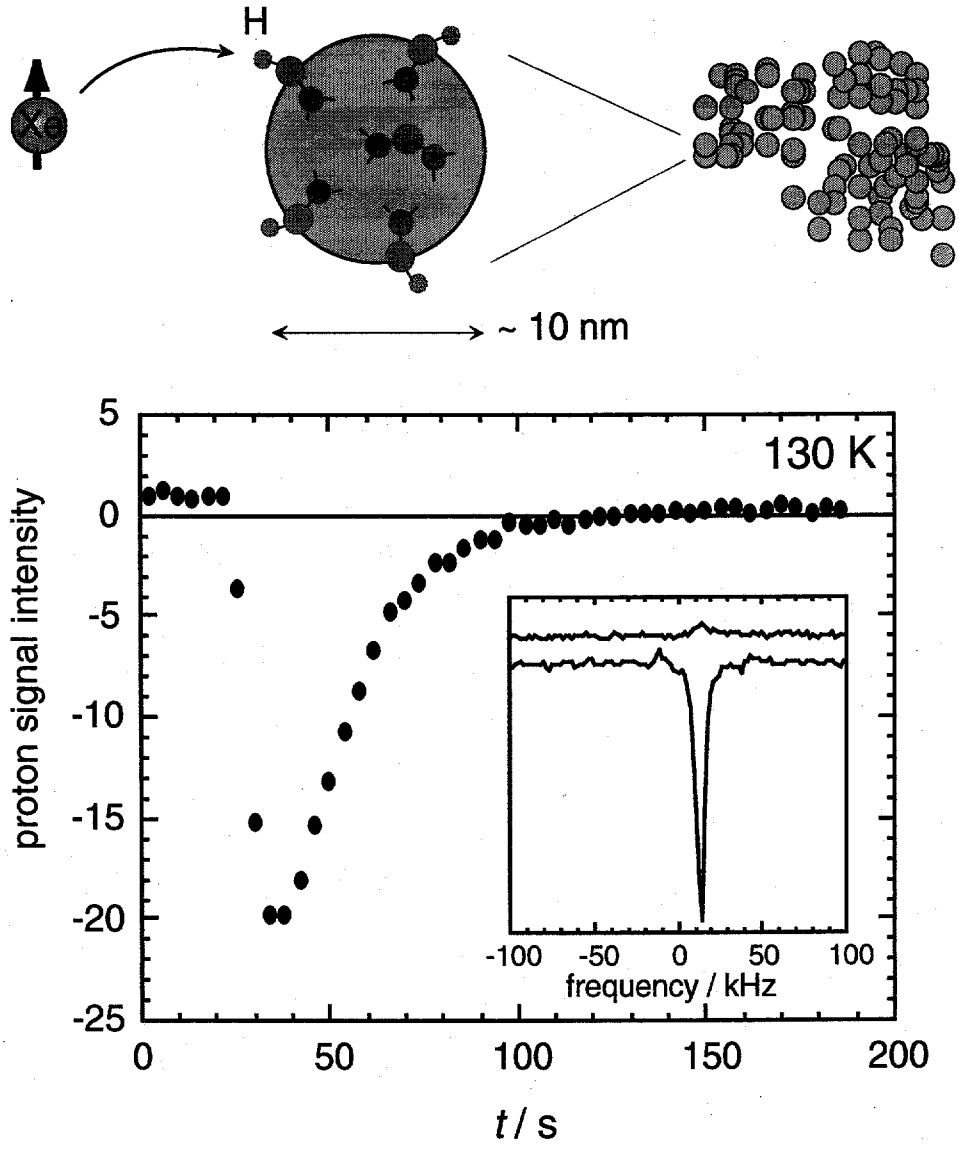

Figure 6.2: SPINOE enhancement of the integrated ^{1}H NMR signal from surface -OH groups on Aerosil130 particles following adsorption of negatively laser-polarized ^{129}Xe [171]. Signals taken prior to xenon absorption early in the experiment are shown for comparison. The largest enhancement factor observed was -20. The inset respectively shows a thermal equilibrium ^{1}H NMR spectrum (top) and the corresponding spectrum obtained when the negative enhancement had reached its maximum. Figure courtesy of Roberto Seydoux.

the SPINOE by a technique called SPINOE-CP [172], despite the low accessibility of these spins to the adsorbed xenon. By adsorbing laser-polarized xenon onto the surfaces of Aerosil300 particles, the polarization of surface protons could be enhanced via the SPINOE; this enhanced polarization could then be rapidly transferred by conventional Hartmann-Hahn cross-polarization methods to neighboring ^{29}Si spins in the material's lattice [172]. Fractional enhancements of 4 to 5 for the ^{29}Si NMR signal could be obtained with this technique.

6.4 Enhancing NMR with Continuous Xenon Flow

By adapting the design of an optical pumping apparatus capable of producing a continuous stream of laser-polarized xenon gas [54], a constant supply of laser-polarized xenon could be delivered to a sample within an NMR magnet [43, 44]. Figure 6.3 shows ^{129}Xe NMR spectra of laser-polarized xenon gas delivered to the NMR magnet under continuous-flow conditions. The steady-state non-equilibrium ^{129}Xe nuclear spin polarization attainable in this system recovers the initial conditions for each acquisition in only 4 s, as shown by the rapid change in the spectra when the optical pumping laser is turned off and then on again. With this apparatus, ^{129}Xe NMR experiments are not limited in time by longitudinal relaxation. Moreover, pulse sequences requiring a steadily renewed nuclear spin polarization can be applied without any restriction, permitting phase cycling, signal averaging, and a variety of multi-dimensional NMR experiments (and MRI experiments, as discussed in the next

chapter).

For example, the continuous delivery of fresh laser-polarized xenon gas permitted the direct observation of xenon exchange between two different zeolites within a powdered sample via two-dimensional exchange spectroscopy (EXSY) [173]. A 2-D ^{129}Xe EXSY spectrum of laser-polarized xenon exchanging between particles of zeolites Y and ZSM-11 taken at 220 K is shown in Fig. 6.4. This experiment was performed with a xenon partial pressure of only 1.3 KPa. The 2-D spectrum shown was obtained with an exchange mixing time of 25 ms. The diagonal peaks at 91 ppm and 150 ppm correspond to xenon residing in zeolite Y and zeolite ZSM-11, respectively. The existence of cross-peaks in the EXSY spectrum is indicative of significant xenon exchange between the two sites within the given exchange period. By analyzing the dependence of the cross-peak signal intensities upon the mixing time, a mean exchange time of 15 ± 5 ms could be determined.

Recently, ^{129}Xe OPNMR was used to study the behavior of xenon in a polycrystalline sample with 5 Å channels under conditions of continuous xenon flow [174]. This subnanoporous material is comprised of tris(*o*-phenylenedioxi)cyclo-phosphazene (TPP) in such a way that the 5 Å channels are formed with nearly perfect cylindrical symmetry, leading to an effectively one-dimensional gas phase for xenon within the material. The use of continuous flow of laser-polarized xenon afforded enormous ^{129}Xe NMR sensitivity, allowing numerous experiments to be rapidly and systematically performed under varying conditions of temperature and xenon partial pressure

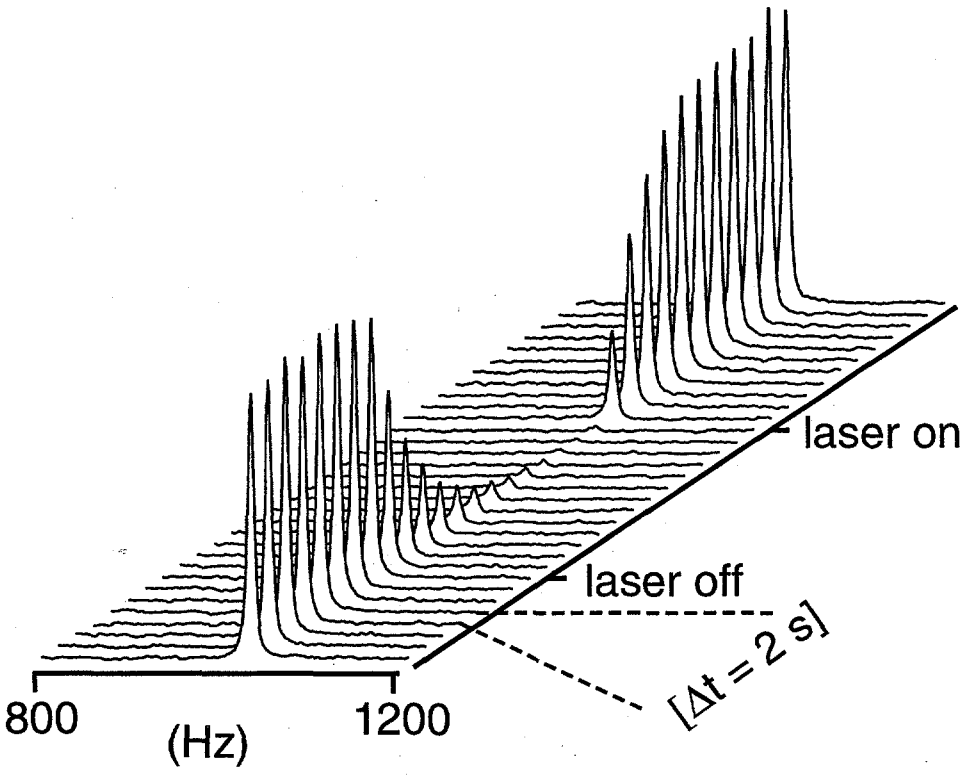

Figure 6.3: Multiple ^{129}Xe NMR spectra obtained at 2 s intervals from a continuous stream of laser-polarized xenon gas flowing through the sample region within an NMR magnet. By turning the pumping laser off and on, the rapid recovery of the xenon polarization can be observed. In this experiment, the signal recovered with a time constant of ~4 s. Figure courtesy of Roberto Seydoux.

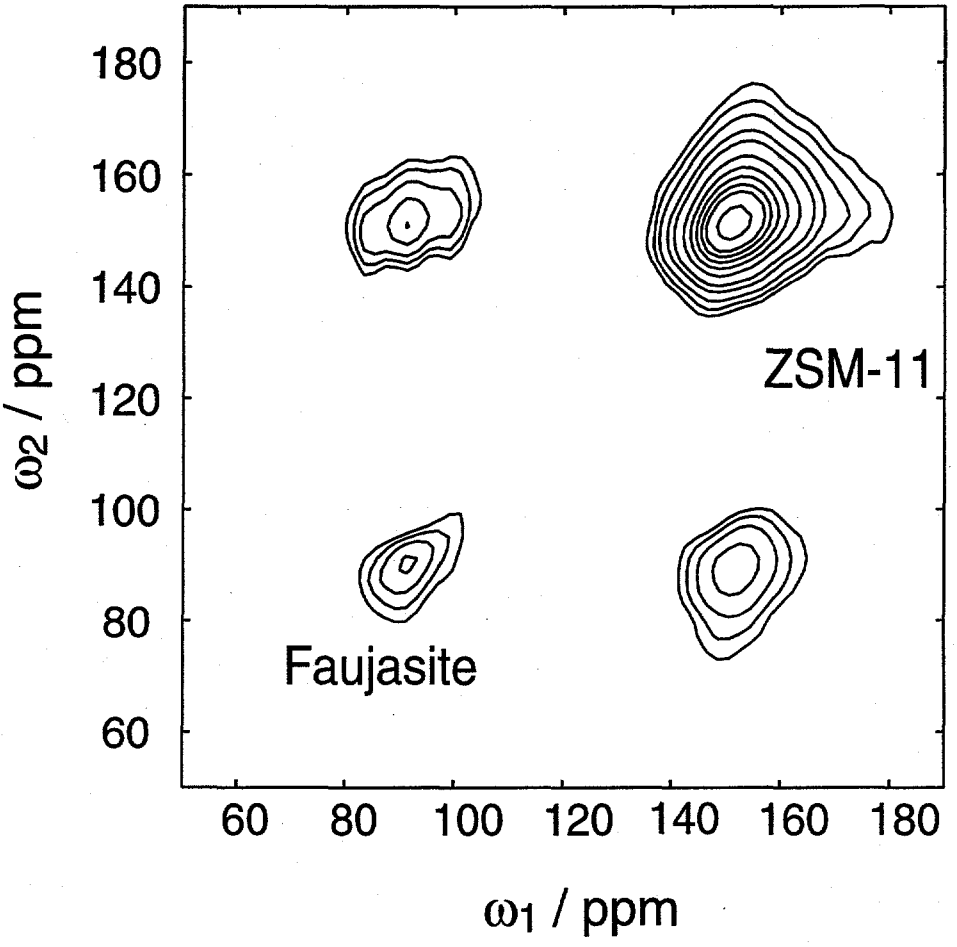

Figure 6.4: Contour plot of a 2D ^{129}Xe EXSY spectrum of laser-polarized xenon adsorbed on a mixture of highly siliceous zeolites Y (Faujasite) and ZSM-11, taken at 220 K with a xenon partial pressure of 1.3 KPa. The existence of cross-peaks shows that significant xenon exchange occurs between the two zeolites during the mixing time of 25 ms. Figure courtesy of Eike Brunner.

within the flowing gas mixture.

When a gas mixture comprised entirely of laser-polarized xenon was flowed through the TPP material, it was observed that the chemical-shift anisotropy (CSA) of the ^{129}Xe signal varied with temperature in such a way that full inversion of the anisotropy could be achieved over the available temperature range, as shown in Fig. 6.5(a). For example, at 373 K, the observed ^{129}Xe lineshape is indicative of a nearly axially symmetric CSA with positive anisotropy. However, decreasing the temperature results in an isotropic line at 333 K, and the sign of the anisotropy becomes inverted by 263 K. The authors note that while such CSA inversions have been observed previously [175, 176], the behavior in the present case is unique because the nearly perfectly axial CSA and the collapse to the isotropic line at 333 K suggest that only two opposing mechanisms exist that govern the distortion of the xenon electron cloud from spherical symmetry. Namely, the authors suggest the two mechanisms to be 1) interactions between xenon atoms and the near-cylindrically symmetric walls of the channels and 2) collisions between xenon atoms and other gas-phase species (i.e. other xenon atoms). Indeed, varying of the xenon concentration within the flowing gas mixture from 1% to 100% at constant (ambient) temperature produced a similar inversion of the axially symmetric CSA, as shown in Fig. 6.5(b). The authors suggest that because such results can be described by simply considering the competing influences of gas-gas and gas-wall interactions, the xenon/TPP system constitutes an ideal system with which to study physisorption and diffusion of gases within nanoporous materials.

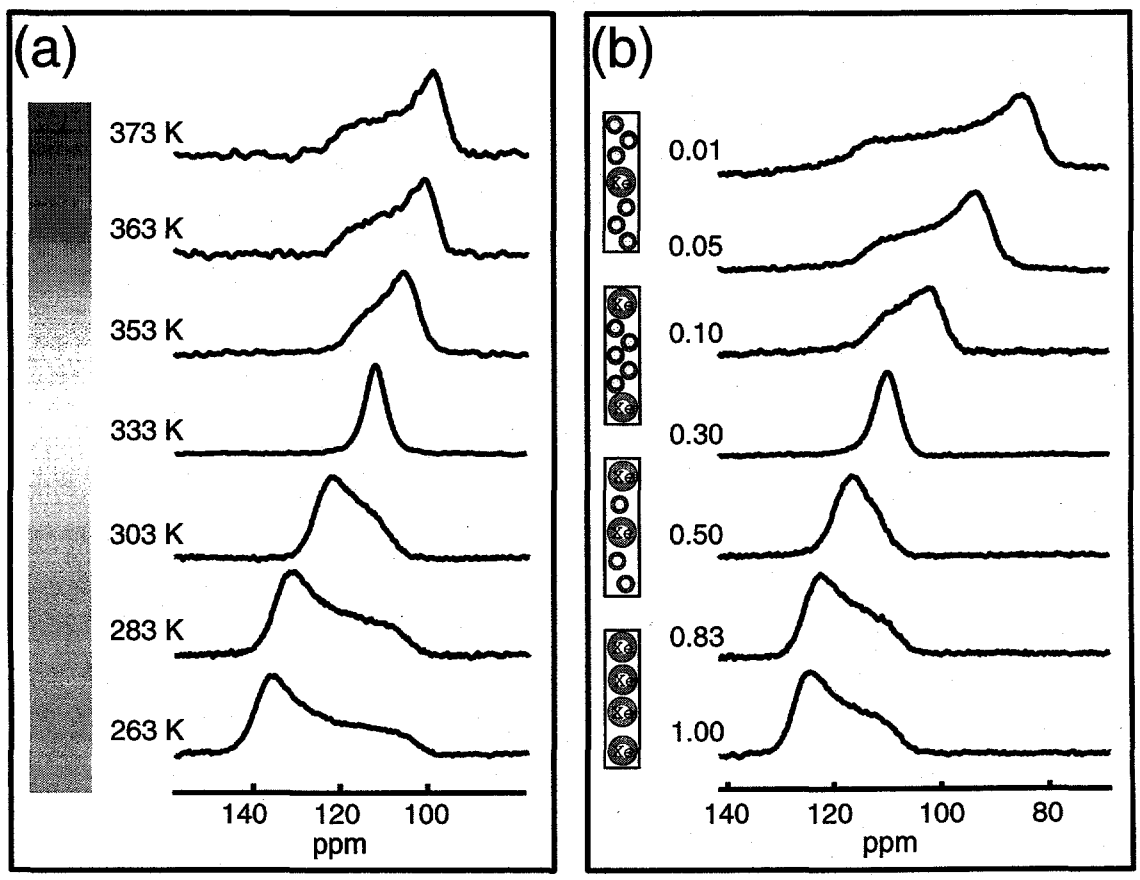

Figure 6.5: Inversion of ^{129}Xe CSA of laser-polarized xenon gas flowing through sub-nanometer channels of TPP. (a) Temperature dependence of ^{129}Xe CSA with gas mixture comprised entirely of laser-polarized xenon. (b) Xenon partial pressure dependence of ^{129}Xe CSA at ambient temperature. Figures courtesy of Roberto Simonutti and John Logan.

Other experiments have recently been performed that take advantage of continuous xenon flow to perform novel polarization transfer experiments. SPINOE polarization transfer to surfaces does not require immobilization of the laser-polarized noble gas. Thus, not only can surface-selective SPINOE experiments be performed over a broader range of temperatures, but they can be carried out indefinitely under conditions of continuous flow. In one demonstration, laser-polarized xenon was streamed continuously over an Aerosil surface to selectively enhance the surface proton spins via the SPINOE [43]. Following delivery of laser-polarized xenon to the sample, the gas was recirculated with a mechanical pump back into the optical pumping cell for re-polarization, permitting the experiment to be performed without interruption for several hours. With this technique, a steady-state enhancement of 200% was achieved (~800% when isotopically-enriched ^{129}Xe was used), with a steady-state ^{129}Xe polarization of only ~0.25% at the sample.

6.5 SPINOE under Magic-Angle Spinning

Subsequent work has been directed towards the development and application of an experimental apparatus capable of delivering a continuous stream of laser-polarized xenon to the sample, while performing magic-angle spinning (MAS) of the sample in order to obtain enhanced, high-resolution surface NMR spectra [177, 178, 179, 184]—a process denoted by Raftery and co-workers as OPMAS. One such OPMAS apparatus used by Pines and co-workers is shown schematically in Fig. 6.6. The first portion

of the apparatus is identical to that used to perform the previous continuous-flow experiments under static sample conditions [43], adapted from the original design of Driehuys *et al.* [54]. As described previously for the continuous-flow apparatus shown in Fig. 2.5, a high-pressure (~800 KPa) gas mixture of xenon, nitrogen and helium streams from a gas cylinder through a heated pumping cell (~400 K) containing a small amount of rubidium metal, where the Rb atoms are optically pumped at the wavelength of the Rb D_1 transition with circularly polarized light produced by a high-power ($\geq$ 100 W) diode laser array. After passing through the pumping cell the gas is expanded to normal pressure, and finally directed into a homebuilt double-resonance probe equipped with a commercial variable-temperature MAS unit (Fig. 6.6 inset).

OPMAS was first demonstrated by Raftery and co-workers in experiments designed to obtain SPINOE enhancement of surface protons with high resolution under conditions of continuous flow of laser-polarized xenon [177]. In these experiments, the ^{1}H NMR signal from water adsorbed onto fumed silica particles (surface area: 420 m^2/g) was enhanced via the SPINOE at 150 K while spinning the sample at ~3000 Hz. The SPINOE provided a two-fold increase in ^{1}H NMR signal compared with the thermal equilibrium signal; the cross-relaxation rate σ_{HXe} was measured to be $\sim 2\times10^{-3}$ s^{-1}.

These experiments were soon followed by work performed by Pines and co-workers in which the OPMAS apparatus shown in Fig. 6.6 was used to obtain high-resolution SPINOE spectra of surface protons of Aerosil300 SiO_2 particles under conditions of

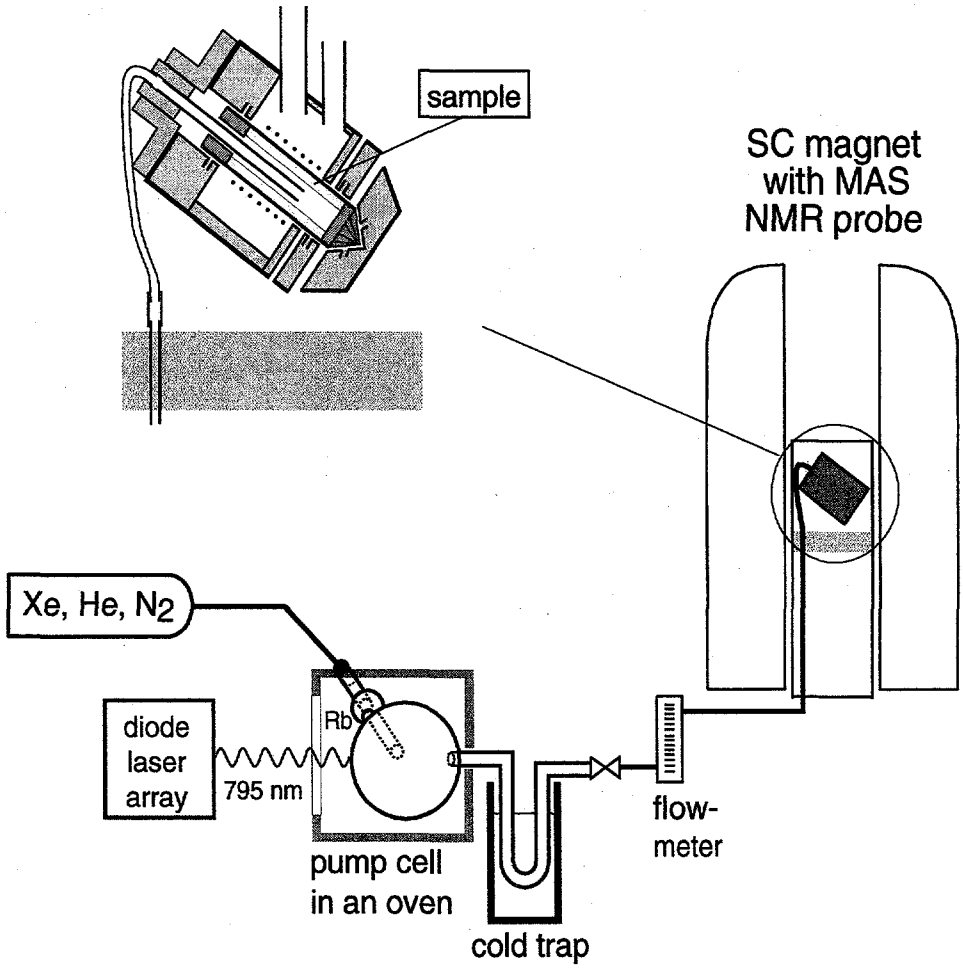

Figure 6.6: Schematic of an apparatus used for OPMAS experiments [178]; see text for description. Figure courtesy of Eike Brunner.

continuous xenon flow [178]. Figure 6.7 shows variable-temperature ^{1}H "SPINOE-MAS" spectra from the Aerosil sample acquired at a resonance frequency of 301.2 MHz and with a sample spinning rate of about 3 kHz; these spectra were obtained by subtracting the signal obtained when the sample was at thermal equilibrium (laser off) from the signal obtained when the xenon was laser-polarized (laser on). The highest SPINOE signal intensity—about 140% of the equilibrium signal—was observed at $\approx$168 K. The efficiency of the spin-polarization transfer strongly decreased with increasing temperature (most likely do to increasingly inefficient xenon adsorption), in agreement with previous observations [171]. One striking feature of the spectra in Fig. 6.7 are the spinning sidebands, denoted by asterisks (*); as expected, these sidebands are each offset from the main ^{1}H Aerosil resonance by the spinning frequency of the MAS rotor.

The above examples demonstrate the ability to observe SPINOE enhancement of proton NMR signals under MAS conditions. However, the surface area of the fumed silica and Aerosil particles used in such studies is high (e.g., 300 m^2/g for Aerosil300). Moreover, enhancing the NMR signals of nuclei other than protons would be advantageous for a number of reasons, including 1) wider chemical shift ranges, giving more sensitivity to local structure in a material; and 2) improved spectral resolution, resulting from reduced line broadening from reduced homonuclear dipolar coupling. In more recent studies, the ability to perform high-resolution SPINOE polarization transfer experiments to other types of nuclei, and on materials with

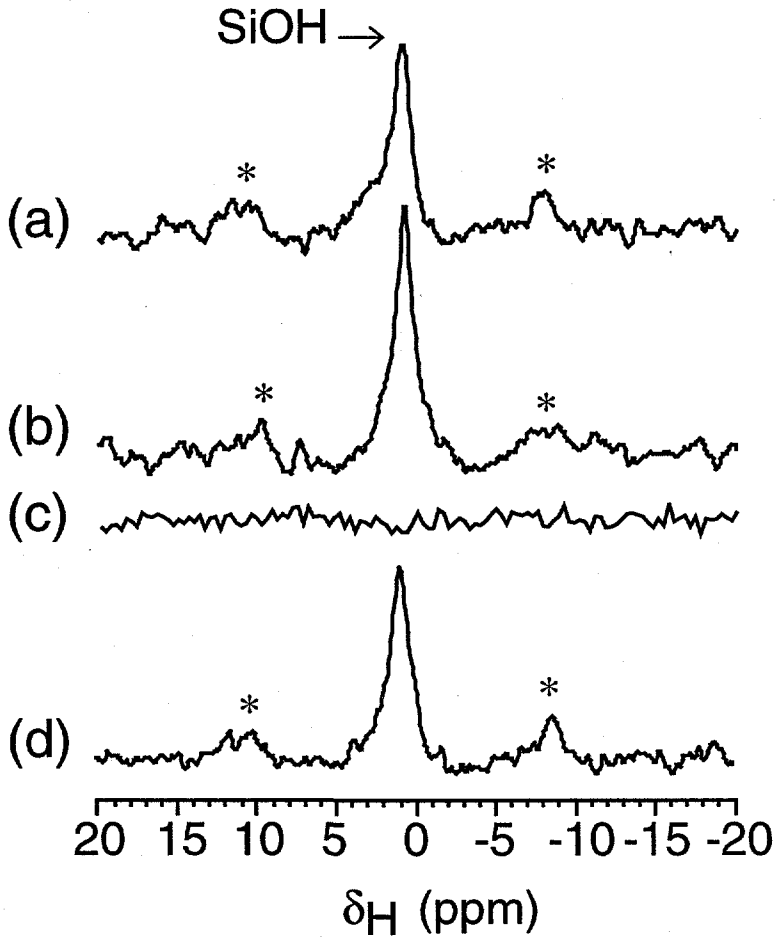

Figure 6.7: SPINOE-MAS ^{1}H difference NMR spectra taken from surface -OH groups on Aerosil300 particles at 173 K (a), 168 K (b,c), and 163 K (d) [178]. Spectrum (c) was obtained under the same conditions as (b), but with thermally-polarized xenon (obtained by turning the optical pumping laser off), demonstrating that the signals shown originate entirely from cross-relaxation with laser-polarized xenon. the asterisks (*) denote spinning sidebands. Each spectrum was taken as the sum of four scans, with a repetition time of 10 s. Figure courtesy of Eike Brunner.

much smaller surface areas, was demonstrated.

In one report, ^{129}Xe-^{13}C SPINOE-MAS experiments were performed on microcrystallites of fullerenes (C_{60} and C_{70}) [179]. Fullerenes are attractive systems to study with such methods because their spin relaxation behavior is well-characterized [180, 181, 182, 183], and the ^{13}C longitudinal relaxation times can be relatively long at low temperatures (e.g., ^{13}C $T_1 \sim 80$ s for C_{60} [181]). However, because the average diameter of the crystallites was large ($\sim$4 μm for the C_{60} sample and $\sim$2 μm C_{70}), the respective surface areas of these samples were estimated to be only $\sim$1 and $\sim$2 m^2/g.

Figure 6.8(a) shows ^{13}C MAS NMR spectra of C_{60} obtained under different conditions. The equilibrium ^{13}C MAS NMR spectrum of C_{60}, denoted Fig. 6.8(a)(*1*), shows the characteristic single line of C_{60} at 144 ppm [182]. The SPINOE spectrum shown in Fig. 6.8(a)(*2*) was obtained as the difference between the spectrum measured when laser-polarized ^{129}Xe was flowing through the rotor, and the spectrum measured when the xenon was thermally polarized. The intensity of the SPINOE signal corresponds to $\sim$15% of the intensity of the spectrum shown in Fig. 6.8(a)(*1*). However, because only a very small fraction of the C_{60} molecules is located on the surface of the crystallites ($\sim$0.0015, estimated from the mean crystallite diameter and the diameter of a C_{60} molecule ($\sim$1 nm)), The actual enhancement of the ^{13}C spins directly (or indirectly) coupled to the laser-polarized xenon was significantly larger. Assuming that the SPINOE polarization transfer occurs only to C_{60} molecules located at

crystallite surfaces, one can conclude that the observed signal enhancement of ~15% would correspond to a polarization enhancement factor of about 100. However, this estimate neglects ^{13}C spin diffusion, which can transport spin polarization into the bulk of the crystallites, resulting in a lower effective magnetization enhancement for the spins. Ideally, such spin diffusion is quenched under fast-MAS conditions (when the sample-spinning rate is greater than the homonuclear linewidth), although the degree of residual spin diffusion was difficult to determine. Nevertheless, by assuming full spin diffusion (i.e., the spin diffusion observed in a static sample), an upper limit for the penetration depth of 30-40 nm could be estimated, resulting in a lower limit for the SPINOE enhancement factor of ~3.

Figures 6.8(b)(*1*) and 6.8(b)(*2*) show the ^{13}C MAS NMR spectra of C_{70} crystallites measured at room temperature and 150 K, respectively, with assignments as given in Ref. [182]. Because the residual linewidths of the ^{13}C MAS spectra increase with decreasing temperature [182], the signal resulting from C1 carbons is poorly resolved at 150 K. While the spectrum in Fig. 6.8(b)(*2*) was measured in the presence of a gas stream carrying thermally-polarized xenon (i.e., with the laser turned off), the spectrum in Fig. 6.8(b)(*3*) was obtained while the laser was on, producing differential enhancements in the ^{13}C spectra. Specifically, Fig. 6.8(b)(*3*) shows an increase in intensity of the signal resulting from carbons in the C2 and C3 positions (147 ppm) of about 25%, more clearly shown in the difference spectrum (Fig. 6.8(b)(*4*)). However, in agreement with the results of previous calculations and measurements [182],

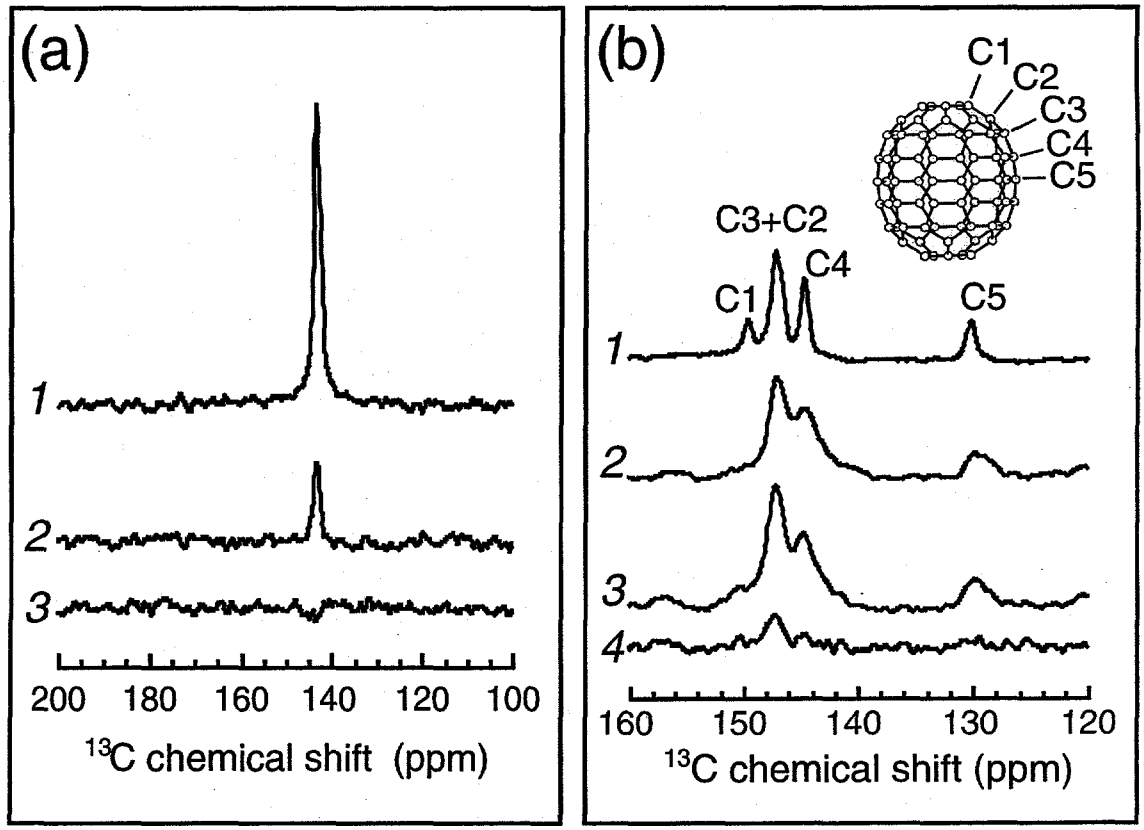

Figure 6.8: ^{13}C MAS spectra obtained from (a) C_{60} and (b) C_{70} crystallites [179]. (a)(*1*) ^{13}C MAS NMR spectrum obtained when the gas stream contained only thermally-polarized xenon (laser off). (*2*) Difference SPINOE-MAS ^{13}C NMR spectrum obtained by subtracting Spectrum (*1*) from a spectrum obtained using laser-polarized xenon. (*3*) Difference spectrum obtained in the absence of laser-polarization. The observed enhancement factor in (*2*) was about 15%. (b) ^{13}C MAS spectra obtained from C_{70} crystallites at room temperature (*1*) and 150 K (*2-4*) [179]. (*1,2*) Spectra obtained in the absence of laser-polarization. (*3*) Spectrum obtained with flow of laser-polarized xenon. (*4*) The signal obtained from subtracting (*2*) from (*3*), showing the differential enhancement of the C2 + C3 resonance. Figures courtesy of Eike Brunner.

identical ^{13}C T_1 values of $\approx$5 s were measured for the C2, C3, C4, and C5 carbons at 150 K. Therefore, it is likely that the greater SPINOE for the C2/C3 resonance results from a higher cross-relaxation rate. The origin of this selectivity is unknown, but may be due to greater xenon accessibility to C2 and/or C3 carbons in the C_{70} crystallites, or a higher heat of adsorption of xenon for these sites.

In a second study, both the SPINOE and SPINOE-CP were used to enhance the NMR signals of ^{13}C and ^{29}Si spins on the surfaces of fumed silica particles [184] under conditions of MAS and continuous xenon flow. In a manner similar to that of Ref. [172], signal enhancement of ^{29}Si spins of the fumed silica particles (surface area: 389 m^2/g) was achieved by first permitting SPINOE polarization transfer from adsorbed laser-polarized xenon to surface protons, and then coherently driving polarization from these surface protons to neighboring ^{29}Si spins via Hartmann-Hahn CP. The observed ^{29}Si NMR signal was enhanced by about 16%. For ^{13}C spins of ^{13}C-labelled methanol chemisorbed onto the fumed silica surfaces, however, it was observed that the SPINOE was more efficient than SPINOE-CP (30% vs. 7.6% enhancement). The authors point out, however, that the observed SPINOE enhancement may actually be the result of a relayed SPINOE through the protons, instead of a direct SPINOE between the xenon and carbon spins.

Chapter 7

Enhanced Imaging of Materials

7.1 Introduction

The non-destructive characterization and imaging of materials continues to be an experimental challenge. For example, the properties of many porous materials can depend not only on the overall porosity, but also on the size distribution and connectivity of the pores within a given material; unfortunately, such parameters can be difficult to study without destroying the material in question. While in principle such materials can be studied by infusing them with water, mercury, or other liquids (often at high pressure), there are various samples whose chemical or physical sensitivity precludes such approaches, including many polymers, catalysts, ceramics, aerogels, food products, and antiquated or fossilized remains (the study of living samples is the subject of the next chapter). As inert gases, xenon and helium can provide contrast

for studies of material inhomogeneity and sample morphology in a non-destructive fashion. Some work has been performed using gaseous ^{129}Xe to image various materials samples (see for example, Ref. [185]). However, a serious limitation of the MRI of gases is the low density in the gas phase compared to that of condensed-phase media (e.g. liquid water), as well as the normally low equilibrium nuclear spin polarization. Luckily, the enormous signal enhancement afforded by optical pumping can more than make up for the low spin density of gas-phase media.

In this chapter, a variety of materials applications of xenon OPMRI are described. The first section contains examples where laser-polarized xenon gas is used to image macroscopic void spaces in samples under static (zero xenon flow) conditions. This section is followed by a discussion of work involving the imaging of laser-polarized xenon in condensed phases. A considerable portion of this chapter (comprising the third section) is dedicated towards the effects of diffusion and boundary-restricted diffusion on MRI; such behavior is especially easy to study with laser-polarized noble gases. Finally, this chapter concludes with a discussion of recent work demonstrating OPMRI of laser-polarized xenon in porous materials under conditions of continuously recirculating flow.

7.2 Gas Imaging Under Static Conditions

7.2.1 First Phantom Studies

Following the use of laser-polarized xenon gas to image the void spaces in excised rat and guinea pig lungs [186, 187] (discussed in greater detail in the next chapter), laser-polarized xenon gas was used to image void spaces in materials under static conditions without the need for signal averaging [188]. Figure 7.1 shows enhanced ^{129}Xe MR images obtained following the admission of laser-polarized xenon gas into structured phantom samples. Specifically, Fig. 7.1(a) shows a FLASH ^{129}Xe MR image of xenon gas in a phantom in which void spaces have been cut to give the chemical symbol for xenon ("Xe"), while Fig. 7.1(b) shows a FLASH ^{129}Xe MR image of xenon gas in a phantom comprised of three nested glass tubes; the gaps between the tubes varied from 0 to 2 mm. It was possible to obtain ^{129}Xe MR images with a resolution of $\sim$100 μm, on the order of the diffusion-limited resolution for gaseous xenon when using typical micro-imaging gradients. The ability to directly image xenon penetration within an aerogel sample as a function of time was also demonstrated.

7.2.2 An Anthropological Application of Polarized Gases?

Following the experiments imaging laser-polarized xenon in the glass phantoms, the potential for using laser-polarized xenon to image void spaces in samples of ar-

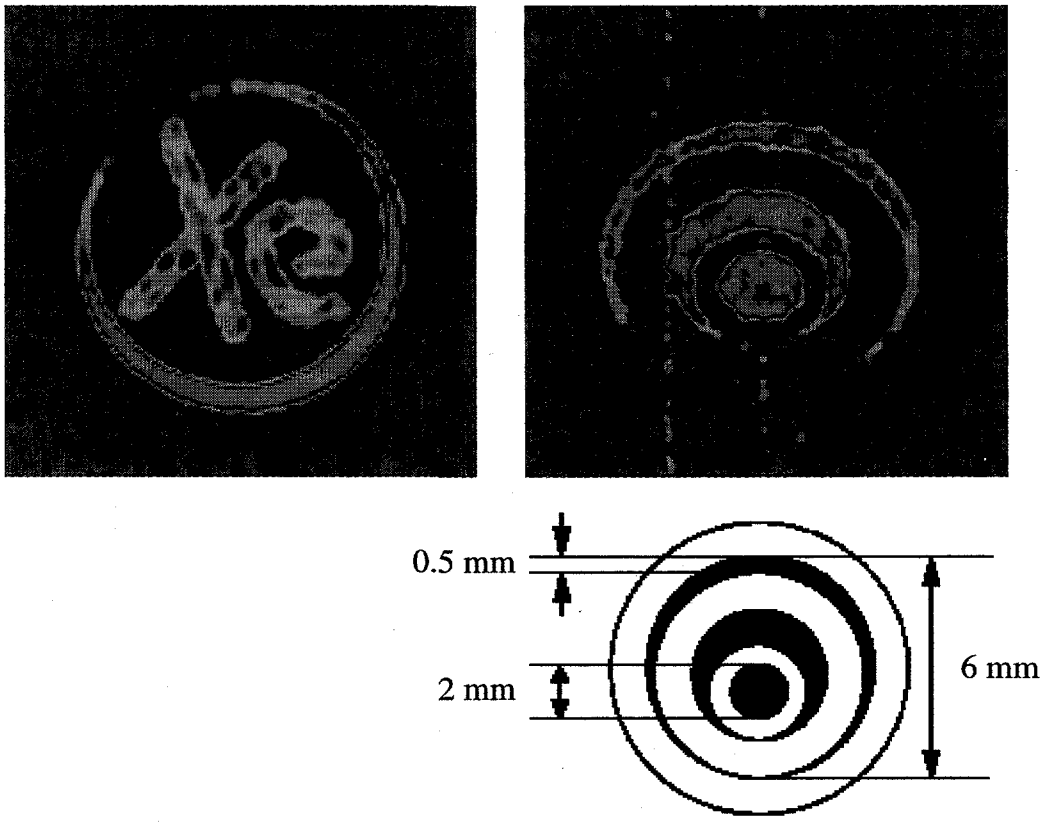

Figure 7.1: Two-dimensional MR images of laser-polarized xenon gas in phantom samples. (a) Image obtained following the admission of laser-polarized xenon in a phantom sample (cross-sectional diameter: ~7 mm) in which void spaces have been cut to give the chemical symbol for xenon ("Xe"). (b) Image obtained following the admission of laser-polarized xenon in a phantom comprised of three nested glass tubes, with geometry as shown in the diagram [188]. Figures courtesy of Yi-Qiao Song.

chaeological or anthropological interest was investigated [189]. Figure 7.2 contains a series of 2-D slice-selected FLASH images of laser-polarized xenon gas in a glass tube containing an ancient human tooth. The tooth was provided by Tim White of the Department of Integrative Biology, UCB. As before with the glass phantom images, areas with bright signal correspond to regions in the sample where laser-polarized xenon is present. The images are shown in order, top to bottom of the tooth (i.e., Fig. 7.2(a) shows a 2-D slice taken from the crown region of the tooth, Figs. 7.2(b,c) show slices taken from the middle region of the tooth, while Fig. 7.2(d) shows a slice taken from the root region). Of particular interest in the images of Fig. 7.2 is the region of moderately bright signal coming from the center of the tooth, which corresponds to laser-polarized xenon gas residing within a cavity of the tooth.

It is difficult to imagine a more non-invasive manner by which to image such a sample than sealing it in a tube with an inert noble gas and measuring the distribution of that gas via the application of non-ionizing (rf) radiation. Unfortunately, it is normally the case that the void spaces of such samples—especially ones of greater antiquity and ones that have become fossilized—would be completely filled with solid mineral deposits or rock during sedimentation processes that take place over thousands (or millions) of years, thereby negating any chance of gleaning useful information via OPMRI (for example, to estimate brain case volumes of hominids by imaging skull remains). Instead, other methods such as X-ray tomography are likely to be better suited in such cases.

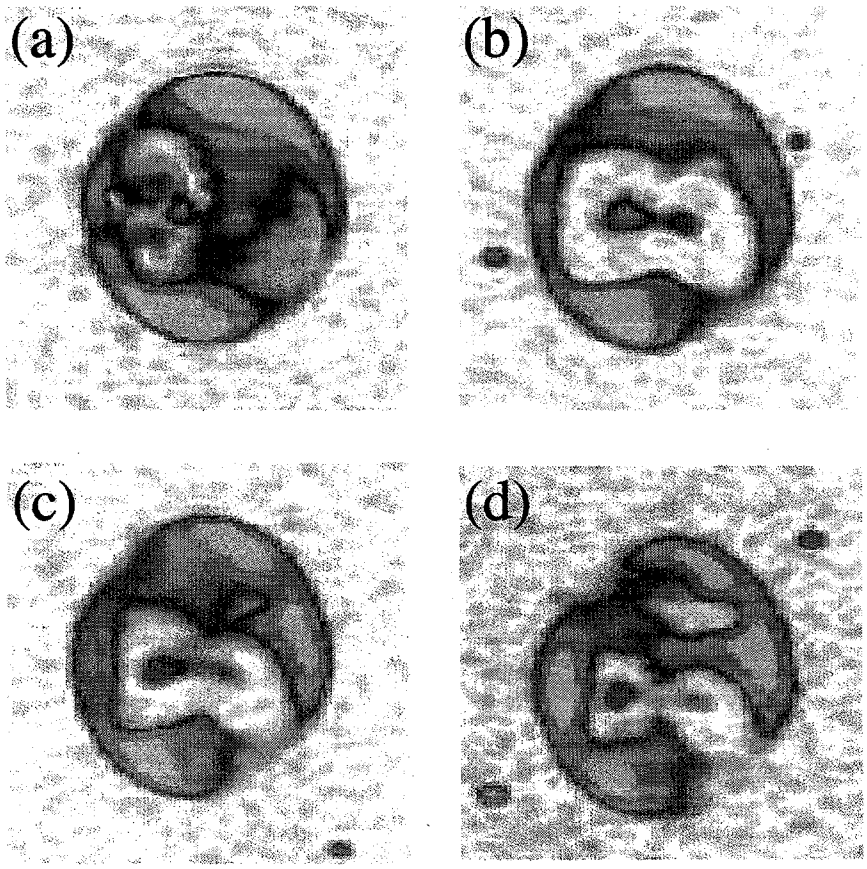

Figure 7.2: False-color ^{129}Xe OPMRI of an ancient human tooth [189]. Color key: yellow–high signal, magenta–medium signal, navy, low signal, light blue/white–no signal. (a) crown. (b) upper middle region of tooth. (c) lower middle region of tooth. (d) root. Human tooth sample provided by Tim White.

7.3 Enhanced Imaging in Condensed Phases

The enormous sensitivity enhancement provided by optical pumping, along with the long spin-lattice relaxation time of ^{129}Xe in benzene, permitted the dissolution and macroscopic transport of xenon in benzene to be observed in detail via OPMRI [89]. Figure 7.3(a) shows a series of 2-D FLASH ^{129}Xe OPMR images taken as a function of time immediately following the exposure of partially deuterated benzene to gaseous laser-polarized xenon. A macroscopic xenon concentration gradient is observed to rapidly form in the tube at short times; this concentration gradient is then observed to become more equilibrated over time by the 4:00 mark. The final image shows an equilibrium distribution of xenon obtained by vigorously shaking the sample. Interestingly, the concentration at early times is observed to be greatest at the *bottom* of the tube. This xenon accumulation at the bottom of the sample likely originates from density differences between the xenon/benzene solution and neat benzene; the heavier, xenon-rich regions that form at the top of the solution following xenon diffusion into the solvent gravitate to the lower regions of the tube via convection.

The dissolution of laser-polarized xenon also permitted the SPINOE enhancement of the benzene proton polarization to be directly imaged. Figure 7.3(b) shows two 2-D ^{1}H "SPINOE MR images" taken two minutes and six minutes following exposure of a fully protonated benzene sample to laser-polarized xenon gas, along side a third proton MR image obtained with the benzene protons at thermal equilibrium. The

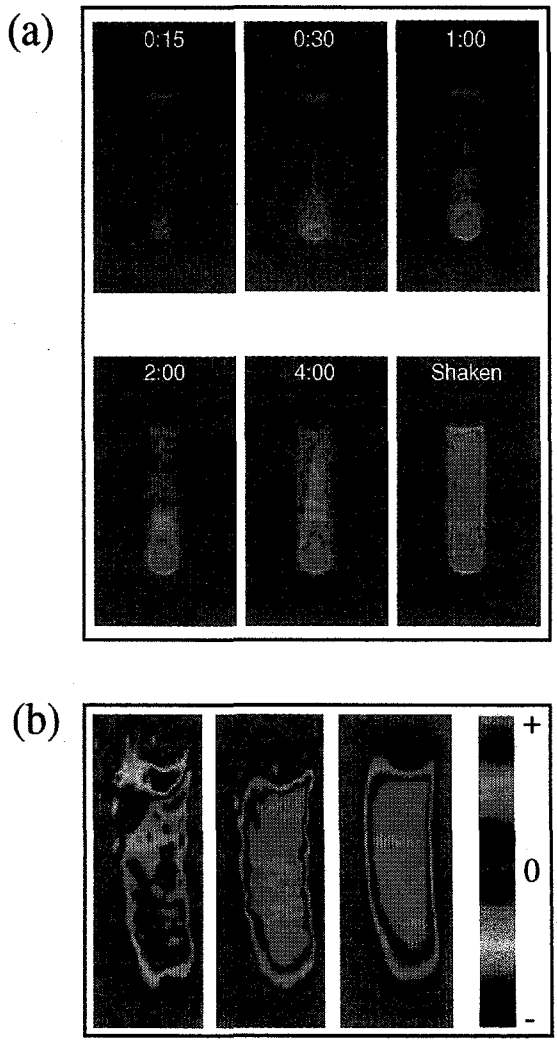

Figure 7.3: Time-dependent OPMRI of laser-polarized xenon dissolving in benzene [89]. The vertical axis of the images is parallel to the external magnetic field and the long axis of the NMR sample tube. (a) Time-resolved false-color 2-D FLASH MR images of the dissolved xenon in a sample tube containing partially deuterated benzene taken immediately following exposure to gaseous laser-polarized xenon. (b) 2-D false-color ^{1}H SPINOE MRI of fully protonated benzene taken 2 minutes (left image) and 6 minutes (middle image) following the introduction of laser-polarized xenon; an equilibrium ^{1}H MR image is also shown (right image). The negative region in the left image (yellow/black region) originates from the expansion of the liquid phase of benzene following the dissolution of xenon. The images were obtained by the EPI method. The distortion of the images reportedly originated from inhomogeneity in the static magnetic field. Figures courtesy of Yi-Qiao Song.

SPINOE images were obtained by subtracting the equilibrium image from the data obtained following xenon dissolution; the maximum enhancement in the first image was 5%, while the maximum enhancement in the second image was 12% (the contrast for the SPINOE images was multiplied by a factor of 8). Note that the concentration gradient seen previously in Fig. 7.3(a) is also observed in the 2 minute SPINOE image (left). This effect is expected, as the SPINOE enhancement of the proton magnetization will normally scale with the local xenon concentration in the absence of strong xenon binding. The uniform appearance of the SPINOE image taken at 6 minutes, however, suggests that the xenon concentration had equilibrated throughout the benzene sample by the time that the image was acquired.

Following work demonstrating the potential for enhanced sensitivity and MRI resolution from the imaging of frozen laser-polarized xenon at 77 K [190], similarly-minded MRI experiments were performed on liquid laser-polarized xenon at 166 K [109]. However in this work, the presence of both liquid and gas phases of xenon within the tube, in addition to the bright NMR signal and long xenon spin-lattice relaxation times, permitted the direct observation xenon exchanging between the phases. Figure 7.4 contains a series of 2-D FLASH ^{129}Xe MR images taken of laser-polarized xenon condensed in a Pyrex tube at various stages of exchange. Specifically, Figure 7.4(a) shows an image of the liquid xenon that has collected at the bottom of the tube, while Fig. 7.4(b) shows the corresponding gas image; Figs. 7.4(c-f) show xenon evaporation as a function of time, while Figs. 7.4(g-j) show the corresponding images

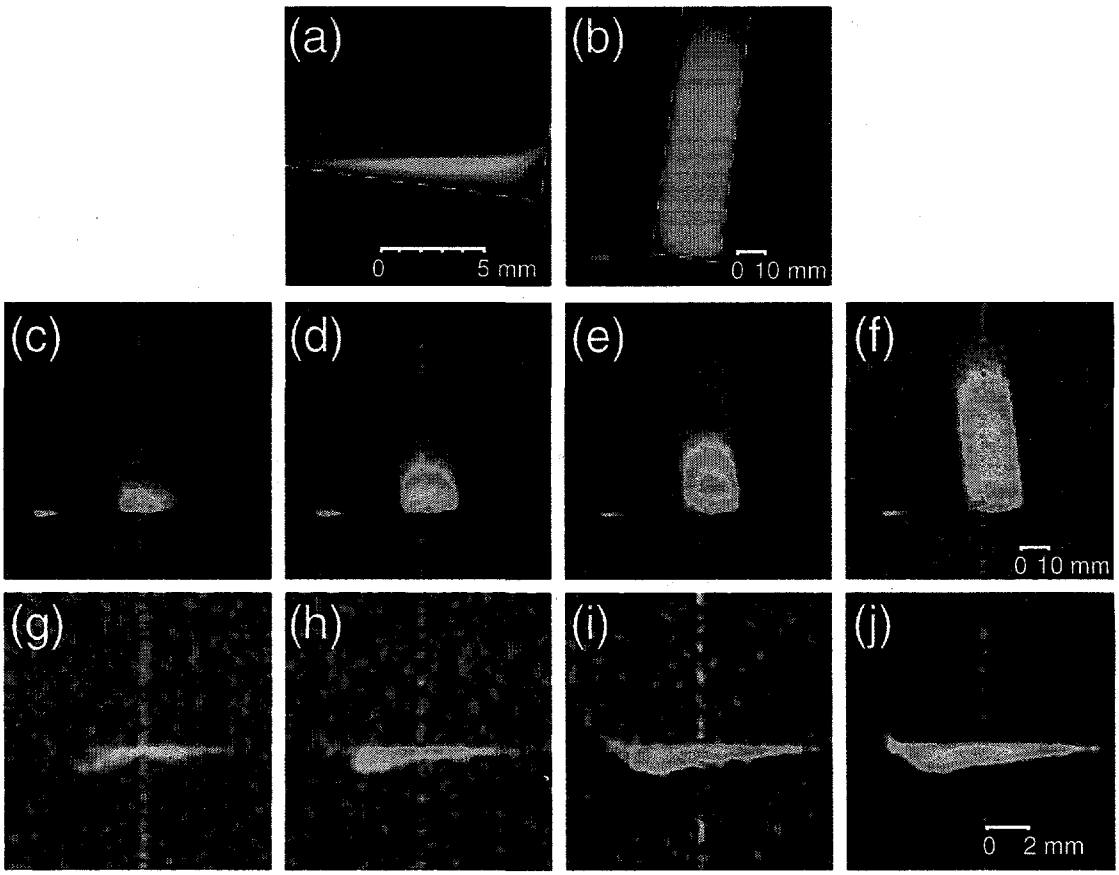

Figure 7.4: ^{129}Xe FLASH MRI of laser-polarized xenon condensed in a tilted glass tube at 166 K [109]. (a) MR image of liquid laser polarized xenon that has condensed at the bottom of the tube. The image resolution was 195 × 195 μm^2, limited by the strength of the applied magnetic field gradients. A displaced liquid xenon signal can also be seen in the xenon gas image in (b) resulting from rf-excited xenon atoms in the gas phase condensing into the liquid phase prior to acquisition. (c-f) Time-resolved MR images tracking the evaporation of liquid laser-polarized xenon, taken 12 s (c), 46 s (d), 3:30 min (e), and 5:15 min (f) after the xenon gas signal was destroyed by the application of multiple selective rf pulses and gradient pulses. (g-j) Time-resolved MR images tracking the condensation of gaseous laser-polarized xenon, taken 25 s (g), 63 s (h), 2:30 min (i), and 6:30 min (j) after the xenon liquid signal was destroyed by the application of multiple selective rf pulses and gradient pulses. Figures courtesy of Glenn Wong and Ronald Walsworth.

of xenon condensation into the liquid phase. The propagation of laser-polarized xenon in the vapor phase (shown in Figs. 7.4(c-f)) is consistent with the xenon gas diffusion coefficient under the given experimental conditions (about 0.02 cm^2/s). In principle, the authors state, liquid laser-polarized xenon MRI could achieve a resolution on the order of 10 μm^3 at 166 K (with gradient strengths on the order of 400 G/cm). The authors suggest many possible applications of the liquid laser-polarized xenon MRI, including studies of density equilibration and convective flow near xenon's critical point and the imaging of microstructure in porous media.

7.4 Effects of Diffusion on Imaging

In condensed phases, the resolution of MRI can reach a few microns under the most ideal of circumstances, and is normally limited by the low signal obtained from the relatively low number of spins in such small regions. However, one limitation on the resolution of laser-polarized gas imaging originates from the rapid diffusion of gases, typically several orders of magnitude higher than in liquids. As previously mentioned, the resolution of the images in Fig. 7.1 was limited to about 100 μm because of the rapid diffusion of the polarized xenon gas.

In addition to limiting the MRI resolution, diffusion may distort the lineshape of MR images for samples containing boundaries or diffusion barriers within the space being imaged. This effect was first suggested by numerical simulations [191, 192] and was later explored experimentally [193, 194] using ^1H NMR of liquid samples.

In one dimension, the diffusion problem has been solved analytically [195, 196, 197]. However, the detailed characterization of such effects has been difficult using ^{1}H NMR. For example, given a value for the diffusion constant of water molecules $D_w \approx 2 \times 10^{-5}$ cm^2/s, the corresponding effects from diffusion would occur over a distance $d = \sqrt{2D_w t}$, or less than 10 μm during a time t of a typical one-dimensional (1-D) imaging experiment ($\sim$10 ms). An imaging resolution below 10 μm is difficult to achieve because the signal from such a small region is often too weak.

The use of laser-polarized xenon gas for studying the effects of boundary restricted diffusion provides two advantages: a strong NMR signal and a large diffusion length. Given a xenon diffusion constant at 1 atm of 0.0565 cm^2/s [198], one obtains a value of $d = 0.034$ cm for $t = 10$ ms, which can be readily measured. In fact, these advantages have been exploited to measure diffusion constants of laser-polarized gases under various conditions [77, 199]. Recently Saam *et al.* [200] used samples of polarized ^{3}He to study the the effects of diffusion on imaging, while demonstrating the ability to image such polarized gases at low field (discussed later in Chapter 9); however, those investigations were performed only in the weak-diffusion regime, where the diffusion length is much smaller than the sample size.

In a more recent study, the effects of diffusion on MRI were examined in greater detail using 1-D samples of laser-polarized xenon gas [201]. In these experiments, the strength of the applied gradient and the geometric dimension of the 1-D sample could be varied, permitting the evolution of diffusion-mediated image distortions between

the regimes of strong and weak diffusion to be studied systematically. By directly measuring the displacement distribution of the polarized xenon atoms, it was shown that in the weak-diffusion regime the image distortions originate from the restricted diffusive motion near the sample boundaries, in agreement with previous theoretical work. Finally, it was shown that diffusion-weighted imaging experiments could be employed to actively enhance the contrast between the boundaries and bulk in the images of polarized gas samples, thereby demonstrating the potential of using polarized gas MRI for boundary detection in porous media. These results suggest that boundary detection schemes that take advantage of diffusion, in addition to studies of boundary-constrained diffusional motion, may have application to medical and materials imaging using laser-polarized noble gases.

7.4.1 Experimental Methods

In order to simplify the analysis of the 1-D imaging experiments, A long rectangular glass tube (0.07 by 0.66 cm in cross-section) was used for all imaging experiments. A spherical xenon reservoir of several cc was attached above the sample tube to provide enough polarized xenon gas to permit several imaging experiments with each optical pumping run. All experiments were performed at 4.3 T with isotopically enriched (^{129}Xe) xenon polarized with a batch optical pumping apparatus; the xenon pressure in the tube was typically about 2 atm. Following optical pumping, laser-polarized xenon was transferred to the tube via cryopumping and subsequently placed

in the imaging probe parallel to the direction ($\vec{z}$) of the static magnetic field ($\vec{B}_0$). The axis parallel to the 0.66 cm side is designated as $\vec{x}$, while the axis parallel to the 0.07 cm side is designated as $\vec{y}$ (imaging experiments were performed along both $\vec{x}$ and $\vec{y}$). In all of these experiments, a slice-selection $\vec{z}$ gradient was applied during the rf excitation, creating a slice depth of about 0.4 cm. The rf coil was a saddle coil 2.0 cm long and 1.2 cm in diameter. The use of such a large coil and slice selection helped to ensure that the rf field would be homogeneous (but significantly reduced the filling factor in these experiments). Having an extremely homogenous static field is also important for such work, as the effects of diffusion are most pronounced at low field gradient and directly manifest themselves as changes in the spectral line shape. Linewidths of 0.6–1.5 Hz were obtained in the absence of applied gradients by shimming directly on the polarized xenon gas samples.

Three pulse sequences were used in these experiments, and are shown in Fig. 7.5. In the pulse sequence used for 1-D imaging (Fig. 7.5(a)), a 500 μs Gaussian excitation pulse (tipping angle: $\leq 5°$) is applied during a slice-selection gradient along $\vec{z}$. Following the excitation pulse, a gradient pulse is applied, and the free induction decay is acquired and Fourier transformed to obtain the image. The displacement distribution measurements were performed using the pulsed-field-gradient spin-echo method (see for example, Ref. [202]). The pulse sequence used in this experiment is shown in Fig. 7.5(b), where the displacement dimension is formed by incrementing G_1, while the second dimension is created from acquisition under G_2. In these experiments, both

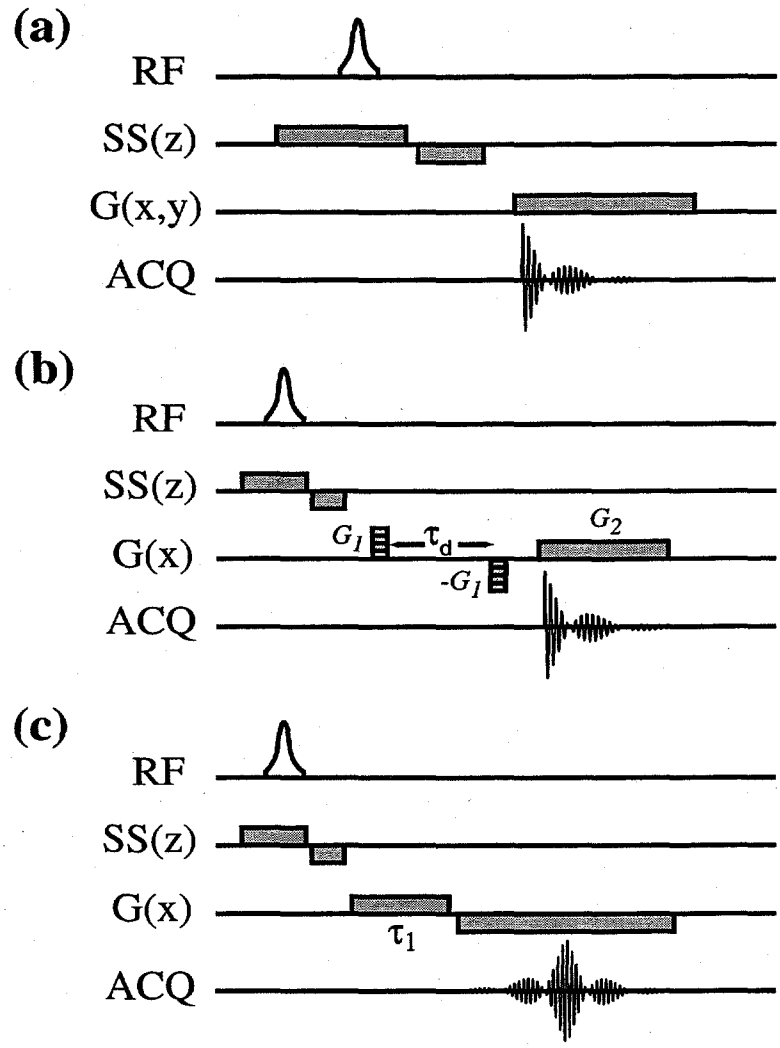

Figure 7.5: Pulse sequences used for various boundary-restricted diffusion experiments [201]. (a) The rf pulse is a Gaussian amplitude-modulated pulse of 500 μs and is applied during a slice selection gradient (SS) along $\vec{z}$. The imaging gradient was applied along either $\vec{x}$ or $\vec{y}$ depending on the experiment. (b) The pulse sequence for the measurement of the displacement distribution in the xenon gas sample. The displacement dimension is formed by stepping the gradient strength G_1; the second gradient is equal to the first gradient in strength but opposite in sign. The second dimension originates from direct imaging with the gradient G_2. (c) The pulse sequence used in the edge-enhancement imaging experiments. Imaging gradients were along $\vec{x}$; the duration τ_1 of the first gradient was varied.

G_1 and G_2 were gradients along $\vec{x}$. Fig. 7.5(c) contains the pulse sequence used for edge-enhanced imaging. In these experiments, both imaging gradients are directed along $\vec{x}$ and the duration of the first gradient τ_1 was varied to change the level of contrast between xenon at the boundaries and the bulk.

7.4.2 Imaging in the Limits of Strong and Weak Diffusion

In order to study how diffusion distorts MR images, two series of 1-D images were taken as a function of the gradient G along both axes of the sample. These series of images are shown respectively in Fig. 7.6 for G along $\vec{y}$ and in Fig. 7.7 for G along $\vec{x}$. To avoid extra line broadening and lineshape distortion, careful optimization of the gradient direction was necessary; this was particularly important when the gradient was applied along $\vec{y}$ because of the sample's shape. For example, a error of only 2° in the direction of the gradient would cause severe distortion of the lineshape, drowning out the effects of diffusion at low gradient strength.

Eight 1-D images are shown in Fig. 7.6 with G along $\vec{y}$ and a gradient range of 0–0.70 G/cm. These images display a smooth evolution of the lineshape from a sharp resonance at zero gradient, to a slightly broadened but still single resonance at small gradient, to the development of two broad lines at higher gradient strength.

Fig. 7.7 is comprised of five images taken with G directed along $\vec{x}$ varying in strength from 0.063–0.63 G/cm. As the gradient strength is increased, the intensity of the signal from the middle region becomes rather flat, and the two broad fea-

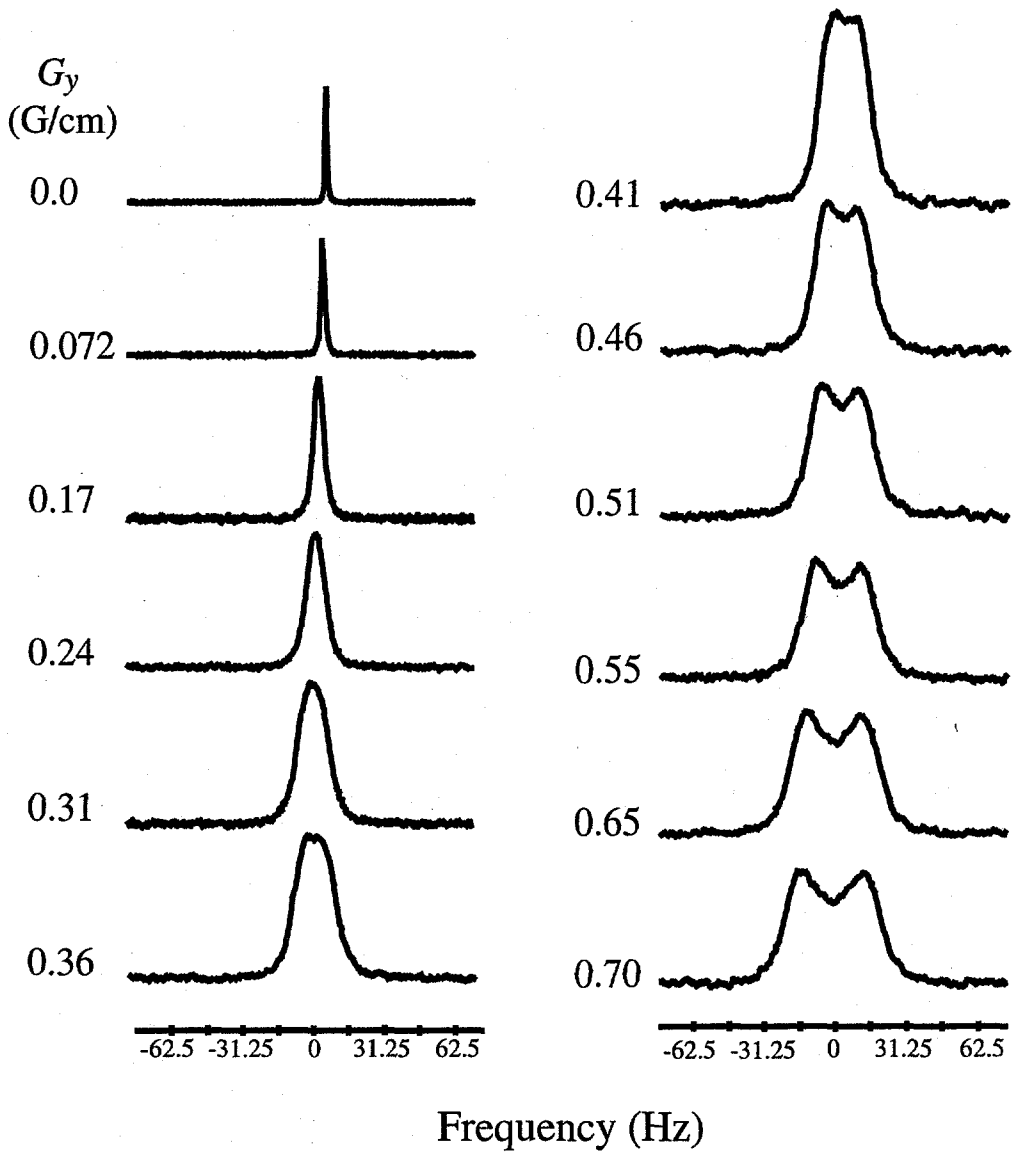

Figure 7.6: 1-D ^{129}Xe MR images taken as a function of applied gradient along $\vec{y}$, obtained with G_y = 0, 0.072, 0.17, 0.24, 0.31, 0.36, 0.41, 0.46, 0.51, 0.55, 0.65, and 0.70 G/cm [201]. These images depict the evolution of the lineshape with increasing gradient strength in the strong-diffusion regime.

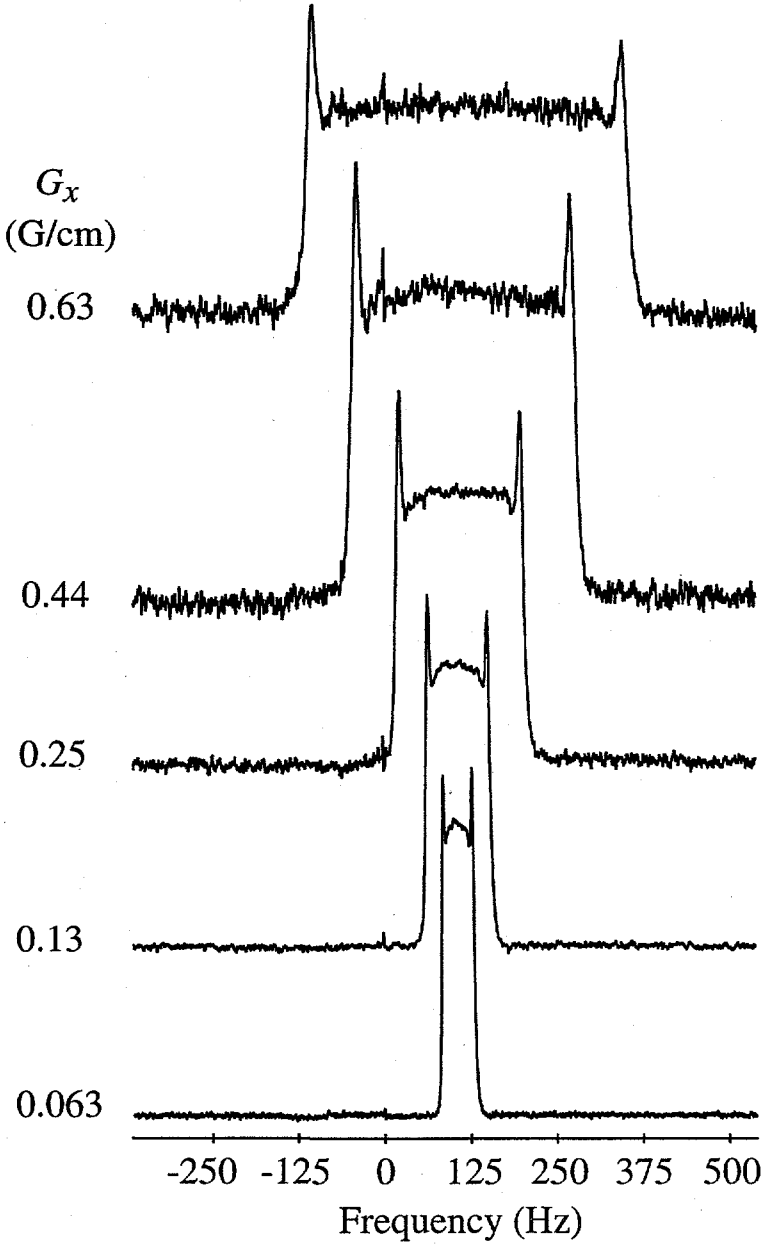

Figure 7.7: 1-D ^{129}Xe MR images taken as a function of applied gradient along $\vec{x}$, obtained with G_x = 0.063, 0.13, 0.25, 0.44, 0.63 G/cm [201]. These images depict the evolution of the lineshape with increasing gradient strength in the weak-diffusion regime. Note the pronounced edge-enhancement effects.

tures seen in the previous images of Fig. 7.6 grow into sharp, well-defined spikes whose locations correspond to positions near the sample boundaries (the so-called "edge-enhancement effect"). Each image also contains a slight but noticeable drop in intensity just inside each of the edge-enhancement peaks, as predicted in previous theoretical work [191, 192, 196]. Edge spikes such as these have been observed (but not characterized) recently in polarized gas samples [200, 203]; Saam *et al.* [200] used this effect to demonstrate edge enhancement in the images of polarized ^{3}He gas samples. However, to date there has been no previous demonstration of strongly diffusion-averaged images such as those shown in Fig. 7.6.

A conceptual understanding of the diffusion-mediated image distortions shown in Figs. 7.6,7.7 is relatively straightforward, at least at the extremes of weak and strong diffusion. De Swiet and Sen [196] have introduced a parameter called the diffusion length, l_g, that characterizes these two regimes:

$$l_g = \sqrt[3]{\frac{D}{\gamma G}}, \tag{7.1}$$

where D is the diffusion coefficient of the substance and γ is the gyromagnetic ratio of the nuclear spin. Simply stated, l_g is the distance that a molecule will diffuse during the time that its nuclear spins acquire a unit of phase under the influence of a gradient of strength G. Fig. 7.8(a) shows a plot of l_g *vs.* G for xenon gas over the range of the gradient strengths produced by a typical MRI spectrometer. The

maximum imaging resolution is limited to about $2l_g$; thus, the resolution that may be obtained from xenon gas imaging is limited to about 100 μm for a typical gradient value in a micro-imaging apparatus (at one atmosphere of xenon pressure).

When l_g is much greater than the geometric dimension l_s of the sample along the direction of the gradient vector (i.e., experiments within the strong-diffusion regime), a spin will diffuse throughout the available space before the dephasing from the gradient can occur. In this case an averaged frequency of the nuclear spin is measured. In other words, all of the spins have essentially lost their memory of their initial positions; thus, all have the same average frequency giving rise to a single resonance line, as shown in the first four spectra of Fig. 7.6. In this regime the effect of the gradient is primarily manifested by an apparent line broadening. Previous theoretical work [196] has shown that in this regime the lineshape can be effectively approximated by a Lorentzian; indeed, the first three images in Fig. 7.6 clearly possess Lorentzian lineshapes. De Swiet [197] has shown that the Lorentzian lineshape should persist until $l_s/l_g = 2$. In this regime, an analytical expression for the time dependence of the NMR signal $S(t)$ is given in Ref. [14]:

$$\frac{S(t)}{S(0)} = \exp\left(-t \cdot \frac{\gamma G l_s^4}{120 \cdot l_g^3}\right), \tag{7.2}$$

while the corresponding frequency domain lineshape is given in Ref. [197]. Figure 7.8(b) contains a comparison of the above theoretical prediction for $1/T_2^* =$

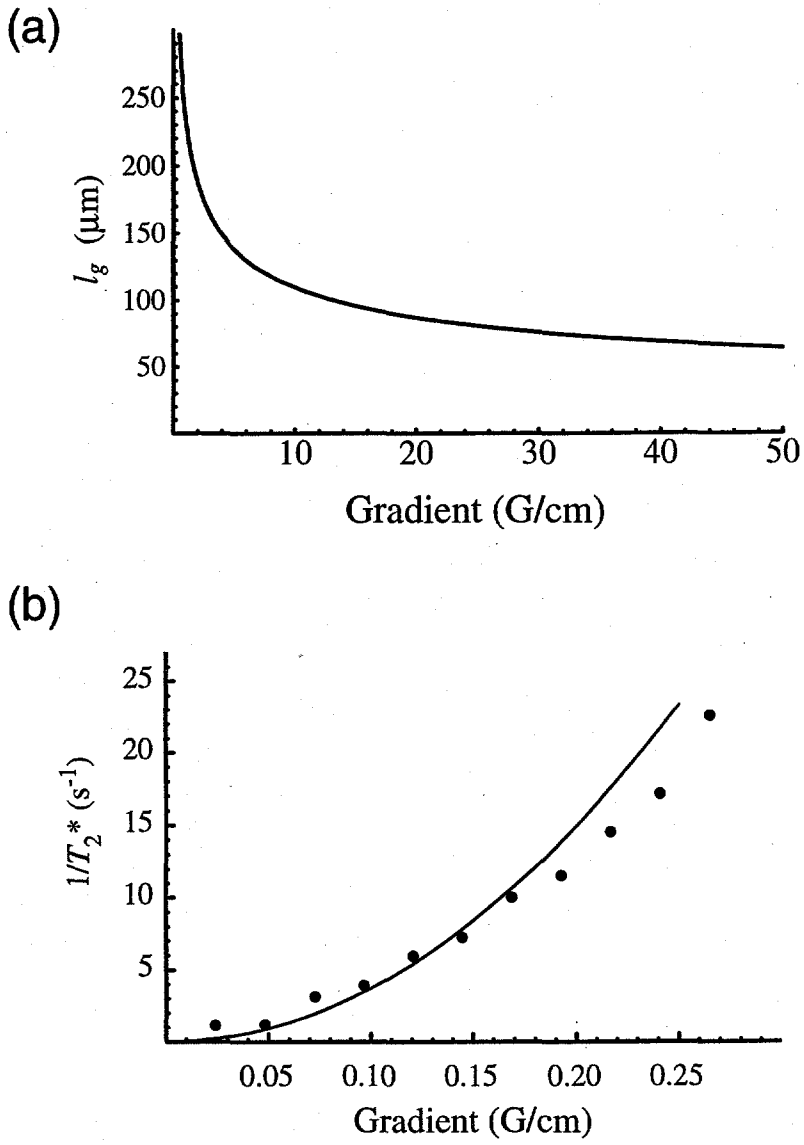

Figure 7.8: (a) Plot of l_g *vs.* gradient strength over the range of a typical MRI spectrometer, for xenon gas pressure of 1 atm [201]. The limit of the MRI resolution is approximately $2l_g$. (b) A plot of $1/T_2^*$ as a function of G [201]. Filled circles are from the time-domain data taken in the strong-diffusion regime, with the contribution from the residual field inhomogeneity removed by subtracting the value of $1/T_2^*$ when $G = 0$. The curve was calculated using Eq. 7.2. Experimental values deviated from the theory when $G > 0.17$ G/cm due to the departure from Lorentzian lineshape.

$\gamma G l_s^4/(120 \cdot l_g^3)$ with experimental values measured from the initial slope of the signal decay for the images in Fig. 7.6 prior to Fourier transform. From the figure one can see that the experimental data matches the theoretical prediction quantitatively for $G \leq 0.17$ G/cm; the deviation at higher gradients originates from the departure from a Lorentzian lineshape.

In circumstances where $l_g << l_s$, (i.e., experiments within the weak-diffusion regime), the effects of diffusion are most clearly observed near the edges (where diffusive motion is restricted). This effect can be understood qualitatively in the following manner. Because xenon atoms near the edges of the sample are reflected back upon collision with the edges, the average displacement of these xenon atoms is smaller than the displacement of the xenon atoms in the middle of the sample during the application of the gradient. In other words, the spins near the edges lose their memory slower than those in the middle of the sample, and thus the decay of the signal from spins near the edges is slower than that for spins in the middle. This slower decay in the time-domain signal causes the pronounced, narrow spikes to appear near the edges in the images of Fig. 7.7 once the signal is Fourier transformed. In addition, the reflection at the edges also leads to each peak being positioned at some distance ($\sim l_g$) from the actual edge. More precisely, theoretical work [197] has shown that this distance is equal to $-a_1' l_g$, where a_1' is the first zero of the derivative of the first Airy function, and $a_1' \approx -1.0188$; This value is consistent with the results presented here [201] and with those of Saam *et al.* [200]. It is important to remember, however,

that such amplitude variations are only relative, and the integral of the image is actually conserved regardless of the diffusion in the sample. An analytical solution of the diffusion problem in one dimension has been reported [195, 197]; it has been shown [197] that the peaks near the edges can be identified with slowly relaxing normal modes.

In order to compare the experimentally obtained images shown in Figs. 7.6,7.7 with theoretical expectations, calculations were performed to simulate the diffusion of xenon in the 1-D sample in the presence of magnetic field gradients. These simulations modeled the effects of xenon diffusion by following the phase accumulated by dimensionless particles making random walks between the sample boundaries. The free-induction-decay signals that were calculated were then Fourier transformed to obtain simulated 1-D images. Up to one million particles were used in order to reduce the noise in the simulations. The algorithm used for these simulations is similar to those used by Hyslop and Lauterbur [191] and Putz *et al.* [192]; the calculations presented here agree with their previous results when given the same set of parameters. Three of these simulated images are shown in Fig. 7.9, and may be compared with the experimentally obtained images taken with the corresponding gradient values. As shown in the figure, the simulations reproduce the experimental results well in all three cases. The principle sources of asymmetry in edge-enhancement spikes of the experimental images are likely to have been inhomogeneity in B_0 and imperfections in the shape of the sample tube.

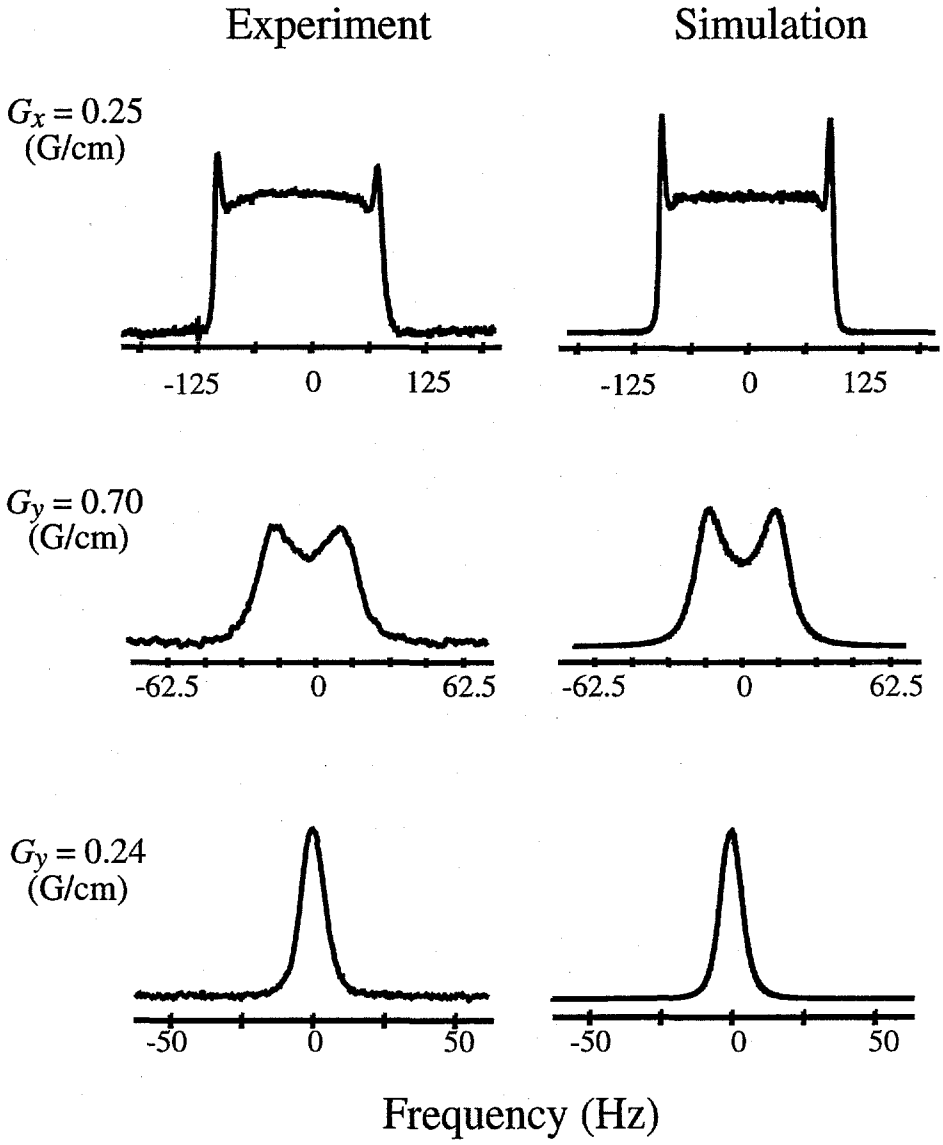

Figure 7.9: Comparison of experimentally obtained images with numerical simulations [201]. 1-D simulations were performed for the images obtained with gradient strengths of 0.24 and 0.70 G/cm along $\vec{y}$ and 0.25 G/cm along $\vec{x}$.

7.4.3 Measurements of the Displacement Distribution

As previously discussed, the difference between the diffusion behavior near the boundaries and that at the center of the sample originates from the impermeability of the glass walls. Xenon atoms adjacent to the sample walls can only diffuse inward, thus altering the displacement distribution of those atoms compared to that of xenon atoms near the center of the sample. This change in the xenon displacement distribution gives rise to two effects: 1) a net displacement of the gas atoms near the edges towards the center; and 2) the range of the displacement for atoms near the edges is significantly reduced. In fact, these two effects correspond, respectively, to the first and second moments of the displacement distribution, which is a Gaussian for diffusion in free space. At the sample edges, however, the displacement distribution is neither Gaussian nor symmetric, and thus higher order moments are also significant. Therefore, it is useful to characterize such boundary-restricted diffusive motion by directly measuring the displacement distribution as a function of position across the sample.

By measuring the displacement distribution, one could obtain, for example, a spatially dependent diffusion constant whose values are expected to be larger in the middle of the sample and smaller near the edges. However, it is interesting to note that the second moment of the displacement distribution actually becomes wider *at* the sample's edges (see Fig. 7.10(d)); thus, any calculated position-dependent diffusion constant would become greater at the boundaries than values calculated

for regions *near* those boundaries. This effect can be rationalized by considering the one-dimensional diffusion of three identical particles over a short time t, with one particle distant from any boundaries, one particle positioned $d/2$ from a boundary, and the last particle positioned at a boundary. The first particle will travel a distance d over t. Over the same amount of time, the particle near the boundary may end up very near its original position due to reflection from a collision with the boundary. The particle at the boundary, however, will tend to travel inward away from the boundary, free from reflection and traveling a longer distance (on average) than that traveled by the second particle. However, because of the limited spatial resolution in the experimental results shown here, it proved difficult to directly observe this phenomenon.

The displacement distribution was measured using the pulse sequence shown in Fig. 7.5(b); the time domain data were Fourier transformed in both dimensions, and are shown in Fig. 7.10(a). When normalized, this figure shows the probability $P(x, x_0, t)$ of displacement $x - x_0$ as a function of the starting position x_0 over a time period t. Because xenon atoms at the edges can only diffuse inward, one would expect that the displacement distributions at the two edges of the sample would slant toward opposite directions, while the displacement distribution would be symmetric at the center. This effect is in fact observed in Fig. 7.10(a), despite the finite resolution of the imaging along $\vec{x}$. The displacement distributions at the two edges and the center are shown in Fig. 7.10(b). As expected, this figure clearly shows that the displacement

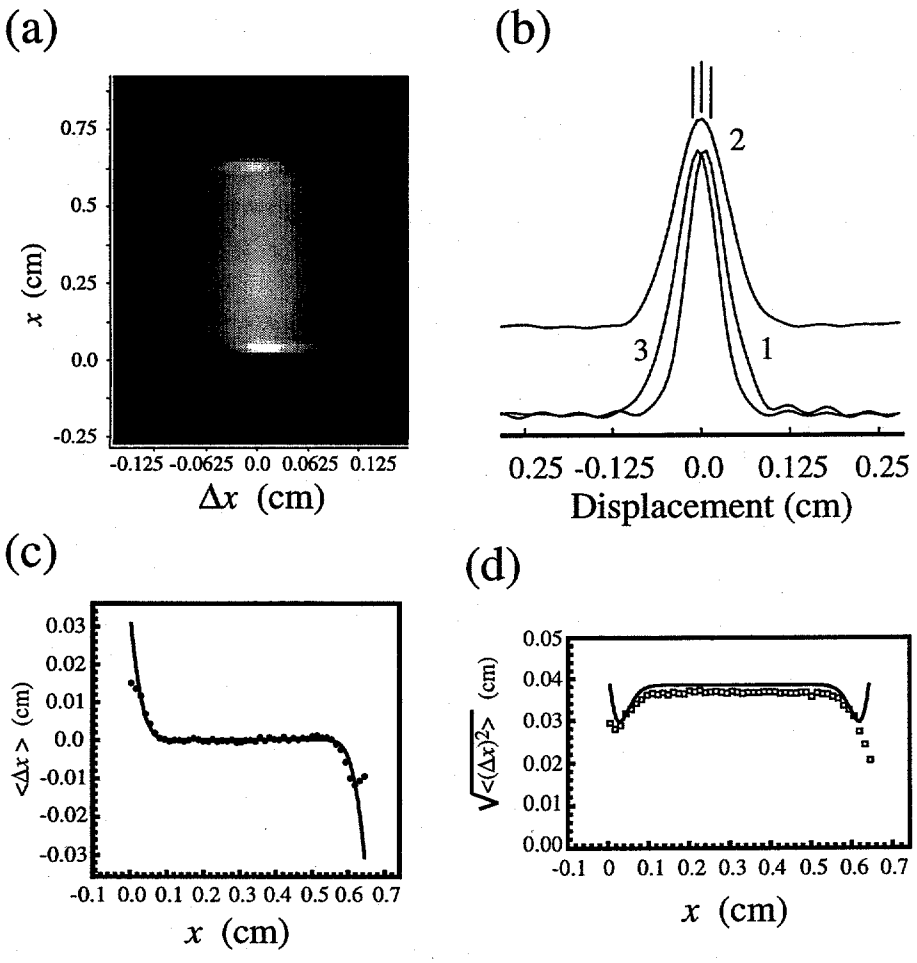

Figure 7.10: (a) Measurement of the displacement distribution as a function of position along $\vec{x}$ at $\tau_d = 25$ ms acquired with the pulse sequence shown in Fig. 7.5(b). Differences in the displacement distribution caused by constrained diffusional motion near the sample boundaries are evident. (b) Normalized displacement distribution near the two edges (slices 1 and 3) and in the center (slice 2). The vertical lines indicate the mean displacement for each distribution. (c) Plot of the mean displacement (first moment) as a function of x. Filled circles are data calculated from (a), and the curve represents theoretical values from Eq. 7.4; experimental data were shifted up $\approx$23 μm to correct for a slight deviation from zero most likely resulting from gradient mismatch. (d) Plot of the range of displacement (second moment) as a function of x. Open squares are data calculated from (a), and the curve represents theoretical values from Eq. 7.5. A decrease in diffusive motion is manifested near the edges; however, the growth at the edges shown in the theoretical values was not observed experimentally because of insufficient resolution.

distributions at both edges of the sample are asymmetric and skew toward opposite directions. Values of both the mean displacement and the second moment of the displacement distribution were calculated for all slices from the data in Fig. 7.10(a), and are shown in Figs. 7.10(c) and (d) respectively. The net displacement toward the center of xenon near the edges, as well as a restriction of diffusive motion near the edges, is clearly shown.

One may analytically solve the diffusion equation near a one-dimensional wall using a Green's-function approach and obtain the probability of finding an atom at a position x after diffusing from the original position x_0 over a time t:

$$P(x, x_0, t) = \frac{1}{\sqrt{4\pi Dt}} \left\{ \exp\left[-(x - x_0)^2/4Dt\right] + \exp\left[-(x + x_0)^2/4Dt\right] \right\}. \qquad (7.3)$$

The position of the boundary is defined to be at $x = 0$. For regions distant from the boundary, $x >> \sqrt{2Dt}$, this function reduces to the familiar Gaussian form for diffusion in free space. Because the sample dimension is much greater than $\sqrt{2Dt}$, the effect of the other boundary can be neglected, and it is therefore sufficient to consider the effect of only one boundary. The average displacement and the width of the displacement distribution can be calculated using Eq. 7.3:

$$\frac{< \Delta x >}{d} = \sqrt{\frac{2}{\pi}} \left\{ \exp\left(-\frac{x_0^2}{2d^2}\right) + \frac{x_0}{d\sqrt{2}} \left[\mathrm{erf}\left(\frac{x_0}{d\sqrt{2}}\right) - 1 \right] \right\}, \qquad (7.4)$$

$$\frac{< (\Delta x)^2 >}{d^2} = 1 - \sqrt{\frac{8}{\pi}} \cdot \frac{x_0}{d} \exp\left(-\frac{x_0^2}{2d^2}\right) + \frac{2x_0^2}{d^2} \left[1 - \mathrm{erf}\left(\frac{x_0}{d\sqrt{2}}\right) \right], \qquad (7.5)$$

where $d = \sqrt{2Dt}$ and $\Delta x = x - x_0$. Plots of the calculated $< \Delta x >$ and $\sqrt{< (\Delta x^2) >}$ values are shown for comparison with the experimentally measured data in Figs. 7.10(c) and (d).

7.4.4 Edge-Enhanced Imaging for Boundary Detection

Diffusion-weighted imaging has been utilized in many areas of magnetic resonance imaging (see for example, Refs. [12, 204, 205]). In fact, it has been suggested that the effects of diffusion on MRI can be used to detect impermeable and semi-permeable membranes [191]. As previously mentioned, it has been shown that diffusion-mediated edge spikes like those seen in Fig. 7.7 can be used to differentiate between the boundaries and bulk of a sample of laser-polarized gas, and thus represent a "passive" form of edge enhancement [200]. However, such contrast between the edge and bulk signals can be greatly increased by the application of a pulse sequence that takes advantage of the different behavior of the diffusion in these regions. In the case of the 1-D sample used in the present experiments, one may understand such an "active" edge-enhancement method in terms of a position-dependent diffusion constant, $D(x)$. According to the displacement distribution, $D(x)$ would be smaller near the boundaries; thus the decay of the NMR signals during the application of a magnetic field gradient should be slower for spins near the boundaries and faster spins distant from the boundaries. Therefore, the contrast between the boundaries and the interior of the sample should become more pronounced if sufficient time is allowed for diffusion

to occur during the application of the pulse sequence.

The pulse sequence used to demonstrate this form of edge-enhanced imaging is shown in Fig. 7.5(c). 1-D edge-enhanced images taken with this sequence are shown in Fig. 7.11, taken with τ_1 = 2, 4, 6, 8, 10 ms. For τ_1 = 2 ms, the diffusion is not significant enough to change the ratio of the signals from the edges and the center of the sample, and thus in such cases an essentially static image is obtained. When $\tau_1 \geq 4$ ms, however, the effect of diffusion is easily discerned, as the signal corresponding to the sample boundaries is brighter than the signal corresponding to the middle of the sample. At $\tau_1 > 6$ ms the signals originating from the center of the sample are almost negligible, and only the xenon near the edges of the sample contributes to the images. This same effect has been observed in the experiments of Callaghan *et al.* [194] using ^{1}H MRI.

While the simple imaging sequence shown in Fig. 7.5(c) can generate enormous contrast between the boundaries and the interior of a sample, this feat is accomplished at the expense of the signal intensity. For example, the signal-to-noise ratio for the $\tau_1 = 8$ ms image is approximately two orders of magnitude less than that for the $\tau_1 =$ 2 ms image. Even with the use of laser-polarized xenon, some signal averaging was necessary in order to obtain the $\tau_1 = 8$ and 10 ms images.

While it is intuitively appealing to describe the behavior observed in the images of Fig. 7.11 in terms of a position-dependent diffusion constant, such a model does not correctly describe the functional form of the signal decay for the edges at long times.

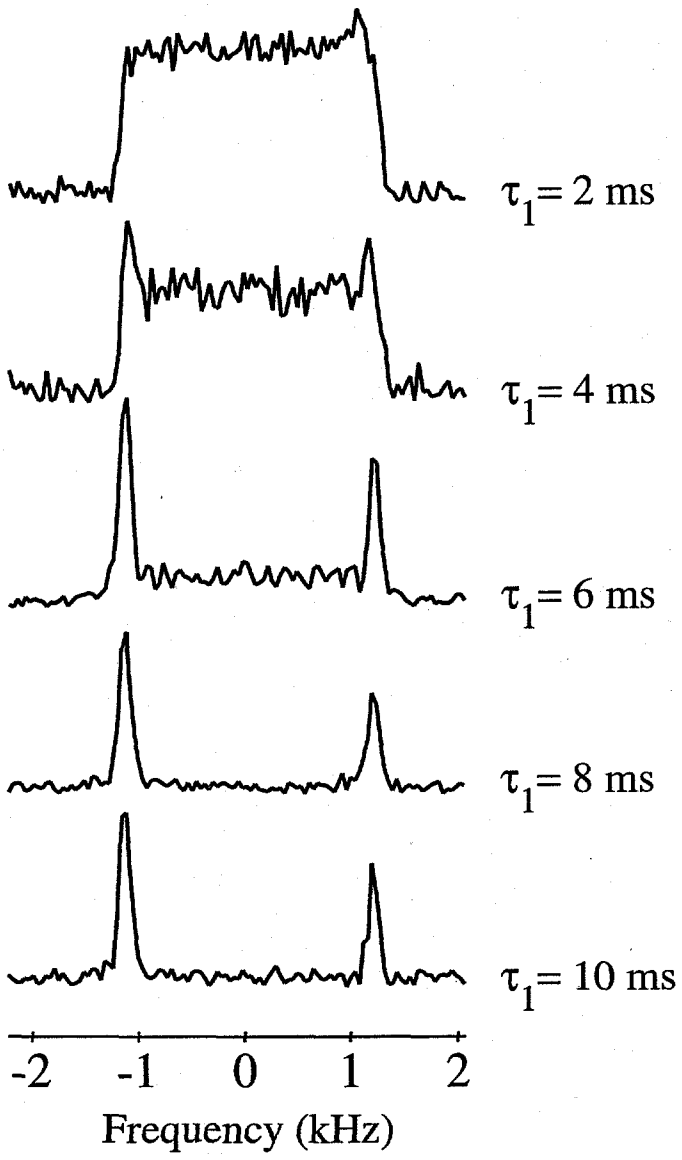

Figure 7.11: Edge-enhanced imaging. Images were obtained using the pulse sequence shown in Fig. 7.5, with τ_1 values of 2, 4, 6, 8, and 10 ms and a gradient of 3.3 G/cm along $\vec{x}$. The images taken with $\tau_1 = 8$ and 10 ms were acquired with 90° excitation pulses and 32 and 64 averages, respectively; the recycle delay was long enough to allow the diffusion in the sample to replenish the polarized xenon in the space being imaged. Restricted diffusion at the edges of the sample reduces the decay of signal suffered in the middle of the sample. The asymmetry in peak heights from the sample edges is most likely due to inhomogeneity in the static magnetic field and contributions from imperfections in the sample's geometry.

De Swiet [197] has shown that the decay of the signal S at the peaks near the edges changes from a τ_1^3 dependence ($\log(S) \propto -\tau_1^3$), to one that is linearly dependent on time ($\log(S) \propto -\tau_1$). Naturally, this change in the time dependence results in greatly extended signals at long times, and hence produces sharp peaks in the images near the sample's edges following Fourier transformation. This exponential time dependence also explains the consistency of the linewidth of the edge peaks over time in the images for τ =6, 8, 10 ms.

7.5 Imaging with Continuous Xenon Flow

Recent work has been directed toward the combination of laser-polarized ^{129}Xe gas MRI with continuous xenon flow [206]. The continuous-flow system described in Chapter 2 was modified so that xenon could be continuously recirculated through a sample within a micro-imaging gradient set. The steady-state nuclear spin polarization of laser-polarized ^{129}Xe can thus be applied without time limitations for MRI of small void spaces in porous materials or studies of flow through miniature constrictions. By using a continuous-flow system, gas-phase NMR signals of laser-polarized xenon can be observed using conventional multi-dimensional imaging pulse sequences and signal averaging. As shown in Fig. 6.3, the steady-state non-equilibrium ^{129}Xe nuclear spin polarization attainable in this system recovers the conditions for each acquisition in a short time (0.2-4 s), depending on the sample density and differential pressure applied. Therefore, MRI experiments are not limited in time by longitudi-

nal relaxation, and multi-dimensional imaging pulse sequences requiring a steadily renewed nuclear spin polarization can be applied.

Figure 7.12 shows a two-dimensional cross-sectional ^{129}Xe MR image of the void spaces of nine capillary tubes (with one tube possessing closed ends), which was acquired using a conventional 2-D "spin-warp" imaging pulse sequence (for review, see Ref. [10]) taken under conditions of continuous flow of laser-polarized xenon (flowing perpendicular to the plane of the image) [206]. The glass walls of the capillaries are visible as dark circles in the image. The capillary that was flame-sealed on both ends contains no xenon and remains dark, producing the signal void in the upper center of the image. The above experiment demonstrates the feasibility of imaging under continuous flow of laser-polarized ^{129}Xe, and suggests that this approach could prove especially useful for imaging studies of porous materials with short longitudinal relaxation times for ^{129}Xe.

The continuous flow of laser-polarized xenon can be further exploited by employing pulse sequences that have velocity-encoding capabilities, permitting various novel experiments designed to study flow in porous materials. For example, the PGSE experiment used in the previous section for measuring displacement distributions may be implemented for simultaneous measurement of a displacement distribution in one dimension and spin density in another orthogonal dimension. In such experiments, a modified PGSE pulse sequence can employ a slice selection gradient chosen in the same direction as the pulsed gradients that encode the flow [207]. The displacement

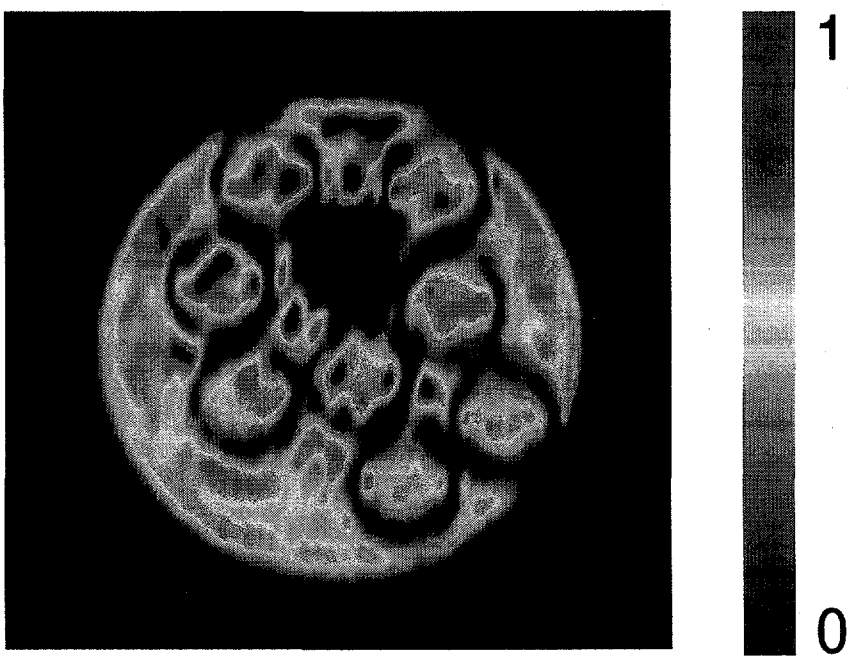

Figure 7.12: 2-D cross-sectional Fourier image of laser-polarized xenon gas flowing through a sample comprised of a glass tube (7 mm i.d.) containing one sealed and eight open-ended capillaries (1.3 mm o.d.) aligned parallel to the gas-flow direction ($\vec{x}$), each having a wall thickness of $\sim$200 μm [206]. The image was processed with zero-filling and fitting with a cubic spline routine. The data was acquired as a 256 $\times$ 128 matrix, using 128 phase-encoding steps and a read gradient of 60 G/cm. Figure courtesy of Lana Kaiser.

of the selected gas spins in the flow direction during the fixed time Δ gives rise to a characteristic echo damping [10]. A second gradient (G_y) is applied to generate the spatial resolution perpendicular to the flow direction. A 2-D data set $S(k,q)$ is acquired as a function of $k = (2\pi)^{-1}\gamma G_y t$ and $q = (2\pi)^{-1}\gamma G_x \delta$. This type of combined k-space and q-space imaging is also known as dynamic NMR microscopy [10]. Fourier transformation with respect to q results in a profile of the displacement probability, containing information about velocity and diffusion. At each point perpendicular to the direction of flow, the mean velocity is given by the position of the signal maximum. The width of the typically Gaussian-shaped line is a function of the apparent diffusion coefficient.

Figure 7.13(a) shows the dynamic displacement profile of laser-polarized ^{129}Xe flowing through a glass tube (inner diameter=6.3 mm) with a 3:1 constriction [206]. The maximum velocity is observed in the center region of the tube ($y = 0$). The lower signal intensity in this region compared to that of other regions originates from the higher velocity in the center region ($\sim$7 cm/s), and is not related to differences in longitudinal relaxation. It is interesting to note the two negative velocity components close to the walls of the tube that arise from xenon back-flow from the constriction. This behavior originates from secondary flow vortices typical for laminar flow.

A combination of four factors, the Reynolds number (Re), determines whether

the flow of a fluid through a tube is laminar or turbulent [208]:

$$Re = \frac{d \cdot v_{ave} \cdot \varrho}{\eta} \tag{7.6}$$

where v_{ave} is the average forward flow velocity, d is the diameter of the tube, ϱ is the density, and η is the viscosity; turbulent flow occurs when $Re \geq 2000$. For the laser-polarized xenon gas mixture in the glass tube, the Reynolds number did not exceed 30, and thus remained well within the regime of laminar flow. The value used for the viscosity in this calculation was determined according to the equation given in Ref. [209] for multi-component gas mixtures. The difference in the speed of the two components with negative velocity reveals that the constriction hole is not located in the center of the tube, most likely a consequence of the glass-blowing process. The location of the back-flow was upstream of the constriction, verified by velocity profiles taken perpendicular to the flow direction.

Figure 7.13(b) shows a dynamic displacement profile of ^{129}Xe flowing through slices of two different polyurethane (PU) foams contained in a 3.5 mm (i.d.) glass tube [206]. The upper PU foam possessed a lower density, and had a larger average pore size; the mean pore radius was determined by optical microscopy to be $\sim$200 μm). In comparison, the medium-density PU foam at the bottom had a smaller pore size, with a mean pore radius of $\sim$100 μm. The mean gas velocity of 5.5 cm/s in the medium density foam is lower than the 8.1 cm/s value observed for the low-density

foam; the friction is naturally greater in the higher-density material [208].

A variety of new applications of gas flow MRI are immediately suggested from the above examples. For example, this new technique may have applications in fluid mechanics, as it may aid in the study of flow under various conditions (e.g., under laminar *vs.* turbulent flow regimes). Other possible applications of this non-destructive technique may include the study of restricted diffusion and flow of gases in porous materials and the measurement of pore size distributions in such systems.

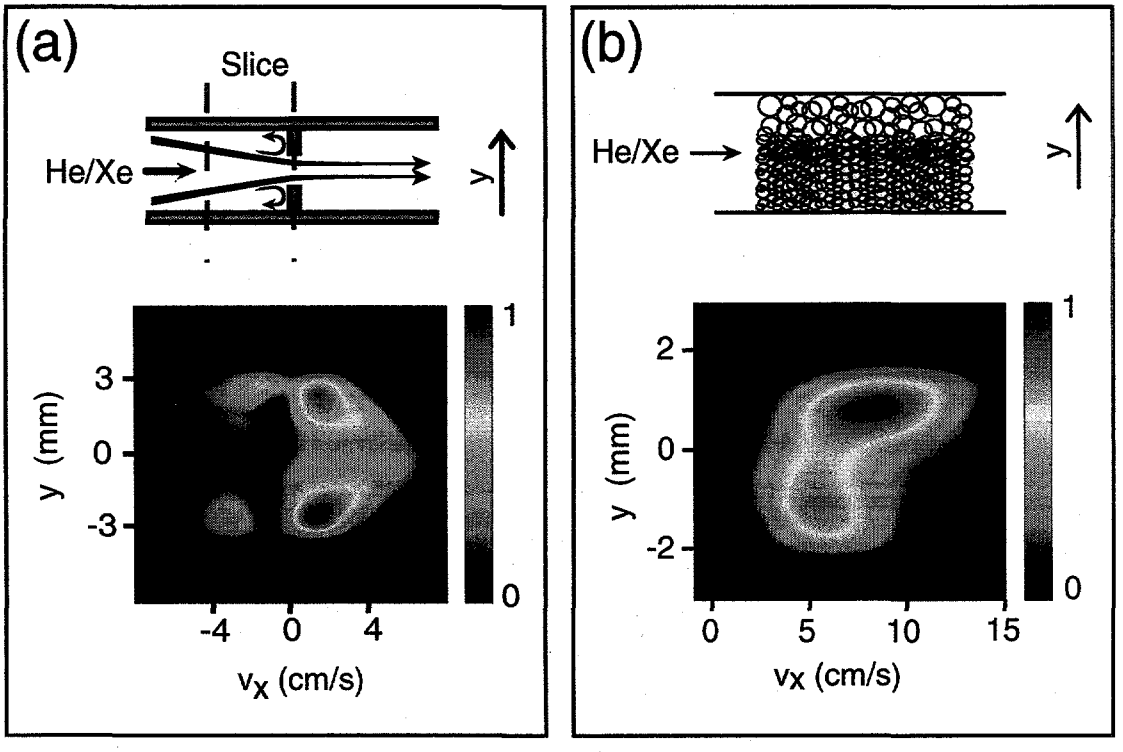

Figure 7.13: Dynamic displacement profiles of laser-polarized xenon flowing through porous materials [206]. (a) Dynamic displacement profile of laser-polarized xenon flowing through a 3:1 constriction. (b) Dynamic displacement profile of laser-polarized xenon flowing through slices of two different polyurethane foams with mean pore sizes of ~200 μm (top) and ~100 μm (bottom). Note the greater average velocity, as well as the greater spread in velocities, in the top portion of the image. The probability displacement profile is consistent with the pore sizes of the different materials. Figures courtesy of Lana Kaiser.

Chapter 8

Biomedical Applications of Laser-Polarized Noble Gases

8.1 Introduction

Laser-polarized noble gases hold enormous potential for enhancing sensitivity and contrast for a variety of *in vivo* NMR and MRI experiments. In addition to void-space imaging in the body, laser-polarized noble gases could be powerful MR probes of tissues and blood flow. Not surprisingly, research involving the development of biomedical applications of laser-polarized noble gases has been particularly vigorous. Readers of this thesis can find reviews of this field in Refs. [63, 17, 74]; Ref. [63] also provides a historical perspective of the field's development.

In this chapter, the general topic of biomedical applications of laser-polarized

noble gases is introduced. The first section is dedicated towards what has become the most noteworthy application of laser-polarized noble gases: the imaging of lung space. The remainder of the chapter is mainly concerned with the application of laser-polarized gases specifically for tissue studies, with special attention paid to the issues of delivery, partitioning, and spin-relaxation of noble gases *in vivo*, including the investigation of noble gas injection methods.

8.2 Void Space Imaging

Void spaces in the body are normally difficult to image with conventional diagnostic methods (e.g. X-ray tomography and ^{1}H MRI) because of the low concentration of signal sources in the gas phase. However, the characteristics that make laser-polarized noble gases advantageous for imaging porous materials (e.g., strong NMR signal and negligible chemical reactivity) also make them extremely promising for imaging void spaces *in vivo*, especially lung space [63, 74]. Such applications are particularly important in light of the morbidity and mortality associated with many pulmonary diseases, including emphysema, lung cancer, and chronic obstructive pulmonary disease (COPD). COPD is currently the fourth leading cause of death in the United States.

The potential held by polarized gases for novel biomedical studies was first demonstrated in 1994, when laser-polarized xenon was used to image the void spaces in excised mouse lungs [186]. Three such ^{129}Xe lung space images are shown in Figs.

8.1(a-c), along with a corresponding ^{1}H image (Fig. 8.1(d)). The polarization enhancement afforded by optical pumping permitted multiple images to be acquired with signal-to-noise and spatial resolution (on the order of 0.14-0.28 mm^3) unrivaled by previous methods. Moreover, the region producing large signals near the center of the ^{1}H image (Fig. 8.1(d)), originating from the mouse's heart, corresponds to regions void of signal in Figs. 8.1(b,c), demonstrating the potential for obtaining excellent contrast between gas space and tissue in such MRI studies. The ^{129}Xe T_1 was measured to be ~30 s for the gas mixture in the mouse lungs; it was projected that the presence of oxygen necessary for a normally breathing animal would reduce the ^{129}Xe T_1 to ~15 s, still long enough to obtain several bright images.

Experiments involving excised animal lungs [186, 187] were soon followed by considerable work involving the imaging of polarized xenon and helium in the lung spaces of living animals (see for example, Refs. [211, 212, 213, 214, 215]). Indeed, progress in this field has been rapid, as multiple studies involving human subjects have now been performed [216, 218, 219, 220, 221]. Delivery of the laser-polarized gas can be achieved easily and in a relatively non-invasive manner via respiration. Such studies could be performed by imaging under continuous-breathing conditions, by gating respiration to the MRI spectrometer to synchronize the breathing cycle with acquisition, or by simply having the patient hold his or her breath during acquisition immediately following inhalation of the laser-polarized gas. Inhalation of laser-polarized xenon has also permitted imaging of the oral cavity [222].

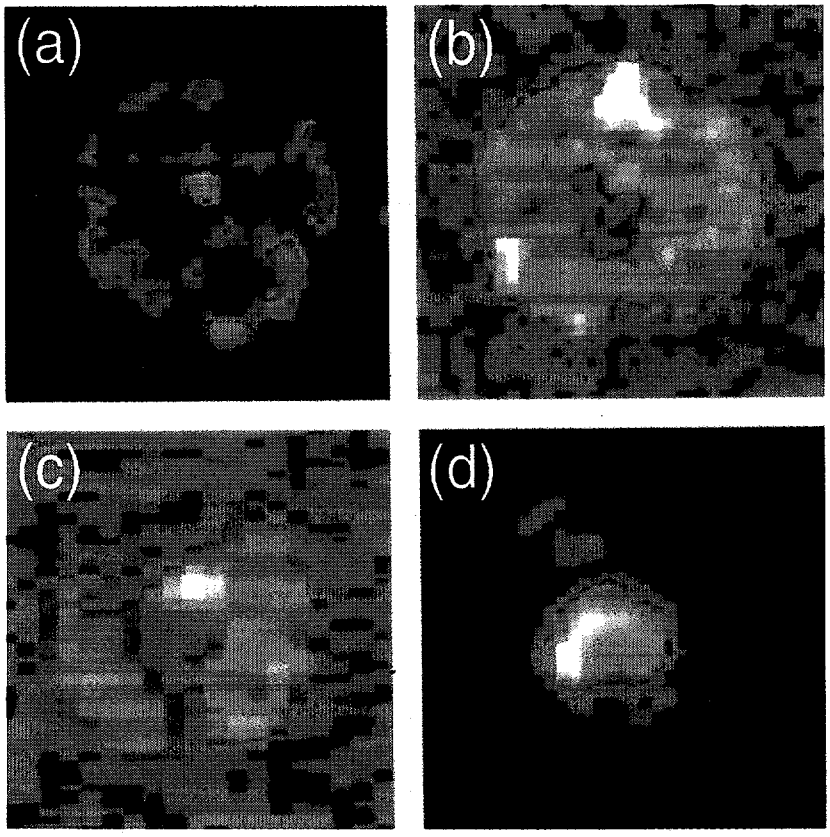

Figure 8.1: MR images taken from the excised lungs and heart of a mouse following delivery of laser-polarized xenon gas [186]. (a-c) ^{129}Xe images respectively taken ~1 s (a), ~2 s (b), and ~7 s (c) following gas delivery via the trachea. (d) corresponding ^{1}H image. Note that the bright region (the heart) corresponds to the central signal void in (c). Figures courtesy of Mitchell Albert.

Figure 8.2 contains a ^{129}Xe MR image taken from the lungs of a healthy human volunteer following respiration of laser-polarized xenon [220]. As with the case of the excised mouse lung images shown in Fig. 8.1, the correlation between the signal voids in the gray-scale ^{1}H MR image (Fig. 8.2(a)) and the bright regions in the corresponding false-color ^{129}Xe MR image (Fig. 8.2(c)) is excellent (shown in the image overlay in Fig. 8.2(b)).

Recent experiments involving both guinea pigs and humans have been performed with the goal of imaging lung space with the highest possible resolution [221]. Previously, most polarized-gas lung images were performed with conventional pulse sequences (e.g. FLASH and GRASS) under held-breath conditions. The authors point out that such experiments permitted observation of the larger airways in the lungs, as well as gas-exchange areas and outlines of the vasculature of the lungs and nearby tissue. However, such methods do not normally permit the smaller lung airways to be resolved; these airways are obstructed from view at full inspiration by the bright signal from the lung periphery. By gating the respiration of the subject, the authors could carefully control the timing of the application of the imaging pulse sequence with respect to the breathing cycle, permitting images to be obtained at different points in the respiration process. This ability, combined with the use of a radial acquisition pulse sequence [223], permitted fourth-order branchings to be observed in the human lung images, and fifth-order branchings to be observed in the guinea pig lung images. Three of a series of high-resolution ^{3}He MR images taken from

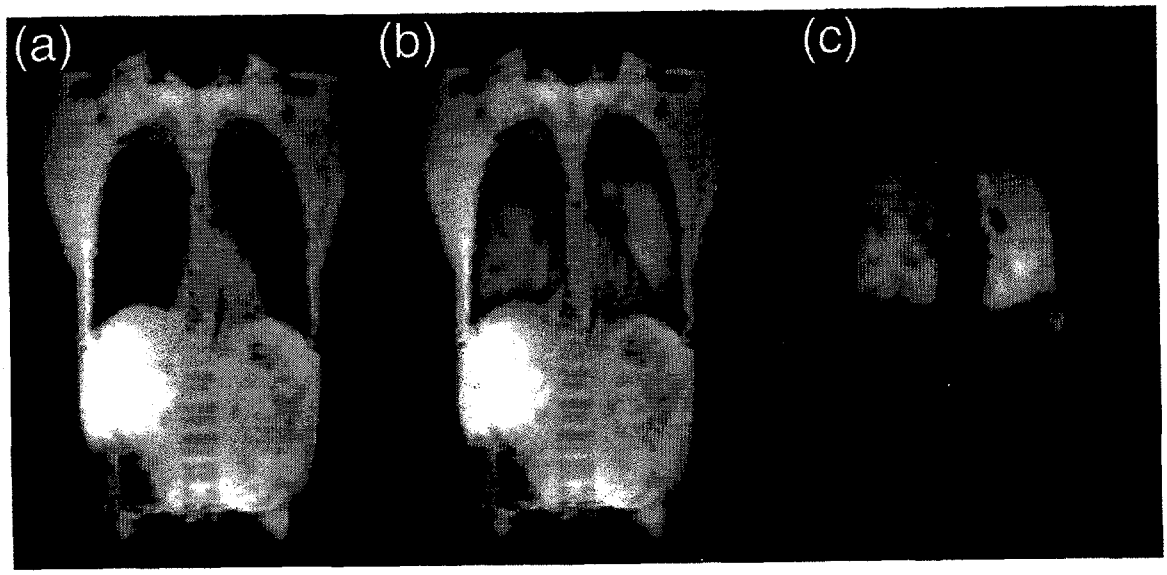

Figure 8.2: *In vivo* MRI of human lung space following respiration of a gas mixture containing laser-polarized xenon [220]. (a) Grey-scale ^{1}H abdominal image. (b) Composite ^{1}H / ^{129}Xe abdominal image comprised of the ^{1}H image in (a) and the false-color ^{129}Xe gas-space image shown in (c). Figures courtesy of James Brookeman.

the lungs of a guinea pig are shown in Fig. 8.3; such images possess an in-plane resolution approaching $100 \times 100\ \mu m^2$. This resolution is particularly impressive in light of the rapid diffusion of gaseous helium. The radial acquisition technique was chosen partially because it minimizes diffusion effects in images; however, the high resolution obtained may also partially result from boundary-restricted diffusion in the small passage ways present in the lungs (refer to Chapter 7 for a discussion of MRI under conditions of boundary-restricted diffusion).

Finally, the results of other recent experiments suggest that the goal of *clinically* using polarized noble gas imaging for studying human lungs may soon be realized. It has been shown that lung images obtained from healthy human volunteers breathing mixtures containing laser-polarized ^{3}He can differ drastically from those of patients suffering from COPD, emphysema, and lung cancer [219]. Such images can exhibit inhomogeneities corresponding to insufficient ventilation at different positions within the diseased lungs. As of the time that this thesis was written, lung imaging with laser-polarized noble gases had advanced to the point of human clinical trials to aid in the diagnosis and treatment of various pulmonary diseases. For example, the identification of diseased portions of lung tissue is crucial to treatment for patients suffering from COPD. The experiments shown in Ref. [219] suggest that imaging laser-polarized gases in the lungs of COPD patients could be instrumental in helping doctors differentiate healthy and pathological tissue, thereby aiding in the selection of lung regions as candidates for surgical removal.

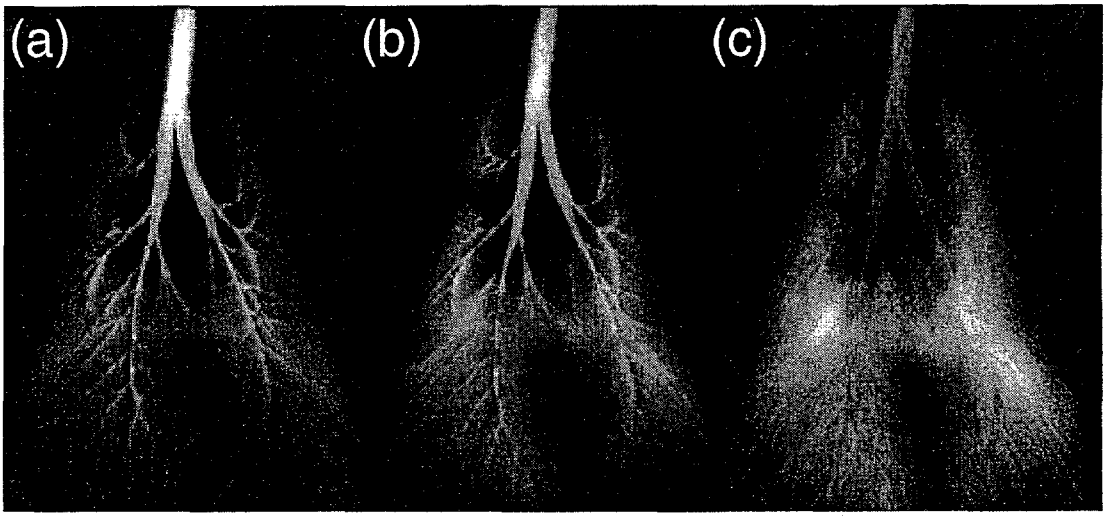

Figure 8.3: Three of a series of high-resolution, non-slice-selective ^{3}He MR images taken from the lung space of a live guinea pig acquired during respiration of laser-polarized helium [221]. The timing of the each image acquisition was varied with respect to the gated respiration of the polarized ^{3}He; the images shown were taken following delays of (a) $\approx$0 ms, (b) 200 ms, and (c) 400 ms. Images were obtained with projection-reconstruction methods, involving the mapping of radial trajectories of k-space. Figures courtesy of Mark Chawla and G. Allan Johnson.

8.3 Enhanced NMR and MRI of Tissues

While the imaging of lung spaces with polarized gases is extremely promising, it is hoped that *in vivo* applications can be expanded to permit novel studies elsewhere in the body. Unlike the case with lung space imaging, however, there is a manifestly high concentration of excellent signal sources in tissues for conventional NMR/MRI experiments ([^{1}H] ~80 M), making the need for using dissolved polarized gases less obvious. However, the signal from polarized gases in tissues need not be greater than the proton signal for a variety of proposed applications to be feasible and useful. The unique characteristics of laser-polarized xenon suggest numerous experiments involving localized ^{129}Xe NMR spectroscopy, chemical shift imaging, functional MRI, exchange spectroscopy, and blood flow/perfusion studies.

8.3.1 First *In Vitro* Studies

The sensitivity of xenon's NMR parameters to its local environment and its relatively high solubility in tissues suggest that laser-polarized xenon may serve as a useful magnetic resonance probe of living tissues. The prospects for such experiments were first explored with a ^{129}Xe NMR study of thermally-polarized xenon dissolved in human blood [224]. Two peaks were resolved in the ^{129}Xe spectra, assigned to xenon in red blood cells (RBCs) and xenon in plasma. These results demonstrated the ability to simultaneously observe xenon residing in different tissue compartments on the cellular level, and suggested a new means of contrast that could be exploited via

chemical-shift imaging (CSI) experiments and *in vivo* localized spectroscopy.

In later work it was shown that laser-polarized xenon could be efficiently delivered to blood samples *in vitro* by pre-dissolving laser-polarized xenon in saline, and subsequently injecting the xenon-saturated solution into open-air test tubes containing fresh human blood [225]; this injection method is described in detail later in this Chapter. The blood samples used for xenon injection were prepared by allowing the RBCs to settle to the bottom of the tube, and then removing a portion of the plasma. Fig. 8.4 contains two ^{129}Xe NMR blood spectra, one taken by signal averaging acquisitions of thermally polarized xenon over 1.5 hr (a), while the second spectrum (b) was taken with a single scan following the injection of laser-polarized xenon. In agreement with the previous studies employing thermally-polarized xenon, two peaks were observed, corresponding to xenon in slow exchange between RBCs (at $\approx$216 ppm) and their plasma/saline surroundings (at $\approx$192 ppm). However, this exchange in much faster than the relaxation rate of ^{129}Xe, characterized by a common ^{129}Xe T_1 for both signals. The enormous signal enhancement shown in Fig. 8.4(b) permitted the ^{129}Xe T_1 to be easily determined from the exponential signal decay observed from multiple acquisitions with small tipping-angle pulses; the ^{129}Xe T_1 was measured to be $\approx$5 s.

Both of these studies used blood with relatively low (ambient) oxygen concentrations. However, higher blood oxygen concentrations have been correlated with longer ^{129}Xe T_1 values [63]. This sensitivity of the ^{129}Xe T_1 to the oxygenation level of

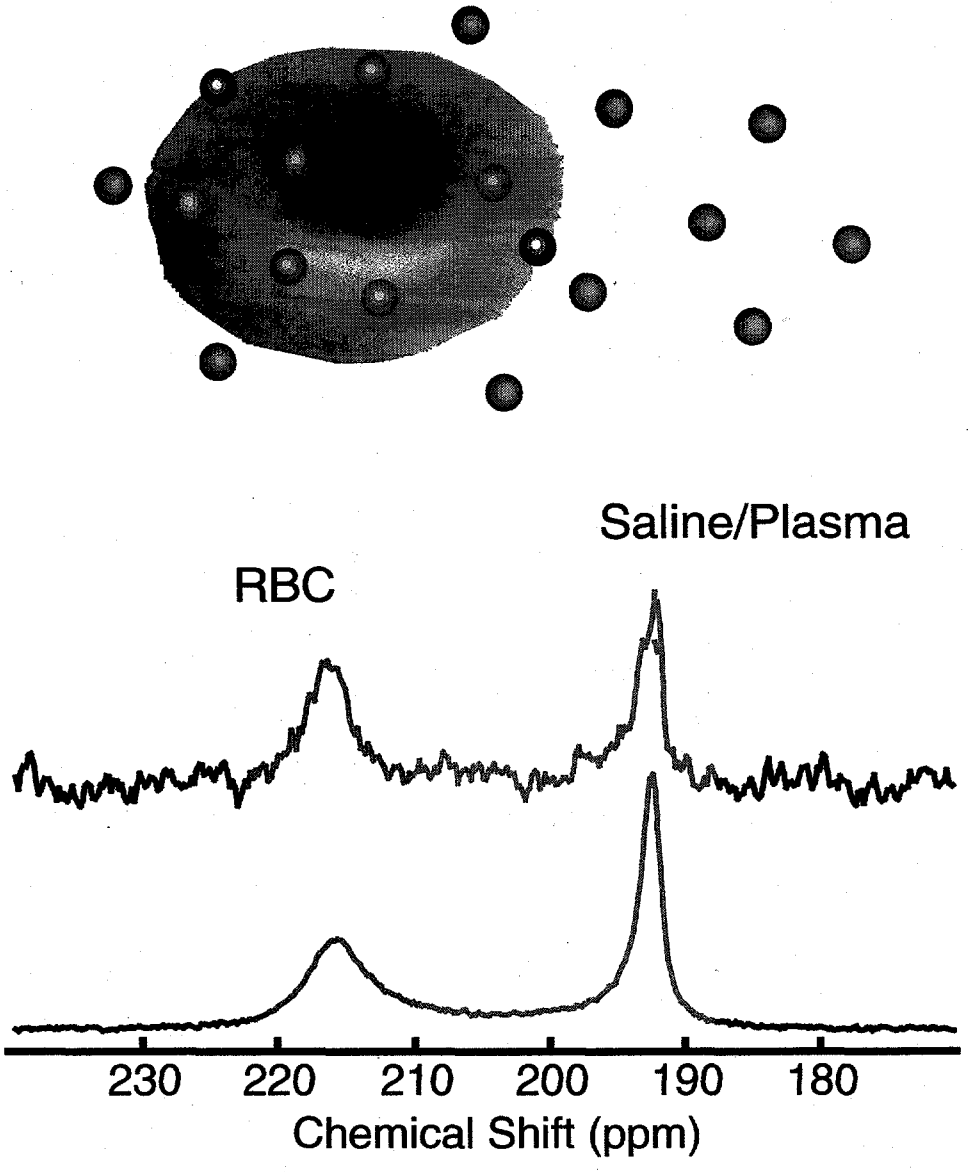

Figure 8.4: ^{129}Xe NMR spectra in fresh human blood, with (b) and without (a) laser-polarization. Spectrum (a) was obtained using thermally-polarized xenon and accumulating 520 scans over 1.5 hours (the xenon over-pressure was about 1 atm). Spectrum (b) was acquired after injection of 1 cc of laser-polarized xenon/saline solution into 1 cc of a concentrated RBC sample [225]. The ^{129}Xe NMR signal at 216 ppm originates from xenon in the RBC, while the signal at 192 ppm originates from xenon in the saline/plasma mixture [224, 225]. The signal enhancement between the two spectra is over 2000.

hemoglobin is believed to originate from the binding of xenon to hydrophobic pockets in hemoglobin [126]; the binding of oxygen reduces the paramagnetic spin of the heme iron. The observed increase in xenon T_1 with increasing blood oxygenation was recently confirmed by Bifone and co-workers, who carefully controlled the experimental conditions (e.g. temperature, magnetic field, and oxygenation level) of *in vitro* samples of laser-polarized xenon in huamn blood. At body temperature (37 °C) and 1.5 T, ^{129}Xe T_1 values were measured to be 6.4±0.5 s and 4.0±0.4 s for xenon in blood samples whose oxygenation levels matched those of arterial and venous blood, respectively [132]. It should be noted, however, that in studies of polarized xenon in blood foam [226], the opposite trend in T_1 was observed (i.e., the ^{129}Xe T_1 was *longer* in deoxygenated blood foam). While the origin of this disparity is uncertain, the authors of the blood foam work point out that extrapolation of their observations to normal physiological conditions gives a ^{129}Xe T_1 of ∼5 s.

The signal enhancement afforded by optical pumping, in addition to the slow xenon exchange and efficient xenon delivery, permitted the direct observation of xenon penetrating the red blood cells. However, it was important to first characterize the mixing process occuring immediately following the xenon/saline injection. The main portion of Fig. 8.5 contains the time-dependent integrated intensities of the ^{129}Xe signals from xenon in RBCs and plasma, normalized by the total signal (the inset shows the unnormalized data). The initial rise of the normalized RBC signal, as well as the initial decay of the normalized saline/plasma signal, originate from the

transfer of xenon from the saline/plasma mixture to the RBCs during mixing. The time dependence of both normalized signals can be described by a simple exponential function of the form

$$S(t) = A + B\exp(-t/T), \tag{8.1}$$

where A and B are constants. The time constant T for the exponential function was determined to be ~200 ms, which reflects the time required for the concentrations to equilibrate following injection. Thus, by delaying acquisition by a second or more following injection (a delay of 3 s was used in the following study), the intrinsic exchange of xenon between RBCs and plasma could be easily studied.

By using a frequency-selective 180° rf pulse, the xenon saline/plasma resonance was inverted, and the subsequent recovery of the ^{129}Xe NMR signals was followed with low-tipping-angle rf observation pulses (Fig. 8.6). The reduction of the RBC signal, S_{RBC}, and the concomitant rise of the saline/plasma signal, S_{pl}, originate from the intrinsic xenon exchange between the RBCs and the plasma/saline environment. By using a two-site xenon-exchange model, the observed behavior can be described with the following relations:

$$\frac{dS_{RBC}}{dt} = -\frac{S_{RBC}}{\tau_{RBC}} + \frac{S_{pl}}{\tau_{pl}}, \tag{8.2}$$

$$\frac{dS_{pl}}{dt} = +\frac{S_{RBC}}{\tau_{RBC}} - \frac{S_{pl}}{\tau_{pl}}, \tag{8.3}$$

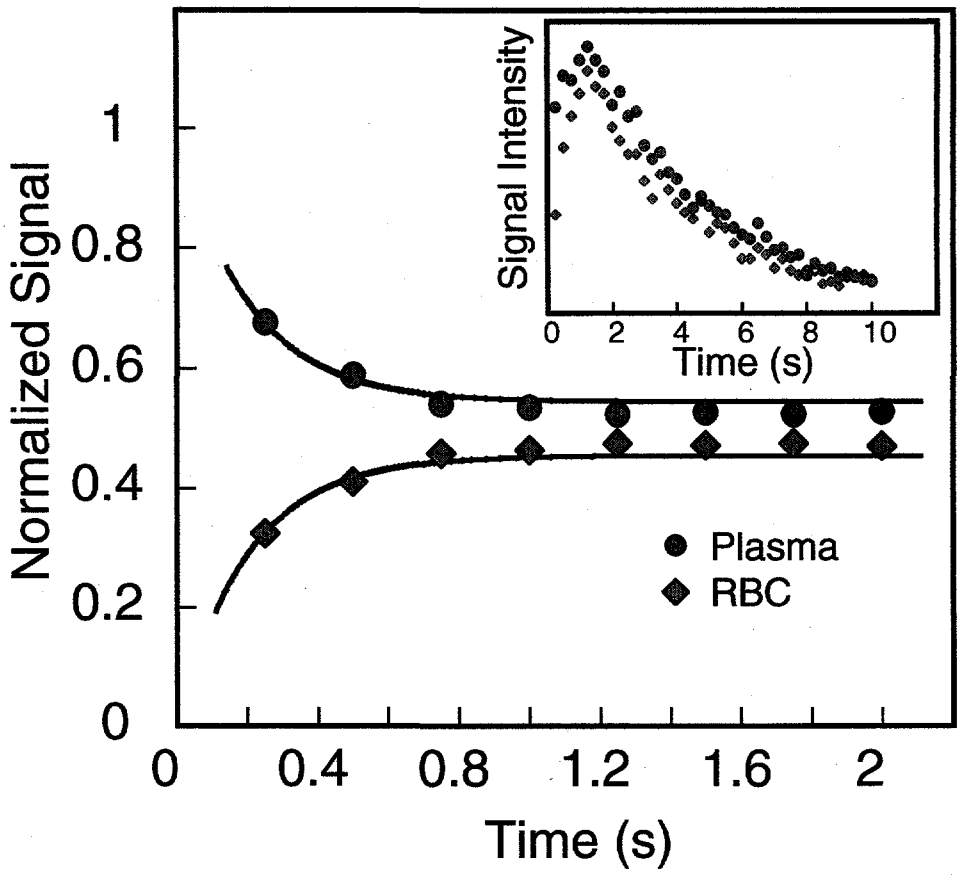

Figure 8.5: Time dependence of the ^{129}Xe NMR signals immediately following the injection of a laser-polarized xenon/saline solution into a test-tube of fresh human blood. Main figure: time dependence of the RBC signal (red) and plasma signal (blue), normalized by the total signal in both compartments. The initial increase of the normalized RBC signal and the reduction of the normalized saline/plasma signal describes the dynamical process of xenon entering the RBCs from the saline/plasma mixture during mixing. Exponential fits (solid lines) described by Eq. 8.1 give a time constant of ~200 ms for the mixing process. Inset: time dependence of the integrated xenon signals from both compartments. By following the signal decay after the first two seconds, the T_1 of the both components was determined to be 5.0 s. The initial rise in the total xenon signal intensity during the first second was likely caused by the blood mixture descending from the walls of the sample tube into the region of the detection coil following the vigorous injection.

where τ_{RBC} and τ_{pl} respectively govern the residence of xenon in the RBCs and plasma. Equations 8.2,8.3 may be solved, yielding:

$$S_{RBC} = (S^0_{RBC} + S^0_{pl})\frac{\tau_{RBC}}{\tau_{RBC}+\tau_{pl}} + S_0 \exp\left(-\frac{t}{\tau}\right), \tag{8.4}$$

$$S_{pl} = (S^0_{RBC} + S^0_{pl})\frac{\tau_{pl}}{\tau_{RBC}+\tau_{pl}} - S_0 \exp\left(-\frac{t}{\tau}\right), \tag{8.5}$$

with

$$S_0 = S^0_{RBC}\frac{\tau_{pl}}{\tau_{RBC}+\tau_{pl}} - S^0_{pl}\frac{\tau_{RBC}}{\tau_{RBC}+\tau_{pl}}, \tag{8.6}$$

where S^0_{RBC} and S^0_{pl} describe the signal intensities for the RBC and the plasma resonances immediately following inversion, and

$$\frac{1}{\tau} = \frac{1}{\tau_{RBC}} + \frac{1}{\tau_{pl}}. \tag{8.7}$$

Assuming $S_{RBC} + S_{pl}$ is constant over the time of the experiment (a valid assumption in light of the relatively slow rate of ^{129}Xe spin-lattice relaxation), the observed exponential decay in $S_{RBC} - S_{pl}$ (shown in Fig. 8.7) gives $\tau = 12.0$ ms (taking into account the magnetization lost from the application of small tipping-angle pulses to observe the signal). Knowing that the pre-inversion value of S_{pl}/S_{RBC} constrains the value of τ_{pl}/τ_{RBC}, it can be shown that $\tau_{RBC} = 20.4$ ms, which reflects the mean residence time of xenon in the RBCs.

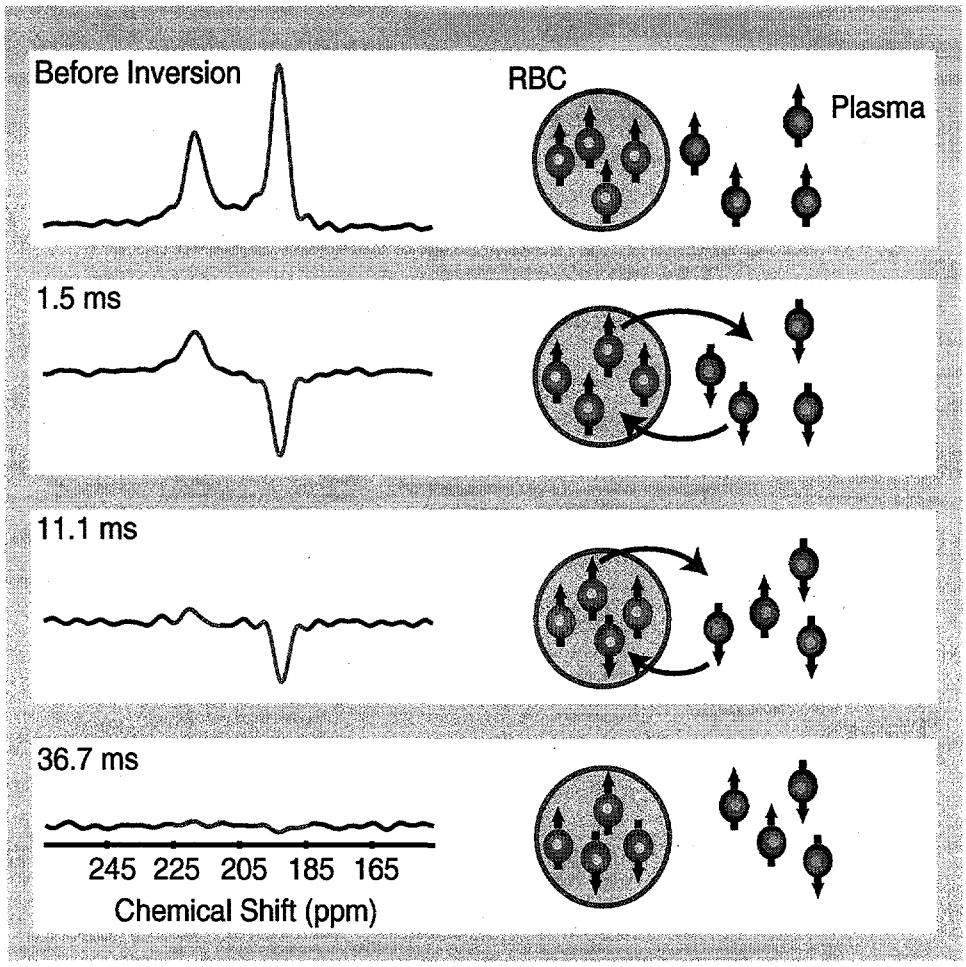

Figure 8.6: Direct observation of xenon penetrating red blood cells. Following selective inversion of the Xe/plasma resonance, the time dependence of the ^{129}Xe spectra was monitored via the application of multiple low tipping-angle rf pulses, as shown in the selected spectra. The recovery of the two xenon resonances to a new equilibrium reflects the intrinsic exchange of xenon between the red blood cells and the plasma [225]. The inversion pulse was an amplitude-modulated (Gaussian) pulse of 1 ms duration centered at the saline/plasma signal; this pulse also reduced the absolute intensity of both signals by about 50%. A 1 ms gradient pulse was applied immediately following the inversion in order to dephase any remaining transverse magnetization.

Given a diffusion constant D for xenon of $\sim 2 \times 10^{-5}$ cm^2 (the approximate value measured in water at room temperature [78, 227], one can calculate an average distance $d = \sqrt{6Dt}$ =15 μm that would be traveled via diffusive motion. This value is significantly larger than the dimensions of a red blood cell (a disk $\approx$7 μm across and roughly 1 μm thick). Thus, the motion of the xenon during exchange is likely restricted or regulated by some physical or biophysical process, possibly the preferential interaction of xenon with the amphiphilic regions of lipid membranes [135].

8.3.2 Enhanced *In Vivo* NMR and MRI via Xenon Respiration

The respiration of a breathing mixture containing laser-polarized xenon by rats permitted enhanced ^{129}Xe NMR spectra to be obtained *in vivo* [212], shown in Fig. 8.8. The spectrum in Fig. 8.8(a) shows three separate tissue resonances downfield from the gas-phase signal originating from xenon in the rat's lungs (at 0 ppm); these tissue resonances were tentatively assigned to xenon residing in red blood cells (at $\approx$213 ppm), lung tissue (at $\approx$199 ppm), and blood plasma/adipose tissue (at $\approx$ 191 ppm). Clearly, the xenon exchange is slow enough to permit the four distinct resonances from the different compartments to be observed. Moreover, by rapidly acquiring ^{129}Xe NMR signals following the rat's breathing cycle, the dynamics of the different xenon resonances could be observed (Fig. 8.8(b)). The observed time dependence reflects the "wash-in"/"wash-out" dynamics of the xenon as it passes

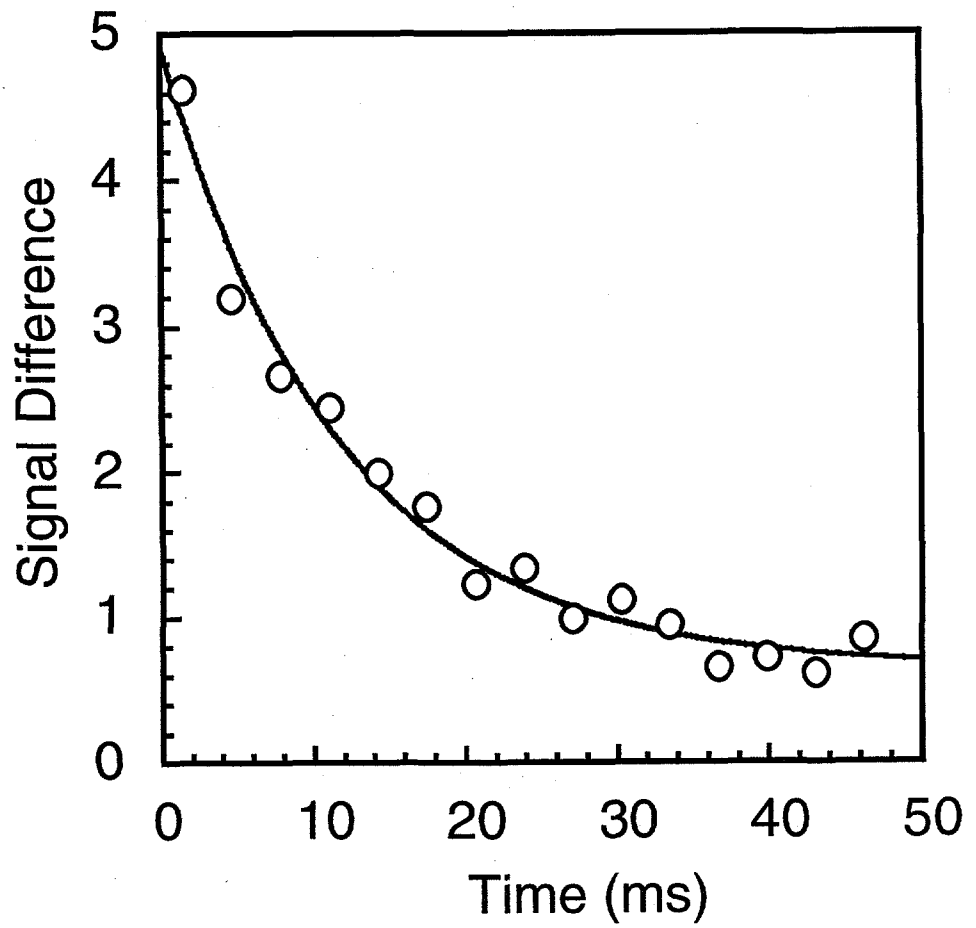

Figure 8.7: Time dependence of the intrinsic exchange of laser-polarized xenon between the two blood compartments following selective inversion of the ^{129}Xe/plasma signal. To increase the dynamic range of the experiment, the difference between the RBC and plasma signals is plotted. The time constant for the fitted exponential decay (solid line) was determined to be $\approx$12 ms.

through the lungs to different tissues in the body, modulated by the spin-lattice relaxation of the laser-polarized xenon and the polarization destruction originating from rf observation pulses. Intrinsic ^{129}Xe T_1 values are difficult to measure in such circumstances because the concentration of laser-polarized xenon is changing with time. Instead, the "apparent" decay constants, T_1^*, of the ^{129}Xe NMR signals were obtained directly from the spectra in Fig. 8.8(b)): 12 s for the xenon/RBC resonance, 26 s for the xenon/lung tissue resonance, and 50 s for the xenon/plasma/adipose tissue resonance. These results demonstrated the feasibility of using laser-polarized xenon to characterize local blood flow in living tissues.

Arguably, the organ that has attracted the greatest interest for study via MRI is the brain. It has been proposed that differences in the relaxation parameters, chemical shift, and solubility of xenon in various tissues under different physiological conditions may provide considerable contrast enhancement that could exploited for several purposes, including functional MRI of the brain [63]. A number of approaches have been suggested to exploit the characteristics of laser-polarized xenon to probe brain function [63]. For example, one potential method would combine two effects expected to increase local ^{129}Xe signal in a manner that would correlate with increased brain activity: 1) a rise in regional blood flow that will result in a transient increase in local polarized xenon concentration, and 2) the longer spin-lattice relaxation time of xenon in oxygenated versus deoxygenated blood (discussed previously). This method would therefore be somewhat similar to BOLD (Blood Oxygenation Level Depen-

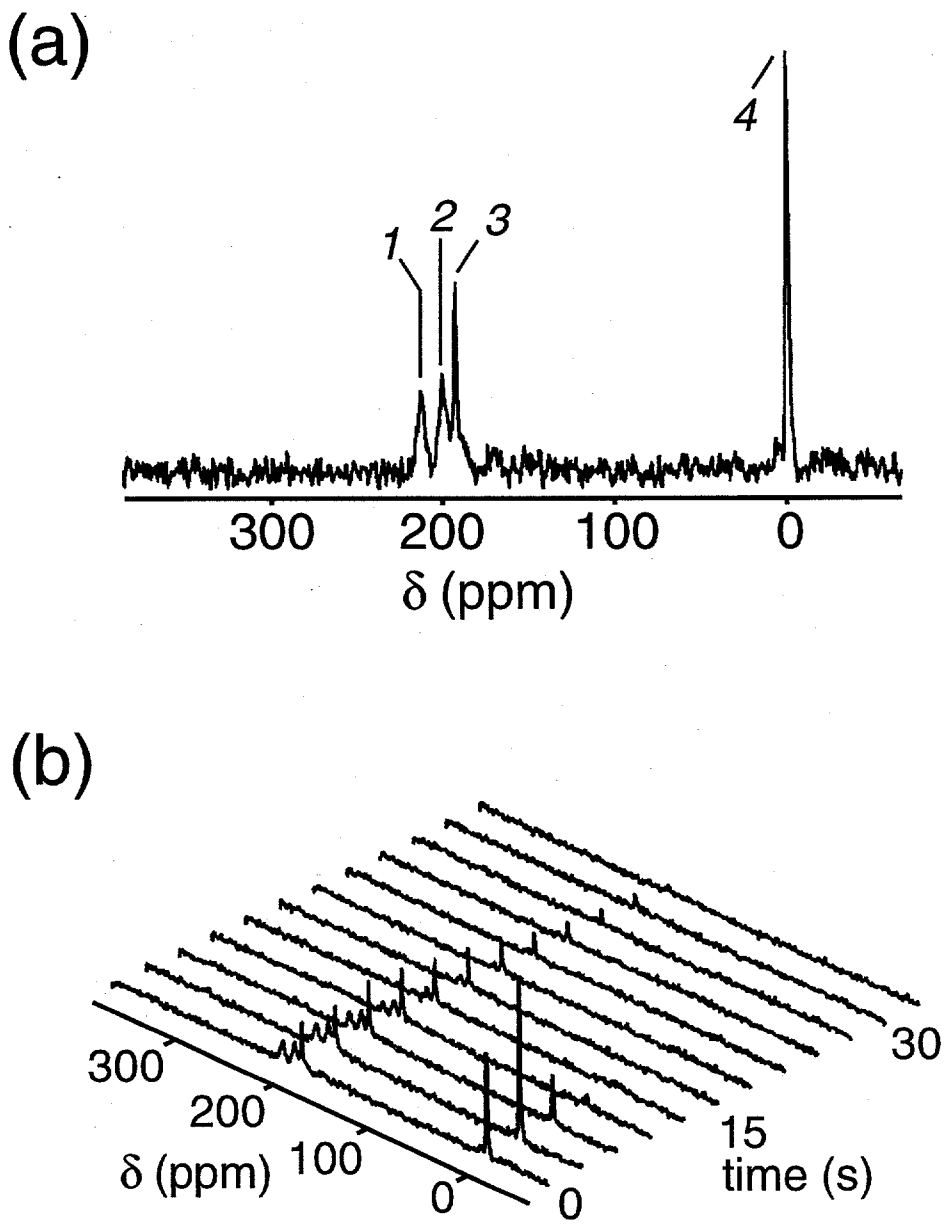

Figure 8.8: *In vivo* ^{129}Xe OPNMR spectroscopy [212]. (a) ^{129}Xe NMR spectrum from the thorax of an anesthetized rat following respiration of laser-polarized xenon. The spectrum was tentatively assigned as follows: *1*–red blood cells, *2*–lung tissue, *3*–blood plasma/adipose tissue, *4*–Xe gas. (b) ^{129}Xe NMR spectra showing the dynamics of the xenon resonances in different tissue compartments. Figures courtesy of Arvind Venkatesh and Mitchell Albert.

dent) contrast experiments (see for example, Refs. [228, 229, 230]), where the higher paramagnetism of deoxygenated hemoglobin is exploited to deplete MR signal from blood water protons via (transverse) relaxation-weighted methods. By using polarized xenon for such studies, it is hoped that changes resulting from brain function could be observed with higher dynamic range (i.e., greater contrast) and without background signal.

Additionally, the differential solubility of xenon in various tissue compartments could provide a novel form of contrast. The concentration of protons differs little across various regions of the body, often giving poor contrast when simply mapping proton density via MRI; however, the xenon concentration can vary by over an order of magnitude between aqueous and lipid-rich environments. Moreover, lipid-rich tissues are typically difficult to image via conventional ^{1}H MRI, because lipid protons usually suffer from rapid transverse relaxation (T_2). Thus, polarized xenon may be potentially useful for studying lipid-rich regions of the body, such as neural tissue [63].

The ability to image laser-polarized xenon in brain tissue was first demonstrated when the head region of a laboratory rat was imaged following respiration of laser-polarized xenon [231]. The first such ^{129}Xe brain image is shown in Fig. 8.9(a) as a false-color overlay upon the corresponding gray-scale ^{1}H MR image. From the image it is clear that the ^{129}Xe signal clearly originates from the rat's brain, predominantly in the cerebrum. A lower limit for T_1^* for the brain tissue resonance was estimated to be $\sim$30 s [232]. Additionally, respiration of laser-polarized xenon by human patients

has also produced detectable ^{129}Xe NMR signals originating from the patient's head region, most likely in the brain tissue [220].

Recently, the resolved differences in chemical shifts for xenon residing in different tissues have been exploited to demonstrate *in vivo* ^{129}Xe chemical shift imaging (CSI) following respiration of laser-polarized xenon by laboratory rats [233]. Two ^{129}Xe CSIs can be found in Figs. 8.9(b,c), which respectively show false-color images of xenon residing in blood (Figs. 8.9(b)) and tissue (Fig. 8.9(c)), each overlaid upon a gray-scale ^{1}H MR image corresponding to the same region in the rat's thorax. The ^{129}Xe signal in Fig. 8.9(b) corresponds to xenon residing in blood in the rat's heart and lung vasculature, while the ^{129}Xe signal in Fig. 8.9(c) was attributed to xenon residing in the rat's lung tissue and myocardium.

It is interesting to note that in this study, only one resonance was observed that could be assigned to blood in the ^{129}Xe NMR spectra (with a chemical shift of $\sim$210 ppm, obtained, for example, from localized NMR spectroscopy from the rat's heart region) [233]. This result suggests that under the conditions of their experiment (e.g., xenon dissolved in rat blood *in vivo* at 37 °C and 2 T) the xenon exchange between RBCs and plasma was fast with respect to the the NMR time scale, in contrast to the previous *in vitro* results involving xenon in human blood at higher fields and ambient conditions [224, 225]. Indeed, this result is particularly surprising considering the new results of Bifone and co-workers [132], where the xenon exchange in human blood was still slow on the NMR time scale even though the experiments

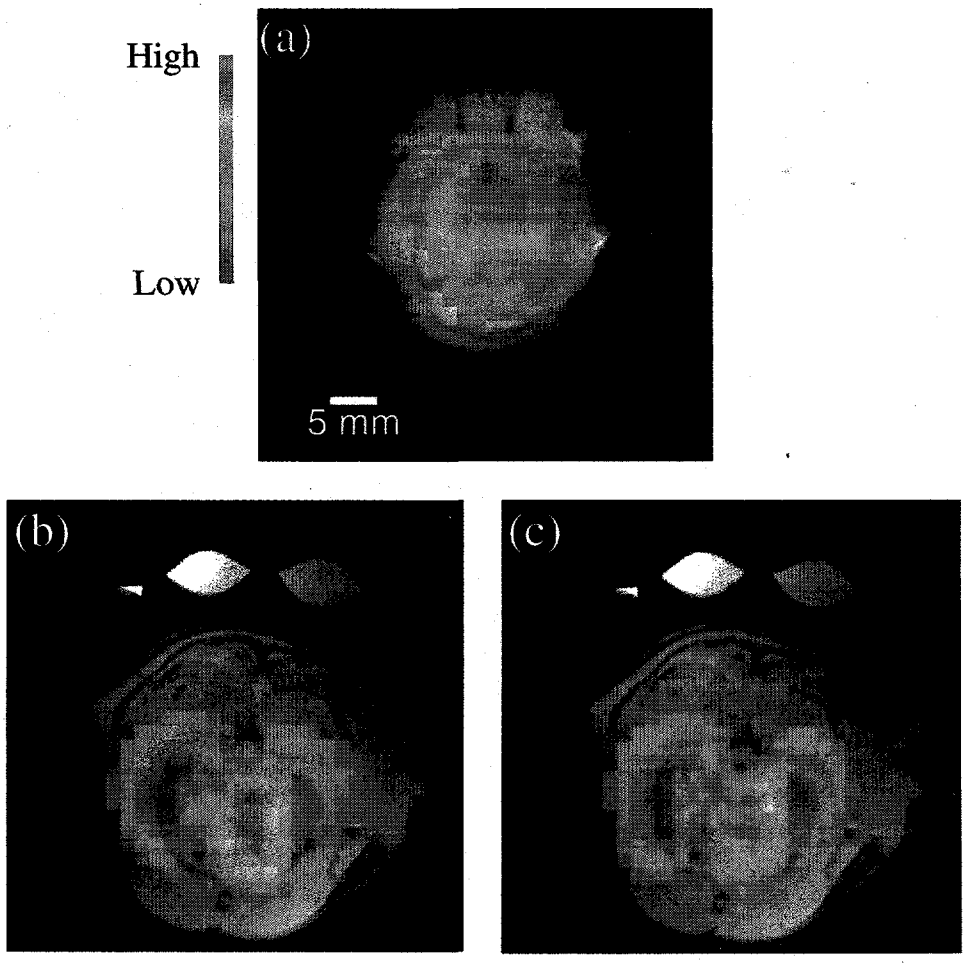

Figure 8.9: *In vivo* ^{129}Xe chemical-shift images from tissues in rats following laser-polarized xenon respiration, with each ^{129}Xe image shown as a false-color overlay of the corresponding gray-scale ^{1}H image. (a) xenon in brain tissue [231]. (b,c) axial, cross-sectional CSIs taken from a rat's thorax, respectively showing xenon in blood (b) and in lung tissue and myocardium environments (c) [233]. Figures courtesy of Scott Swanson.

were performed at 37 °C and only 1.5 T. The origin of this disparity is uncertain, but the possibility that it originates from some differences in sample preparation (i.e., *in vitro vs. in vivo* samples), or some difference between the behavior of xenon exchange in human and rat RBCs, has not been ruled out. Nevertheless, based on their results the authors of the *in vivo* rat work suggest a slight alteration of the assignment of the three tissue resonances (like those observed in Fig. 8.8); 210 ppm, blood; 199 ppm, tissue (e.g. lung parenchyma); and 192 ppm, epicardial fat. Certainly, such ^{129}Xe CSI experiments could become a powerful diagnostic tool, permitting lung ventilation and perfusion to be studied simultaneously.

8.4 Injection Delivery of Laser-Polarized Gases

While not as well-developed as the void-space imaging applications, the use of laser-polarized gases for novel *in vivo* tissue studies clearly possesses great potential. Despite the promising results described above, however, the use of polarized gases for tissue studies may be limited by the difficulty of delivering the gas to targeted regions with high enough local concentration and polarization. Indeed, overcoming the difficulty of delivering laser-polarized noble gases to tissues with sufficient polarization and concentration may be critical to the ultimate viability of many proposed *in vivo* studies.

Respiration delivery can suffer from many factors that can ultimately limit the concentration and polarization of laser-polarized gas that can be achieved in tissues,

especially those distant from the lungs. When delivered by respiration, polarized xenon is diluted throughout the body. More worrisome, however, are the short spin-lattice relaxation times of ^{129}Xe in some living tissues (e.g. blood). Thus, much of the polarization may be destroyed in transit before the xenon has reached tissues distant from the lungs. Respiration also requires the preparation and use of large volumes of polarized xenon for human tissue studies, making it financially impractical to use isotopically enriched xenon to increase the signal; the cost of ~80% ^{129}Xe-enriched xenon is roughly two orders of magnitude higher than xenon with natural ^{129}Xe abundance. Additionally, the anesthetic properties of xenon may in some circumstances limit its concentration in breathing mixtures. Finally, respiration delivery is limited to xenon because of the low solubility of helium in tissues.

At the cost of increasing the invasiveness of the experiment, the injection of biologically compatible polarized gas carriers may prove useful for combating all of the difficulties concerning tissue delivery mentioned above [17]. Various solvents can be chosen which possess high xenon solubility, and which partition xenon away from paramagnetic centers in the body, thereby increasing the *in vivo* ^{129}Xe MR signal. Instead of dissolving the noble gas, it has also been shown that stable gas bubbles can be formed in certain solutions, thereby permitting helium gas to be administered to the body in relatively large amounts for use as an MRI tracer. The injection methods permit rapid, efficient, and localized delivery of the polarized gas to a targeted region in the body. However, it is important that the advantages of injection delivery be

weighed carefully against the possible danger of increasing the invasiveness of any study (diagnostic or otherwise) involving human subjects.

8.4.1 A Model of Injection Delivery of Laser-Polarized Xenon

Models predicting the amount polarized xenon that could be delivered to tissues via respiration and injection can be found respectively in Refs. [234, 235] and Ref. [236]; the simple formalism adapted to model injection delivery of xenon is repeated here. Specifically, this model is designed to predict the *effective concentration* of laser-polarized xenon delivered, where the effective concentration refers to the number of moles of 100% polarized, 100% isotopically labeled ^{129}Xe per unit volume, given an actual amount of xenon with known fractional polarization and isotopic labeling (100% isotopic labeling is assumed for simplicity).

Consider a one-compartment uptake/washout model of a bolus injection using an inert, freely diffusible tracer (polarized xenon) (see, for example Ref. [237]). Such an injection could in principle be performed intravenously, intra-arterially, or directly into the target organ. Momentarily neglecting the delivery time from the injection site to the target tissue, one can write a differential equation that governs the effective concentration C of polarized xenon in the tissue as a function of time:

$$\frac{dC}{dt} = k_1 A - k_2 C, \tag{8.8}$$

where A is the time-dependent concentration of polarized xenon entering the tissue, k_1 is the specific volume flow in the tissue, and k_2 is the effective washout rate defined by:

$$k_2 = \left(\frac{k_1}{\lambda} + \frac{1}{T_1^{Xe}}\right); \tag{8.9}$$

here, λ is the tissue/blood partition coefficient and T_1^{Xe} is the xenon spin-lattice relaxation time in the tissue. The general solution to Equation 8.8 is:

$$C(t) = k_1 \int_0^t A(t') e^{k_2(t'-t)} dt'. \tag{8.10}$$

In order to simplify the model and account for the delivery time loss of polarization due to relaxation, the analysis is separated as follows. $A(t')$ is treated as a rectangular pulse transiting to the targeted region over a delivery time T_d, with time extent T_i and constant concentration A, where

$$A = \frac{IV_i}{PT_i}. \tag{8.11}$$

Here I is the initial effective concentration of polarized xenon in the solvent, V_i is the total volume injected, and P is the flow rate between the site of the injection and the target. This formalism assumes that $(V_i/T_i) < P$; if $(V_i/T_i) \geq P$, then $A = I$. Additionally, if the polarized xenon solution is injected directly into the target organ,

then k_1 must be replaced by the injection rate divided by the effective tissue volume. The effects of recirculation are assumed to be rendered negligible by the short *in vivo* relaxation times and dilution of polarized xenon throughout the body. The model is further simplified by assuming homogeneous and instantaneous equilibration of the xenon in the targeted tissue. Additionally, because the primary effect of T_d is the loss of xenon polarization due to relaxation during xenon delivery, one can now include the appropriate exponential decay term (governed by the spin-lattice relaxation time T_{1s}^{Xe} of polarized xenon in the solvent/blood environment) into the simplified solution of Equation 8.8. We now obtain the relation for the effective concentration of polarized xenon in the targeted tissue following injection:

$$C(t) = \begin{cases} 0, & t \leq T_d; \\ \frac{k_1 A}{k_2} \cdot e^{-T_d/T_{1s}^{Xe}} \cdot \left[1 - e^{-(t-T_d)k_2}\right], & T_d < t \leq T_p; \\ C_{T_p} \cdot e^{-(t-T_p)k_2}, & T_p < t, \end{cases} \tag{8.12}$$

where the peak time $T_p = T_d + T_i$, and C_{T_p} is the effective concentration of polarized xenon in the tissue at T_p.

The above model predicts that laser-polarized xenon could be delivered to certain tissues more efficiently by injection than by respiration [236]. For example, it was suggested that by assuming reasonable values for the parameters in Eq. 8.12 (summarized below in Table 8.4.1), injection delivery of laser-polarized xenon dissolved in a lipid suspension (described later) could improve the local concentration of po-

larized xenon in the brain by severalfold over what could be achieved by respiration as predicted by a model for respiration delivery [235]. By using Eq. 8.12 and the parameters in the table, it was calculated that a peak polarized xenon concentration of $\sim 7 \times 10^{-2}$ mM could be obtained at $T_p = 5$ s. Naturally, this concentration could be increased by using xenon with improved initial polarization, the injection of more solution, having a greater xenon overpressure in the shaker (within reason!), or by using a biologically tolerable carrier with higher xenon solubility. This xenon injection model does not include a number of complicating physiological issues, such as the differing perfusion rates, xenon solubilities, and xenon relaxation times of different brain tissues.

In comparison, the respiration models predict a peak polarized xenon concentration that is severalfold less; for example, the interactive model of Martin [235] predicts a peak brain concentration of 8.2×10^{-3} mM following a single held breath of a gas mixture containing 80% xenon (a value calculated using the same experimental and physiological parameters as those used in the injection estimate, excepting those parameters exclusive to respiration, for which the respiration model's default values were used). Furthermore, the respiration model predicts that continuous breathing of a 35% xenon mixture (a xenon concentration low enough to avoid potentially unwanted anesthetic effects [62]) would give a peak polarized xenon concentration of 3.3×10^{-3} mM.

The increase in peak polarized xenon concentration predicted by the simple in-

Parameter	Value
V_i	5 ml
T_i	3 s
I	8.7 mM[a]
k_1	[0.00917 s^{-1}][b]
P	4.9 ml/s[c]
λ	1[d]
T_{1s}^{Xe}	16 s [225]
T_1^{Xe}	30 s [232]
T_d	2 s

Table 8.1: Parameter values used for xenon injection model.

[a]Estimated from the relative solubility of xenon in the Intralipid emulsion [225], and assuming a 5-atm equilibrium xenon overpressure, an initial xenon polarization of 0.1 (10%), and 100% isotopic labeling.
[b]From a brain blood flow rate of 52.9 ml/min per 100 g [238], a brain mass of 1400 g, and a specific gravity of 1.04 [239].
[c]Estimated as the total volume of blood per second supplied by one carotid artery, given the value for k_1.
[d]Effective value estimated from those of white and grey matter given in Ref. [240] (*in vitro* data from dogs).

jection model over that predicted with the respiration model primarily originates from rapid, localized xenon delivery, high initial concentration (obtained with high xenon solubility in the carrier) and extended *in vivo* ^{129}Xe relaxation time. However, it should be noted that the peak polarized xenon concentrations predicted by such models depend greatly upon the values of the experimental and physiological parameters used in the calculations, some of which are not well-known for all physiological conditions.

8.4.2 Experimental Methods

The original implementation of noble gas injection dates back to the 1960's, and involved the injection of saline solutions containing dissolved radioactive xenon isotopes (e.g. ^{133}Xe) to study local blood flow in muscular tissue [241, 242]. However, only recently was injection explored in conjunction with delivering laser-polarized xenon [225] to exploit the intrinsic advantages of magnetic resonance techniques (e.g., high spatial resolution, improved contrast and signal-to-noise, and lack of ionizing radiation).

A cartoon summarizing the general experimental procedure for polarized noble gas injection is shown in Fig. 8.10. Following batch optical pumping, polarized xenon is frozen into the cold-finger of the "shaker" and stored while exposed to a magnetic field provided, for example, by a strong permanent magnet. Once the shaker has been transported to the NMR spectrometer, the xenon is rapidly sublimated, and

delivered at moderately high pressure (a few atm) to a degassed, non-toxic solution. Degassing removes paramagnetic oxygen from the solution, thereby increasing the polarization lifetime of the dissolved xenon. Following vigorous shaking, the xenon-saturated solution is withdrawn through a high-pressure septum with a syringe, and subsequently injected into the sample of interest. For *in vivo* studies, the injection can be administered intravenously, intraarterially, or directly into the target organ, depending on the application. Intraarterial injection is often the most efficient route for tissue delivery, but is also the most invasive.

8.4.3 Investigations of Potential Noble Gas Carriers

Saline is a good carrying agent for laser-polarized xenon because it possesses a long ^{129}Xe T_1 ($\approx$66 s, $\sim$1000 s when deuterated [225]) and high biological compatibility. However, it possesses a xenon Ostwald solubility coefficient of only 0.0945 at 27°C [240], yielding a concentration of only $\sim$4 mM/atm. The Ostwald coefficient is derived from the volume, at standard temperature and pressure, of a gas that can be dissolved in 1 liter of liquid at 1 atm of gas pressure for a given temperature. For comparison, the Ostwald solubility of xenon in blood is about 0.18 [240]. Furthermore, in many circumstances it would be desirable to partition the xenon away from paramagnetic centers in the body, thereby increasing the observed T_1 following injection. For these reasons, a variety of alternative noble gas carriers have been investigated for potential *in vivo* use.

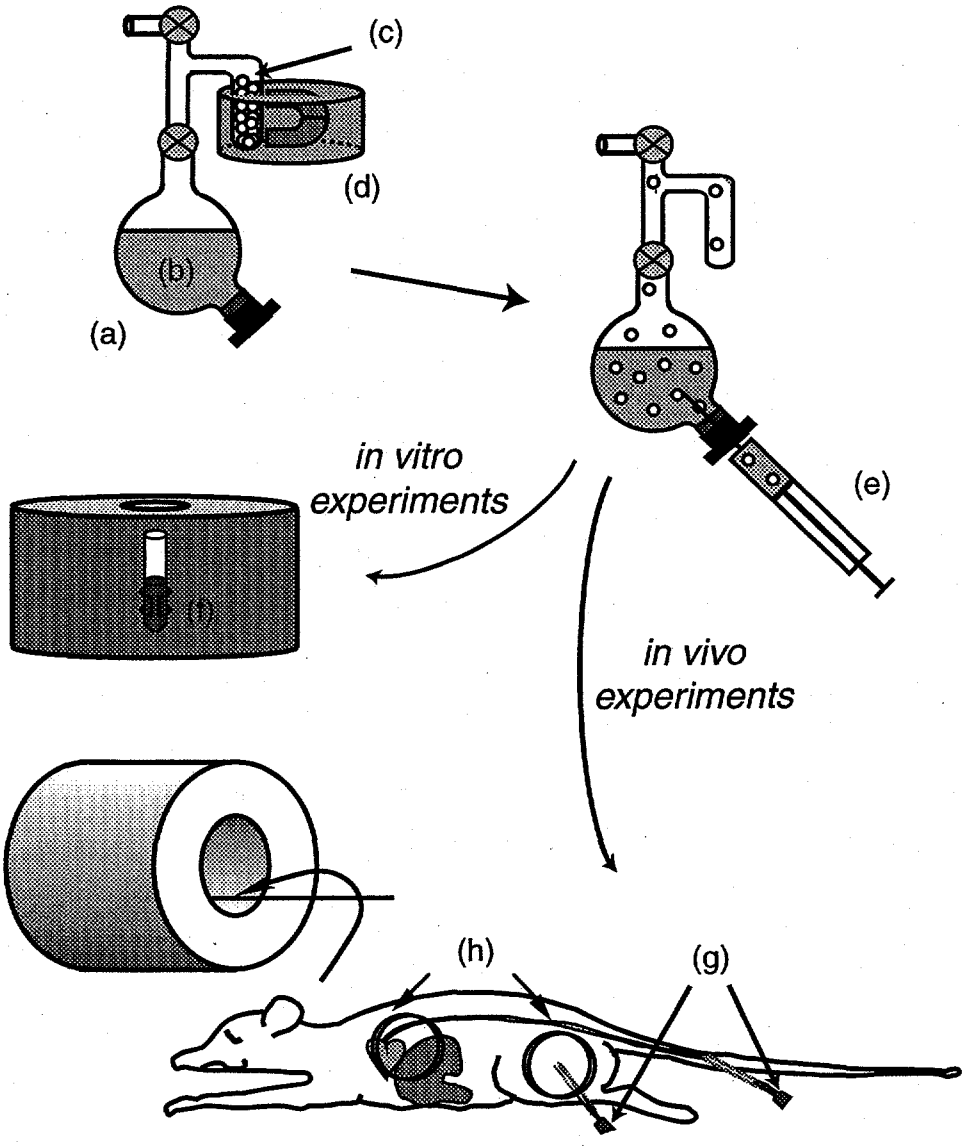

Figure 8.10: Schematic of an experimental procedure used for polarized gas injection. Following optical pumping, xenon is cryopumped into the sample ((a), in this case, a shaker containing a few ml of degassed solvent (b)) by immersing the cold finger (c) in a dewar of liquid nitrogen (d) containing a strong permanent magnet (~1 T). Immediately prior to the experiment the xenon is sublimated and admitted to the solution with vigorous shaking. The saturated gas solution is then withdrawn via a syringe (e) through a high-pressure rubber septum. The polarized gas solution can then be injected into samples for *in vitro* magnetic resonance studies (f) or delivered via a catheter (g) for *in vivo* studies. Surface detection coils (h) are often used in such circumstances to improve signal strength.

Figure 8.11 contains ^{129}Xe spectra taken from various polarized xenon solvents following *in vitro* or *in vivo* injection. One class of noble gas carriers are lipid emulsions. The first such carrier to be investigated was Intralipid (Pharmacia), an aqueous suspension of lipid vesicles known to be well-tolerated biologically; in fact, Intralipid emulsions are used clinically as nutrient supplements in hospitals. The ^{129}Xe T_1 in 20% Intralipid solutions was determined in different studies to be 40 s [225] and 49 s [243]. The ^{129}Xe spectra taken from a xenon/Intralipid solution injected into a test tube of human blood is shown in Fig. 8.11(a). The spectrum shows a strong resonance at $\approx$194 ppm (corresponding to xenon in the Intralipid), over six times greater than the signal from xenon residing in red blood cells at $\approx$216 ppm. This observation is consistent with the lipophilic nature of xenon, and is responsible for two desirable effects: 1) higher xenon concentration (roughly 4 times that of saline) and 2) extended polarization lifetime in the blood, with a new ^{129}Xe T_1 of 16 s (for the Intralipid resonance). The signal in Fig. 8.11(a) was strong enough to obtain an MR image, as shown by the 2-D FLASH ^{129}Xe image in the inset.

Another class of substances that has been investigated for carrying xenon are perfluorocarbon compounds and their emulsions. These substances are of particular interest in the medical community because of their ability to dissolve and transport oxygen and carbon dioxide, making them potentially useful as blood substitutes [244]. The first perfluorocarbon substance studied was Fluosol (Green Cross), a 20% perfluorodecalin emulsion. A spectrum taken following *in vitro* injection of a polarized

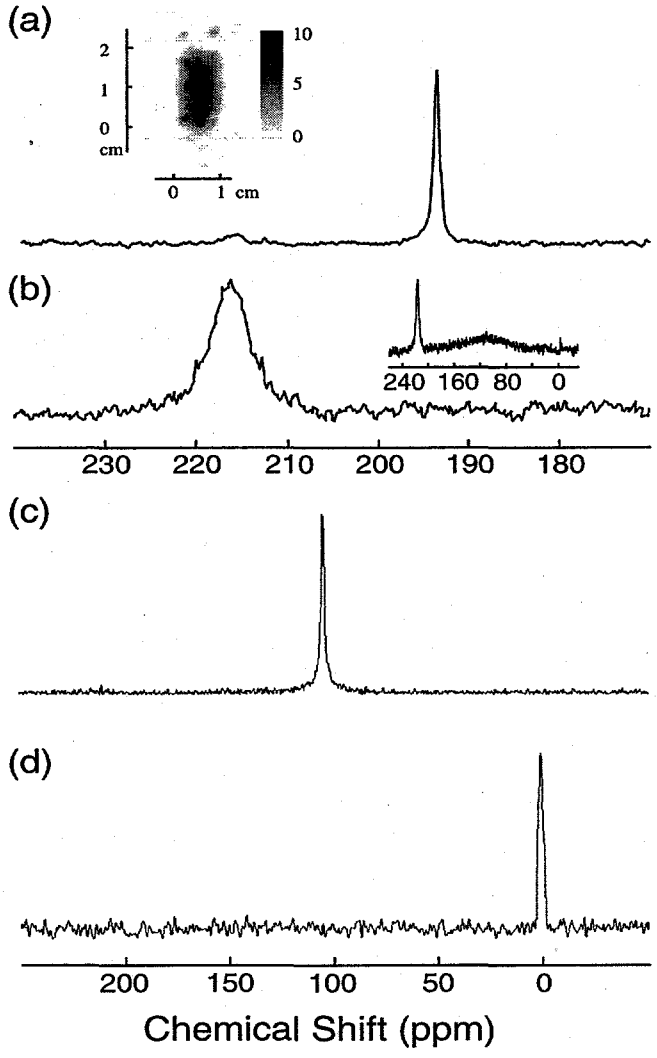

Figure 8.11: Xenon in various biologically compatible carrier solvents. NMR spectra in fresh human blood obtained using laser-polarized ^{129}Xe in (a) 20% Intralipid solution and (b) Fluosol [225]. The ^{129}Xe NMR signal at a chemical shift of 216 ppm is characteristic of xenon in the RBC, and the signal at 194 ppm is from xenon in the plasma/lipid mixture. The **inset** of (a) contains a ^{129}Xe FLASH image taken of a test tube containing a blood/Intralipid mixture. In the **inset** of (b), the broad peak centered around 110 ppm is due to xenon in Fluosol. (c-d) ^{129}Xe spectra taken of laser-polarized xenon in pure PFOB (c) and xenon-gas-filled liposomes (d) following intravenous injection into laboratory rats. Spectra (c) and (d) courtesy of Arvind Venkatesh and Mitchell Albert, reproduced from Refs. [243, 247]

xenon/Fluosol solution into human blood is shown in Fig. 8.11(b). The now-familiar peak at 216 ppm corresponds to xenon in the red blood cells; however, the signal from xenon residing in the Fluosol is so broad that it cannot be observed until the whole spectrum is shown (Fig. 8.11(b) inset). The peak from xenon in the Fluosol is roughly 80 ppm wide (most likely broadened from exchange), making Fluosol unfavorable for carrying polarized xenon for the purposes of tracing local blood flow. However it is interesting to note that the T_1 of the ^{129}Xe red blood cell signal was 13 s, a significant increase from that observed when xenon is delivered in saline. This T_1 extension suggests that Fluosol may be useful as a xenon "reservoir" for chemical-shift imaging and localized spectroscopy of tissues.

Numerous other perfluorinated compounds have since been studied for use as possible polarized xenon carriers. Pure perfluorooctyl bromide (PFOB) possesses a high xenon Ostwald solubility (~1.2 [245]) and can be injected in relatively small volumes; the ^{129}Xe spectrum taken following the intravenous injection of a polarized xenon/PFOB solution into a laboratory rat is shown in Fig. 8.11(c) [243]. Xenon residing in the PFOB produces a strong signal at 106 ppm [245]. No signal is observed that could be assigned to xenon residing in the tissues [243]. Thus, pure PFOB appears to be very effective at partitioning the xenon away from paramagnetic species in the blood and other tissues, a fact especially evident in the long effective ^{129}Xe T_1 of 94 s [243]. However, the perfluorocarbon substances must ultimately be emulsified in order to facilitate tissue absorption. Thus, other work has been directed

towards optimizing the emulsions of perfluorinated compounds. For example, the composition of PFOB emulsions was varied in order to maximize xenon concentration, while minimizing the broad linewidth of the ^{129}Xe signal normally observed in perfluorocarbon emulsions [245, 246]. By varying the concentration of the emulsifying agent (egg lechithin) in a 90% (weight/volume) PFOB emulsion, the exchange rate of xenon between the PFOB "droplets" and their surroundings could be altered. The lower the emulsifier concentration, the larger the droplet size, and the slower the exchange, yielding a narrower Xe/PFOB signal. With 0.85% emulsifier, the average PFOB droplet size was roughly 2 μm, and gave a relatively narrow linewidth for the ^{129}Xe/PFOB resonance ($\leq$3 ppm). Lowering the emulsifier concentration further yielded larger PFOB droplet sizes and narrower lines, but made the emulsions more unstable.

Instead of dissolving the polarized noble gas in a solution, it has also been suggested that injection could be used to deliver it in *gaseous* form. For example, it has been shown that liposomes can be stably prepared to contain polarized xenon gas [247]. Solutions of these xenon-filled liposomes can then be safely injected into living organisms (Fig. 8.11(d)). The observed ^{129}Xe T_1 of xenon gas in the liposomes once intravenously injected into a laboratory rat was as long as 54 s [247].

Finally, by flushing polarized helium gas through Hexabrix (Mallinckrodt), a viscous, commercially available radiographic contrast agent, polarized helium microbubbles could be formed and stably suspended [248]. The ^{3}He T_1 was measured to be

at least 42 s in the microbubble suspension. While the sizes of the microbubbles were larger than what would be desired for clinical use ($\approx$32 μm, with a standard deviation of about 10 μm), this approach demonstrates the feasibility of utilizing the higher signal afforded by laser-polarized ^{3}He as a magnetic resonance blood-flow tracer. In order for the helium injection approach to be clinically feasible, the average dimension of the microbubbles must be decreased toward the size of red blood cells to insure safe circulatory passage; therefore, future attempts will be directed towards decreasing the microbubble size and increasing their effective concentration, while retaining a suitably long ^{3}He T_1. Data concerning some potential polarized noble gas carriers are summarized in Table 8.2.

8.4.4 *In Vivo* Studies

The feasibility of using injectable carriers of laser-polarized xenon to perform *in vivo* NMR and MRI was demonstrated in living laboratory rats [236]. In each experiment of this work, $\sim$1 cc of a saturated polarized xenon solution was prepared according to the procedure described in Section 8.4.2. Male rats weighing 200-250 g were prepared and handled by Dr. K.M. Brennan (LBNL). The rats were anesthetized intramuscularly with ketamine/xylazine/acepromazine (30/3/0.6 mg/kg), with supplemental doses administered as needed. A venous catheter was placed either into a tail vein in the muscle of the rat's thigh, depending on the desired location of the injection. The NMR signals were detected with a receiver/transmitter surface coil

Carrier	Ostwald Solubility[a]	Gas T_1^a	Gas T_1 in Tissue[a]	Chemical Shift[a]
Saline	0.0945 [240] (27 °C)	66 s [225]	5 s (blood) [225]	≈192 ppm [225]
DMSO	∼0.66 [249] (25 °C)	100's of seconds		245.8 ppm [250]
Olive Oil[b]	≈2.04 [240] (27 °C)			198 ppm [66]
Intralipid (20%)	∼0.4 [225]	40 s (9.4 T) [225], 49 s (4.7 T) [243]	16 s (blood) [225]	194 ppm [225]
Intralipid (30%)	≈0.6 [251]	25 s[c] (2 T) [252]		194.5 ppm [251]
Lyposyn II	≈0.4 [251]	23 s[c] (2 T) [251]		194.5 ppm [251]
Lecithin[b]	1.477 (37 °C) [249]			200.6 ppm [66]
PFOB	∼1.2 [245]		97 s (rat) [243]	106 ppm [245]
PFOB (20%)	∼0.22[d]	110 s [243]	34 s / 67 s (blood: RBC/PFOB) [243]	∼110 ppm [243]
PFOB (90%)	∼0.62[d]			111 ppm [245]
Perfluortributylamin	1.513 (20 °C) [253]			
Fluosol (20%)	∼0.3		13 s (blood: RBC) [225]	∼110 ppm [225]
Oxyphenol (20%)	0.251 [253]			
Gas-filled Lyposomes		118 s (114 s in saline) [247]	45 s (blood), 54 s (rat) [243]	≈0.5 ppm [247]
Hexabrix (^{3}He microbubbles)	*e*	≥ 42 s (for ^{3}He) [248]		≈0 ppm (^{3}He)

Table 8.2: Summary of properties of potential noble gas carriers.
[a]For ^{129}Xe, unless otherwise stated.
[b]Listed for comparison.
[c]Lower value than that determined for Intralipid (20%) may indicate a field-dependent relaxation rate.
[d]Estimated from the xenon solubility in pure PFOB and the volume/volume ratio of the mixture.
[e]About 20% of the injected volume was polarized helium gas in the form of microbubbles.

(diameter: 3.5 cm).

In one experiment, a saturated polarized xenon/Intralipid (20%) solution was injected intravenously into a rat's tail vein (Fig. 8.12). The surface coil was used to monitor ^{129}Xe NMR signals from the rat's liver region, permitting the wash-in/wash-out dynamics of the xenon in this region to be observed, as shown in inset of Fig. 8.12. Spectra were obtained every second with rf pulses of tipping angle $\approx 20°$. Following injection, it was anticipated that the Intralipid would accumulate in the liver; it is likely that the initial rise in signal reflects this accumulation, while the subsequent decay is due to wash-out, relaxation, and magnetization loss from the rf observation pulses. The chemical shift of the ^{129}Xe NMR signal shown in main portion of Fig. 8.12 (at $\sim$190 ppm downfield from a $\sim$5 atm ^{129}Xe gas signal) is consistent with xenon residing predominantly in the Intralipid solution.

In a second experiment, ^{129}Xe MR images were obtained following intramuscular injection of a saturated polarized xenon/saline solution into the upper hind leg of a laboratory rat. Figure 8.13 shows six of a series of series of 10 near-axial, cross-sectional images taken at intervals of 6-7 s. The ^{129}Xe images were taken with the FLASH pulse sequence [210], with pulse tipping angle $\approx 5°$. Despite the relatively low resolution of these preliminary images, the position of the rat's femur can be observed, corresponding to the signal void near the center of the image. The signal remained strong enough to be seen through the final acquisition, 70 s into the experiment. The signal decay was mostly due to the rf observation pulses, with only small contributions

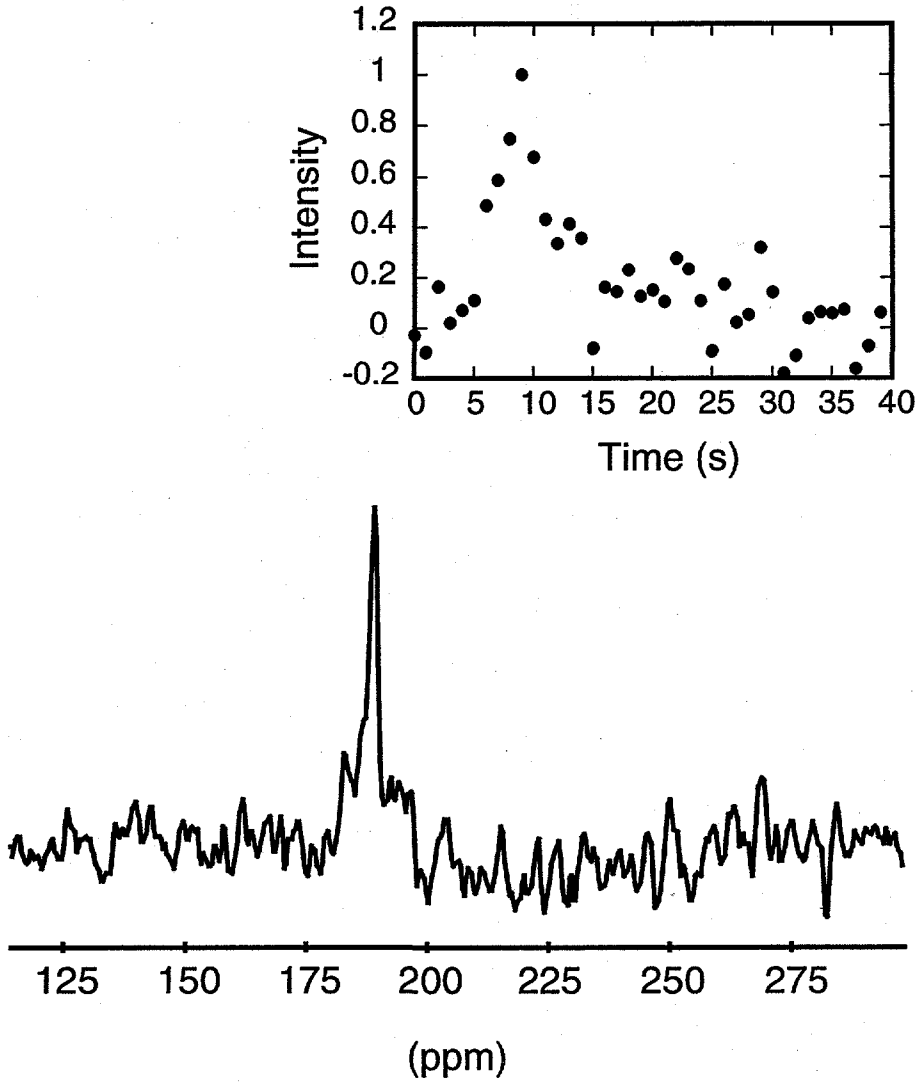

Figure 8.12: *In vivo* ^{129}Xe NMR spectrum obtained by summing the 7th through 12th acquisitions following the intravenous injection of a laser-polarized xenon/Intralipid solution [236]. The signals were detected with a surface coil placed over the rat's liver region. The chemical shift ~190 ppm downfield of a ~5 atm reference signal is consistent with xenon in the Intralipid. The time dependence of the integrated ^{129}Xe NMR signal is shown in the inset.

from relaxation and xenon wash-out.

More recently, Intralipid (30%) solutions have been used to deliver polarized xenon to the vasculature of rats, permitting ^{129}Xe MR images to be obtained with significantly improved resolution [251, 252]. Two such magnetic resonance angiograms (MRAs) taken following separate injections into the tail vein of a laboratory rat are shown in Figs. 8.14(a-b). An MRA taken from the rat's pelvic region is shown in Fig. 8.14(a), depicting the region's vasculature in some detail (specifically, the right common iliac vein and the inferior vena cava can be clearly seen in the brighter portions of the image, and the middle caudal vein is also shown. Readers can find a detailed description of the anatomical features of laboratory rats in Ref. [254]). Fig. 8.14(b) was taken from the rat's abdominal region, and both left and right common iliac veins can be seen as they join to form the inferior vena cava. The local blood flow rate was also quantitatively measured in different veins, giving results that agreed well with previous measurements—once the artificial increase caused by the injection was considered. Using polarized xenon injection permitted high-contrast images and measurements to be obtained without background signal, obviating the need for background suppression techniques. A relatively large amount of the polarized xenon/Intralipid solution was injected in order to perform these studies (5-6 ml in $\sim$10 s delivered to rats weighing $\sim$400-500 g). This amount corresponds to a higher value than what would be practical for future clinical applications in humans [252]. While this volume and injection rate was well-tolerated by the rats, higher

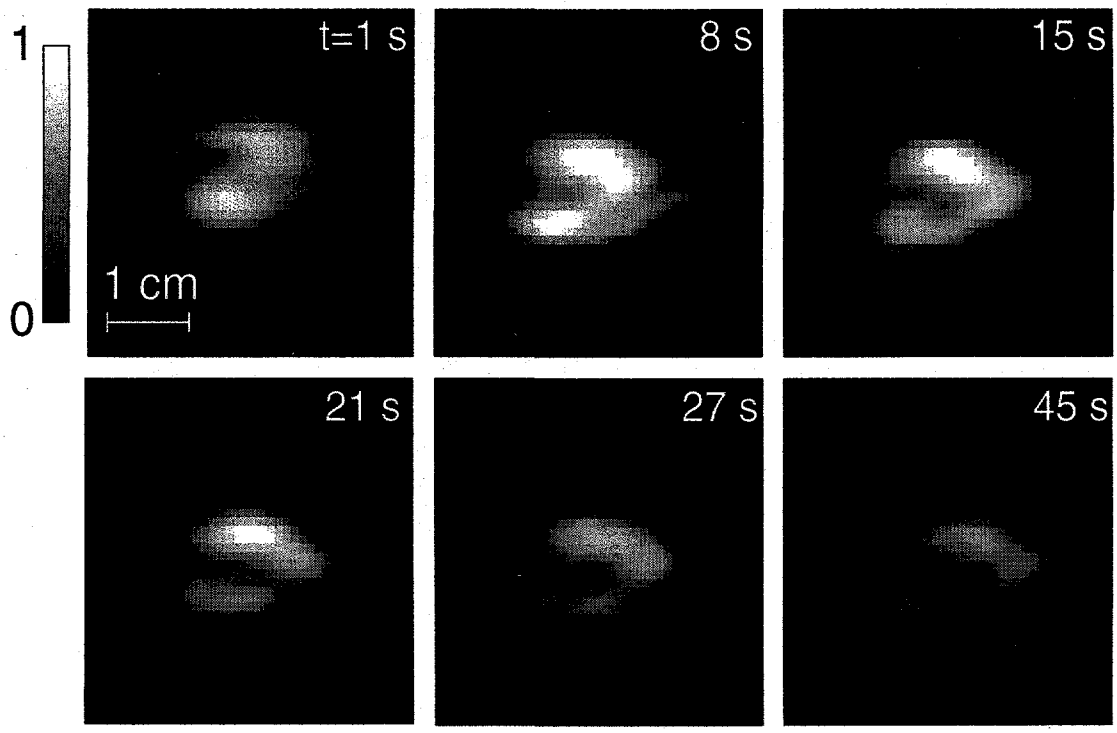

Figure 8.13: ^{129}Xe MR images of a laser-polarized xenon/saline solution injected into the upper hind leg of a living rat [236]. Acquisitions began immediately following the injection at 1, 8, 15, 21, 27, and 45 s. Displayed image intensities were normalized to the second image. Images as shown were prepared by zero-filling in both dimensions (giving a 256 × 256 matrix), and 50 Hz Gaussian apodization along the frequency-encoding dimension. Images were acquired using the FLASH method [210]. The image resolution was approximately 1 mm × 5 mm, with a 10 mm slice depth. The signal void near the center of the image corresponds to the rat's femur.

injection rates led to reduced heart rates and subsequent death. However, by using carriers with higher xenon solubilities and improved xenon polarization, it should be possible to perform identical experiments with the same signal-to-noise while using much lower injected volumes.

Finally, by suspending microbubbles of laser-polarized ^{3}He in an injectable solution, it should be possible to exploit the advantages provided by ^{3}He for use as an MRI tracer (e.g., brighter signal resulting from higher gyromagnetic ratio and greater ease in creating higher nuclear polarization). The promise of this technique was recently demonstrated by the injection of a polarized ^{3}He/Hexabrix microbubble solution into the vasculature of rats [248]. As shown in Figs. 8.14(c-d), this approach permitted high-resolution images to be obtained following both intraarterial (Fig. 8.14(c)) and intravenous injection (Fig. 8.14(d)): in (c), the abdominal aorta, common iliac arteries, and external iliac arteries can be seen; in (d), the vena cava, common iliac veins, and caudal veins are shown. Naturally, performing such tissue studies with laser-polarized helium would be extremely difficult using respiration delivery, because the solubility of helium in tissues is 10-100 times lower than that of xenon [59]. As was the case with the above *in vivo* Intralipid imaging experiments, an impracticably large volume ($\sim$7 ml) of the microbubble suspension was injected to obtain these ^{3}He images. Again, however, increasing the effective helium concentration and polarization should greatly reduce the injected volume necessary to obtain the same excellent signal-to-noise and resolution of the images in Fig. 8.14.

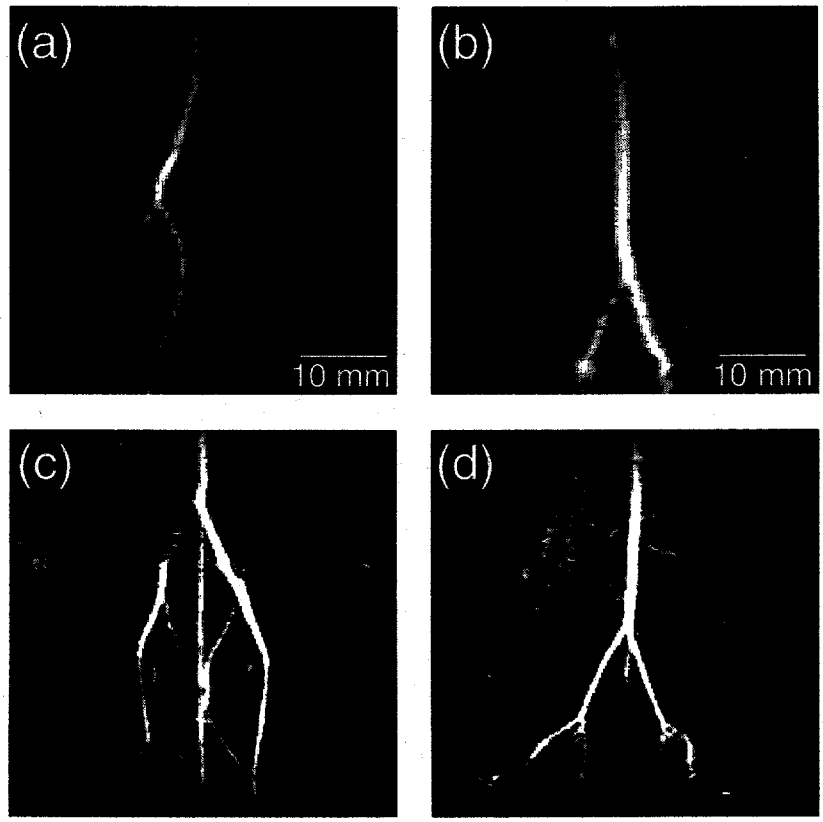

Figure 8.14: *In vivo* vascular images taken following injection of polarized noble gas carriers [252]. (a-b) Coronal projection ^{129}Xe MR images taken following injection of a polarized xenon/Intralipid (30%) solution into a rat's tail vein. (a) ^{129}Xe signal from the pelvic region (hypogastric and caudal veins, right common iliac vein, and inferior vena cava); (b) ^{129}Xe signal from the abdominal region (right and left common iliac veins and inferior vena cava). Figures courtesy of Harald Möller and G. Allan Johnson. (c-d) Coronal projection ^{3}He MR images taken following injection of a polarized helium microbubble/Hexabrix suspension performed intraarterially (c) and intravenously (d) [248]. (c) ^{3}He signal from the abdominal region (abdominal aorta, common iliac arteries, and external iliac arteries); (d) ^{3}He signal from the pelvic region (caudal veins, common iliac veins, and vena cava). Digital in-plane resolution for (c,d): 0.31 mm $\times$ 0.31 mm. Figures courtesy of Mark Chawla and G. Allan Johnson.

Chapter 9

Low/Zero-Field OPNMR/MRI

9.1 Introduction

Because the nuclear polarization of laser-polarized noble gases is endowed by the optical pumping process, and not the external magnetic field, high magnetic fields are not necessary to obtain strong NMR signals or bright magnetic resonance images. Therefore, the non-equilibrium polarization of laser-polarized noble gases can be exploited to perform NMR and MRI experiments at low fields. This intriguing possibility of performing "MRI without the magnet" has attracted increasing interest for a variety of reasons, not the least of which is the fact that the savings obtained by not having to purchase and maintain an MRI magnet well outweighs the cost of the optical pumping equipment.

This final chapter discusses some of the recent work demonstrating the potential

of low/zero-field OPNMR/MRI to perform novel experiments of interest in materials science and biomedicine, with special attention given to the use of superconducting quantum interference devices as highly sensitive detectors of low-frequency magnetic resonance signals.

9.2 Conventional Detection

The potential of laser-polarized gases for performing low-field NMR/MRI was first demonstrated in studies investigating the field dependence of ^{129}Xe relaxation in solid laser-polarized xenon [48]. ^{129}Xe NMR spectra were obtained from samples of frozen laser-polarized xenon at fields as low as 50 G (0.005 T) at 4.2 K [48], a field roughly a thousand times weaker than what is typically used in conventional magnetic resonance experiments. Optically detected signals from laser-polarized xenon at low field within optical pumping cells were reported about a year later [255].

Low-field MRI was first reported when 1-D MR images were obtained from glass cells containing 0.2-2.5 atm of laser-polarized ^{3}He gas at room temperature and only 31 G [200]. As described in Chapter 7, the resolution of these images was sufficient to resolve edge enhancements caused by restricted diffusion of the helium diffusion at the sample boundaries.

More recently, laser-polarized gases have been used to image the void spaces in human lungs at moderate field strengths, as shown in Fig. 9.1. In this work, large quantities ($\sim$1 L) of laser-polarized ^{3}He gas were prepared via metastability exchange

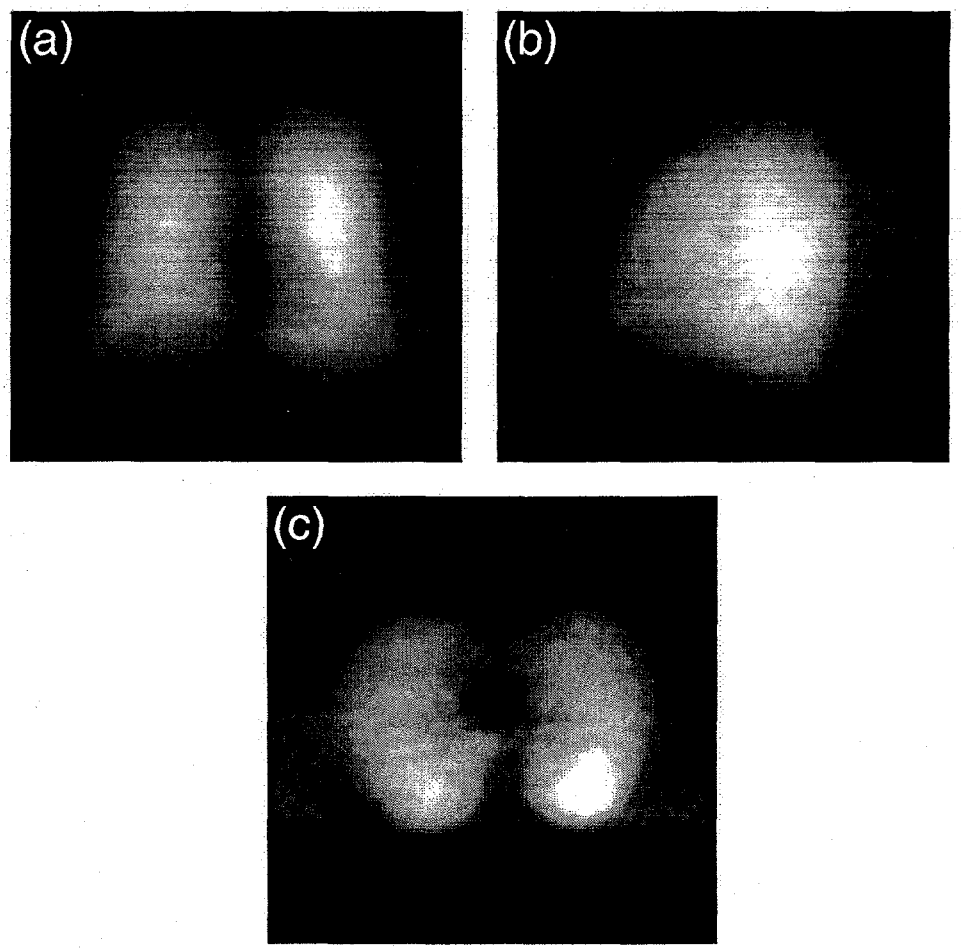

Figure 9.1: MRI of human lungs at 0.1 T. Coronal (a), sagittal (b), and transverse (c) ^{3}He MR images taken from human lungs following respiration of laser-polarized helium [256]. Figures courtesy of Genevieve Tastevin.

optical pumping. Following respiration of laser-polarized helium by a healthy human volunteer, ^{3}He MR images were obtained from the patient's lungs in a field of only 0.1 T [256]. While this field strength is an order of magnitude lower than those normally employed in conventional MRI (greatly improving upon the cost and ease of management of the MRI apparatus), there are many potential advantages to performing such experiments at fields ≥ 100 times weaker. Specifically, by eliminating the need for strong, enormous magnets to generate nuclear polarization, the cost, comfort, flexibility, safety, and portability of MRI could be greatly improved.

A low-field MRI apparatus was recently built to obtain multi-dimensional high-resolution images of laser-polarized gases [257]. A collection of images obtained with this apparatus is shown in Fig. 9.2. Specifically, the images in this figure demonstrate an additional advantage of low-field MRI—reduced magnetic susceptibility distortions. Figure 9.2(a) shows a high-field (4.7 T) ^{1}H MR image from a water-filled W-shaped cell; Fig. 9.2(b) however, shows the detrimental effect of placing sealed tubes of paramagnetic substances nearby the cell during an otherwise-identical imaging experiment. Figure 9.2(c) shows a ^{3}He image obtained at only 21 G by placing laser-polarized helium within a triangle-shaped cell. Finally, Fig. 9.2(d) shows the minimal effect of placing the paramagnetic sample tubes nearby when imaging polarized helium gas at such low fields.

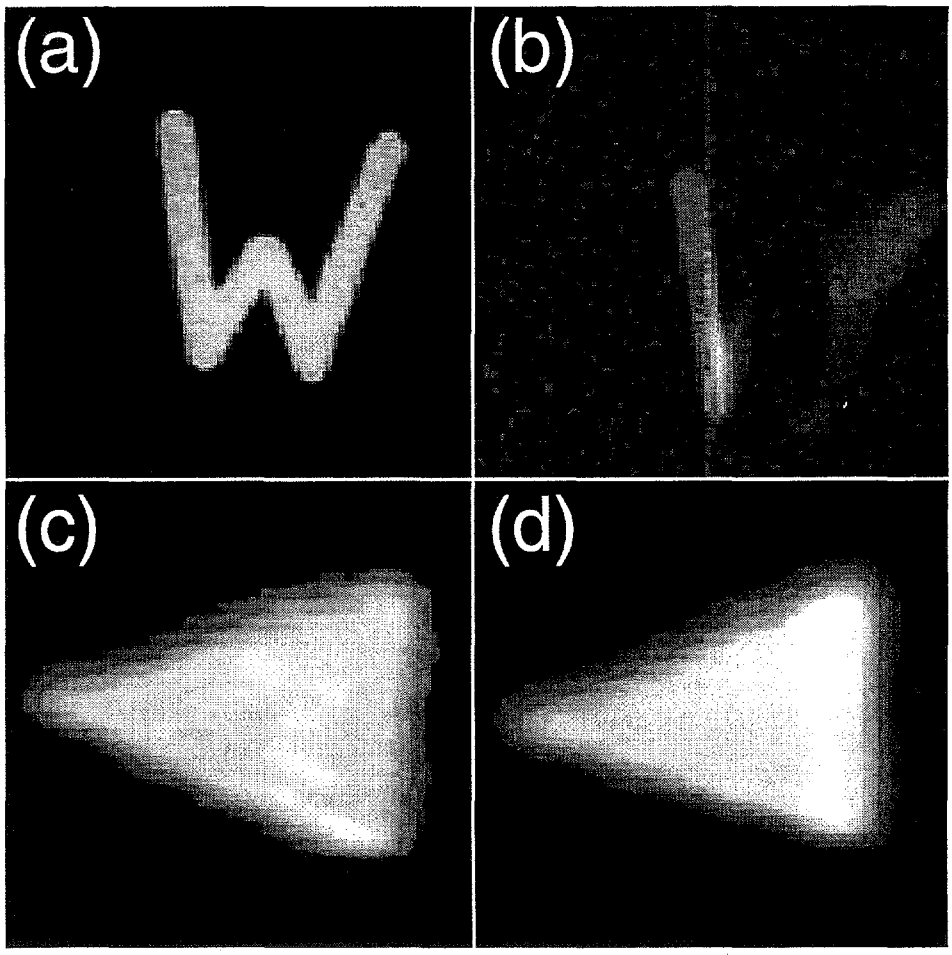

Figure 9.2: Demonstration of low-field MRI of polarized gases with greatly reduced magnetic susceptibility distortions [257]. (a) Room-temperature high-field ^{1}H MR image from a water-filled W-shaped cell. (b) same as (a), but with the cell placed near paramagnetic materials. (c) low-field (21 G) ^{3}He MR image from a triangular glass cell containing laser-polarized helium gas. (d) same as (c), but with the cell placed near the paramagnetic materials. Images were obtained with a standard gradient echo imaging sequence, and the signal was detected with a conventional Faraday induction coil. Figures courtesy of Glenn Wong and Ronald Walsworth.

9.3 SQUID Detection of Polarized Gases

Conventional detection of nuclear magnetic resonance signals is performed by measuring the voltage induced in a coil by the change in magnetic flux caused by the precessing nuclear spins. For a given sample, the NMR signal detected is proportional to both the polarization and the frequency, i.e., to B_0^2 (if the sample is thermally polarized) or ω_0^2. Thus, the sensitivity of conventional Faraday detectors is highly dependent upon the strength of the external magnetic field; a Faraday detector will be less sensitive when detecting the precession of nuclei in weaker magnetic fields.

An alternative approach enabling one to obtain NMR signals at much lower frequencies (and thus much lower fields) employs a Super-conducting QUantum Interference Device (SQUID) detector (for a review of SQUID fundamentals and applications, the reader is directed to Ref. [258]). While conventional Faraday detectors measure the changes in the oscillating magnetic flux as a function of time ($d\Phi/dt$), a SQUID measures the magnetic flux directly; independent of nuclear polarization, a SQUID's sensitivity does not (in principle) scale with frequency at low frequencies. Thus, SQUIDs may be advantageous for lower-frequency NMR and MRI experiments. Recent work is described below combining SQUID detection with optical pumping to further increase the sensitivity of NMR and MRI of laser-polarized xenon and helium at low magnetic fields.

9.3.1 Low-Temperature Experiments

A series of ^{129}Xe NMR spectra are shown in Figs. 9.3(a,b) taken of frozen laser-polarized xenon at 4.2 K at incrementally lower external magnetic field strengths, permitting the field dependence of the ^{129}Xe T_1 to be studied in great detail [259]. As shown in Fig. 9.3(b), it was possible to obtain ^{129}Xe NMR spectra with Larmor frequencies as low as ~200 Hz, corresponding to a field strength of only 0.19 G (Earth's field: ~0.6 G).

Figure 9.4 shows a 2-D ^{129}Xe MR image of laser-polarized xenon frozen within a Pyrex tube, taken at 4.2 K with an external field of 10 G (corresponding to a Larmor frequency of 11.8 kHz), and with an applied imaging gradient strength of 0.046 T/m [11]. Because the imaging gradient could be applied in only one direction (due only to technical limitations of the first-generation apparatus), the image in Fig. 9.4 was obtained by sequentially rotating the cylindrical sample tube along an axis perpendicular to the gradient field, making it possible to reconstruct the distribution of spins in the xy plane from the radial sampling and subsequent projection reconstruction. The raw 2-D image shown in Fig. 9.4(a) was obtained with 12 sample orientations, with 30 free induction decay points per orientation. A linear, four-point spline interpolation of these data was used to produce the image shown in Fig. 9.4(b). From the figure, it is obvious that xenon was frozen to one side of the sample tube. From the calibrated gradient strength and the known apparent linewidth of frozen xenon without the application of the gradient (520 Hz), the resolution was estimated to be

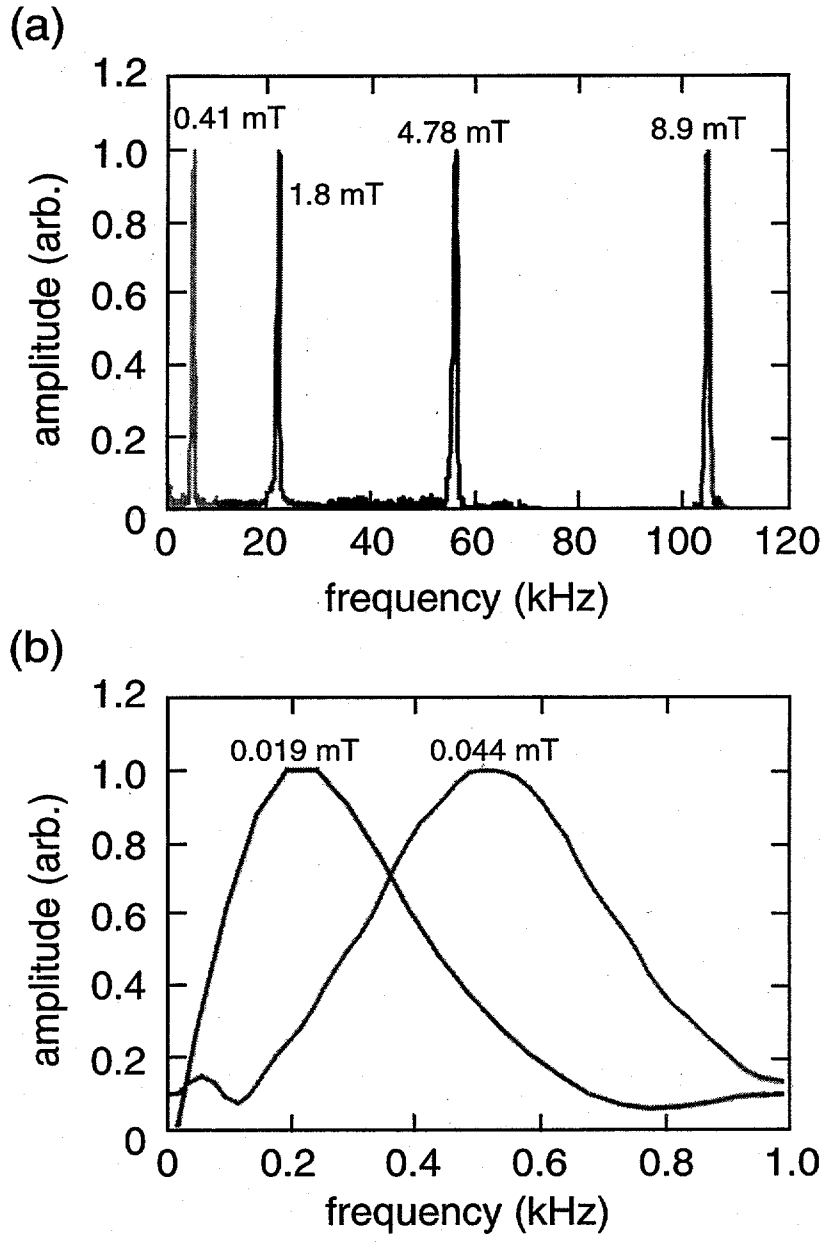

Figure 9.3: SQUID-detected ^{129}Xe NMR spectra of frozen laser-polarized xenon at 4.2 K obtained with external magnetic field strengths of (a) 0.41 mT, 1.8 mT, 4.78 mT, and 8.9 mT; (b) 0.019 mT and 0.044 mT [259]. Figure courtesy of Dinh TonThat.

$\sim$1 mm $\times$ 1 mm for the 2-D image.

9.3.2 Room-Temperature Experiments

The spectra and images shown in Figs. 9.3,9.4 were obtained with low-T_c SQUID detectors (meaning that the SQUID's threshold for superconduction was only several Kelvin), requiring the sample to be at liquid helium temperatures (4.2 K) in order for the SQUID to remain superconducting. Naturally, this temperature regime prohibits many of the types of experiments that could be performed, particularly ones involving living organisms. However, A high-T_c SQUID dewared to permit room-temperature experiments has recently been developed [261]. The high-T_c SQUID apparatus is shown schematically in Fig. 9.5.

Four recent preliminary results obtained with the high-T_c SQUID apparatus are shown in Fig. 9.6. In order to test the sensitivity of the SQUID detector, samples containing high concentrations of *thermally-polarized* protons were used (Fig. 9.6(a,b)). The quality of results obtained in these experiments proved to be highly SQUID-dependent, with the signal-to-noise varying over a factor of twenty when different SQUIDs were used in the apparatus. In addition to these experiments, it was impressively demonstrated that one SQUID detector was even sensitive enough to observe an extremely weak thermal proton signal (signal-to-noise: $\sim$2:1) from a proton-rich mineral oil sample at 20 G in a single scan [261], and could obtain similar signals in thousands of scans at Earth's field.

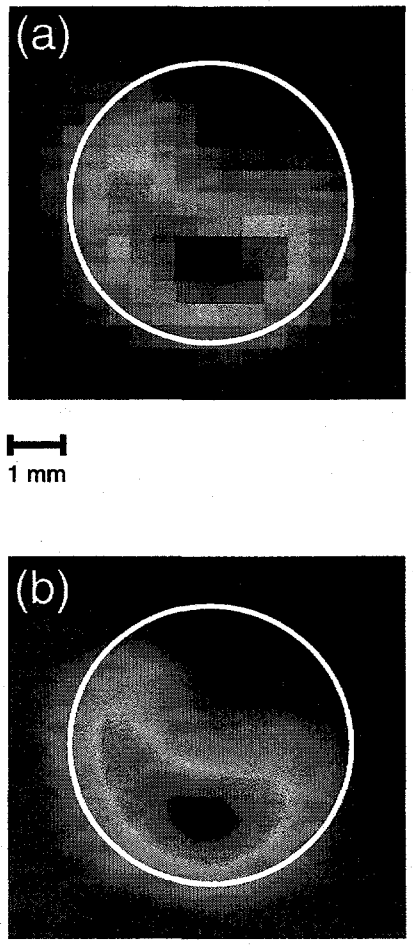

Figure 9.4: ^{129}Xe MR images taken of laser-polarized xenon frozen to the side of a glass tube immersed in liquid helium (4.2 K) at 10 G (0.001 T) [260]. The ^{129}Xe signal was detected with a low-T_c SQUID (color scheme: highest signal–dark red; lowest signal–dark blue). (a) raw data. (b) Processed image obtained following zero-filling and the application of cubic spline routines. Figures courtesy of Annjoe Wong-Foy.

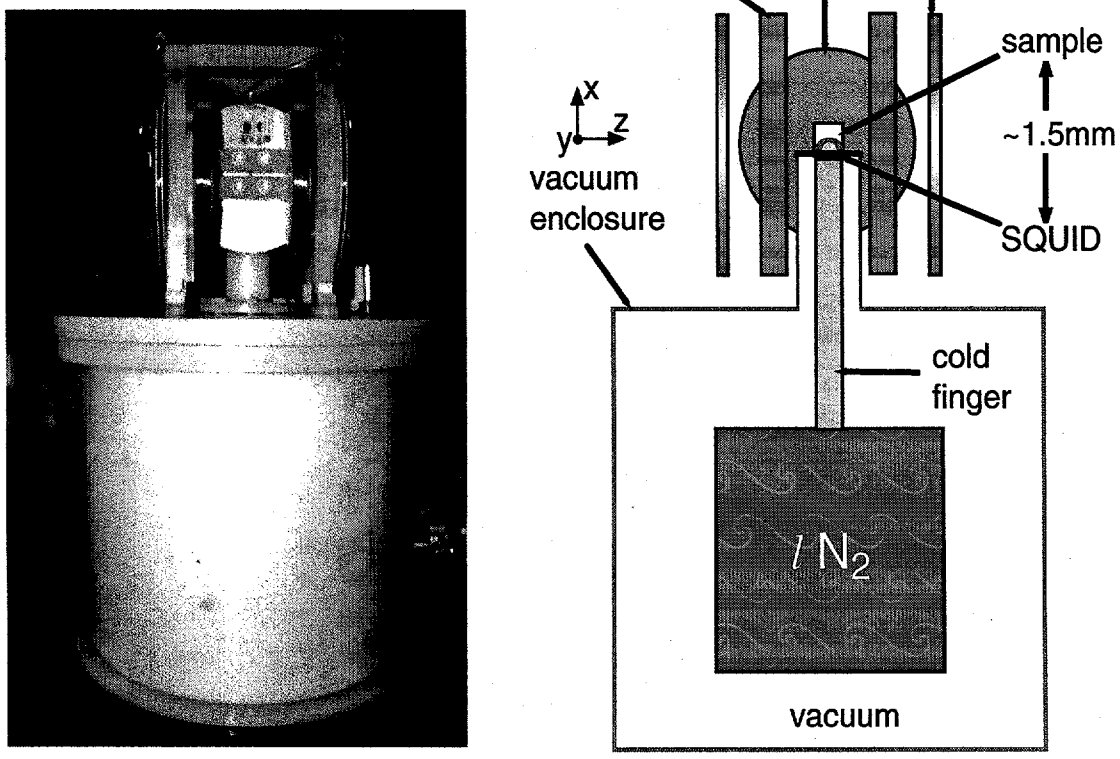

Figure 9.5: Picture and diagram depicting the High-T_c SQUID detector apparatus used for low-field room-temperature NMR/MRI experiments [261]. Note that the gradient coils are arranged parallel to static field coils, which in turn are arranged perpendicular to the audio-frequency (af) coils used to pulse on the nuclear spins. Figures courtesy of Annjoe Wong-Foy.

This apparatus has recently been used to obtain spectra from laser-polarized xenon gas at room temperature (Fig. 9.6(c)). Finally, a continuously recirculating-flow/optical pumping apparatus [54, 43, 44] was recently integrated with the high-T_c SQUID apparatus, permitting the 1-D ^{129}Xe projection image shown in the Fig. 9.6(d) to be obtained ($P_{Xe} \sim 0.1 - 1\%$). By providing the SQUID detector with a constant source of polarization, it should be possible to further optimize the SQUID apparatus to increase its signal-to-noise characteristics. Although this first image required 40,000 scans to obtain, recent improvements in the SQUID magnetometer has permitted improved images to be obtained in less than 15,000 scans. Relatively low xenon polarization and the use of naturally-abundant ^{129}Xe contributed to the relatively low signal-to-noise ratio of these experiments (compared to the thermal proton experiments). Even so, future improvements of the SQUID sensitivity of a factor of 10 or more are immediately anticipated, and the addition of multi-dimensional imaging capabilities (i.e., the addition of a complete x, y, z gradient set) is underway.

In the future, the combination of laser-polarized xenon delivery with polarization transfer to other nuclei in solution [89, 103, 110, 47] and on surfaces [171, 43] may be useful for enhancing *their* NMR signals at low fields, thereby permitting novel magnetic resonance experiments with a variety of potential biomedical and materials science applications.

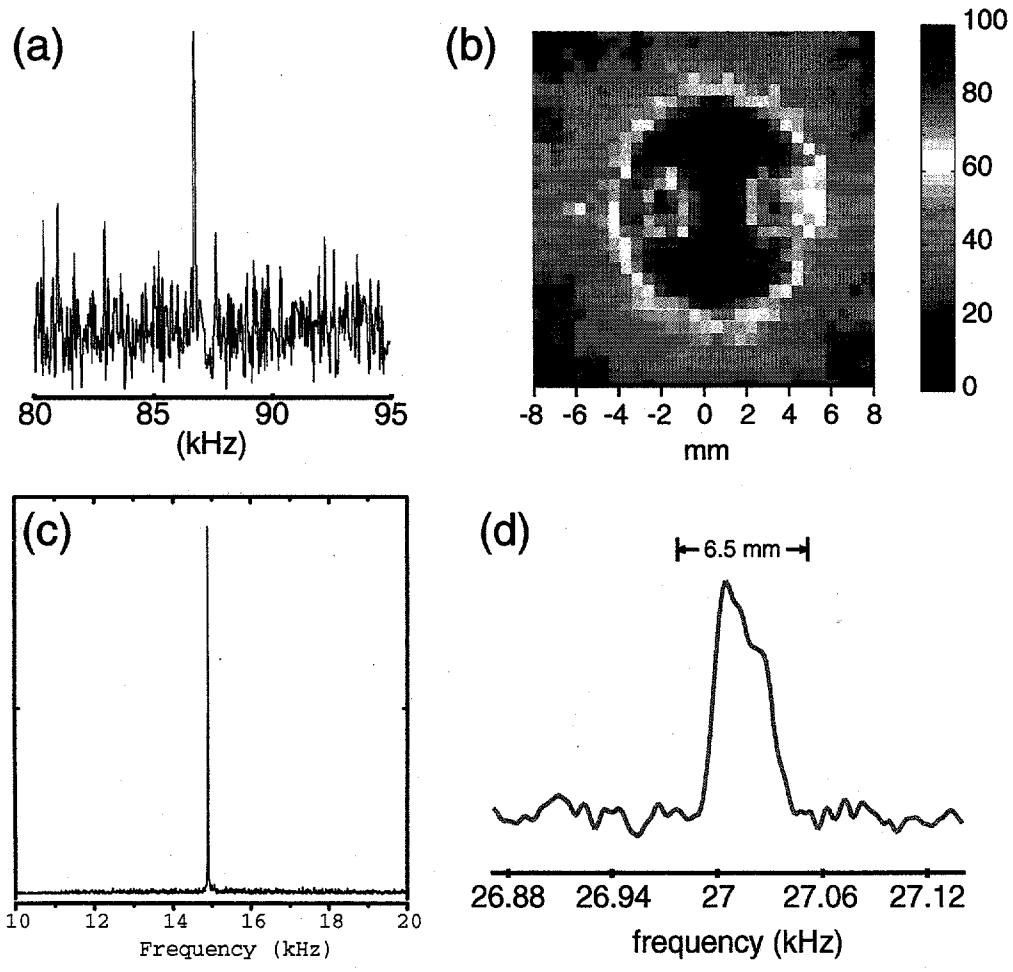

Figure 9.6: Preliminary results of room-temperature NMR/MRI experiments using a high-T_c SQUID detector [261]. (a) ^{1}H NMR signal obtained from 10,000 scans of a scientist's (thermally polarized) finger placed directly over the SQUID detector at 20 G. (b) ^{1}H MRI of thermally polarized mineral oil sample at 20 G; image was obtained via radial acquisition/ projection reconstruction following ~12 hr signal acquisition (recycle delay: ~30 ms). (c) ^{129}Xe OPNMR from a single scan from laser-polarized xenon gas at 12.6 G. S:N ~ 100:1. (d) 1-D projection ^{129}Xe image of continuously recirculating laser-polarized xenon gas obtained with 40,000 acquisitions, with applied gradient of 0.1 G/cm [262].

Bibliography

[1] A. Abragam, *Principles of Nuclear Magnetism.* (Oxford) 1961.

[2] M. Mehring, *High Resolution NMR Spectroscopy in Solids, 2nd Ed.* (Springer, Berlin) 1983.

[3] R.R. Ernst, G. Bodenhausen, and A. Wokaun, *Principles of Nuclear Magnetic Resonance in One and Two Dimensions.* (Oxford) 1994.

[4] L. Emsley and A. Pines, Lectures on pulsed NMR (2nd edition). (B. Maraviglia, editor). *Proceedings of the International School of Physics "Enrico Fermi."* 1994.

[5] T.C. Farrar and J.E. Harriman, *Density Matrix Theory and Its Applications in NMR Spectroscopy, 2nd Ed.* (Farragut, Madison, WI) 1995.

[6] C.P. Slichter, *Principles of Magnetic Resonance, 3rd Ed.* (Springer-Verlag, Berlin) 1996.

[7] C. Cohen-Tannoudji, B. Diu, and F. Laloë, *Quantum Mechanics.* (Hermann, Paris) 1977.

[8] L. Allen and J.H. Eberly, *Optical Resonance and Two-Level Atoms.* (Dover, New York) 1987.

[9] J.J. Sakurai, (S.F. Tuan, editor) *Modern Quantum Mechanics.* (Addison-Wesley; Reading, Mass.) 1994.

[10] P.T. Callaghan, *Principles of Nuclear Magnetic Resonance Microscopy.* (Oxford) 1991.

[11] Y. Xia, Contrast in NMR imaging and microscopy. *Concepts Magn. Reson.* **8**, 205-225 (1996).

[12] F.W. Wehrli, From NMR diffraction and zeugmatography to modern imaging and beyond. *Prog. NMR Spectrosc.* **28**, 87-135 (1995).

[13] W.S. Price, NMR Imaging. *Annual Reports on NMR Spectroscopy* **35**, 140-191 (1998).

[14] R.C. Wayne and R.M. Cotts, *Phys. Rev.* **151**, 264 (1966).

[15] S.M. De Paul, *Solid-State Nuclear Magnetic Resonance Studies of Cross Polarization from Quadrupolar Nuclei.* Ph.D. Dissertation, U.C. Berkeley, 1997.

[16] S. Wang, *Two-Dimensional Nuclear Magnetic Resonance of Quadrupolar Systems.* Ph.D. Dissertation, U.C. Berkeley, 1997.

[17] B.M. Goodson, Using injectable carriers of laser-polarized noble gases for enhancing NMR and MRI. *Concepts Magn. Reson.* **11**, 203-223 (1999).

[18] J. Brossel and A. Kastler, La détection de la résonance magnétique des Niveaux Excités: L'effet de Dépolarization des radiations de résonance optique et de fluorescence. *Compt. Rend.* **229**, 1213-1215 (1949).

[19] A. Kastler, Qulques Suggestions concernant la production optique et la détection optique d'une inégalité de population des niveaux de quantification spatiale des atomes. application à l'expérience de Stern et Gerlach et à la résonance magnétique. *J. Phys. Radium.* **11**, 255-265 (1950).

[20] A. Kastler, Optical methods of atomic orientation and of magnetic resonance, *J. Opt. Soc. Am.* **47**, 460-165 (1957).

[21] M.R. Bouchiat, T.R. Carver, and C.M. Varnum, Nuclear polarization in He^3 gas induced by optical pumping and dipolar exchange. *Phys. Rev. Lett.* **5**, 373-375 (1960).

[22] W. Happer, E. Miron, S. Schaefer, D. Schreiber, W.A. van Wijngaarden, and X. Zeng, Polarization of the nuclear spins of noble-gas atoms by spin exchange with optically pumped alkali metal atoms. *Phys. Rev. A* **29**, 3092-3110 (1984).

[23] T.G. Walker and W. Happer, Spin-exchange optical pumping of noble-gas nuclei. *Rev. Mod. Phys.* **69**, 629-642 (1997).

[24] R. Tycko and J.A. Reimer, Optical pumping in solid state nuclear magnetic resonance. *J. Phys. Chem.* **100**, 13240-13250 (1996).

[25] S.E. Barrett, R. Tycko, L.N. Pfeiffer, K.W. West, Directly detected nuclear magnetic resonance of optically pumped GaAs quantum wells. *Phys. Rev. Lett.* **72**, 1368-1371 (1994).

[26] S.E. Barrett, G. Dabbagh, L.N. Pfeiffer, K.W. West, and R. Tycko, Optically pumped NMR evidence for finite-size skyrmions in GaAs qunatum Wells near Landau level filling $\nu = 1$. *Phys. Rev. Lett.* **74**, 5112-5115 (1995).

[27] R. Tycko, S.E. Barrett, G. Dabbagh, L.N. Pfeiffer, and K.W. West, Electronic states in gallium arsenide quantum wells probed by optically pumped NMR. *Science* **268**, 1460-1463 (1995).

[28] J.A. Marohn, P.J. Carson, J.Y. Hwang, M.A. Miller, D.N. Shykind, and D.P. Weitekamp, Optical larmor beat detection of high-resolution nuclear magnetic resonance in a semiconductor heterostructure. *Phys. Rev. Lett.* **75**, 1364-1367 (1995).

[29] T. Pietraß, A. Bifone, T. Room, and E.L. Hahn, Optically enhanced high-field NMR of GaAs. *Phys. Rev. B* **53**, 4428-4433 (1996).

[30] S.E. Barrett, G. Dabbagh, L.N. Pfeiffer, K.W. West, and R. Tycko, Optically pumped nuclear magnetic resonance in the quantum Hall regimes. *Semicond. Sci. Tech.* **11**, 1488-1492 (1996).

[31] S.E. Barrett, G. Dabbagh, L.N. Pfeiffer, K.W. West, and R. Tycko, NMR Mea-

surement of the spin magnetization and spin dynamics in the quantum Hall regimes. *Surf. Sci.* **362**, 261-266 (1996).

[32] R. Tycko, Optical pumping of dipolar order in a coupled nuclear spin system. *Mol. Phys.* **95**, 1169-1176 (1998).

[33] C.A. Michal and R. Tycko, Nuclear spin polarization transfer with a single radio-frequency field in optically pumped indium phosphide. *Phys. Rev. Lett.* **81**, 3988-3991 (1998).

[34] R. Tycko, Optical pumping in indium phosphide: P-31 NMR measurements and potential for signal enhancement in biological solid state NMR. *Solid State Nucl. Magn. Reson.* **11**, 1-9 (1998).

[35] T. Pietraß, and M. Tomaselli, Optically pumped NMR in CdS single crystals. *Phys. Rev. B* **59**, 1986-1989 (1999).

[36] Y.-Q. Song, B.M. Goodson, K. Maranowski, and A.C. Gossard, Reduction of spin polarization near Landau filling factor $\nu = 3$ in GaAs/AlGaAs quantum wells. *Phys. Rev. Lett.* **82**, 2768-2771 (1999).

[37] G. Eckert, W. Heil, M. Meyerhoff, E.W. Otten, R. Surkau, M. Werner, M. Leduc, P.J. Nacher, and L.D. Schearer, A dense polarized He-3 target based on compression of optically pumped gas. *Nucl. Inst. and Meth. in Phys. Res. A* **320**, 53-65 (1992).

[38] E. Stolz, M. Meyerhoff, N. Bigelow, M. Leduc, P.J. Nacher, and G. Tastevin, High nuclear polarization in He-3 and He-3-He-4 gas mixtures by optical pumping with a laser diode. *Appl. Phys. B* **63**, 629-633 (1996).

[39] R.A. Bernheim, *Optical Pumping: An Introduction.* (Benjamin, New York) 1965.

[40] E. Brunner, Enhancement of surface and biological NMR spectroscopy using laser-polarized ^{129}Xe. *Concepts Magn. Reson.* **11**, 313-335 (1999).

[41] B.T. Saam, and M.S. Conradi, Low frequency NMR polarimeter for hyperpolarized gases. *J. Magn. Reson.* **134** 67-71 (1998).

[42] M.E. Wagshul and T.E. Chupp, Optical pumping of high-density Rb with a broadband dye laser and GaAlAs diode laser arrays: application to ^{3}He polarization. *Phys. Rev. A* **40**, 4447-4454 (1989).

[43] M. Haake, A. Pines, J.A. Reimer, and R. Seydoux, Surface-enhanced NMR using continuous-flow laser-polarized xenon. *J. Am. Chem. Soc.* **119**, 11711-11712 (1997)

[44] R. Seydoux, M. Haake, A. Pines, and J.A. Reimer, NMR with a continuously circulating flow of laser-polarized ^{129}Xe. *J. Phys. Chem. B* **103**, 4629-4637 (1999).

[45] T. Pietraß and H.C. Gaede, Optically polarized ^{129}Xe in NMR spectroscopy. *Adv. Mat.* **7**, 826-838 (1995).

[46] D. Raftery, H. Long, T. Meersmann, P.J. Grandinetti, L. Reven, and A. Pines, High-field NMR of adsorbed xenon polarized by laser pumping. *Phys. Rev. Lett.* **66**, 584-587 (1991).

[47] M. Luhmer, B.M. Goodson, Y.-Q. Song, D.D. Laws, L. Kaiser, M.C. Cyrier, and A. Pines, Study of xenon binding in cryptophane-A using laser-induced NMR polarization enhancement. *J. Am. Chem. Soc.* **121** 3502-3512 (1999).

[48] M. Gatzke, G.D. Cates, B. Driehuys, D. Fox, W. Happer, and B. Saam, Extraordinarily slow nuclear spin relaxation in frozen laser-polarized ^{129}Xe. *Phys. Rev. Lett.* **70**, 690-693 (1993).

[49] M.P. Augustine and K.W. Zilm, Optical pumping magnetic resonance in high magnetic fields - characterization of nuclear relaxation during pumping. *J. Chem. Phys.* **105**, 2998-3011 (1996).

[50] M.P. Augustine and K.W. Zilm, Optical pumping magnetic resonance in high magnetic fields - characterization of the optical properties of Rb-Xe mixtures. *Mol. Phys.* **89**, 737-752 (1996).

[51] M.P. Augustine and K.W. Zilm, Optical pumping magnetic resonance in high magnetic fields: Measurement of high field spin exchange cross sections. *Chem. Phys. Lett.* **280**, 24-30 (1997).

[52] H.J. Jänsch, T. Hof, U. Ruth, J. Schmidt, D. Stahl, and D. Fick, NMR of surfaces:

sub-monolayer sensitivity with hyperpolarized 129Xe. *Chem. Phys. Lett.* **296**, 146-150 (1998).

[53] U. Ruth, T. Hof, J. Schmidt, D. Fick, and H.J. Jänsch, Production of nitrogen-free, hyperpolarized Xe-129 gas. *Appl. Phys. B* **68**, 93-97 (1999).

[54] B. Driehuys, G.D. Cates, E. Miron, K. Sauer, D.K. Walter, and W. Happer, High-volume production of laser-polarized ^{129}Xe. *Appl. Phys. Lett.* **69**, 1668-1670 (1996).

[55] M.S. Rosen, T.E. Chupp, K.P. Coulter, R.C. Welsh, and S.D. Swanson, Polarized Xe-129 optical pumping/spin exchange and delivery system for magnetic resonance spectroscopy and imaging studies. *Rev. Sci. Inst.* **70**, 1546-1552 (1999).

[56] G.D. Cates, D.R. Benton, M. Gatzke, W. Happer, K.C. Hasson, and N.R. Newbury, Laser production of large nuclear-spin polarzation in frozen xenon. *Phys. Rev. Lett.* **65**, 2591-2594 (1990).

[57] D. Raftery and B. Chmelka, Xenon NMR spectroscopy. In: *NMR Basic Principles and Progress* (P. Diehl, E. Fluck, H. Günther, R. Kosfeld, and J. Seelig, editors). (Berlin Heidelberg: Springer-Verlag) Vol. **30**, p. 111-158 (1994).

[58] M. Haake, B.M. Goodson, D.D. Laws, E. Brunner, M.C. Cyrier, R.H. Havlin, and A. Pines, NMR of supercritical laser-polarized xenon. *Chem. Phys. Lett.* **292**, 686-690 (1998).

[59] P.K. Weathersby and L.D. Homer, Solubility of inert gases in biological fluids and tissues: a review. *Undersea Biomed. Res.* **7**, 277-296 (1980).

[60] S.C. Cullen and E.G. Gross, The anesthetic properties of xenon in human and animal beings, with additional observations on krypton. *Science* **113**, 580-582 (1951).

[61] R.R. Kennedy, J.W. Stokes, and P. Downing, Anaesthesia and inert gases with special reference to xenon. *Anaesth. Intens. Care* **20**, 66-70 (1992).

[62] A.M. Bidabé, D.G. de Beaufort, A.M. Gin, and J.M. Caillé, Measurements of cerebral blood-flow by the stable xenon computerized-tomography method. *J. Neuroradiol.* **17**, 103-124 (1990).

[63] M.S. Albert and D. Balamore, Development of hyperpolarized noble gas MRI. *Nucl. Instr. and Meth. in Phys. Res. A* **402**, 441-453 (1998).

[64] R.L. Streever and H.Y. Carr, Nuclear magnetic resonance of ^{129}Xe in natural xenon. *Phys. Rev.* **121**, 20-25 (1961).

[65] C.J. Jameson, A.K. Jameson, and S.M. Cohen, Temperature and density dependence of ^{129}Xe chemical shift in xenon gas. *J. Chem. Phys.* **59** 4540-4546 (1973).

[66] K.W. Miller, N.V. Reo, A.J.M.S. Uiterkamp, D.P. Stengle, T.R. Stengle, and K.L. Williamson, Xenon NMR: chemical shifts of a general anesthetic in common

solvents, proteins, and membranes. *Proc. Natl. Acad. Sci. USA* **78**, 4946-4949 (1981).

[67] C.I. Ratcliffe, Xenon NMR. *Annual Reports on NMR Spectroscopy* **36**, 124-208 (1998).

[68] J. Fraissard and T. Ito, ^{129}Xe n.m.r. study of adsorbed xenon: A new method for studying zeolites and metal-zeolites. *Zeolites* **8**, 350-361 (1988).

[69] P.J. Barrie and J. Klinowski, ^{129}Xe NMR as a probe for the study of microporous solids: a critical review. *Prog. NMR Spectrosc.* **24**, 91-108 (1992).

[70] J. Jokisaari, NMR of noble-gases dissolved in isotropic and anisotropic liquids. *Prog. NMR Spectrosc.* **26**, 1-26 (1994).

[71] C. Dybowski and N. Bansal, NMR spectroscopy of xenon in confined spaces: clathrates, intercalates, and zeolites. *Annu. Rev. Phys. Chem.* **42**, 433-464 (1991).

[72] Y.-Q. Song, B.M. Goodson, and A. Pines, NMR and MRI using laser-polarized xenon. *Spectroscopy*, in press.

[73] B.M. Goodson, L. Kaiser, and A. Pines, NMR and MRI of laser-polarized noble gases in molecules, materials, and organisms. *Proceedings of the International School of Physics "Enrico Fermi"*, in press.

[74] J.P. Mugler III, P.L. Bororad, B. Driehuys, and J.R. Brookeman, Nuclear Magnetic Resonance using hyperpolarized noble gases. *J. Magn. Reson. Anal.*, in press.

[75] L. Zhao and M.S. Albert, Biomedical imaging using hyperpolarized noble gas MRI: pulse sequence considerations. *Nucl. Instr. and Meth. in Phys. Res. A* **402**, 454-460 (1998).

[76] L. Zhao, R. Mulkern, C-H Tseng, D. Williamson, S. Patz, R. Kraft, R.L. Walsworth, F.A. Jolesz, and M.S. Albert, Gradient-echo imaging considerations for hyperpolarized ^{129}Xe MR. *J. Magn. Reson. B* **113**, 179-183 (1996).

[77] B.R. Patyal, J.-H. Gao, R.H. Williams, J. Roby, B. Saam, B.A. Rockwell, R.J. Thomas, D.J. Stolarski, and P.T. Fox, Longitudinal relaxation and diffusion measurements using magnetic resonance signals from laser-hyperpolarized ^{129}Xe nuclei. *J. Magn. Reson.* **126**, 58-65 (1997).

[78] J. Wolber, S.J. Doran, M.O. Leach, and A. Bifone, Measuring diffusion of xenon in solution with hyperpolarized ^{129}Xe NMR. *Chem. Phys. Lett.* **296**, 391-396 (1998).

[79] V.A. Rabinovich, A.A. Vasserman, V.I. Nedostup, and L.S. Veksler, *Thermophysical properties of neon, argon, krypton, and xenon.* (Standard Publishers: Moscow) 1976; (English translation: Hemisphere: Washington) 1988.

[80] J. Sandström *Dynamic NMR Spectroscopy.* (Academic Press: London) 1982.

[81] R.F. Tilton Jr. and I.D. Kuntz Jr., Nuclear magnetic resonance studies of xenon-129 with myoglobin and hemoglobin. *Biochemistry* **21**, 6850-6857 (1982).

[82] C.R. Bowers, H.W. Long, T. Pietraß, H.C. Gaede, and A. Pines, Cross polarization from laser-polarized solid xenon to $^{13}CO_2$ by low-field thermal mixing. *Chem. Phys. Lett.* **205**, 168-170 (1993).

[83] B. Driehuys, G.D. Cates, W. Happer, H. Mabuchi, B. Saam, M.S. Albert, and A. Wishnia, Spin transfer between laser-polarized xe-129 nuclei and surface protons. *Phys. Lett. A* **184**, 88-92 (1993).

[84] S.R. Hartmann and E.L. Hahn, *Phys. Rev.* **128**, 2042 (1962).

[85] A. Pines, M.G. Gibby, and J.S. Waugh, Proton-enhanced nuclear induction spectroscopy. A method for high resolution NMR of dilute spins in solids. *J. Chem. Phys.*, **56**, 1776-1777 (1972).

[86] A. Pines, M.G. Gibby, and J.S. Waugh, Proton enhanced NMR of dilute spins in solids. *J. Chem. Phys.* **59**, 569-590 (1973).

[87] H.W. Long, H.C. Gaede, J. Shore, L. Reven, C.R. Bowers, J. Kritzenberger, T. Pietraß, A. Pines, P. Tang, and J.A. Reimer, High field cross polarization NMR from laser polarized xenon to a polymer surface. *J. Am. Chem. Soc.* **115**, 8491-8492 (1993).

[88] H.C. Gaede, Y.-Q. Song, R.E. Taylor, E.J. Munson, J.A. Reimer, and A. Pines, High-field cross polarization NMR from laser-polarized xenon to surface nuclei. *Appl. Magn. Reson.* **8**, 373-384 (1995).

[89] G. Navon, Y.-Q. Song, T. Rõõm, S. Appelt, R.E. Taylor, and A. Pines, Enhancement of solution NMR and MRI with laser-polarized xenon. *Science* **271**, 1848-1851 (1996).

[90] A.W. Overhauser, Polarization of nuclei in metals. *Phys. Rev.* **92**, 411-415 (1953).

[91] T.R. Carver and C.P. Slichter, *Phys. Rev.* **92**, 212-213 (1953).

[92] I. Solomon, Relaxation processes in a system of two spins. *Phys. Rev.* 99, 559-565 (1955).

[93] J.H. Noggle and R.E. Shirmer, *The Nuclear Overhauser Effect: Chemical Applications.* (Academic Press, New York, London), 1971.

[94] D. Neuhaus and M.P. Williamson, *The Nuclear Overhauser Effect in Structural and Conformational Analysis.* (VCH, New York, Cambridge), 1989.

[95] J. Cavanagh, W.J. Fairbrother, A.G. Palmer, and N.J. Skelton, *Protein NMR Spectroscopy: Principles and Practice*, Academic Press: San Diego, 1996.

[96] Y.-Q. Song, Spin-polarization induced nuclear Overhauser effect: an application of laser-polarized xenon. *Concepts Magn. Reson.*, submitted.

[97] M. Luhmer, A. Moschos, and J. Reisse, Intermolecular dipole-dipole spin relaxation of xenon-129 dissolved in benzene. A molecular-dynamics simulation study. *J. Magn. Reson. A* **113**, 164-168 (1995).

[98] M. Luhmer and J. Reisse, Quadrupole NMR relaxation of the noble gases dissolved in simple liquids and solutions - A critical review of experimental data in the light of computer simulation results. *Prog. Nucl. Magn. Reson. Spectrosc.* **33**, 57-76 (1998).

[99] J. Stonehouse, P. Adell, J. Keeler, and A.J. Shaka, Ultrahigh quality NOE spectra. *J. Am. Chem. Soc.* **116**, 6037-6038 (1994).

[100] K. Stott, J. Keeler, Q.N. Van, and A.J. Shaka, One-dimensional NOE experiments using pulsed field gradients. *J. Magn. Reson.* **125**, 302-324 (1997).

[101] M. Garwood and Y. Ke, Symmetrical pulses to induce arbitrary flip angles with compensation for rf inhomogeneity and resonance offsets. *J. Magn. Reson.* **94**, 511-525 (1991).

[102] T.L.. Hwang, P.C.M. van Zijl, and M. Garwood, Fast broadband inversion by adiabatic pulses. *J. Magn. Reson.* **133**, 200-203 (1998).

[103] Y.-Q. Song, B.M. Goodson, R.E. Taylor, D.D. Laws, G. Navon, and A. Pines, Selective enhancement of NMR signals for α-cyclodextrin with laser-polarized xenon. *Angew. Chem., Int. Ed. Engl.* **36**, 2368-2370 (1997).

[104] P.M. Rentzepis and D.C. Douglass, Xenon as a solvent. *Nature* **293**, 165-166 (1981).

[105] M.B. Sponsler, B.H. Weiller, P.O. Stoutland, and R.G. Bergman, Liquid xenon: an effective inert solvent for C-H oxidative addition reactions. *J. Am. Chem. Soc.* **111**, 6841-6843 (1989).

[106] L.D. Field, A.V. George, B.A. Messerle, and H. Ionn, Sample tube for medium-pressure nuclear magnetic resonance spectroscopy in liquid xenon. *Anal. Chem.* **63**, 184-186 (1991).

[107] K.L. Sauer, R.J. Fitzgerald, and W. Happer, Laser-polarized liquid xenon. *Chem. Phys. Lett.* **277**, 153-158 (1997).

[108] M. Haake, R. Seydoux, J.A. Reimer, and A. Pines, *39th Rocky Mountain Conference on Analytical Chemistry*, Denver, CO 1997.

[109] C.H. Tseng, R.W. Mair, G.P. Wong, D. Williamson, D.G. Cory, and R.L. Walsworth, Magnetic resonance imaging of laser-polarized liquid xenon. *Phys. Rev. E.*, in press.

[110] R.J. Fitzgerald, K.L. Sauer, and W. Happer, Cross-relaxation in laser-polarized liquid xenon. *Chem. Phys. Lett.* **284**, 87-92 (1998).

[111] P.E. Savage, S. Gopalan, T.I. Mizan, C.J. Martino, and E.E. Brock, Reactions

at supercritical conditions - applications and fundamentals. AIChE J. **41**, 1723-1778 (1995).

[112] S. Ikawa and Y. Fujita, Intramolecular and intermolecular hydrogen-bonds of 4-hydroxy-4-methylpentan-2-one in supercritical xenon. *J. Phys. Chem.* **97**, 10607-10612 (1993).

[113] E. Castillo, A. Marty, D. Combes, and J.S. Condoret, Polar substrates for enzymatic-reactions in supercritical CO2 - how to overcome the solubility limitation. *Biotech. Lett.* **16**, 169-174 (1994).

[114] M. Poliakoff, S.M. Howdle, and S.G. Kazarian, Vibrational spectroscopy in supercritical fluids: from analysis and hydrogen bonding to polymers and synthesis. *Angew. Chem. Int. Ed. Engl.* **34**, 1275-1295 (1995).

[115] I.T. Horvath and J.M. Millar, NMR under high gas pressure. *Chem. Rev.* **91**, 1339-1351 (1991).

[116] J.W. Rathke, R.J. Klingler, and T.R. Krause, Propylene hydroformylation in supercritical carbon-dioxide. *Organometallics* **10**, 1350-1355 (1991).

[117] J.W. Rathke, R.J. Klingler, and T.R. Krause, Thermodynamics for the hydrogenation of dicobalt octacarbonyl in supercritical carbon-dioxide. *Organometallics* **11** 585-588 (1992).

[118] F. Okada, and V.A. Apkarian, Electonic relaxation of Xe2 Cl in gaseous and supercritical fluid xenon. *J. Chem. Phys.* **94**, 133-144 (1991).

[119] S.V. Kamat, E.J. Beckman, and A.J. Russell, Enzyme-activity in supercritical fluids. *Crit. Rev. Biotech.* **15**, 41-71 (1995).

[120] N. Fontes, E. Nogueiro, A.M. Elvas, T.C. de Sampaio, and S. Barreiros, Effect of pressure on the catalytic activity of subtilisin Carlsberg suspended in compressed gases. *Biochim. Biophys. Acta* **1383**, 165-174 (1998).

[121] S.M. Howdle, M. Jobling, and M. Poliakoff, Spectroscopic investigations of organometallic photochemistry in supercritical fluids. *ACS Symposium Ser.* **488** 121-131 (1992).

[122] H. Destaillats and R. Fernndez-Prini, Solubility of I_2 (s) and equilibrium concentration of the (I_2 + C_6H_6) charge transfer complex in supercritical xenon with added C_6H_6. *J. Chem. Thermod.* **29**, 1209-1221 (1997).

[123] E.R. Hunt and H.Y. Carr, Nuclear magnetic resonance of Xe^{129} in natural xenon. *Phys. Rev.* **130**, 2302-2305 (1963).

[124] D.R. Lide (Ed.), *CRC Handbook of Chemistry and Physics 1990-1991* (CRC Press, Boca Raton) 1990.

[125] B.P. Schoenborn, H.C. Watson, and J.C. Kendrew, Binding of xenon to sperm whale myoglobin. *Nature* **207**, 28-30 (1965).

[126] B.P. Schoenborn, Binding of xenon to horse haemoglobin, *Nature* **208**, 760-762 (1965).

[127] R.F. Tilton Jr., I.D. Kuntz Jr., and G.A. Petsko, Cavities in proteins: structure of a metmyoglobin-xenon complex solved to 1.9 Å. *Biochemistry* **23**, 2849-2857 (1984).

[128] S. McKim and J.F. Hinton, Evidence of xenon transport through the gramicidin channel - a xe-129-NMR study. *Biochim. Biophys. Acta* **1193**, 186-198 (1994).

[129] M. Shlitz, T. Prangé, and R. Fourme, On the preparation and X-ray data collection of isomorphous xenon derivatives. *J. Appl. Cryst.* **27**, 950-960 (1994).

[130] M. Shlitz, R. Fourme, I. Broutin, and T. Prangé, The catalytic site of serine proteinases as a specific binding cavity for xenon. *Structure* **3**, 309-316 (1995).

[131] T. Prangé, M. Shlitz, L. Pernot, N. Colloc'h. S. Longhi, W. Bourget, and R. Fourme, Exploring hydrophobic sites in proteins with xenon or krypton. *Prot. Struc. Func.* **30**, 61-73 (1998).

[132] J. Wolber, A. Cherubini, A.S.K. Dzik-Jurasz, M.O. Leach, and A. Bifone, Spin-lattice relaxation of laser-polarized xenon in human blood. *Proc. Natl. Acad. Sci. USA* **96**, 3664-3669 (1999).

[133] J.A. Ripmeester, C.I. Ratcliffe, and J.S. Tse, The nuclear magnetic resonance of

^{129}Xe trapped in clathrates and some other solids. *J. Chem. Soc. Faraday Trans. 1*, **84**, 3731-3745 (1988).

[134] T. Pietraß, H.C. Gaede, A. Bifone, A. Pines, and J.A. Ripmeester, Monitoring xenon clathrate hydrate formation on ice surfaces with optically enhanced ^{129}Xe NMR. *J. Am. Chem. Soc.* **117**, 7520-7525 (1995).

[135] Y. Xu and P. Tang, Amphiphilic sites for general anesthetic action? Evidence from ^{129}Xe-^{1}H intermolecular nuclear Overhauser effects. *Biochim. Biophys. Acta* 1323, 154-162 (1997).

[136] D.J. Cram, M.E. Tanner, and C.B. Knobler, Guest release and capture by hemicarcerands introduces the phenomenon of constrictive binding. *J. Am. Chem. Soc.* **113**, 7717-7727 (1991).

[137] T.A. Robbins, C.B. Knobler, D.R. Bellew, and D.J. Cram, A highly adaptive and strongly binding hemicarcerand. *J. Am. Chem. Soc.* **116**,111-122 (1994).

[138] N. Branda, R.M. Grotzfeld, C. Valdés, and J. Rebek Jr., Control of self-assembly and reversible encapsulation of xenon in a self-assembling dimer by acid-base chemistry. *J. Am. Chem. Soc.* **117**, 85-88 (1995).

[139] K. Bartik, M. Luhmer, S.J. Heyes, R. Ottinger, and J. Reisse, Probing molecular cavities in α-cyclodextrin solutions by xenon NMR. *J. Magn. Reson. B* **109**, 164-168 (1995).

[140] E.B. Brouer, J. Enright, and J.A. Ripmeester, Solid-state NMR and diffraction studies of *p-tert*butylcalix[4]arene·nitrobenzene·xenon. *Chem. Commun.*, 939-940 (1997).

[141] T.K. Hitchens and R.G. Bryant, Noble-gas relaxation agents. *J. Magn. Reson.* **124**, 227 (1997).

[142] K. Bartik, M. Luhmer, J.-P. Dutasta, A. Collet, and J. Reisse, ^{129}Xe and ^{1}H NMR study of the reversible trapping of xenon by cryptophane-A in organic solution. *J. Am. Chem. Soc.* **120**, 784-791 (1998).

[143] P. Seeman, The membrane actions of anesthetics and tranquilizers. *Pharmacol. Rev.* **24**, 583-655 (1972).

[144] K.W. Miller, The nature of the site of general anesthesia. *Int. Rev. Neurobiol.* **27**, 1-61 (1985).

[145] N.P. Franks and W.R. Leib, What is the molecular nature of general anesthetic target sites? *Trends Parmacol. Sci.* **8**, 169-174 (1987).

[146] N.P. Franks and W.R. Leib, Molecular and cellular mechanisms of general anethesia. *Nature* **367**, 607-614 (1994).

[147] J. Szejtli, *Cyclodextrin Technology.* (Kluwer-Academic, Dordrecht) 1988.

[148] F.C. Cramer, and F.M. Henglein, *Chem. Ber.* **90**, 2561-2571 (1957).

[149] F.C. Cramer, and F.M. Henglein, *Chem. Ber.* **90**, 2572-2575 (1957).

[150] W. Saenger and M. Noltenmeyer, X-ray structure analysis of the α-cyclodextrin-krypton inclusion complex: a noble gas in an organic matrix. *Angew. Chem. Int. Ed. Engl.* **13**, 552-553 (1974).

[151] P.D. Kirchhoff, M.B. Bass, B.A. Hanks, J.M. Briggs, A. Collet, and J.A. McCammon, Structural fluctuations of a cryptophane host: A molecular dynamics simulation. *J. Am. Chem. Soc.* **118**, 3237-3246 (1996).

[152] J. Canceill and A. Collet, *J. Chem. Soc., Chem. Commun.*, 1137-1139 (1981).

[153] J. Canceill and A. Collet, 2-Step Synthesis of D3 and C3H cryptophanes. *J. Chem. Soc., Chem. Commun.*, 582-584 (1988).

[154] P.A. Jennings, M.J. Stone, and P.E. Wright, Overexpression of myoglobin and assignment of its amide, C-alpha and C-beta resonances. *J. Biomol. NMR* **6**, 271-276 (1995).

[155] M. Luhmer, manuscript in preparation.

[156] T. Samejima and J.T. Yang, *J. Mol. Biol. B*, 863-871 (1964).

[157] D.W. Smith and R.J.P. Williams, *Biochem J.* **110**, 297-301 (1968).

[158] R.E. Taylor, J. Heller, B.M. Goodson, D.D. Laws, Y.-Q. Song, H.M. Bitter, and A. Pines, unpublished results.

[159] A.E. Eriksson, W.A. Baase, X.J. Zhang, D.W. Heinz, M. Blaber, E.P. Baldwin, and B.W. Matthews, Response of a protein-structure to cavity-creating mutations and its relation to the hydrophobic effect. *Science* **255**, 178-183 (1992).

[160] A.E. Eriksson, W.A. Baase, J.A. Wozniak, and B.W. Matthews, A cavity-containg mutant of T4 lysozyme is stabilized by buried benzene. *Nature* **355**, 371-373 (1992).

[161] V.A. Feher, E.P. Baldwin, and F.W. Dahlquist, Access of ligands to cavities within the core of a protein is rapid. *Nature Struct. Biol.* **3**, 516-521 (1996).

[162] S.M. Rubin, B.M. Goodson, D.D. Laws, A. Pines, and D.E. Wemmer, unpublished results.

[163] F.R. Salsbury Jr. and R.A. Harris, Estimation of the Fermi contact contribution to the xenon-hydrogen and xenon-xenon spin-spin coupling constants. *Mol. Phys.* **94**, 307-312 (1998).

[164] G.C. Chingas, A.N. Garroway, W.B. Moniz, and R.D. Bertrand, Adiabatic J cross-polarization in liquids for signal enhancement in NMR. *J. Am. Chem. Soc.* **102**, 2526-2528 (1980).

[165] J.W. Emsley and J.C. Lindon, *NMR spectroscopy using liquid crystal solvents.* (Pergamon, Oxford) 1975.

[166] R.Y. Dong, *Nuclear magnetic resonance of liquid crystals, 2nd ed.* (Springer-Verlag, New York) 1997.

[167] F. Castiglione, New techniques of spectral simplification and automatic analysis of complex anisotropic spectra. Ph.D. Thesis, Università delgi Studi della Calabria 1997-1998.

[168] M.G. Kubinec, M. Marjanska, I.L. Chuang, and A. Pines, manuscript in preparation.

[169] N. Tjandra and A. Bax, Direct measurement of distances and angles in biomolecules by NMR in a dilute liquid crystalline medium. *Science* **278**, 1111-1114 (1997).

[170] D. Raftery, L. Reven, H. Long, A. Pines, P. Tang, and J.A. Reimer, Spin-polarized ^{129}Xe NMR study of a polymer surface. *J. Phys. Chem.* **97**, 1649-1655 (1993).

[171] T. Rõõm, S. Appelt, R. Seydoux, A. Pines, and E.L. Hahn, Enhancement of surface NMR by laser-polarized noble gases. *Phys. Rev. B* **55**, 11604-11610 (1997).

[172] T. Pietraß, R. Seydoux, and A. Pines, Surface selective ^{1}H/^{29}Si CP NMR by NOE Enhancement from Laser-Polarized Xenon. *J. Magn. Reson.* **133**, 299-303 (1998).

[173] E. Brunner, M. Haake, A. Pines, J. Reimer, and R. Seydoux, Enhanced surface

NMR of zeolites and related materials using laser-polarized xenon. *J. Mat. Res. Soc.*, in press.

[174] R. Simonutti, T. Meersmann, J.W. Logan, A. Commotti, P. Sozzani, S. Calderelli, and A. Pines, Properties of the 1-dimensional gas phase in sub-nano-channels detected by optically polarized ^{129}Xe NMR, manuscript in preparation.

[175] M.A. Springuelhuet and J. Fraissard, Xe-129 NMR of xenon adsorbed on the molecular-sieves ALPO4-11 and SAPO-11 - chemical shift anisotropy related to the asymmetry of the adsorption zones. *Chem. Phys. Lett.* **154**, 299-302 (1989).

[176] J.A. Ripmeester and C.I. Ratcliffe, The anisotropic chemical-shift of Xe-129 in the molecular-sieve ALPO-11 - a dynamic averaging model. *J. Chem. Phys.* **99**, 619-622 (1995).

[177] D. Raftery, E. MacNamara, G. Fisher, C.V. Rice, and J. Smith, Optical pumping and magic angle spinning: sensitivity and resolution enhancement for surface NMR obtained with laser-polarized xenon. *J. Am. Chem. Soc.* **119**, 8746-8747 (1997).

[178] E. Brunner, R. Seydoux, M. Haake, A. Pines, and J.A. Reimer, Surface NMR using laser-polarized ^{129}Xe under magic angle spinning conditions. *J. Magn. Reson.* **130**, 145-148 (1998).

[179] E. Brunner, M. Haake, A. Pines, J.A. Reimer, and R. Seydoux, Enhancement

of C-13 NMR signals in solid C-60 and C-70 using laser-polarized xenon. *Chem. Phys. Lett.* **290**, 112-116 (1998).

[180] R.D. Johnson, C.S. Yannoni, H.C. Dorn, J.R. Salem, and D.S. Bethune, C-60 rotation in the solid state - dynamics of a faceted spherical top. *Science* **255**, 1235-1238 (1992).

[181] R. Tycko, G. Dabbagh, R.M. Fleming, R.C Haddon, A.V. Makhija, and S.M. Zahurak, Molecular dynamics and the phase transition in solid C60. *Phys. Rev. Lett.* **67**, 1886-1889 (1991).

[182] R. Tycko, G. Dabbagh, G.B.M. Vaughan, P.A. Heiney, R.M. Strongin, M.A. Cichy, and A.B. Smith III, Molecular orientational dynamics in solid C-70 - investigation by one-dimensional and 2-dimensional magic angle spinning nuclear magnetic resonance. *J. Chem. Phys.* **99**, 7554-7564 (1993).

[183] R. Blinc, J. Seliger, J. Dolinšek, and D. Arčon, 2-dimensional C-13 NMR study of orientational ordering in solid C60. *Phys. Rev. B* **49**, 4993-5002 (1994).

[184] E. MacNamara, G. Fisher, J. Smith, C.V. Rice, S.-J. Hwang, and D. Raftery, Cross polarization and cross relaxation from laser-polarized xenon to surface species. *J. Phys. Chem. B* **103**, 1158-1160 (1999).

[185] D.M. Gregory, R.E. Gerald II, and R.E. Botto, Pore-structure determinations

of silica aerogels by Xe-129 NMR spectroscopy and imaging *J. Magn. Reson.* **131**, 327-335 (1998).

[186] M.S. Albert, G.D. Cates, B. Driehuys, W. Happer, B. Saam, C.S. Springer Jr., and A. Wishnia, Biological magnetic resonance using laser-polarized ^{129}Xe. *Nature* **370**, 199-201 (1994).

[187] H. Middleton, R.D. Black, B. Saam, G.D. Cates, C.P. Cofer, R. Guenther, W. Happer, L.W. Hedlund, G.A. Johnson, K. Juvan, and J. Swartz, MR-imaging with hyperpolarized He-3 gas. *Magn. Reson. Med.* **33**, 271-275 (1995).

[188] Y.-Q. Song, H.C. Gaede, T. Pietraß, G.A. Barrall, G.C. Chingas, M.R. Ayers, and A. Pines, Spin-polarized ^{129}Xe gas imaging of materials. *J. Magn. Reson. A* **115**, 127-130 (1995).

[189] Y.-Q. Song, R.E. Taylor, B.M. Goodson, and A. Pines, unpublished results.

[190] Y.-Q. Song, R.E. Taylor, and A. Pines, Imaging of laser-polarized solid xenon. *Solid State Nucl. Magn. Reson.* **10**, 247-250 (1998).

[191] W.B. Hyslop and P. C. Lauterbur, Effects of restricted diffusion on microscopic NMR imaging. *J. Magn. Reson.* **94**, 501-510 (1991).

[192] B. Putz, D. Barsky, and K. Schulten, Edge enhancement by diffusion in microscopic magnetic-resonance-imaging. *J. Magn. Reson.* **97**, 27-53 (1992).

[193] D. Barsky, B. Putz, K. Schulten, J. Schoeniger, E.W. Hsu, and S. Blackband, Diffusional edge enhancement observed by NMR in thin glass-capillaries. *Chem. Phys. Lett.* **200**, 88-96 (1992)

[194] P.T. Callaghan, A. Coy, L.C. Forde, and C.J. Rofe, Diffusive relaxation and edge enhancement in NMR microscopy. J. Magn. Reson. A **101**, 347-350 (1993).

[195] S.D. Stoller, W. Happer, and F.J. Dyson, Transverse spin relaxation in inhomogeneous magnetic-fields. *Phys. Rev. A* **44**, 7459-7477 (1991).

[196] T.M. de Swiet and P.N. Sen, Decay of nuclear magnetization by bounded diffusion in a constant field gradient. *J. Chem. Phys.* **100**, 5597-5604 (1994).

[197] T.M. de Swiet, Diffusive edge enhancement in imaging. it J. Magn. Reson. B **109**, 12-18 (1995).

[198] P.W.E. Peereboom, H. Luigjes, and K.O. Prins, An NMR spin-echo study of self-diffusion in xenon. *Physica A* **156**, 260-276 (1989).

[199] D.M. Schmidt, J.S. George, S.I. Penttila, A. Caprihan, and E. Fukushima. Diffusion imaging with hyperpolarized He-3 gas. *J. Magn. Reson.* **129**, 184-187 (1997).

[200] B. Saam, N. Drukker, and W. Happer, Edge enhancement observed with hyperpolarized ^{3}He. *Chem. Phys. Lett.* **263**, 481-487 (1996).

[201] Y.-Q. Song, B.M. Goodson, B. Sheridan, T.M. de Swiet, and A. Pines, Effects of diffusion of magnetic resonance imaging of laser-polarized xenon gas. *J. Chem. Phys.* **108**, 6233-6239 (1998).

[202] J. Karger and W. Heink, *J. Magn. Reson.* **51**, 1 (1983).

[203] R.E. Taylor, Y.-Q. Song, T. Rõõm, S. Appelt, R. Seydoux, A. Bifone, D. de Graw, B. Goodson, D. Laws, and A. Pines, 37th Experimental Nuclear Magnetic Resonance Conference, Pacific Grove, CA 1996.

[204] D. Le Bihan, E. Breton, D. Lallemand, P. Grenier, E. Cabanis, and M. Laval-Jeantet, Radiology **161**, 401 (1986).

[205] R. Turner and D. Le Bihan, Single-shot diffusion imaging at 2.0 Tesla. *J. Magn. Reson.* **86**, 445-452 (1990).

[206] E. Brunner, M. Haake, L. Kaiser, A. Pines, and J.A. Reimer, Gas flow MRI using circulating laser-polarizing xenon. *J. Magn. Reson.* **138**, 155-159 (1999).

[207] P.T. Callaghan, C.D. Eccles, and Y. Xia, NMR Microscopy of dynamic displacements - k-space and q-space imaging. *J. Phys. E: Sci. Instrum.* **21**, 820-822 (1988).

[208] A.E. Sheidegger, *The Physics of Flow Through Porous Media*, (MacMillan, New York) 1957.

[209] I.F. Golubev, *Viscosity of Gases and Gas Mixtures* (trans., Israel Program for Scientific Translation) Jerusalem, 1970.

[210] A. Haase, J. Frahm, D. Matthaei, W. Hanicke, and K.D. Merboldt, FLASH imaging. Rapid NMR imaging using low flip-angle pulses. *J. Magn. Reson.* **67**, 258-266 (1986).

[211] R.D. Black, H.L. Middleton, G.D. Cates, G.P. Cofer, B. Driehuys, W. Happer, L.W. Hedlund, G.A. Johnson, M.D. Shattuck, and J.C. Swartz, *In vivo* He-3 MR images of guinea pig lungs. *Radiology* **199**, 867-870 (1996).

[212] K. Sakai, A.M. Bilek, E. Oteiza, R.L. Walsworth, D. Balamore, F. Jolesz, and M.S. Albert, Temporal dynamics of hyperpolarized ^{129}Xe resonances in living rats. *J. Magn. Reson. B* **111**, 300-304 (1996).

[213] M.E. Wagshul, T.M. Button, H.F. Li, Z. Liang, C.S. Springer Jr., K. Zhong, and A. Wishnia, *In vivo* MR imaging and spectroscopy using hyperpolarized ^{129}Xe. *Magn. Reson. Med.* **36**, 183-191 (1996).

[214] G.A. Johnson, G. Cates, X.J. Chen, G.P. Cofer, B. Driehuys, W. Happer, L.W. Hedlund, B. Saam, M.D. Shattuck, and J. Swartz, Dynamics of magnetization in hyperpolarized gas MRI of the lung. *Magn. Reson. Med* **38**, 66-71 (1997).

[215] X.J. Chen, M.S. Chawla, G.P. Cofer, L.W. Hedlund, H.E. Möller, and G.A.

Johnson, Hyperpolarized ^{3}He NMR lineshape measurements in the live guinea pig lung. *Magn. Reson. Med* **40**, 61-65 (1998).

[216] J.R. Macfall, H.C. Charles, R.D. Black, H. Middleton, J.C. Swartz, B. Saam, B. Driehuys, C. Erickson, W. Happer, G.D. Cates, G.A. Johnson, and C.E. Ravin, Human lung air spaces: potential for MR imaging with hyperpolarized He-3. *Radiology* **200**, 553-558 (1996).

[217] M. Ebert, T. Großmann, W. Heil, W.E. Otten, R. Surkau, M. Leduc, P. Bachert, M.V. Knopp, L.R. Schad, and M. Thelen, Nuclear magnetic resonance imaging with hyperpolarised helium-3. *Lancet*, **347**, 1297-1299 (1996).

[218] P. Bachert, L.R. Schad, M. Bock, M.V. Knopp, M. Ebert, T. Großmann, W. Heil, D. Hofmann, R. Surkau, and E.W. Otten, Nuclear magnetic resonance imaging of airways in humans with use of hyperpolarized ^{3}He. *Magn. Reson. Med.* **36**, 192-196 (1996).

[219] H.U. Kauczor, D. Hofmann, K.F. Kreitner, H. Nilgens, R. Surkau, W. Heil, A. Potthast, M.V. Knopp, E.W. Otten, and M. Thelen, Normal and abnormal pulmonary ventilation: visualization at hyperpolarized He-3 MR imaging. *Radiology* **201**, 564-568 (1996).

[220] J.P. Mugler III, B. Driehuys, J.R. Brookeman, G.D. Cates, S.S. Berr, R.G. Bryant, T.M. Daniel, E.E. del Lange, J.H. Downs III, C.J. Erickson, W. Happer, D.P. Hinton, N.F. Kassel, T. Maier, C.D. Phillips, B.T. Saam, K.L. Sauer, and

M.E. Wagshul, MR imaging and spectroscopy using hyperpolarized ^{129}Xe gas: preliminary human results. *Magn. Reson. Med.* **37**, 809-815 (1997).

[221] X.J. Chen, M.S. Chawla, L.W. Hedlund, H.E. Möller, J.R. MacFall, and G.A. Johnson, MR microscopy of lung airways with hyperpolarized ^{3}He. *Magn. Reson. Med.* **39**, 79-84 (1998).

[222] M.S. Albert, C.H. Tseng, D. Williamson, E.R. Oteiza, R.L. Walsworth, B. Kraft, D. Kacher, B.L. Holman, and F.A. Jolesz, Hyperpolarized Xe-129 MR imaging of the oral cavity. *J. Magn. Reson. B* **111**, 204-207 (1996).

[223] M.D. Shattuck, S.L. Gewalt, G.H. Glover, L.W. Hedlund, and G.A. Johnson, Spatial and temporal dynamics of magnetization in hyperpolarized gas MRI of the lung. *Magn. Reson. Med.* **38**, 938-942 (1997).

[224] M.S. Albert, V.D. Schepkin, and T.F. Budinger, Measurement of ^{129}Xe T_1 in blood to explore the feasibility of hyperpolarized ^{129}Xe MRI. *J. Comput. Assisted Tomogr.* **19**, 975-978 (1995).

[225] A. Bifone, Y.-Q. Song, R. Seydoux, R.E. Taylor, B.M. Goodson, T. Pietraß, T.F. Budinger, G. Navon, and A. Pines, NMR of laser-polarized xenon in human blood. *Proc. Natl. Acad. Sci. USA* **93**, 12932-12936 (1996).

[226] C.H. Tseng, S. Peled, L. Nascimben, E. Oteiza, R.L. Walsworth, and F.A.

Jolesz, NMR of laser-polarized ^{129}Xe in blood foam. *J. Magn. Reson.* **126**, 79-86 (1997).

[227] H. Weingartner, R. Haselmeier, and M. Holz, ^{129}Xe NMR as a new tool for studying gas diffusion in liquids: self-diffusion of xenon in water. *Chem. Phys. Lett.* **195**, 596-601 (1992).

[228] K.R. Thulborn, J.C. Waterton, P.M. Matthews, and G.K. Radda, Oxygenation dependence of the transverse relaxation time of water protons in whole blood at high field. *Biochim. Biophys. Acta* **714**, 265-270 (1982).

[229] R. Turner, D. Le-Bihan, C.T.W. Moonen, D. Despres, and J. Frank, Echo-planar time course MRI of cat brain oxygenation changes. *Magn. Reson. Med.* **22**, 159-166 (1991).

[230] S.J. Ogawa, D.W. Tank, R. Menon, J.M. Ellemann, S.G. Kim, H. Merkle, and K. Ugurbil, Intrinsic signal changes accompanying sensory stimulation: functional brain mapping with magnetic resonance imaging. *Proc. Natl. Acad. Sci. USA* **89**, 5951-5955 (1992).

[231] S.D. Swanson, M.S. Rosen, B.W. Agranoff, K.P. Coulter, R.C. Welsh, and T.E. Chupp, Brain imaging with laser-polarized ^{129}Xe. *Magn. Reson. Med.* **38**, 695-698 (1997).

[232] R.C. Welsh, T.E. Chupp, K.P. Coulter, M.S. Rosen, S.D. Swanson, and B.W.

Agranoff, Magnetic resonance imaging with laser-polarized ^{129}Xe. *Nucl. Instr. and Meth. in Phys. Res. A* **402**, 461-463 (1998).

[233] S.D. Swanson, M.S. Rosen, K.P. Coulter, R.C. Welsh, and T.E. Chupp, Distribution and dynamics of laser-polarized ^{129}Xe magnetization *in vivo*. *Magn. Reson. Med.*, submitted.

[234] S. Peled, F.A. Jolesz, C.H. Tseng, L. Nascimben, M.S. Albert, and R.L. Walsworth, Determinants of tissue delivery for ^{129}Xe magnetic resonance in humans. *Magn. Reson. Med.* **36**, 340-344 (1996).

[235] C.C. Martin, R.F. Williams, J.-H. Gao, L.D.H. Nickerson, J. Xiong, and P.T. Fox, The pharmacokinetics of hyperpolarized xenon: implications for cerebral MRI. *J. Magn. Reson. Imag.* **7**, 848-854 (1997). An interactive web site containing a xenon respiration model can be found at http://ric.uthscsa.edu/staff/charlesmartinphd.html.

[236] B.M. Goodson, Y.-Q. Song, R.E. Taylor, V.D. Schepkin, K.M. Brennan, G.C. Chingas, T.F. Budinger, G. Navon, and A. Pines, *In vivo* NMR and MRI using injection delivery of laser-polarized xenon. *Proc. Natl. Acad. Sci. USA* **94**, 14725-14729 (1997).

[237] T.F. Budinger and R.H. Huesman, Ten precepts for quantitative data acquisition and analysis. *Circulation* **72**, 53-62 (1985).

[238] A.L. Cowles, H.H. Borgstedt, and A.J. Gillies, Tissue weights and rates of blood flow in man for the prediction of anesthetic uptake and distribution. *Anesthesiology* **35**, 523-526 (1971).

[239] W.S. Snyder (Chair), Report of the task group on reference man. *Ann. ICRP* **23**, 121 (1975).

[240] R.Y.Z. Chen, F.-C. Fan, S. Kim, K.-M. Jan, S. Usami, and S. Chien, Tissue-blood partition coefficient for xenon: temperature and hematorcrit dependence. *J. Appl. Physiol.* **49**, 178-183 (1980).

[241] N.A. Lassen, J. Lindbjerg, and O. Munck, Measurement of blood-flow through skeletal muscle by intramuscular injection of xenon-133. *Lancet* **1**, 686-689 (1964).

[242] R.V. Pozderac, T.A. Miller, and S.M. Lindenauer, 133Xe muscle clearance: a screening test for arterial occlusive disease. *Radiology* **117**, 633-635 (1975).

[243] L. Zhao, A. Venkatesh, D. Balamore, F.A. Jolesz, and M.S. Albert, Vascular infusion of hyperpolarized ^{129}Xe for MRI. *Proc. ISMRM*, 6th Scientific Meeting. Sydney; 1998.

[244] D. Beauregard, Artificial Blood. *Chemistry and Industry* **12**, 459-460 (1995).

[245] J. Wolber, I.J. Rowland, M.O. Leach, and A. Bifone, Perfluorocarbon emulsions as intravenous delivery media for hyperpolarized xenon. *Magn. Reson. Med.* **41**, 442-449 (1999).

[246] J. Wolber, I.J. Rowland, T. Prock, D.J. Collins, G.S. Payne, M.O. Leach, and A. Bifone, Intravenous delivery of hyperpolarized xenon. *Proc. ISMRM*, 6th Scientific Meeting. Sydney; 1998.

[247] A. Venkatesh, L. Zhao, D. Balamore, F.A. Jolesz, and M.S. Albert, Hyperpolarized ^{129}Xe imaging using gas-filled liposomes. *Proc. ISMRM*, 6th Scientific Meeting. Sydney; 1998.

[248] M.S. Chawla, X.J. Chen, H.E. Möller, G.P. Cofer, C.T. Wheeler, L.W. Hedlund, and G.A. Johnson, *In vivo* magnetic resonance vascular imaging using laser-polarized ^{3}He microbubbles. *Proc. Natl. Acad. Sci. USA* **95**, 10832-10835 (1998).

[249] H.L. Clever (editor), *Vol. 2: krypton, xenon and radon - gas solubilities.* (Oxford: Pergamon) 1979.

[250] T.R. Stengle, N.V. Reo, and K.L. Williamson, Nuclear magnetic relaxation of xenon-131 in solution. The influence of solvent electric moment and dynamics on solute relaxation. *J. Phys. Chem.* **88**, 3225-3228 (1984).

[251] H.E. Möller, M.S. Chawla, X.J. Chen, B. Driehuys, K.C. Hasson, L.W. Hedlund, C.T. Wheeler, and G.A. Johnson, Vascular ^{129}Xe imaging in live rats. *Proc. ISMRM*, 6th Scientific Meeting. Sydney; 1998.

[252] H.E. Möller, M.S. Chawla, X.J. Chen, B. Driehuys, L.W. Hedlund, C.T.

Wheeler, G.A. Johnson, Magnetic resonance angiography with hyperpolarized ^{129}Xe dissolved in a lipid emulsion. *Magn. Reson. Med.* **41**, 1058-1064 (1999).

[253] G.L. Pollack, R.P. Kennan, and G.T. Holm, Solubility of inert-gases in PFC blood substitute, blood plasma, and mixtures. *Biomat. Artif. Cell. Im.* **20**, 1101-1104 (1992).

[254] E.C. Greene, *Anatomy of the Rat.* (New York: Hafner) 1963.

[255] D. Raftery, H.W. Long, D. Shykind, P.J. Grandinetti, and A. Pines, Multiple-pulse nuclear magnetic resonance of optically pumped xenon in a low magnetic field. *Phys. Rev. A* **50**, 567-574 (1994).

[256] L. Darrasse, G. Guillot, P.J. Nacher, and G. Tastevin, *Proc. ISMRM*, 6th Scientific Meeting. Sydney; 1998.

[257] C.H. Tseng, G.P. Wong, V.R. Pomeroy, R.W. Mair, D.P. Hinton, D. Hoffmann, R.E. Stoner, F.W. Hersman, D.G. Cory, and R.L. Walsworth, Low-field MRI of laser-polarized noble gas. *Phys. Rev. Lett.* **81**, 3785-3788 (1998).

[258] J. Clarke, SQUID fundamentals. In: *SQUID Sensors: Fundamentals, Fabrication and Applications* (H. Weinstock, ed.). (the Netherlands: Kluwer Academic), 1-62, 1996.

[259] D.M. TonThat, M. Ziegeweid, Y.-Q. Song, E.J. Munson, S. Appelt, A. Pines,

and J. Clarke, SQUID detected NMR of laser-polarized xenon at 4.2 K and at frequency down to 200 Hz. *Chem. Phys. Lett.* **272**, 245-249 (1997).

[260] M.P. Augustine, A. Wong-Foy, J.L. Yarger, M. Tomaselli, A. Pines, D.M. Ton-That, and J. Clarke, Low field magnetic resonance images of polarized noble gases obtained with a dc superconducting quantum interference device. *Appl. Phys. Lett.* **72**, 1908-1910 (1998).

[261] K. Schlenga, R.F. McDermott, J. Clarke, R.E. de Souza, A. Wong-Foy, and A. Pines, High T_c SQUIDs for low-field NMR and MRI of room temperature samples. *IEEE Trans. on Appl. Supercond.* **9**, 4424-4427 (1999).

[262] A. Wong-Foy, S. Saxena, R.F. McDermott, H.M. Bitter, A. Moule, B.M. Goodson, J. Clarke, and A. Pines, unpublished work.